Numerical simulation of multiphase jet fragmentation using Smoothed Particle Hydrodynamics

Thomas Chun Long Yue, BSc., MSc.

Thesis submitted to The University of Nottingham

for the degree of Doctor of Philosophy,

February 2015

Abstract

This thesis is devoted to the study of multiphase jet fragmentation using Smoothed Particle Hydrodynamics (SPH). The theoretical aspects of three hydrodynamic instabilities, namely the Kelvin-Helmholtz instability (KHI), Rayleigh-Taylor instability (RTI), and Rayleigh Plateau instability (RPI) are reviewed. The linear growth rate of the combined KHI and RTI are derived by means of linear perturbation in chapter 2. The linear growth rate of the multiphase RPI is presented in chapter 7.

An overview of the Smoothed Particle Hydrodynamics is given in chapter 3. A pseudo-consistent SPH scheme is presented for the simulation of multiphase flow problems. Additionally, two interface stabilisation models are presented: quasi-buoyancy model and gas-repulsion model. When used in combination with the pseudo-consistent SPH scheme, these models are found to be superior than those presented in the weakly-compressible SPH literature and allows for the simulations for density ratio up to three-magnitudes.

The development of an idealised KHI and a KHI subjected to constant gravitational acceleration (stratified shear instability) is examined in chapter 5. The extracted linear growth rate are compared with the theoretical growth rate presented both in the literature and in chapter 2 for the purpose of validation. The development of a single- and multi-mode RTI are studied by means of SPH in chapter 6. Chapter 7 presents the results for the three-dimensional RPI occurring between two fluids. Based on the knowledge acquired in chapter 5-7, the multiphase jet fragmentation driven by the previously mentioned hydrodynamic instabilities are presented in chapter 8. Finally, the major research findings and recommendations are summarised in chapter 9.

First Supervisor: Dr. Frazer R. Pearce

Second Supervisor: Dr. Arno C.H. Kruisbrink

Internal Examiner: Dr. Mike Swift (University of Nottingham)

External Examiner: Prof. Justin Read (University of Surrey)

Submitted: Oct 15 2014

Examined: Feb 4 2015

Final Version: Feb 9 2015

Declaration

I declare that the thesis is the result of my own work which has been mainly undertaken during the period of registration as a PhD candidate at the University of Nottingham unless otherwise referenced. Chapters 3 (sections 4.4.2, 3.11.3, 3.11.4), 4, 5, 6, 7 are based on the following articles.

Journal articles

1. Numerical Simulations of two-dimensional Kelvin-Helmholtz Instability using weakly compressible Smoothed Particle Hydrodynamics, T. Yue, F. Pearce, A.C.H. Kruisbrink, H. Morvan, International Journal for Numerical Methods in Fluids, Date of submission: June 13 2014, status: accepted for publication.

2. Numerical Simulations of single and multi-mode Rayleigh-Taylor Instabilities using weakly-compressible Smoothed Particle Hydrodynamics, T. Yue, F. Pearce, A.C.H. Kruisbrink, H. Morvan, International Journal for Numerical Methods in Fluids, Date of submission: February 6 2015, status: submitted.

3. Numerical simulation of a stratified shear instability using Smoothed Particle Hydrodynamics, T. Yue, F. Pearce, A.C.H. Kruisbrink, H. Morvan, International Journal for Numerical Methods in Fluids, status: drafted and ready for submission.

Conference proceedings

1. SPH concepts for continuous wall and pressure boundaries, A.C.H. Kruisbrink, F.R. Pearce, T. Yue, K.A. Cliffe and H.P. Morvan, Proceedings of 6^{th} international SPHERIC workshop, Hamburg, Germany, 2011, 298-304.

2. SPH multi-fluid model with interface stabilization based on quasi-buoyancy correction, A.C.H. Kruisbrink, F.R. Pearce, T. Yue, K.A. Cliffe and H.P. Morvan, Proceedings of 7^{th} international SPHERIC workshop, Prato, Italy, 2012, 285-302.

3. Numerical simulation of jet fragmentation in multi-fluid medium using Smoothed Particle Hydrodynamics, T. Yue, A.C.H Kruisbrink, F.R. Pearce, H.P. Morvan, Proceedings of 9^{th} international SPHERIC workshop, Paris, France, 2014, 80-86.

4. Momentum conserving methods that reduce particle clustering in SPH, Proceedings of 9^{th} international SPHERIC workshop, S. Korzilius, A.C.H. Kruisbrink, T. Yue, W. Schilders and M. Anthonissen, Paris, France, 2014, 268-274.

Journal articles in preparation

1. SPH particle collisions for multi-fluid applications and walls, A.C.H. Kruisbrink, S.P. Korzilius, T. Yue, F.R. Pearce and H.P. Morvan, intended journal for submission: Journal of Computational Physics.

2. Generalization of SPH multi-fluid models with interface stabilization based on pressure gradient correction, A.C.H Kruisbrink, F.R. Pearce, T. Yue, K.A. Cliffe, H.P. Morvan, intended journal for submission: Journal of Computational Physics.

Articles published but not do not form part of the discussion in this thesis

1. SPH surface tension model without need for calibration or evaluation of curvature, A.C.H. Kruisbrink, F.R. Pearce, T. Yue, K.A. Cliffe and H.P. Morvan, Proceedings of 8^{th} international SPHERIC workshop, Trontheim, Norway, 2013, 31-37

2. Smoothed particle hydrodynamics simulations of flow separation at bends, Computers & Fluids, Jan 2014:90:138-146.

3. Subhaloes gone Notts: Spin across subhaloes and finders, Monthly Notices of the Royal Astronomical Society 12/2012; 429(3)

Acknowledgements

Foremost, I would like to express my sincere gratitude to my supervisors Prof. Frazer Pearce and Dr. Arno Kruisbrink, and collaborators Prof. Andrew Cliffe, Prof. Herve Morvan, Dr. Hanni Lux and Dr. Claudio Dalla Vecchia for everything I learned from them and for their encouragement during my studies. In particular, I am thankful for Prof. Frazer Pearce for granting me the opportunities to attend annual CosmoComp conferences, and Dr. Claudio Dalla Vecchia for organising the visitor position at the Max-Planck Institute for extraterrestrial Physics. These opportunities enable an once astronomer enthusiasts like myself to transform from a never-was to a want-to-be astronomer. I sincerely hope that the knowledge and experience acquired would enable me to conduct further research in numerical astrophysics. I would like to thank the School of Physics and Astronomy, University of Nottingham High Performance Computing center and Rolls Royce Plc. for funding this research project.

I am forever grateful to my family for their support and love throughout the years. Particularly my father for paving my way through an adventurous journey into Mathematics and Sciences. I must express my gratitude to my beloved (proposal awaiting) fiancé Elaine Chan for her patience and effort in our relationship over the past decade. I would also like to thank my brothers for their unconditional support, especially to those who reached out their hands during the darkest moments of my life. Finally, a special thanks to Dr. M.X. Chen for his mentor-ship and encouragement since my undergraduate studies.

Contents

List of Figures

List of Tables

Nomenclature

Empty your mind, be formless, shapeless - like water.

Now you put water in a cup, it becomes the cup.

You put water into a bottle it becomes the bottle.

You put it in a teapot it becomes the teapot.

Now water can flow or it can crash.

Be water, my friend.

-Bruce Lee

Chapter 1

Introduction

1.1 Motivation

Jets, collimated streams of matter that carry higher momentum than their surrounding ambient medium, are found in many scientific and technological applications. In astrophysics, jets play a significant role in young stellar objects [8, 9, 10], proto-planetary nebulae [11, 12] as well as active galactic nuclei [13, 14]. In technological applications, jets are important in precision cutting machinery [15, 16, 17], ink-jet printing technologies [18, 19, 20] and jet-engine propulsion systems [21, 22]. Jets occur at a vast variety of length-scales and are driven by many physical effects. For instance, astrophysical jets have length-scale that vary from $\mathcal{O}(10^{16}\text{m})$ to $\mathcal{O}(10^{22}\text{m})$ where the jet medium consist of plasmas travelling in the supersonic regime [23, 24] under the influence of magnetohydrodynamical effects. In combustion engine propulsion systems, jets have a typical length-scale of $\mathcal{O}(10^{-3}\text{m})$ and their characteristics are influenced by the presence of solid boundaries, the ambient medium as well as heat transfer mechanisms [21, 25, 26]. Jets in a ink-jet printer have a typical length-scale of $\mathcal{O}(10^{-3}\text{m})$ driven by the combination of viscous effects and surface tension [27, 28, 29].

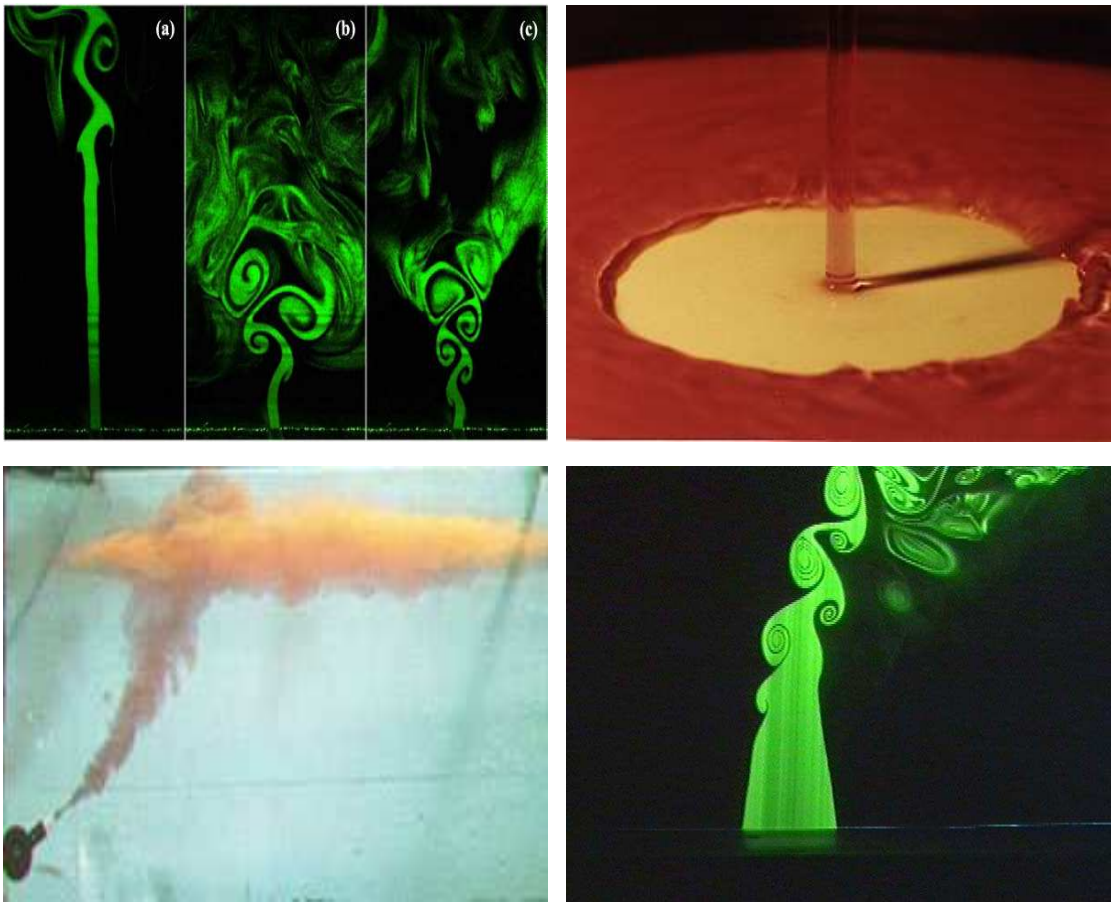

Figure 1.1: Experimental results presented in the literature. (top left) free jet subjected to multi-mode acoustic perturbations [1], (top right) liquid jet impingement onto a solid boundary [2], (bottom left) buoyant jet, (bottom right), jet in a cross flow [3].

Given their wide range of applications, jet flows have received significant attention from the physical science and the engineering community. From an academic point of view, researchers are primarily interested in the conditions for the transition from laminar flow to turbulent flow. From a practical point of view, engineers are interested in flow regimes that lead to the atomisation of jets into droplets, the thermal and hydrodynamic characteristics of jet impingement on solid boundaries, as well as jet flows subjected to different orifice designs.

Jet flows have been investigated by many researchers since the 14^{th} century. One of the earliest accounts of jet flow can be found in the work of Leonardo-da-Vinci in the Codex of Leicester [30], where the author investigated qualitatively that the break-up of a water jet into droplets is due to the competition between

gravity and the cohesive force between water particles. Since then, extensive research has been conducted to further understand jet flows under different conditions. Over a period of time, this has evolved into four fields: free jet flow [31, 32], jet impingement [33, 34, 35], buoyant jet flow [36] and jet in cross-flow [37, 38, 39]. Given the relevance of these flow scenarios in industrial applications, the research question naturally differs as well. For instance, the study of free jet flow is relevant to nozzle and orifice design optimisations, where researchers aim to answer questions such as the rate of jet break-up, the average droplet size, and the generation of secondary droplets after the primary break-up has occurred. The study of jet impingement is relevant to cooling and lubrication processes in oil-engine systems [40, 41, 42]. In particular, researchers are interested in the rate of cooling and the control of splashing when a jet impacts a solid boundary [35, 43]. The understanding of buoyant jets is crucial to sewage or industrial waste water treatment processes, where researchers aim to quantify the rate of dilution and its dependence on the initial stratification of the ambient fluid [44, 45, 46, 47]. Finally, jets in a cross-flow are commonly found in combustion chambers and chemical reactors, where researchers aim to understand the mixing process occurring at the interface between fluids [48, 49, 50].

The dynamics of jets is governed by the interplay of hydrodynamic instabilities occurring at the interface between the jet medium and its surrounding ambient medium. For instance, a low Mach number liquid jet subjected to a constant acceleration is governed by three hydrodynamic instabilities: the Kelvin-Helmholtz instability, the Rayleigh-Taylor instability and the Rayleigh-Plateau instability. The Kelvin-Helmholtz instability is driven by the shearing motion between fluid layers. The Rayleigh-Taylor instability becomes important when the pressure gradient due to gravity opposes the change in density between the two fluids. Finally, the Rayleigh-Plateau instability is crucial if the jet occurs in a flow regime dominated by effects of surface tension.

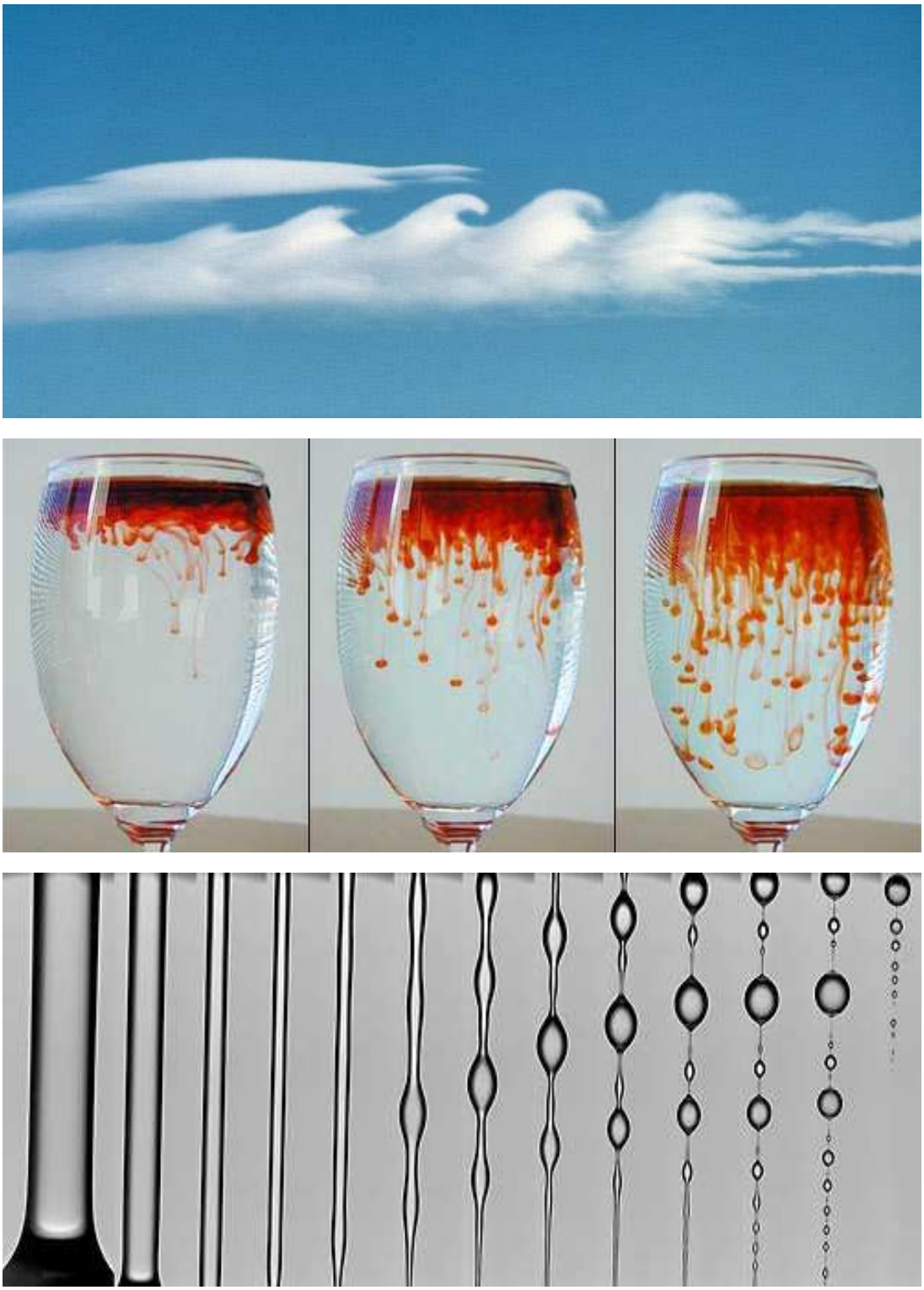

Figure 1.2: Hydrodynamic instabilities relevant to this thesis. From top to bottom, the Kelvin-Helmholtz instability (photo credit: Brooks Martner, NOAA), Rayleigh-Taylor instability (photo credit: James Riordon, AIP), Rayleigh-Plateau instability (photo credit: A. Wagner et al).

Developments of the theory behind hydrodynamic instability prospered during the 18^{th}-19^{th} century. This area focuses on the stability and instability of fluid flow problems. A flow is considered stable if all initially small perturbations remain small in time. Whereas the flow is deemed unstable if at least one initially small perturbation is amplified into a large perturbation after some finite time. It is well understood from experiment that the growth of hydrodynamic instabilities mentioned above can rapidly lead to a transition laminar flow to turbulent flow [51]. More importantly, the onset of turbulence leads to velocity fluctuations that generate eddies of sizes. The interaction of these eddies gives rise to a chaotic behaviour which challenges the physical modelling of turbulent flow. Turbulence is a complex subject. Richard Feynman once said:*"Turbulence is the most important unsolved problem of classical physics"* [52].

Advances in computational fluid dynamics (CFD) over the past decades have enabled researchers to study the dynamics of hydrodynamic jet by means of numerical simulations. The conventional mesh-based CFD techniques rely on the discretisation of the Navier-Stokes equations onto a mesh, where the field quantities are numerically approximated at the nodal mesh points. Generally speaking, there are two main approaches within the CFD community to model turbulence: direct numerical simulation (DNS) [53, 54] and the utilisation of turbulence models [55, 56]. The essence of the DNS is to resolve all small scale motions without the use of additional models. Nevertheless, this approach requires a resolution which is far beyond the computational resource offered by state-of-the-art computers. At the time of writing this thesis, the highest Reynold number achieved with DNS approach is $Re = 5200$ and utilises 786K CPUs [57] applied to a channel flow. On the other hand, the majority of research groups have taken the practical path of developing sub-grid turbulence models [55, 56] that encapsulate the effects of turbulence. While the conventional turbulence models are widely available in commercial CFD codes, the fundamental aspect

of hydrodynamic instabilities as well as the onset of the transition from laminar to turbulent flow remains a challenging topic in fluid dynamics [51].

Furthermore, despite the popularity of CFD for the simulation of turbulent jets, these methods are known to suffer from three shortcomings. Firstly, mesh-based methods generally suffer from numerical diffusion which violates the conservation of mass and momentum [58]. Secondly, the use of an adaptive mesh refinement procedure introduces additional computational complexity. Thirdly, the use of interface tracking techniques are mandatory when the spatial distribution of physical quantities are discontinuous. In addition, the performance of these front tracking techniques varies depending on the specific implementation [59]. To avoid these shortcomings, extensive research has been conducted to simulate fluid flow by means of mesh-free methods such as Smoothed Particle Hydrodynamics. Gingold and Monaghan [60], Lucy [61] first introduced SPH to study hydrodynamic problems in astrophysics. In recent years, it has been extended to simulate subsonic terrestrial fluid flow problems [62]. The mesh-free particle nature of SPH does not require the use of interface tracking routines and as such it is advantageous for modelling flows with large morphological variations as well as being Galilean invariant and satisfies conservation of mass, momentum, and energy.

Witnessing the comparative advantages of SPH over conventional CFD methods, a collaborative research project was initiated between the School of Physics and Astronomy, School of Mathematical Science and the Department of Mechanical, Materials and Manufacturing Engineering at the University of Nottingham in partnership with Rolls Royce Plc. in 2010. The aim of this project is to conduct a feasibility study into the propagation of hydrodynamics jets in an ambient medium, including simulation of multiphase flow with SPH. The aim of this project is further broken down into five major objectives: (i) review of the theoretical hydrodynamic instability literature, (ii) assess and review existing

multiphase SPH schemes, in particular those relevant to weakly-compressible hydrodynamics, (iii) development of a multiphase SPH scheme suitable for high density ratios, (iv) systematic investigation of multiphase hydrodynamic instabilities: Kelvin-Helmholtz instability, Stratified Shear instability, Rayleigh-Taylor instability and Rayleigh-Plateau instability, and (v) development of SPH software that is suitable for aero-engineering applications.

1.2 Outline of present work

In chapter 2, we review the theoretical aspects of two fundamental hydrodynamic instabilities that are relevant to multiphase jet fragmentation. We extend the results in the literature by deriving a linear growth rate for the combined Kelvin-Helmholtz instability (KHI) and Rayleigh-Taylor instability (RTI) from the linearised Navier-Stokes equation. In particular, we focus on two scenarios where the linear growth rate can be derived analytically, namely for inviscid fluids with a smoothed interface and viscous fluids with a sharp interface. This allows for a quantitative comparison of the effects of viscosity, gravity, and smoothing of the initial density and velocity distribution against the results reported in the literature as well as the numerical results from SPH simulations in the subsequent chapters of this thesis.

The Smoothed Particle Hydrodynamics method is introduced in chapter 3. The first part of the chapter discusses the principles of SPH for solving the fluid dynamical equations. The concept of a kernel density estimate used in mesh-free methods is discussed, followed by the desired properties of kernel functions. We demonstrate that the spatial derivative approximations found in the literature can be derived from a generalised spatial derivative approximation. Based on the generalised spatial derivatives, we show that a consistent set of SPH fluid dynamical equations can be derived from the Euler-Lagrange equation. Finally,

we discuss SPH artificial viscosity models and equation-of-states commonly employed in the SPH literature.

The second part of the chapter focuses on multiphase SPH. A survey of the literature of multiphase SPH methods within the astrophysical and terrestrial fluid dynamics community is presented. A pseudo-consistent multiphase SPH scheme suitable for low density ratios is introduced. Afterwards, we identify additional challenges in modelling multiphase flow in weakly-compressible SPH and present additional models to enhance the stability of the multiphase SPH scheme for density ratios up to three magnitudes. The performance of these SPH schemes is compared against other multiphase schemes in the terrestrial fluid dynamics SPH literature.

The SPH software implemented and used for the simulations presented herein is described in chapter 4. A survey of the literature is given to review the features of existing SPH codes in the research community. Details regarding the data structure, neighbour-list search algorithm, boundary treatment methods and time integration scheme implemented in our SPH code `Draco` are discussed.

Chapter 5 presents the results of the multiphase KHI. In particular, we focus on the idealised KHI (without the influence of gravity) and the KHI subjected to gravity, also known as the stratified shear instability (SSI) [63]. The results are compared with the linear growth rates derived in chapter 2 and those found in the literature [5, 7, 64, 65, 66].

The numerical results for single- and multi-mode RTI are presented in chapter 6. In order to validate the single-mode results, the numerical results are compared with the linear growth rate [5] during the linear regime and the drag-buoyancy model [67, 68, 69, 70] during the nonlinear regime. The fitted coefficient for the self-similar relationship reported in the literature [71, 72, 73, 74] is used for the comparison between numerical results, theory and experiments for the multi-mode RTI.

The numerical results for the Rayleigh-Plateau instability (RPI) are presented in chapter 7. A pre-investigation study is performed to validate the surface tension model introduced by Adami et al. [75] for some standard test cases. The RPI is then simulated in three dimensions, where the influence of artificial viscosity parameters, initial perturbation and Atwood number is studied.

Based on the knowledge acquired from the three hydrodynamic instabilities, we apply the multiphase SPH scheme in chapter 8 to simulate the fragmentation of a hydrodynamic jet driven by the KHI, RTI and RPI separately. The simulations herein give qualitative insight into the modelling of laminar hydrodynamic jet with SPH. Finally, a summary of our major research findings and list of recommendations for future work is given in chapter 9 .

Chapter 2

Theory

2.1 Introduction

In this chapter, the theoretical aspects of hydrodynamic instabilities are reviewed. In particular, the discussion herein concentrates on the analytical linear growth rates for two fundamental instabilities, namely the Kelvin-Helmholtz instability (KHI) and the Rayleigh-Taylor instability (RTI). A Literature review regarding the numerical and experimental work will be provided in the respective chapters (chapter 5 for KHI and chapter 6 for RTI).

The content of this chapter is organised as follows: starting from the three dimensional Navier-Stokes equations, linear stability analysis is applied to obtain a system of linearised differential equations that models the initial stage of the instability. Based upon Squire's theorem and Rayleigh inflection point theorem, a generalised model equation that encapsulates the combined growth rate of KHI and RTI is presented. We demonstrate the derived growth rates from the model confirms earlier results in the literature. Finally, we apply the model to examine the scenarios relevant to the SPH simulations presented in chapters 5-6.

2.2 Background

Kelvin [76] and Helmholtz [77] pioneered the investigation of shear instabilities by studying the relative motion between two adjacent fluids subjected to a tangential velocity difference. This phenomenon has subsequently become known as the Kelvin-Helmholtz instability (KHI). In the absence of damping mechanisms such as gravity, viscosity and surface tension, the interface between the two fluids is unstable and consequently any perturbation grows with time. Parallel to the discovery of KHI, Rayleigh [78] and Taylor [79] investigated the instability between fluids of different densities subjected to acceleration; therefore coined the name Rayleigh-Taylor instability (RTI). The RTI occurs, for example, when a high density fluid is superposed onto a low density fluid and both fluids are subject to gravitational acceleration. In this case, the instability is unconditionally unstable, hence any perturbation grows provided the density gradient opposes the pressure gradient.

The KHI and RTI are the most fundamental forms of hydrodynamic instabilities and can be observed nature. For example: internal waves propagating in planetary atmospheres [80, 81], mixing processes occurring in the ocean [82], astrophysical jet collisions [83], supernova explosions [84] and inertial fusion reactors [85, 86]. Given their crucial importance, the analytical theory for these instabilities has undergone significant development since the 18^{th} century. Chandrasekhar [5] derived the linear growth rate of the KHI and RTI, assuming the base-flow[1] consists of two fluids separated by a sharp interface. In that case, the growth rate of the combined instabilities depends on the perturbation wavenumber (k), the tangential velocity difference (Δu), the gravitational acceleration ($\vec{g}$), and the density ratio between the fluids.

Following the work of Chandrasekhar [5], there has been extensive research over the past decades to incorporate additional physical effects into the linear

[1] In the context of hydrodynamic stability, the unperturbed flow is a base-flow[87]

growth rate. Miles [88] derived the necessary condition for the growth of KHI in a stratified medium. Bayly et al. [89] investigated the transition of the KHI into the turbulent regime. Bellman and Pennington [90] as well as Mikaelian [91] derived the linear growth rate of a RTI taking into account the effects of viscosity and surface tension. Junk et al. [64] extended the work of Chandrasekhar [5] to derive the analytical growth rate for a sharp interface viscous KHI. Recently, the research group of Wang et al. [7, 65], Ye et al. [66] published a series of articles in the context of plasmas physics concerning the linear growth rate for the combined KHI and RTI for smoothed initial velocity and density profiles.

The growth rates reported in the early research literature [5, 76, 77, 78, 79] are available in standard hydrodynamic instability texts [92, 93, 94]. Although the exact formulation of the base-flow varies from one text to another, linear stability analysis is employed to linearise the system of Partial Differential Equations (PDEs) that describes the fluid flow. Nonetheless, these growth rates are based on sharp interfaces and they are not suitable for modelling scenarios where smoothed base-flow profiles are considered. Therefore, a model that encapsulates the growth of the KHI and RTI is derived from the Navier-Stokes equations for incompressible fluids to allow for a quantitative comparison between SPH results and linear growth rates for smoothed initial profiles.

2.3 Mathematical model

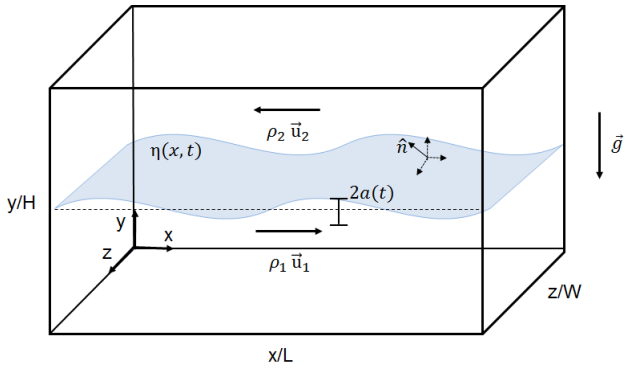

Figure 2.1: Pictorial description of three-dimensional hydrodynamic instabilities.

The dynamics of Newtonian fluids are governed by a system of PDEs, given in Cartesian coordinates as (2.1)-(2.5)

$$\frac{\partial u}{\partial t} + u\frac{\partial u}{\partial x} + v\frac{\partial u}{\partial y} + w\frac{\partial u}{\partial z} = -\frac{1}{\rho}\frac{\partial P}{\partial x} + \nu\nabla^2 u, \tag{2.1}$$

$$\frac{\partial v}{\partial t} + u\frac{\partial v}{\partial x} + v\frac{\partial v}{\partial y} + w\frac{\partial v}{\partial z} = -\frac{1}{\rho}\frac{\partial P}{\partial y} + \nu\nabla^2 v - g, \tag{2.2}$$

$$\frac{\partial w}{\partial t} + u\frac{\partial w}{\partial x} + v\frac{\partial w}{\partial y} + w\frac{\partial w}{\partial z} = -\frac{1}{\rho}\frac{\partial P}{\partial z} + \nu\nabla^2 w, \tag{2.3}$$

$$\frac{\partial \rho}{\partial t} + u\frac{\partial \rho}{\partial x} + v\frac{\partial \rho}{\partial y} + w\frac{\partial \rho}{\partial z} + \rho\left(\frac{\partial u}{\partial x} + \frac{\partial v}{\partial y} + \frac{\partial w}{\partial z}\right) = 0, \tag{2.4}$$

$$\frac{\partial u}{\partial x} + \frac{\partial v}{\partial y} + \frac{\partial w}{\partial z} = 0, \tag{2.5}$$

where $\vec{v} = (u, v, w)$ represents the velocity field in a Eulerian frame of reference and the gravitational acceleration is defined as $\vec{g} = (0, -g, 0)$. Equation (2.1)-(2.3) is the momentum equation for incompressible fluids, equation (2.4) is the continuity equation, and equation (2.5) is the incompressible criterion. For

simplicity, a base-flow is assumed only in the y direction and the perturbation wave vector is orthogonal to the y direction such that $\vec{k} = (k_x, 0, k_z)$ as shown in Figure 2.1. Applying the perturbations [95, 96],

$$\begin{aligned} \rho &\approx \rho_o + \epsilon\tilde{\rho} + O(\epsilon^2) \\ u &\approx u_o(y) + \epsilon\tilde{u} + O(\epsilon^2) \\ v &\approx \epsilon\tilde{v} + O(\epsilon^2) \\ w &\approx \epsilon\tilde{w} + O(\epsilon^2) \\ P &\approx P_o + \epsilon\tilde{P} + O(\epsilon^2), \end{aligned} \tag{2.6}$$

to equation (2.1)-(2.5) and neglecting the terms above $\mathcal{O}(\epsilon^2)$ yields a system of PDE that describes the dynamics of a first-order perturbed $\mathcal{O}(\epsilon)$ fluid system.

$$\rho_o\left(\frac{\partial\tilde{u}}{\partial t} + u_o\frac{\partial\tilde{u}}{\partial x} + \tilde{v}\frac{\partial u_o}{\partial y}\right) = -\frac{\partial\tilde{P}}{\partial x} + \nu\rho_o\nabla^2\tilde{u} + \nu(\rho_o + \tilde{\rho})\frac{\partial^2 u_o}{\partial y^2}, \tag{2.7}$$

$$\rho_o\left(\frac{\partial\tilde{v}}{\partial t} + u_o\frac{\partial\tilde{v}}{\partial x}\right) = -\frac{\partial\tilde{P}}{\partial y} + \nu\rho_o\nabla^2\tilde{v} - \tilde{\rho}|\vec{g}|, \tag{2.8}$$

$$\rho_o\left(\frac{\partial\tilde{w}}{\partial t} + u_o\frac{\partial\tilde{w}}{\partial x}\right) = -\frac{\partial\tilde{P}}{\partial z} + \nu\rho_o\nabla^2\tilde{w}, \tag{2.9}$$

$$\frac{\partial\tilde{\rho}}{\partial t} + u_o\frac{\partial\tilde{\rho}}{\partial x} + \tilde{v}\frac{\partial\rho_o}{\partial y} + \tilde{w}\frac{\partial\rho_o}{\partial z} = 0, \tag{2.10}$$

$$\frac{\partial\tilde{u}}{\partial x} + \frac{\partial\tilde{v}}{\partial y} + \frac{\partial\tilde{w}}{\partial z} = 0. \tag{2.11}$$

Allowing for perturbations of the following form

$$\begin{Bmatrix} \tilde{u}(\vec{r},t) \\ \tilde{v}(\vec{r},t) \\ \tilde{P}(\vec{r},t) \\ \tilde{\rho}(\vec{r},t) \end{Bmatrix} = \begin{Bmatrix} \hat{u}(y) \\ \hat{v}(y) \\ \hat{P}(y) \\ \hat{\rho}(y) \end{Bmatrix} e^{i(\vec{k}\cdot\vec{r}+nt)} \quad , \tag{2.12}$$

where $\vec{r} = (x, y, z)$ is the position vector and $n \in \mathbb{C}$ is the temporal frequency.

Applying the perturbations to equation (2.7)-(2.9) yields

$$\rho_o \left[i(n + u_o k_x)\tilde{u} + \tilde{v}\frac{du_o}{dy} \right] = -ik_x \tilde{P} + \nu\rho_o \left(-k^2\tilde{u} + \frac{d^2\tilde{u}}{dy^2} \right) + \nu \left(\rho_o + \tilde{\rho} \right) \frac{d^2 u_o}{dy^2}, \tag{2.13}$$

$$\rho_o i \left(n + u_o k_x \right) \tilde{v} = -\frac{d\tilde{P}}{dy} + \rho_o \nu \left(-k^2\tilde{v} + \frac{d^2\tilde{v}}{dy^2} \right) - \tilde{\rho} g, \tag{2.14}$$

$$\rho_o i \left(n + u_o k_x \right) \tilde{w} = -ik_z \tilde{P} + \rho_o \nu \left(-k^2\tilde{w} + \frac{d^2\tilde{w}}{dy^2} \right). \tag{2.15}$$

Similarly, the continuity equation (2.10) becomes

$$\tilde{\rho} = \frac{i\tilde{v}}{n + k_x u_o} \frac{\partial \rho_o}{\partial y}, \tag{2.16}$$

and the incompressible version of the continuity equation (2.11) becomes

$$i(k_x \tilde{u} + k_z \tilde{w}) = \frac{d\tilde{v}_1}{dy}. \tag{2.17}$$

The system of equations (2.13)-(2.17) are applicable to three-dimensional hydrodynamic instabilities. Nevertheless, the derivation of a three-dimensional growth rate is extremely complicated. Therefore a model reduction is usually performed to reduce a three-dimensional problem to a two-dimensional problem. The validity of such a model reduction is motivated by Squire's theorem, which guarantees the growth of a two-dimensional shear flow problem to be strictly greater than its corresponding three-dimensional shear flow problem.

Theorem 2.3.1. *Squire's theorem: For each unstable three-dimensional wave solution of a perturbed system, there exist an associated two-dimensional wave solution which is unstable at a higher wave-number.*

Although the original Squire's theorem [97] is only applicable to inviscid incompressible flow, many extensions have been proposed in the literature for more complicated scenarios. Yih [98] extended the Squire's theorem for multi-

phase viscous flows. Hesla et al. [99] formulated Squire's theorem for stratified fluids, including the effects of surface tension. Chen and Fried [100] found that the Squire's theorem is applicable to the RTI provided that there is no mass transport process across the interface. The Squire's transform is applied to the three-dimensional problem. Combining equation (2.13)-(2.14) by eliminating the pressure gradient term results in the following equation.

$$\frac{d}{dy}\left[\rho_o\left(n+u_o k\right)\frac{d\hat{v}}{dy}-\rho_o k\hat{v}\frac{du_o}{dy}\right]-k^2\rho_o\left(n+u_o k\right)\hat{v}+\frac{d}{dy}\left[k\nu\left(\rho_o+\tilde{\rho}\right)\frac{d^2u_o}{dy^2}\right]$$
$$-ik^2\frac{d}{dy}\left(\rho_o\nu\frac{d\hat{v}}{dy}\right)+i\frac{d}{dy}\left(\rho_o\nu\frac{d^3\hat{v}}{dy^3}\right)+ik^4\rho_o\nu\hat{v}-ik^2\frac{d}{dy}\left(\rho_o\nu\frac{d\hat{v}}{dy}\right)+$$
$$ik^2\frac{d\hat{v}}{dy}\frac{d\left(\rho_o\nu\right)}{dy}-\frac{k^2\hat{v}}{n+ku_o}\frac{d\rho_o}{dy}g=0. \tag{2.18}$$

Equation (2.18) describes the growth of KHI and RTI between incompressible Newtonian fluids, and it is a generalisation of the model equations found in classical hydrodynamics literature. When combined with appropriate initial and boundary conditions, it forms an initial boundary value problem such that the linear growth rates may be determined. For instance, for a single phase viscous fluid in a confined geometry, and neglecting the influence due to gravity, equation (2.18) reduces to the Orr-Sommerfeld equation for viscous parallel flow [101, 102, 103]. A further simplification can be made when the fluid is inviscid. In that case, equation (2.18) simplifies to the Rayleigh's equation for inviscid parallel flow [78]. For inviscid fluids under the influence of gravity, equation (2.18) is analogous to the Taylor-Goldstein equation [94].

Nonetheless, the scenarios mentioned above suffer from three major limitations from a modelling perspective. Firstly, the initial conditions of the base-flow vary across the literature. This introduces difficulties for the comparison between SPH and analytical theory. Secondly, it is not possible to examine the combi-

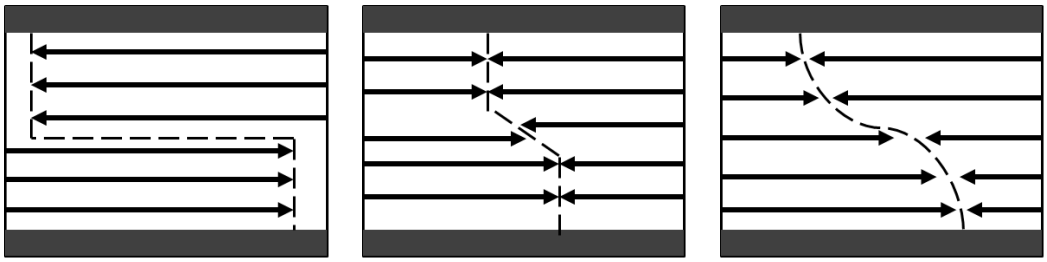

discontinuous [5] piecewise linear [104, 105] smoothed [7, 65, 66, 106]

Figure 2.2: Common base-flow velocity profiles in the literature.

nation of the effects due to viscosity, gravity and stratification in a systematic manner. Thirdly, a fully explicit analytical growth rate for multiphase viscous shear instability subjected to smoothed base-flow has not been obtained. In practice, the utilisation of computational methods is necessary to obtain the linear growth rates. Given these reasons, our discussionherein concentrates on scenarios where the analytical growth rates can be explicitly determined. Cases where the growth rate can only be obtained using numerical techniques are beyond the scope of this thesis.

Thus far we have focused on derivation of the model equation (2.18), and details regarding the formulation of the base-flow has been deliberately postponed until this point. The condition for the growth of the instability is governed by another important result in mathematical hydrodynamics, known as the *Rayleigh inflection point theorem*. The common base-flow velocity profiles in the shear flow literature are plotted in Figure 2.2[2].

Theorem 2.3.2. *Rayleigh inflection point theorem: For the occurrence of inviscid shear instability, it is necessary but not sufficient for the base-flow velocity profile to contain at least one inflexion point within the domain of interest.*

[2]The theorem does not cover the sharp profile scenario as the second derivative of a Heaviside step function is defined in terms of distributional derivatives.

2.4 Linear growth rates

In this section, we apply the model equation (2.18) to determine the linear growth rates relevant to chapter 5-6. Consider the following base flow distributions

$$u_o(y) = \begin{cases} u_1 - \frac{\Delta u}{2}\, e^{-|y-y_o|/L_u} & y > y_o \\ u_2 + \frac{\Delta u}{2}\, e^{|y-y_o|/L_u} & y < y_o \end{cases}, \tag{2.19}$$

$$\rho_o(y) = \begin{cases} \rho_1 - \frac{\Delta \rho}{2}\, e^{-|y-y_o|/L_\rho} & y > y_o \\ \rho_2 + \frac{\Delta \rho}{2}\, e^{|y-y_o|/L_\rho} & y < y_o \end{cases}, \tag{2.20}$$

where $y_o = 0$ is the position of the interface of the base-flow and $u_{1,2}$, $\rho_{1,2}$ are the far-field velocities and densities away from the fluid interface. The difference in tangential velocities with respect to the initial interface (horizontal velocities) and density across two fluid layers are defined as $\Delta u = u_1 - u_2$ and $\Delta \rho = \rho_1 - \rho_2$. In addition, L_u (L_ρ) represents the half thickness of the velocity (density) transition layer, also known as the velocity (density) gradient in literature [7, 65, 66]. Some typical velocity profiles are plotted in Figure 2.3, the density profile is in the same fashion. It follows from our definition that a larger gradient corresponds to a smoother interface, whereas the sharp interface conditions in classical hydrodynamics is given by $L_{u,\rho} = 0$.

2.4.1 Sharp interface fluid instabilities

This section focuses on the scenarios with sharp interface, where the fluids are initially separated at the interface, where the base flow properties remain constant in their respective regions. A kinematic and dynamic boundary condition are required to close the set of equations. The kinematic boundary condition ensures no flux across the interface. Therefore suppose that the initial interface undergoes a slighted perturbation $\eta(x,t) = Ae^{i(kx+nt)}$, so that the location of the

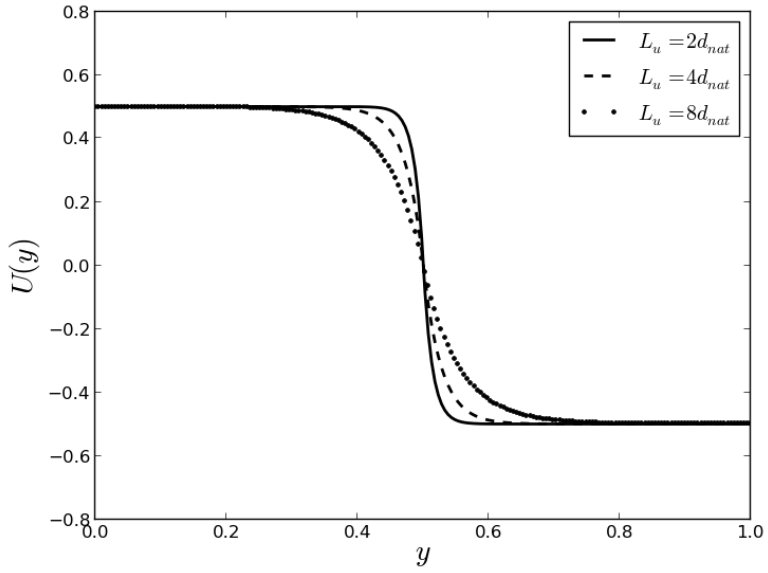

Figure 2.3: Initial velocity profile for various velocity transition layer width (L_u).

interface is given by $y = y_o + \eta(x,t)$. The kinematic boundary condition requires the Lagrangian derivative of the interface to vanish [94]. This may be written as

$$\frac{\partial \eta}{\partial t} + u_o \frac{\partial \eta}{\partial x} = \hat{v} \quad y = y_o + \eta(x,t). \tag{2.21}$$

In our case, the kinematic boundary condition simplifies to

$$i(n + ku_o)\eta = \hat{v} \quad y = y_o + \eta(x,t). \tag{2.22}$$

The dynamic boundary condition requires normal stress balance across the interface [94, 96, 107], which can be obtained from the integral of equation (2.18).

$$\left[\rho_o (n + u_o k) \frac{d\hat{v}}{dy} - \rho_o k \hat{v} \frac{du_o}{dy} + k\nu (\rho_o + \tilde{\rho}) \frac{d^2 u_o}{dy^2} + i\rho_o \nu \frac{d^3 \hat{v}}{dy^3} - 2ik^2 \rho_o \nu \frac{d\hat{v}}{dy}\right]_{y_o-\epsilon}^{y_o+\epsilon}$$
$$+ \int_{y_o-\epsilon}^{y_o+\epsilon} \left[ik^4 \rho_o \nu \hat{v} - k^2 \rho_o (n + u_o k)\hat{v} + ik^2 \nu \frac{d\hat{v}}{dy}\frac{d\rho_o}{dy} - \frac{k^2 \hat{v} g}{n + ku_o}\frac{d\rho_o}{dy}\right] dy = 0. \tag{2.23}$$

The integration region in equation (2.23) is an the infinitesimal distance near the interface $|y - y_o| = \epsilon$ and $\eta \to 0$. The fluids away from the interface are required to satisfy

$$\rho_{1,2}\left\{\left[(n + ku_{1,2}) - 2i\nu k^2\right]\frac{d^2\hat{v}}{dy^2} + i\nu\frac{d^4\hat{v}}{dy^4} - k^2[(n + ku_{1,2}) - i\nu k^2]\hat{v}\right\} = 0. \quad (2.24)$$

In addition $\hat{v}$ must be continuous across the interface (2.21) and to ensure boundedness of the solution, it is also required that $\hat{v}$ vanishes as $y \to \pm\infty$. Thus, it is described by the piecewise function

$$\hat{v} = \begin{cases} A(n + ku_1)e^{-ky} & y > y_o \\ A(n + ku_2)e^{ky} & y < y_o \end{cases}. \quad (2.25)$$

Applying the dynamic boundary condition (2.23) at the interface results the dispersion relation which describes the temporal growth of the KHI and RTI for sharp interface initial distributions.

$$n^2+2\left[k(\alpha_1u_1 + \alpha_2u_2) - \frac{ik^2\nu}{2}\right]n+k^2(\alpha_1u_1^2+\alpha_2u_2^2)-ik^3\nu(\alpha_1u_1+\alpha_2u_2)+kgA_T = 0, \quad (2.26)$$

where $\alpha_{1,2}$ is defined as follows

$$\alpha_1 = \frac{\rho_1}{\rho_1 + \rho_2} \quad , \quad \alpha_2 = \frac{\rho_2}{\rho_1 + \rho_2}. \quad (2.27)$$

The linear growth rate for sharp interface base flow is given by (2.26)

$$n = -k(\alpha_1u_1 + \alpha_2u_2) + i\left[\frac{k^2\nu}{2} \pm \sqrt{k^2\alpha_1\alpha_2\Delta U^2 + \frac{k^4\nu^2}{4} + kgA_T}\right], \quad (2.28)$$

where A_T is the Atwood number defined as

$$A_T = \frac{\rho_1 - \rho_2}{\rho_1 + \rho_2}. \quad (2.29)$$

Note that the perturbation quantities in equation (2.12) is proportional to e^{int}, where n is a complex number ($n = n_r + in_c$). The real part $Re(n) = n_r$ describes the oscillatory component and the imaginary part $Im(n) = n_c$ describes the growth (or) decay of the initial perturbation. In particular, $n_c < 0$ corresponds to the instability whereas $n_c > 0$ corresponds to the decay of the initial perturbation.

Inspecting (2.28), one should be aware that the sharp interface initial conditions are unstable for all wave-numbers, with the high wave number mode grows fastest. Nonetheless, in numerical solutions the high wave number modes are likely to be seeded by the noise in the initial conditions; hence making the comparison of numerical simulations and analytical growth rate difficult. The sensitivity to initial conditions for KHI have been analysed in the literature [58, 108, 109]. Analysing the results of numerous mesh-based simulation codes, Robertson et al. [58] reported that the numerical diffusion in presence of a bulk flow softens the initial sharp interface; therefore the small-scale structure of the KHI are resolution dependent. In particular, their results indicates that for low resolution simulations, the KHI instabilities may not develop even in the presence of bulk flows. However, they showed that such KHI do develop with sufficient resolution. In addition, the authors argued the presence of a bulk flow softens the initially sharp discontinuity between fluids. This changes the growth of the unstable modes, which gives rise to small-scale structures that qualitatively reassembles artificial secondary instabilities near the interface that is resolution dependent. Furthermore, a series of simulations was also carried out to investigate the sharp and smoothed interface KHI. Analysing their numerical results, the authors reported the sharp interface initial conditions actually amplifies the growth of the small-scale noise. In contrast, the utilisation of smoothed interface initial conditions stabilise the growth of the small-scale noise. As a consequence, this allows the seeded perturbation mode to growth unimpeded. McNally et al.

[108] performed SPH simulations (with artificial conduction [110]) for sharp and smoothed initial conditions. The authors reported similar findings as Robertson et al. [58] that small-scale noise in the initial conditions is responsible for the growth of secondary instabilities at the interface, and the smoothed initial conditions guarantee the dominated growth to be the seeded perturbation. Summarising the above, although it is less mathematically challenging to derive analytical growth rates for sharp interface initial conditions, such idealisation is a pathological case which lacks the physical motivation and is disfavoured for numerical simulations.

Sharp interface Kelvin-Helmholtz Instability

In the absence of gravity, equation (2.28) simplifies to the growth rate presented in Junk et al. [64] for a sharp interface viscous KHI. The classical growth rate for inviscid KHI in Chandrasekhar [5] is recovered by direct substitution (i.e. $\nu = 0$, $g = 0$). In Figure 2.4, the square of the growth rates is plotted as a function of the wave number for numerous kinematic viscosities. It is found that viscosity suppresses the growth with increasing wave numbers. In addition, the growth rate is found to decrease with increasing Atwood number as shown in Figure 2.5. The growth of a sharp interface viscous KHI is governed by various parameters (e.g Δu, k, A_T, ν), where A_T and ν are responsible for the suppression of the growth rate, and the tangential velocity difference Δu, and wavenumber k are responsible for the increase of the KHI growth rate. This explains the nature of the KHI that for fixed viscosity and perturbation wave number, an increase in density ratio suppresses the instability. Whereas, an increase in the tangential velocity difference amplifies the instability.

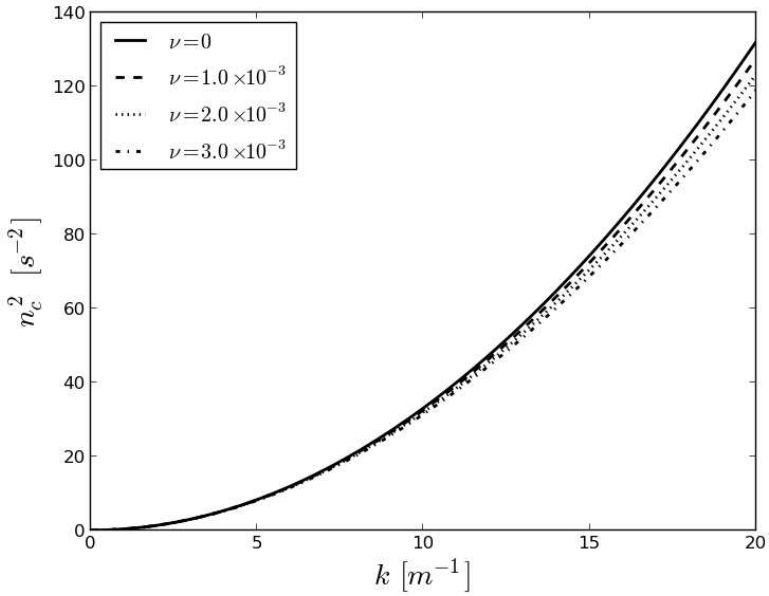

Figure 2.4: Viscous KHI growth at various kinematic viscosities plotted against wave number, with $g = 0\text{m/s}^2$, $\rho_1 = 10\text{kg/m}^3$, $\rho_2 = 1\text{kg/m}^3$, $u_1 = 1\text{m/s}$, $u_2 = -u_1$, $A_T = 0.\bar{8}$. The solid line corresponds to the growth rate for classical inviscid KHI. The presence of viscosity in the fluid system results in a less pronounced growth rate for all wave numbers.

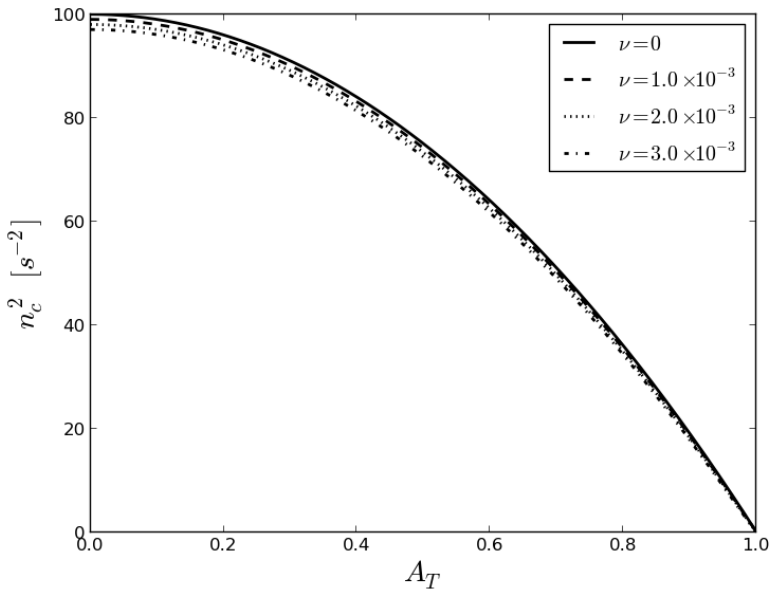

Figure 2.5: Analytical growth rate of a viscous KHI plotted as a function of Atwood number, with $k = 10\text{m}^{-1}$, $\rho_1 = 10\text{kg/m}^3$, $u_1 = 1\text{m/s}$, $u_2 = -u_1$. An increase in viscosity leads to an overall suppression of the linear growth rate for all Atwood numbers.

Sharp interface Rayleigh-Taylor Instability

When both fluids are subjected to a gravitational field, the fluid system in unstable against the RTI provided the density of the top fluid is greater than the density of the bottom fluid. For simplicity, we consider the case without tangential velocity difference, the classical growth rate for inviscid RTI presented in Chandrasekhar [5] can once again be interpreted as a special case of equation (2.28). A comparison between the inviscid and viscous growth rates suggests the presence of viscosity suppresses the RTI. More interestingly, the growth function exhibits a concave cave as shown in Figure 2.6. The growth increases rapidly in the low wave number region towards a maxima $k_{max} = 1/2(gA_T/\nu^2)^{1/3}$ prior to the successive decrease for $k > k_{max}$ as shown in Figure 2.6. Furthermore, it can

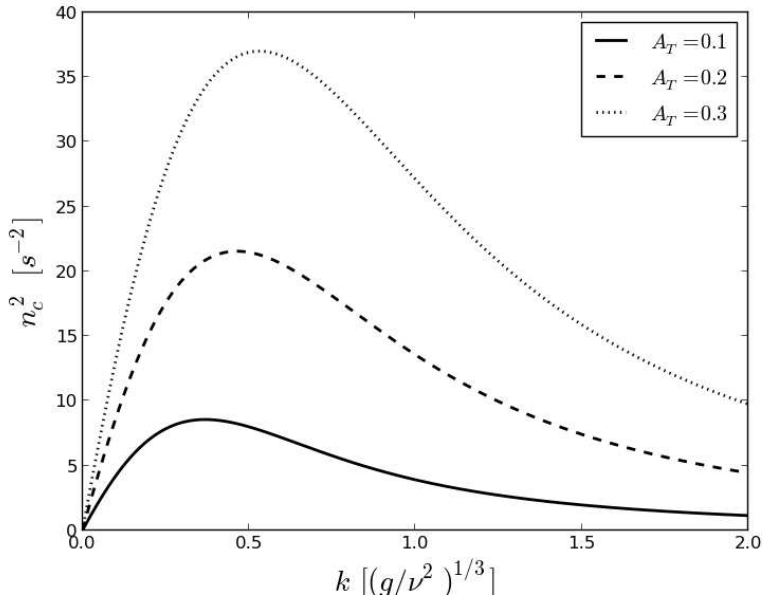

Figure 2.6: Viscous RTI growth plotted as a function of Atwood numbers, with $\rho_1 = 1\text{kg/m}^3$, $g = 1\text{m/s}^2$ and $\nu = 1 \times 10^{-4}\text{m}^2/\text{s}$.

be shown that the evolution of the interface as given by the dynamic amplitude $a(t)$ increases with time and has the bi-exponential form

$$a(t) = C_1 e^{n_c t} + C_2 e^{-n_c t}, \tag{2.30}$$

where the constants $C_{1,2} = 0.5$ are determined from the initial and boundary condition. Details of this derivation can be found in appendix 9.2.1.

2.4.2 Smoothed interface fluid instabilities

We next consider the inviscid instabilities for finite velocity and density gradients. The growth rates for KHIs, RTIs, as well as stratified shear instabilities (SSI) are presented in a systematic manner. For inviscid fluids, equation (2.18) simplifies to the differential equation in [7, 65, 66].

$$\frac{d}{dy}\left[\rho_o\left(n+u_o k\right)\frac{d\hat{v}}{dy}-\rho_o k\hat{v}\frac{du_o}{dy}\right]-k^2\rho_o\left(n+u_o k\right)\hat{v}-\frac{k^2\hat{v}}{n+ku_o}\frac{d\rho_o}{dy}g=0. \quad (2.31)$$

Utilising the approximate separable form of the vertical velocity function $\hat{v}\left(y\right)=\left(n+ku_o\right)e^{-k|y|}$ [5] and integrating (2.31) gives

$$\int_{-\infty}^{+\infty}\left[\rho_o\left(n+ku_o\right)\hat{v}+\frac{g\hat{v}}{n+ku_o}\frac{d\rho_o}{\mathrm{d}y}\right]dy=0. \quad (2.32)$$

Solving the integral analytically yields the dispersion relation

$$n^2+2k(\alpha_1u_1+\alpha_2u_2)n+k^2(\alpha_1u_1^2+\alpha_2u_2^2)+\frac{kgA_T}{kL_\rho+1}+\frac{A_T\Delta uk^2\left(n+k\bar{u}\right)}{k+1/L_u+1/L_\rho}+\frac{k^3}{4}\frac{\Delta u^2}{k+2/L_u}-\frac{\Delta uk^2A_T\left(n+k\bar{u}\right)}{k+1/L_\rho}-\frac{\Delta uk^2\left[nA_T+k(\alpha_1u_1-\alpha_2u_2)\right]}{k+1/L_u}=0, \quad (2.33)$$

where $\bar{u}=(u_1+u_2)/2$ denotes the velocity at the interface. Note that the perturbation herein (2.12) is proportional to $e^{i(\vec{k}\cdot\vec{r}+n\cdot t)}$, whereas perturbation quantities in Wang et al. [7, 65], Ye et al. [66] for smoothed initial conditions. Furthermore, the growth rate is proportional to $e^{(i\vec{k}\cdot\vec{r}+n\cdot t)}$. Despite the difference in notations, our results are consistent with the literature for smoothed initial conditions [7, 65, 66]. The dispersion relation (2.33) is utilised to study the KHI,

RTI and SSI between two superposed inviscid fluid layers for smoothed base-flow. In order to perform a systematic analysis, the smoothed interface KHI is first considered, followed by the smoothed interface RTI. Lastly, the KHI subjected to the damping of gravity is discussed in the context of stratified shear instability.

Smoothed interface Kelvin-Helmholtz Instability

The influence of the density gradients and velocity gradients is studied separately. The simplified analysis forms the basis to understand the finite velocity and density gradients KHI.

($L_u > 0$, $L_\rho = 0$): In the absence of density gradient, the growth of KHI is dependent on the following parameters (k, Δu, L_u, A_T). Figure 2.7 plots the growth rates at different Atwood numbers as a function of velocity gradient. It is found the velocity gradient leads to a less pronounced KHI growth rate. This is because the tangential velocity difference between adjacent horizontal fluid layers decreases with increasing velocity gradient; hence resulting in a less pronounced KHI. In contrary, for a fixed density gradient and an infinitesimal velocity gradient ($L_u \to 0$), the relative tangential velocity between horizontal layers is effectively the same as the relative far-field velocities Δu and the corresponding growth rate therefore converges to the classical value as given by the dotted lines in Figure 2.7.

($L_\rho > 0$, $L_u = 0$): In the finite density gradient, zero velocity gradient case, the growth rate is dependent on (k, Δu, L_ρ, A_T). In Figure 2.8, the KHI growth rate is plotted as a function of density gradient. It is found that an increase in density gradient reduces the local density ratios between adjacent fluid layers; therefore, results in a more pronounced growth rate than the classical results reported in Chandrasekhar [5].

($L_\rho > 0$, $L_u > 0$): Our results suggest an increase in velocity gradient suppresses the growth rate, and the increase in density gradient amplifies the

growth rate. Nevertheless, it is unclear how the combination of finite velocity and density gradient effects the overall KHI growth rate. For this purpose, we define the length scale ratio as $D = L_\rho/L_u$, with the velocity gradient being the parametrised variable. Figure 2.11 plots the growth rates at different length scales ratios. It is observed that when the density gradient is larger than the velocity gradient ($D > 1$), the destabilising effect of a smoothed density field dominates the stabilising effect of velocity smoothing near the interface, resulting in a slightly larger growth rate than the equal length scale case ($D = 1$). More importantly, it is found that the high wave number modes are heavily suppressed as $L_{u,\rho} \to \infty$ as shown in Figure 2.9-2.10. Overall speaking, the use of smoothed initial distributions yields smaller KHI growth rates than the classical values.

Smoothed interface Rayleigh-Taylor Instability

In the absence of tangential velocity difference, the fluid system is stable against KHI and unstable against RTI. The smoothed interface growth rate is then dependent on the following parameters (k, A_T, L_ρ). It is found that the presence of a finite density gradient reduces the local Atwood number between adjacent fluid layers; therefore, decreases in growth of RTI as illustrated in Figure 2.12.

Stratified shear Instability

Finally, the inviscid stratified shear instability is examined. The SSI is dominated by the KHI, with the density of the bottom fluid is larger than that of top fluid and both fluids are subjected to a gravitational acceleration. The gravity and density ratio (Atwood number) terms in equation (2.33) are both responsible for damping the growth of the instability, when compared against the inviscid KHI. The SSI is a conditionally unstable system that depends on four key parameters (k, Δu, A_T, g). Except the velocity difference, all of these parameters act to suppress the growth of the instability. Figure 2.13 plots the square of the growth

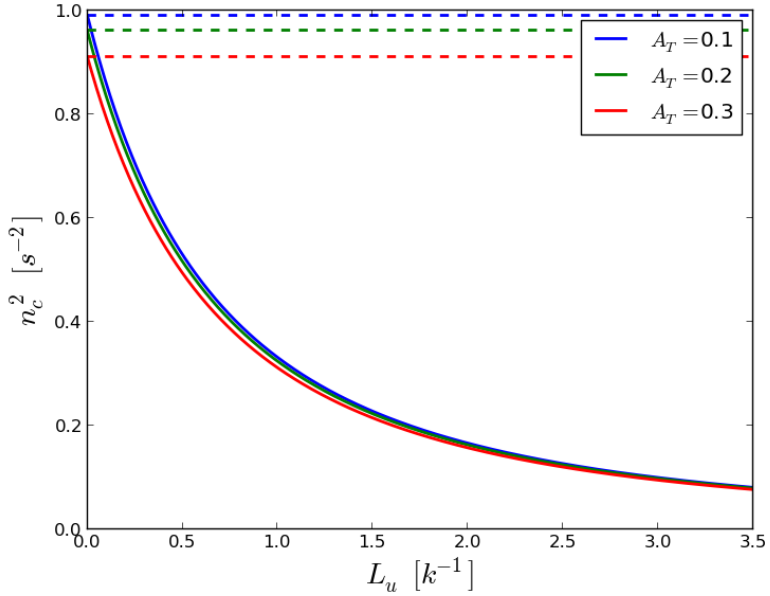

Figure 2.7: The square of the linear KHI growth rate plotted against velocity gradient, with $g = 0\text{m/s}^2$, $L_\rho = 0$, $u_1 = 1\text{m/s}$, $u_2 = -u_1$, $k = 1$. The dotted lines corresponds to the classical linear growth rate for KHI.

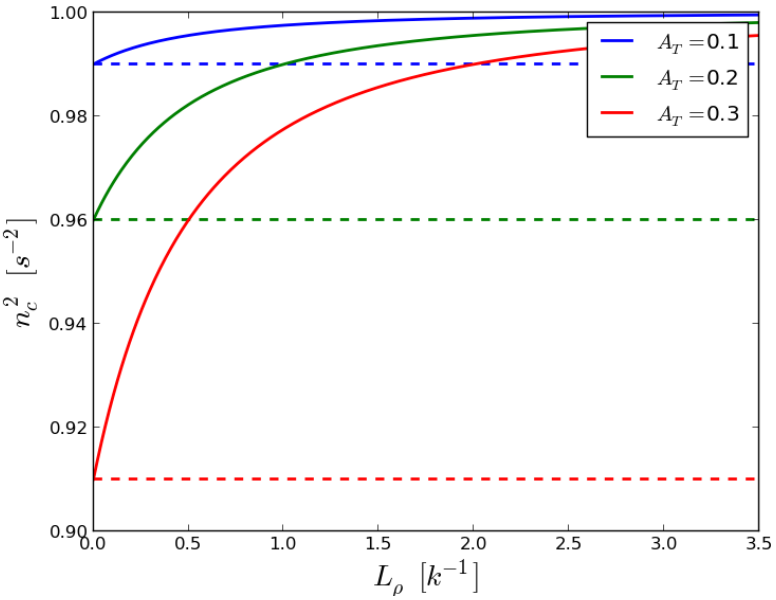

Figure 2.8: The square of the linear KHI growth rate plotted against density gradient, with $g = 0\text{m/s}^2$, $L_u = 0$, $\rho_1 = 10\text{kg/m}^3$, $k = 1$, $u_1 = 1\text{m/s}$, $u_2 = -u_1$. The dotted lines corresponds to the classical linear growth rate for KHI.

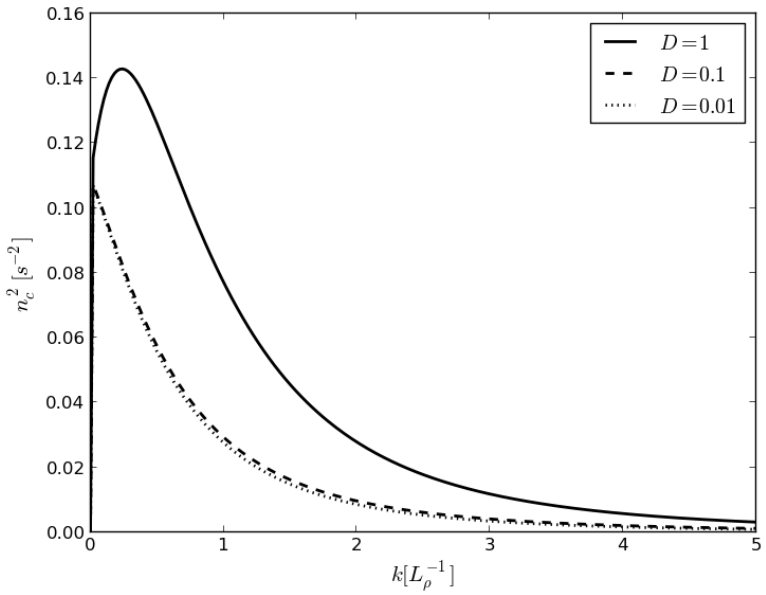

Figure 2.9: The square of the linear KHI growth rate plotted for different wave numbers with $L_\rho = 0.001$, $g = 0\text{m/s}^2$, $u_1 = 1\text{m/s}$, $u_2 = -u_1$ for multiple length scale ratios D.

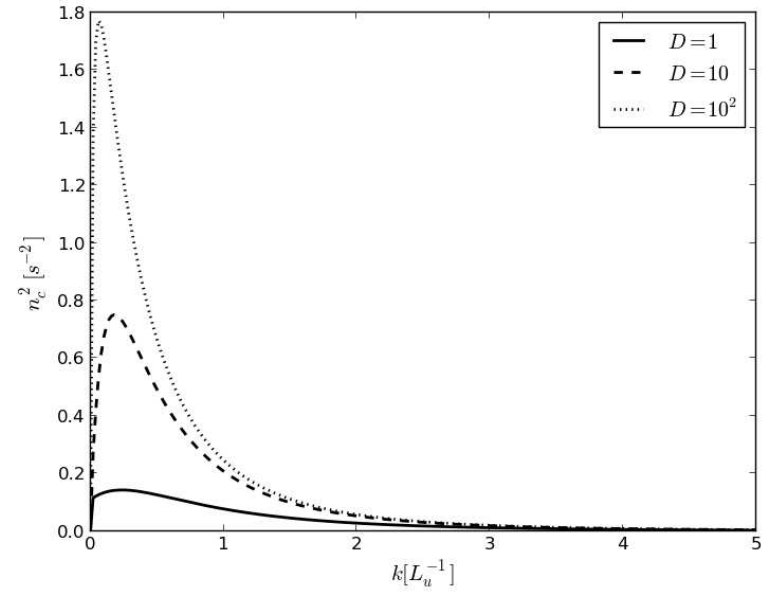

Figure 2.10: The square of the linear KHI growth rate plotted for different wave numbers with $L_u = 0.001$, $g = 0\text{m/s}^2$, $u_1 = 1\text{m/s}$, $u_2 = -u_1$ for multiple length scale ratios D.

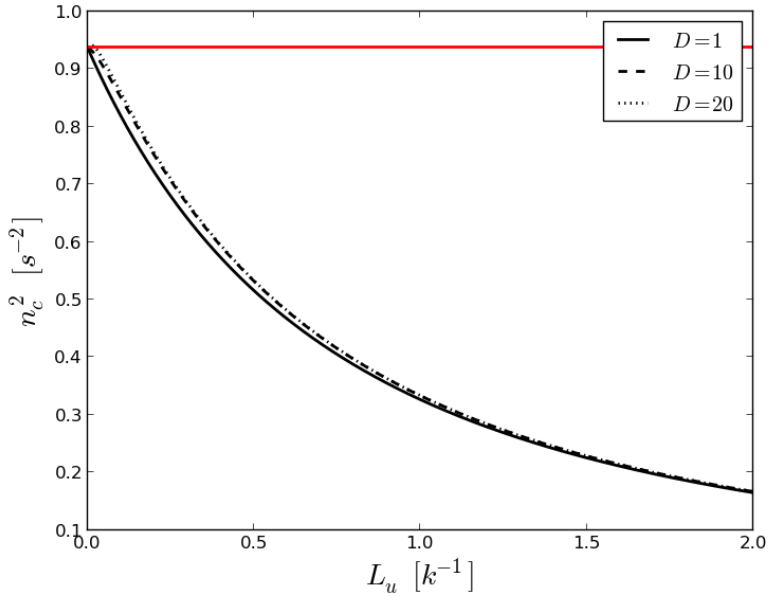

Figure 2.11: The KHI growth rate for finite velocity and density gradients plotted as a function of velocity gradient for numerous length scales ratios D, with $g = 0\text{m/s}^2$, $\rho_1 = 10\text{kg/m}^3$, $A_T = 0.25$, $k = 1$, $u_1 = 1\text{m/s}$, $u_2 = -u_1\text{m/s}$. The classical linear growth rate is plotted in red.

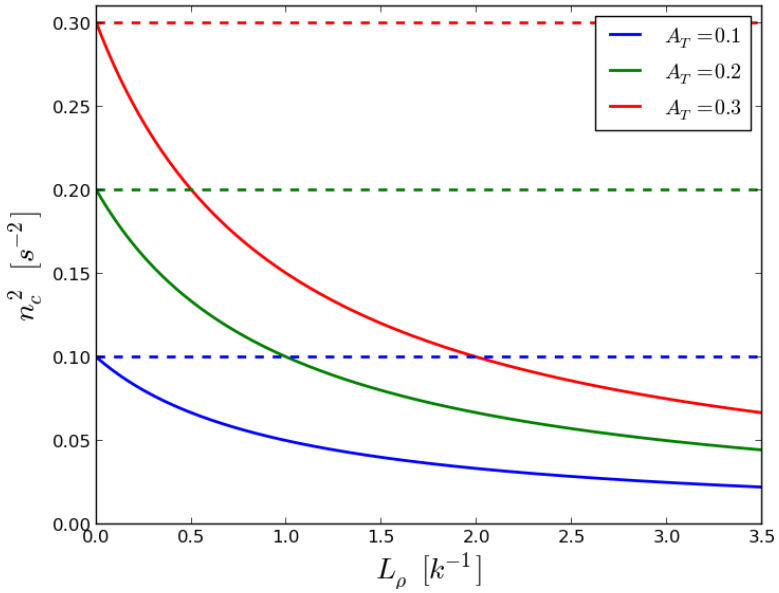

Figure 2.12: RTI growth rate plotted as a function density gradient at different Atwood numbers. The corresponding classical growth rates are plotted in dotted lines.

rate for different length scale ratios. It is found that the results closely reassemble the previous results for smoothed interface KHI in Figure 2.12. That is, for a fixed density gradient, the growth rate decreases with increasing velocity gradient. In contrast, for fixed velocity gradient, the presence of a larger density gradient (or equivalently a larger length-scale ratio D) leads to a more pronounced SSI. In addition, the growth rates for the finite density and velocity gradients case are found to be significantly lower than the classical expectations as shown in Figure 2.13.

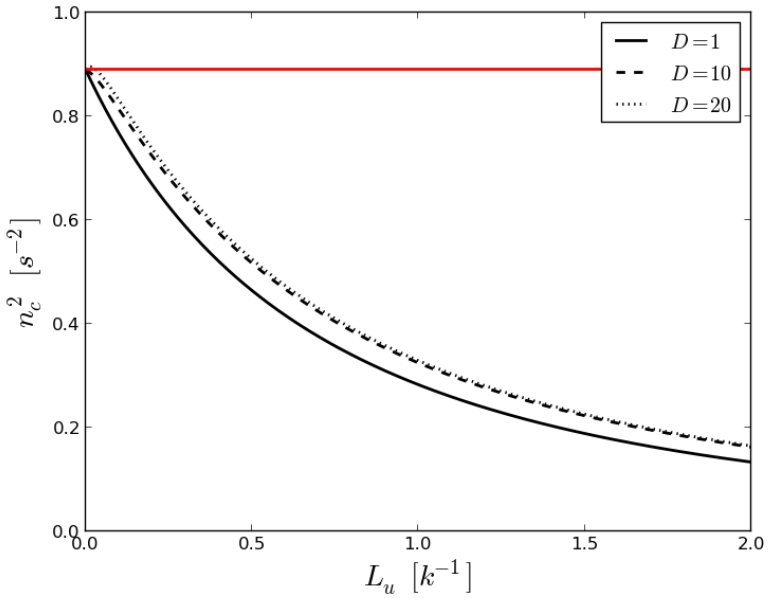

Figure 2.13: The square of growth rate plotted against velocity gradient, with $g = 1\text{kg/m}^3$, $L_\rho = 0.001$ $A_T = 0.81$, $k = 1$, $u_1 = 1\text{m/s}$, $u_2 = -u_1$. The classical linear growth rate for KHI is plotted in red.

2.5 Summary

In this chapter, the theoretical aspects of two fundamental instabilities - namely the Kelvin-Helmholtz instability and Rayleigh-Taylor instability were reviewed. The linear perturbation was applied to obtain first order accurate equations from the three dimensional Navier-Stokes equations. Motivated by the Squire's

theorem and the Rayleigh inflection point theorem, the model equation which describes the combined KHIs and RTIs was constructed (2.18).

The analysis considered in this chapter have been partitioned into two parts: (i) sharp interface viscous cases (section 2.4.1) and (ii) smoothed interface inviscid cases (section 2.4.2). A parameter study was conducted to gain insight of how each parameter affects the growth of the instability. It was found that an increase in density ratio and viscosity suppresses the KHI, whereas an increase in the tangential velocity difference amplifies the KHI. We also found that the viscosity causes major suppression for the large wave number modes while the growth correspond to the small wave number modes are less influenced. Similarly, the increase in viscosity was also found to suppress the growth of RTI. However, in the case of a pure RTI the growth rate is strictly negative (i.e. $n_c < 0$); therefore even though viscosity acts to slow down the growth of a RTI, it would never cause an overall stabilisation to the instability.

The evolution of inviscid KHI and RTI with smoothed velocity and density base-flow distribution was examined. In lieu of density gradient, an increase in velocity gradient strongly suppresses the KHI. In contrast, for sharp velocity gradient, an increase in the density gradient amplifies the KHI growth rate when the density gradient has infinitesimal thickness. We found that the presence of a finite density and velocity transition layer leads to an overall suppression of the KHI growth which is significantly smaller than the classical values. In smoothed density distribution RTI, the growth rate decrease with increasing density gradient. In the context of SSI, a larger density gradient amplifies the growth of the instability, whereas a larger velocity gradient damps the growth of the instability. Nonetheless, for realistic flow scenarios, both the velocity and density transitions layers are of finite widths, and the generation of these boundary layers results in a smaller growth rate than the classical expectations.

Finally, we would like to point out that the analysis performed in this chapter

provides an extension to the existing semi-analytical hydrodynamic theories. In particular, the model equation (2.18) is applicable to incompressible multiphase viscous fluid systems and encapsulate the essential physical phenomena which KHI and RTI take place. While our discussion focusses on cases where analytical solution is feasible, in principle it is possible to extend the analysis by solving the model equation (2.18) numerically for the viscous smoothed initial distribution case. This enables one to construct a systematic comparison study between semi-analytical theory and results obtained from numerical simulations.

Chapter 3

Smoothed Particle Hydrodynamics

3.1 Introduction

This chapter serves both as a review of the SPH literature and as a discussion of the models required for high density contrast multiphase flows. This material in this chapter is divided into two parts: the first part reviews the SPH principles (section 3.3-3.10), while the second part of the chapter (section 3.11) is devoted to multiphase SPH. Sections 3.3-3.4 discuss the fundamentals of the Lagrangian scattered data approximation and the essential properties of SPH kernel functions. Section 3.5 examines the theoretical accuracy of the continuum approximation and the particle discretisation of SPH. Section 3.7 demonstrates that the spatial derivative formulation found in the literature can be derived directly from the chain rule. In section 3.8, we demonstrate that a consistent set of SPH fluid dynamical equations can be derived from the discretised fluid Lagrangian with the inclusion of an arbitrary function ϕ. The properties of the artificial viscosity models and popular equation of states employed in SPH are discussed in sections 3.9-3.10. The second part of the chapter (section 3.11) is de-

voted to multiphase SPH. A literature review of multiphase SPH is presented in section 3.11.1. In particular, our discussion focuses on the challenges faced when applying SPH to high density ratio weakly-compressible multiphase fluid systems. Two interface stabilisation models are presented in sections 3.11.3-3.11.4. Their performance are compared against other methods from the weakly-compressible SPH literature.

3.2 Literature review

The field of numerical analysis has prospered since the 19^{th} century. One of the primary applications of numerical analysis is the area of numerical solutions of PDEs, within which there are two areas of particular focus: the mesh-based method such as the Finite Difference Method (FDM) and Finite Volume Method (FVM) determine fluid quantities of a set of fixed nodal points, and the mesh-free methods based on the concept of scattered data interpolations. Recent advances in mesh-based methods have lead to the development of adaptive mesh refinement (AMR) techniques that offer dynamic increase of resolution where needed. The combination of these methods (FDM, FVM) and AMR techniques forms the basis of modern day CFD simulation codes in both academia and industrial research. Nonetheless, mesh-based methods are known to suffer from numerous shortcomings. Firstly, mesh-based methods generally suffer from numerical diffusion (spurious advection) which violates the conservation of mass and momentum [58]. Secondly, the AMR procedure introduces additional complexity when mapping a set of predefined nodal points to a new set of discretisation points. Thirdly, the use of interface tracking techniques are mandatory when the spatial distribution of physical quantities (e.g. velocity, density) are discontinuous; however, the performance of these techniques varies depends on the specific implementation [59].

Due to the various disadvantages of mesh-based methods, extensive research has been conducted to develop mesh-free methods. Unlike their mesh-based counterparts, mesh-free methods enable arbitrary scalar or vector functions to be estimated from a set of scattered interpolation points. There are generally two classes of mesh-free methods: probabilistic and deterministic. The former class are generally known as Monte Carlo method and it has advantageous properties over classical mathematical methods for high dimensionality problems which involves many independent variables [111]. Deterministic mesh-free methods have also undergone significant development over the past decades, some of the popular deterministic mesh-free methods include: Smoothed Particle Hydrodynamics (SPH) [60, 61], Radial Basis Function (RBF) [112, 113], Moving Particle Semi-implicit method (MPS) [114] and Particle-in-cell (PIC) [115]. Despite the differences in their specific formulations, the deterministic mesh-free methods are based on the concept of a *kernel density estimate* [116][1] performed on a set of scattered data points. In the context of fluid dynamics, if these scattered data points follow the fluid flow, then the methods are called Lagrangian particle methods. SPH was pioneered by Lucy [61] and Gingold and Monaghan [60] in the 1970s to simulate gas dynamics problems in astrophysics and fission hypothesis. It is one of the earliest Lagrangian particle methods in the literature and has been widely employed in astronomy to simulate the evolution of large scale astrophysical structures. An extension was later made by Monaghan [62] to simulate free surface flows. The following paragraphs present a review of the concept of SPH.

[1] A kernel function is the same concept as a probability density function in statistics.

3.3 SPH interpolation

The concept of SPH is to estimate physical quantities as integral interpolants. This allows functions to be evaluated from a set of scattered Lagrangian interpolation points. Each interpolation point carries a mass m_i, density ρ_i, viscosity μ_i, pressure p_i, velocity $\vec{v}_i$, position $\vec{r}_i$ and other fluid quantities depending on the problem of interest. A scalar function $f(\vec{r})$ can be written in terms of the convolution integral

$$f(\vec{r}) = \int_{\Omega} f(\vec{r}\,')\delta(\vec{r} - \vec{r}\,')d\vec{r}\,', \quad \forall \vec{r} \in \Omega \tag{3.1}$$

where Ω is the domain of interest, $d\vec{r}\,'$ is the differential volume element and $\delta(\vec{r} - \vec{r}\,')$ is the Dirac-delta function

$$\lim_{\epsilon \to 0} \delta_\epsilon(r) = \begin{cases} 0 & r < \frac{\epsilon}{2} \\ 1/\epsilon & -\frac{\epsilon}{2} < r < \frac{\epsilon}{2} \\ 0 & r > \frac{\epsilon}{2} \end{cases}. \tag{3.2}$$

The interpolation approximation (3.1) can be generalised by replacing the Dirac-delta function with a kernel function $W(\vec{r} - \vec{r}\,', h)$ that depends on the distance between the region of interest $\vec{r}$ and the arbitrary field point $\vec{r}\,'$ and a length-scale known as the smoothing length h [112]. In order to preserve the properties of a Dirac-delta function, the kernel function must satisfy

$$\lim_{h \to 0} W(\vec{r} - \vec{r}\,', h) = \delta(\vec{r} - \vec{r}\,'), \tag{3.3}$$

and

$$\int_{\Omega} \delta(\vec{r} - \vec{r}\,', h)d\vec{r}\,' = 1. \tag{3.4}$$

The first condition (3.3) requires that for an infinitesimal smoothing length the kernel function should behave similarly to a Dirac-delta function. The second condition (3.4) requires the integral of the kernel function to be unity and it is called the *normalisation condition*. If conditions (3.3)-(3.4) are satisfied, then the integration (3.1) is formally defined as the *kernel density estimate* [112, 116, 117] of the function $f(\vec{r})$.

$$\langle f(\vec{r})\rangle = \int_{\Omega} f(\vec{r}\,')W(\vec{r}-\vec{r}\,')d\vec{r}\,'. \tag{3.5}$$

The *kernel density estimate* (3.5) is applied such that the continuum fluid is represented by a set of Lagrangian interpolation points known as particles. Replacing the differential volume by the volume of SPH particles $d\vec{r}_j\,' \approx V_j$ gives

$$\begin{aligned} \langle f(\vec{r})\rangle &= \int_{\Omega} f(\vec{r}\,')W(\vec{r}-\vec{r}\,',h)d\vec{r}\,' && (3.6)\\ &\approx \sum_j \frac{m_j}{\rho_j} f(\vec{r}_j)W(\vec{r}-\vec{r}_j,h). && (3.7) \end{aligned}$$

As a result, the interpolation of the function $f(\vec{r})$ at the location of a particle i is given by the particle approximation ($V_j = m_j/\rho_j$), where m_j and ρ_j are the mass and mass-density of particle j.

$$f_i(\vec{r}_i) = \sum_j V_j f(\vec{r}_j)W(\vec{r}-\vec{r}_j,h). \tag{3.8}$$

Equation (3.8) is the discrete particle form of the *kernel density estimate* (3.5), where the influence of a nearby particle j is proportional to its volume (V_j) and the inter-particle distance, the smoothing length (h), and the value the function f at the sampling points.

3.4 Kernel functions

In the previous section, we have shown that if the kernel function fulfils the normalisation condition and converges to a Dirac-delta function for infinitesimal smoothing length, the kernel density estimate of a continuum scalar field can be represented by the particle approximation (3.8). For SPH to be called a truly mesh-free method, its kernel function must satisfy additional properties, one of which is the *partition of unity* [118].

Definition 1. [118] Let $\Omega \subset \mathbb{R}^{N_{dim}}, N_{dim} \in [1,3]$ be an open bounded domain. Let $\{\Omega_i\}_{i \in N_p}$ be a family of open set in $\mathbb{R}^{N_{dim}}$ and

- the family of open set $\{\Omega_i\}_{i \in N_p}$ generates a cover of the domain Ω (i.e. $\Omega \subset \{\Omega_i\}_{i \in N_p}$).
- there exist a set of continuous functions $\{W_i\}_{i \in N_p}$ such that $supp\{W_i\} \in \Omega_i$
- $W_i(\vec{r}) \in [0,1] \quad \forall \vec{r} \in \Omega_i$
- $\sum_i W_i(\vec{r}) = 1 \quad \forall \vec{r} \in \Omega_i$

then the set of interpolation basis functions (i.e. kernel functions) $\{W_i\}_{i \in N_p}$ forms a *partition of unity subordinate* of the open set $\{\Omega_i\}_{i \in N_p}$ that covers Ω.

The first property requires the global domain Ω to be partitioned into a set of sub-domains which are allowed to overlap each other as long as the subsequent set $\{\Omega_i\}_{i \in N_p}$ covers the entire domain. The second property states that within each of the partitioned sub-domain, there exits some compactly supported interpolation basis function $\{W_i\}_{i \in N_p}$. The third and fourth conditions restrict the boundedness of the interpolation basis functions such that the weights are positive and range from zero to unity. To gain better intuition for these properties see Figure 3.1.

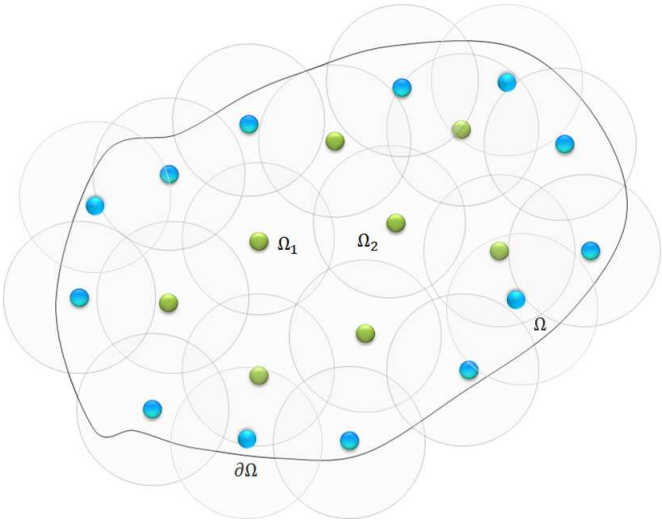

Figure 3.1: SPH domain where the shaded circles represents the support of the kernel functions, where $\Omega_{1,2}$ are the sub-domains of individual kernel function, Ω represents the entire fluid domain of interest, and $\partial\Omega$ represents the boundary of the fluid domain. Particles residing within the domain Ω are coloured in green. Whereas particles with truncated kernel are coloured in blue.

In addition to the conditions inherited from the *partition of unity*, there are further requirements to the kernel function motivated by the physical nature of classical mechanics. In order to take into account effects of short-range forces, the kernel is required to decrease monotonically away from its center. This implies particles located further away from the center of the kernel contribute less to the overall kernel interpolation[2]. Finally, because SPH aims to solve the strong form of the hydrodynamic equations, the kernel function should be k-th order differentiable, where the constant k generally refers to the highest order spatial derivative in the PDE system. For inviscid hydrodynamics, the highest spatial derivative corresponds to the pressure gradient (i.e. $k = 1$). The desired properties of kernel functions are summarised in Table 3.1. Utilising the properties in Table 3.1, the SPH kernel function can be expressed in terms of the dimensionless form

$$W(|\vec{r} - \vec{r}'|, h) = \frac{1}{h^{N_{dim}}} W(q), \tag{3.9}$$

[2]Although in the original SPH article Gingold and Monaghan [60] employ an infinite support (C^∞) Gaussian function, its steeply monotonically decreasing characteristic effectively satisfies the requirement of a compactly supported kernel.

• $supp\{W(\vec{r}-\vec{r}')\} \in \Omega_i$	compactly supported
• $\lim_{\lvert\vec{r}-\vec{r}'\rvert\to\infty} W(\vec{r}-\vec{r}',h) \to 0$	monotonically decreasing
• $W(\vec{r}-\vec{r}',h) \in [0,1]$	positive definite
• $W(\vec{r}-\vec{r}',h) = W(\vec{r}'-\vec{r},h) = W(\lvert\vec{r}-\vec{r}'\rvert,h)$	radially symmetric
• $\int W_i(\vec{r}-\vec{r}',h) = 1$	normalised to unity
• $W(\vec{r}-\vec{r}',h) \in C^k(\mathbb{R}^{N_{dim}}), k \geq 1, N_{dim} \in [1,3]$	sufficiently differentiable
• $\lim_{h\to 0} W(\vec{r}-\vec{r}',h) = \delta(\vec{r}-\vec{r}')$	Dirac-delta convergence
• provides an accurate density estimate	
• stable against particle pairing	

Table 3.1: Desired properties of SPH kernel functions.

where q is the dimensionless quantity $q = |\vec{r}-\vec{r}'|/h$. Monaghan [119] demonstrated the cubic-spline (CS) kernel (3.10) to be computationally accurate for most test cases. Since then, it has become a standard SPH kernel function in literature. The CS kernel has the form

$$W_{CS}(q) = G_{CS} \begin{cases} 1 - \frac{3}{2}q^2 + \frac{3}{4}q^3 & 0 \leq q \leq 1 \\ \frac{1}{4}(2-q)^3 & 1 < q \leq 2 \\ 0 & q > 2 \end{cases} \tag{3.10}$$

where G_{CS} is the normalisation constant, where $G_{CS} = 1/h, 10/(7\pi h^2), 1/(\pi h^3)$ for one, two and three dimensions. This kernel has the advantage of possessing compact support and sufficiently differentiable for inviscid hydrodynamics problems. Thus, provided the support of the kernel is properly filled and particles are well distributed, the particle approximation is second order accurate [119, 120]. The cubic-spline kernel and its first two derivatives are plotted in Figure 3.2. Although this kernel has been widely adopted in SPH simulations, Schuessler and Schmitt [121] pointed out that the gradient of the CS kernel is unstable for large number of neighbours (or equivalently large h in weakly-compressible SPH) and *pairing instability* (also known as particle clumping) may occur depending on the ratio of the smoothing length h to initial particle separation distance d_{nat},

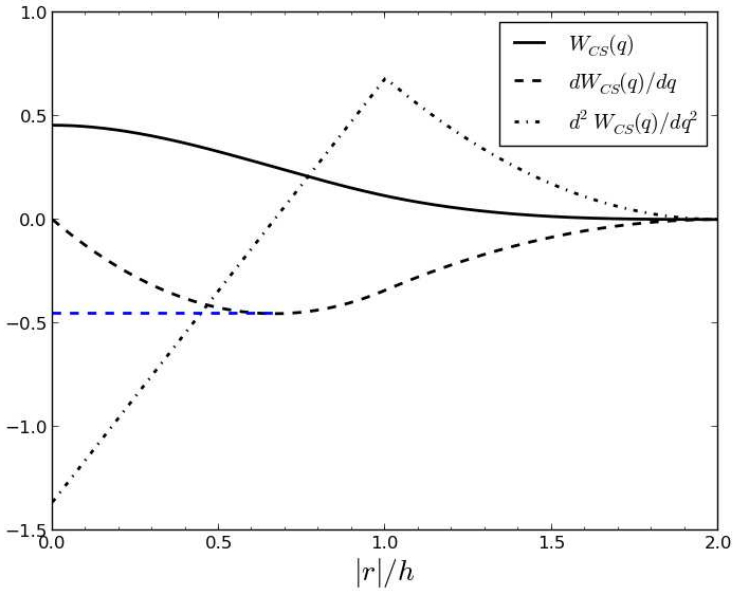

Figure 3.2: Cubic-spline kernel and its first two derivatives. The improvement proposed by Couchman et al. [4] to cure pairing instability is plotted in blue.

i.e. $\kappa = h/d_{nat}$. This is because the CS kernel function has an inflection point at $q = 2/3$ such that the kernel gradient contains a minima at $q = 2/3$ and tends to zero towards the origin. This implies the mutual repulsive force due to the pressure gradient decreases for neighbouring particles within the region $0 \leq q \leq 2/3$ of the kernel gradient. Hence, two particles spaced closer than $q \leq 2/3$ form a pair that eventually coincides at the same spatial location which decreases the effective resolution of SPH.

There have been investigations to remedy the *pairing instability*. Couchman et al. [4] suggested using an augmented form of the gradient of the CS kernel,

$$W'_{CS}(q) = G_{CS} \begin{cases} -1 & 0 \leq q \leq \frac{2}{3} \\ -3\,q + \frac{9}{4}\,q^2 & \frac{2}{3} \leq q \leq 1 \\ -\frac{3}{4}\,q^2 & 1 < q \leq 2 \\ 0 & q > 2 \end{cases} \tag{3.11}$$

with $W(q)$ and the normalisation G_{CS} unchanged. In this case, particles within the region $0 \leq q \leq 2/3$ have the same gradient value and the *pairing instability*

is eliminated. Price [122] pointed out that the kernel gradient (3.11) is no longer correctly normalised. Hence, the kernel gradient contains a higher sampling rate within the region $q < 2/3$ which may potentially lead to substantial systematic error in the inter-particle pressure gradient forces [122]. More importantly, the use of the modified gradient creates an inconsistency between the kernel function and its gradient which may potentially violate conservation of energy.

Morris [123] was the first to point out that the stability of a kernel function against the *pairing instability* is related to the properties of its Fourier transform. In particular, the stability is significantly improved for large number of neighbours provided that the Fourier transforms decays rapidly. Read et al. [109] discovered the use of a higher order core-triangular kernel (HOCT4) with 422 neighbour particles improves the performance of SPH in mixing problems (c.f. section 3.11). The major distinctions between the HOCT and cubic-spline kernel is that the former has a larger weighting at the origin and does not have an inflection point.

Dehnen and Aly [124] compared the convergence properties of different SPH kernels. In contrast to the conventional understanding of the pairing instability based on the inflection point argument, they pointed out that the pairing instability is caused by the re-ordering capability of SPH that has a tendency to re-order particles into a lower energy state. Moreover, they conducted a series of test cases using the family of Wendland kernel functions [117] and demonstrated that the kernels are stable for large number of neighbours even though the Wendland functions have inflection points. Furthermore, they proposed that the appropriate condition for stability against the *pairing instability* is that the Fourier transform of the kernel function is non-negative. An extensive discussion about Wendland kernels functions can be found in [112, 117, 124]. Unless stated otherwise, the simulations in this thesis are performed using the 5^{th} degree class

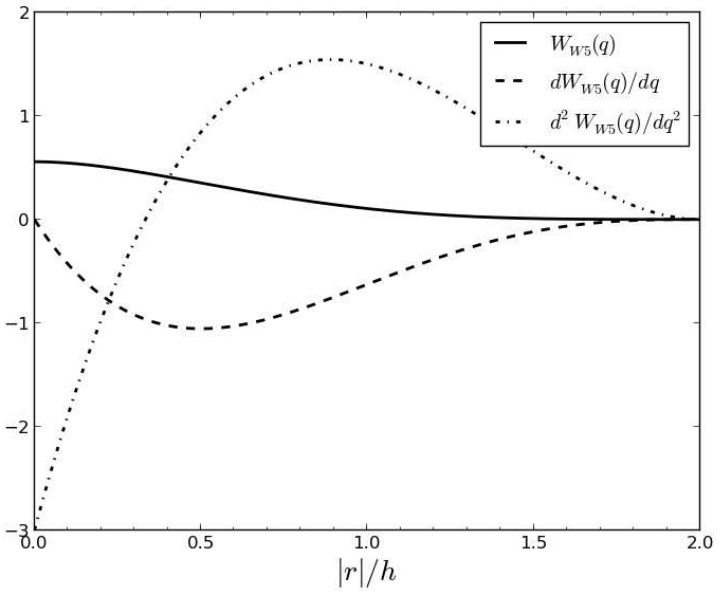

Figure 3.3: Fifth order Wendland kernel (Quintic kernel) and its first two derivatives.

2 Wendland kernel similar to those in [125, 126, 127], and has the form

$$W_{wendland}(q) = G_{W5} \begin{cases} (1 - \frac{q}{2})^4 (1 + 2q) & 0 \leq q < 2, \\ 0 & q > 0 \end{cases} \tag{3.12}$$

where $G_{W5} = 7/(4\pi h^2)$ in two dimensions and $G_{W5} = 7/(8\pi h^3)$ in three dimensions. The Wendland (Quintic) kernel and its first and second derivatives are plotted in Figure 3.3.

3.5 Accuracy of SPH interpolation

3.5.1 spatial discretisation error

The interpolation error analysis is performed considering a one-dimensional case. Taylor expanding around $\vec{r}$ and keeping terms up to second order gives

$$\begin{aligned}
\langle f(\vec{r})\rangle &= \int_\Omega f(\vec{r}')W(\vec{r}-\vec{r}',h)d\vec{r}' \\
&= \int_\Omega \left[f(\vec{r}) + \frac{df}{d\vec{r}}(r-r') + \frac{1}{2}\frac{d^2f}{d\vec{r}^2}(\vec{r}-\vec{r}')^2\right] W(\vec{r}-\vec{r}',h)d\vec{r}' \\
&= f(\vec{r})\int_\Omega W(\vec{r}-\vec{r}',h)d\vec{r}' + \frac{df}{d\vec{r}}\int_\Omega (\vec{r}-\vec{r}')W(\vec{r}-\vec{r}',h)d\vec{r}' + \\
&\quad \frac{1}{2}\frac{d^2f}{d\vec{r}^2}\int_\Omega (\vec{r}-\vec{r}')^2W(\vec{r}-\vec{r}',h)d\vec{r} \\
&= f(\vec{r}) + \frac{1}{2}\frac{d^2f}{d\vec{r}^2}\int_\Omega (\vec{r}-\vec{r}')^2W(\vec{r}-\vec{r}',h)d\vec{r}.
\end{aligned}$$

Since the kernel function must satisfy the properties in Table 3.1 of being an even radially symmetric even function, the odd order terms vanish and the highest order residual term corresponds to the second order Taylor expansion. It can be shown that the spatial discretisation error is second order accurate $\mathcal{O}(h^2)$ (see Appendix 9.2.2).

3.5.2 Consistency

Another important aspect of a mesh-free methods is its reproducing capabilities. Formally, an interpolation method is k-th order consistent if any polynomial up to order k can be represented. In what follows, we discuss zero-th and first order consistency considering the interior region of a fluid domain.

Condition 3.5.1. For a zero-th order polynomial $f(\vec{r}) = c_o$, the *kernel density*

estimate must satisfy

$$\begin{aligned} f(\vec{r}) &= \int_{\Omega'} c_o W(\vec{r}-\vec{r}')d\vec{r}' \\ &= c_o \int_{\Omega'} W(\vec{r}-\vec{r}')d\vec{r}' \\ &= c_o. \end{aligned}$$

Condition 3.5.2. For a zero-th order polynomial $f(\vec{r}) = c_o$, the kernel gradient must satisfy

$$\nabla f(\vec{r}) = c_o \int_{\Omega'} \nabla W(\vec{r}-\vec{r}')d\vec{r} = 0 \tag{3.13}$$

Condition 3.5.3. For a first order polynomial $f(\vec{r}) = c_o + c_1\vec{r}$, the *kernel density estimate* must satisfy

$$f(\vec{r}) = \int_{\Omega'} (c_o + c_1\vec{r}')W(\vec{r}-\vec{r}')d\vec{r}' = c_o + c_1\vec{r}.$$

Based on the normalisation condition (3.4) and subtracting $\vec{r}'$ on both sides gives,

$$\int_{\Omega'} (\vec{r}-\vec{r}')W(\vec{r}-\vec{r}')d\vec{r}' = 0. \tag{3.14}$$

Summarising the above, condition (3.5.1) requires a constant function to be reproduced and condition (3.5.2) requires the gradient of a zero-th order polynomial to be zero. Finally, condition (3.5.3) requires the first moment of the kernel function to vanish. The higher order reproducing conditions are generalised in the literature [118, 128, 129, 130, 131]. Note that the consistency conditions (3.5.1)-(3.5.3) are derived for continuous kernel interpolation, with the assumption that the integration domain lies within the interior region Ω'. However, these conditions are no longer satisfied when the integration region

involves boundaries $\partial\Omega$ as illustrated in Figure 3.1. This phenomena is known as *truncated kernel*, and it is a major disadvantage of all mesh-free methods based on *kernel density estimate* [112, 116, 117]. This is because in lieu of boundary particles, the support of the kernel is not fully filled. Hence, despite the fact that the kernel function is radially symmetric, the contribution from outside the domain are not taken into account (see Figure 3.1), and the kernel interpolation violates the normalisation condition (3.4) and conditions (3.5.1)-(3.5.3). The particle analogue of (3.5.1)-(3.5.3) are given as

Condition 3.5.4. For a zero-th order polynomial $f(\vec{r}) = c_o$, the SPH particle approximation must satisfy

$$f(\vec{r}_i) = \sum_j c_o \frac{m_j}{\rho_j} W(\vec{r}_i - \vec{r}_j, h). \tag{3.15}$$

Condition 3.5.5. For a zero-th order polynomial $f(\vec{r}) = c_o$, the SPH particle approximation must satisfy

$$\nabla f(\vec{r}_i) = \sum_j c_o \frac{m_j}{\rho_j} \nabla_i W(\vec{r}_i - \vec{r}_j, h) = 0. \tag{3.16}$$

Condition 3.5.6. For a first order polynomial $f(\vec{r}) = c_o + c_1\vec{r}$, the first moment of the SPH particle approximation must satisfy

$$\sum_j \frac{m_j}{\rho_j} (\vec{r}_i - \vec{r}_j) W(\vec{r}_i - \vec{r}_j, h) = 0. \tag{3.17}$$

Even though the consistency conditions (3.5.1)-(3.5.3) are satisfied for continuous kernel interpolation, it is not guaranteed that the particle form of these conditions (3.5.4)-(3.5.6) will be satisfied. In fact, it is well known that the accuracy of the SPH particle approximations decreases when particles are irregularly distributed [109, 130, 131, 132]. The inconsistency is attributed to the

discrepancy between the continuous and discrete kernel interpolation. That is, the SPH particle approximation does not reproduce the zero-th order polynomial. By the same token, the anti-symmetric condition (3.5.5), and the first-moment condition (3.5.6) do not hold for irregular particle distributions. Further discussions on improvements for restoring consistency have been proposed in literature [128, 129, 130, 131, 132].

3.6 Smoothing length

In astrophysics, SPH is very often used in conjunction with tree based gravity solver to simulate the evolution of astrophysical objects. The presence of voids and highly dense regions within these simulations requires adaptive smoothing length that can resolve the dynamics in computationally efficient manner. This approach is commonly known as the variable h SPH in literature and it has been become a standard implementation in the astrophysics community. Numerous techniques have proposed in the literature for choosing the smoothing length:

1. keep the number of neighbours N_n approximately constant [133].

2. adapt the smoothing length to be proportional to the number density, namely $h \sim= n^{1/N_{dim}}$, $n = \sum_j W_{ij}$ [120].

3. evolve the smoothing length according to $h_i = \xi(m_i/\rho_i)^{1/N_{dim}}$.

4. evolve the smoothing length according to the time derivative of the continuity equation.

$$\frac{dh_i}{dt} = \frac{1}{3} h_i \nabla \cdot \vec{v}_i \tag{3.18}$$

Nonetheless, the variable smoothing length approach introduces a so called $\nabla - h$ term error that needs to be corrected. Since the density variation is negligible for the low Mach number fluid problems considered in this thesis, a decision

was made to use a constant smoothing length for all particles. Further details regarding to the implementation aspects of our fixed smoothing length SPH code will be described in chapter 4.

3.7 Spatial derivatives in SPH

Since SPH solves PDEs which govern fluid dynamics, it is unquestioned that the accuracy of the spatial derivatives holds a significant role in its accuracy. Without lost of generality, we consider the derivation of the divergence if a vector function $\vec{f}(\vec{r})$, the spatial derivatives of scalar function can be derived in the same fashion. Monaghan [119] recommended two golden rules for the construction of SPH spatial derivatives. The first golden rule states that when deriving kernel approximations, one should assume the kernel function is a Gaussian function. The second golden rule states that one should rewrite formulas with density inside operators. Many variations of SPH spatial derivatives can be derived using these golden rules. In what follows, we review the basic spatial derivatives used in SPH in section 3.7.1 and show that other popular choice of SPH spatial derivatives can be derived based on the combined use of the chain rule and the Monaghan's second golden rule in section 3.7.2.

3.7.1 SPH divergence formula I

As a first approximation, the divergence of a vector function can be computed directly from the kernel interpolation. The spatial derivatives of a vector function $\vec{f}(\vec{r})$ can be approximated from equation (3.5). Assuming the kernel function satisfies the properties in Table 3.1, the spatial derivative of $\vec{f}(\vec{r})$ is given as

$$\begin{aligned} \langle \nabla \cdot \vec{f}(\vec{r}) \rangle &= \nabla \cdot \left[\int_{\Omega} \vec{f}(\vec{r}\,') W(\vec{r} - \vec{r}\,' d\vec{r}\,') \right] \\ &= \int_{\Omega} \vec{f}(\vec{r}\,') \nabla \cdot W(\vec{r} - \vec{r}\,') d\vec{r}\,'. \end{aligned} \tag{3.19}$$

Applying the particle approximation gives

$$\langle \nabla \cdot \vec{f}_i(\vec{r}_i) \rangle = \sum_j \frac{m_j}{\rho_j} \vec{f}_j \cdot \nabla_i W_{ij}. \tag{3.20}$$

While equation (3.20) serves as a straight forward method for gradient approximation, it suffers from zero-th order inconsistency. Thus, the direct application of such derivatives is rarely used in practice.

3.7.2 SPH divergence formula II

Many variations of SPH divergence can be found in the literature. Following Read et al. [109], applying the chain rule to the combined spatial derivative approximation based on an arbitrary scalar function ϕ and density gives

$$\nabla \cdot \left(\frac{\rho}{\phi} \vec{f} \right) = \vec{f} \nabla \cdot \left(\frac{\rho}{\phi} \right) + \frac{\rho}{\phi} \nabla \cdot \vec{f}. \tag{3.21}$$

It is found that equation (3.21) is a generalised form of the spatial derivative in SPH and covers the variations presented in the literature. For instance, substituting $\phi = 1$ in equation (3.21) gives

$$\langle \nabla \cdot \vec{f}_i(\vec{r}_i) \rangle = -\frac{1}{\rho_i} \sum_j m_j (\vec{f}_i - \vec{f}_j) \nabla_i W_{ij}, \tag{3.22}$$

which is used for the approximation of velocity divergence in Balsara [134]. Similarly, substituting $\phi = \rho^2$ in equation (3.21) gives

$$\left\langle \frac{\nabla \cdot \vec{f}_i(\vec{r}_i)}{\rho_i} \right\rangle = \sum_j \frac{m_j}{\rho_j} \left(\frac{\vec{f}_j}{\rho_i^2} + \frac{\vec{f}_i}{\rho_j^2} \right) \nabla_i W_{ij}. \tag{3.23}$$

Furthermore, if $\phi = \rho$ then equation (3.21) simplifies to

$$\langle \nabla \cdot \vec{f}_i(\vec{r}_i) \rangle = -\sum_j \frac{m_j}{\rho_j} (\vec{f}_i - \vec{f}_j) \cdot \nabla_i W_{ij}. \tag{3.24}$$

Equation (3.24) is zero-th order consistent. In fact, if one considers $\phi = \rho^{2-\varphi}$ where $\varphi \in \mathbb{R}$ then equation (3.21) results in the spatial derivative approximation in [110, 118].

$$\langle \rho_i \nabla \cdot \vec{f}_i(\vec{r}_i) \rangle = -\rho_i^{2-\varphi} \sum_j \frac{m_j}{\rho_j^{2-\varphi}} (\vec{f}_i - \vec{f}_j) \nabla_i W_{ij}. \tag{3.25}$$

3.8 SPH Lagrangian fluid dynamics

The SPH equations can be derived from two different viewpoints. On one hand, one can discretise the spatial derivatives in the fluid dynamical equations based on the SPH gradients in section 3.7 and explicitly show that the corresponding SPH scheme satisfies conservation of mass, momentum and energy. On the other hand, it is possible to derive SPH from the Lagrangian of non-dissipative hydrodynamics and the principle of least action. Monaghan and Price [135] showed that the standard SPH scheme can be derived from the discrete fluid Lagrangian [136], an extension is made in Price and Monaghan [120] which includes the ∇h error term in the derivation. While the derivation in the literature mainly concerns standard SPH [120, 135, 137, 138], the derivation presented herein extends the earlier results and demonstrates a consistent set of SPH fluid dynamical equations based on any arbitrary scalar function ϕ can be derived from the Euler-Lagrange equation. Consider the Lagrangian of a perfect fluid [136, 139]

$$\mathcal{L} = \int \rho \left(\frac{\vec{v} \cdot \vec{v}}{2} - e(\rho, s) \right) dV, \tag{3.26}$$

where dV represents the differential volume of a fluid particle. Following the work of Price and Monaghan [120], the Lagrangian for a set of discrete particles is given as

$$\mathcal{L} = \sum_j m_j \left[\frac{v_j^2}{2} - e_j \left(\rho_j, s_j \right) \right]. \tag{3.27}$$

The Lagrangian herein is dependent on the mass, density, internal energy per unit mass and entropy per unit mass (s_j) of the particles. The SPH momentum equations are derived from the Euler-Lagrange equation of a particle system, namely

$$\frac{D}{Dt}\left(\frac{\partial \mathcal{L}}{\partial \vec{v}_i} \right) - \frac{\partial \mathcal{L}}{\partial \vec{r}_i} = 0. \tag{3.28}$$

Substituting the particle Lagrangian (3.27) into the first term of the Euler-Lagrange equation (3.28) gives

$$\frac{D}{Dt}\left(\frac{\partial \mathcal{L}}{\partial \vec{v}_i} \right) = \frac{D}{Dt}\left[\frac{\partial}{\partial \vec{v}_i} \sum_j m_j \left(\frac{\vec{v}_j^2}{2} - e_j \left(\rho_j, s_j \right) \right) \right]. \tag{3.29}$$

Assuming the mass particles is time independent, equation (3.30) simplifies to the force acting on a particle i, namely

$$\frac{D}{Dt}\left(\frac{\partial \mathcal{L}}{\partial \vec{v}_i} \right) = \frac{D}{Dt}\left(m_i \vec{v}_i \right). \tag{3.30}$$

The second term of the Euler-Lagrange equation (3.28) is written as

$$\begin{aligned} \frac{\partial \mathcal{L}}{\partial \vec{r}_i} &= \frac{\partial}{\partial \vec{r}_i}\left[\sum_j m_j \left(\frac{v_j^2}{2} - e_j(\rho_j, s_j) \right) \right] \\ &= -\sum_j m_j \frac{\partial e_j}{\partial \rho_j}\Big|_{s_j} \frac{\partial \rho_j}{\partial \vec{r}_i}. \end{aligned} \tag{3.31}$$

For an adiabatic reversible process ($ds = 0$), the differential volume is given by $DV = -1/\rho^2 D\rho$. In addition, the relation between internal energy and pressure

work is described by the first law of thermal dynamics

$$de = -PdV + Tds. \tag{3.32}$$

Replacing the differential volume in equation (3.32) by $dV = -1/\rho^2 d\rho$ gives the relation

$$\frac{\partial e_j}{\partial \rho_j}\Big|_{s_j} = \frac{P}{\rho^2} \tag{3.33}$$

Substituting (3.33) into equation (3.31) gives

$$\frac{\partial \mathcal{L}}{\partial \vec{r}_i} = -\sum_j m_j \frac{P}{\rho^2} \frac{\partial \rho_j}{\partial \vec{r}_i} \tag{3.34}$$

Expressing the velocity divergence in the continuity equation (2.4) by the generalised spatial derivative formula (3.21) gives

$$\frac{D\rho_i}{Dt} = \sum_j m_j \frac{\phi_i}{\phi_j} \vec{v}_{ij} \cdot \nabla_i W_{ij}, \tag{3.35}$$

which is commonly known as the *differential form continuity equation* density estimate. In contrast, one can consider the integral form of the continuity equation, which is known as the *summation density* approach in the literature

$$\rho_i = \sum_j m_j \frac{\phi_i}{\phi_j} W_{ij}. \tag{3.36}$$

To avoid confusion, a dummy index q is introduced for the approximation of the density of particle j. Rewritting equation (3.36) in terms of the dummy index gives

$$\rho_j = \sum_q m_q \frac{\phi_j}{\phi_q} W\left(\vec{r}_i - \vec{r}_q, h\right). \tag{3.37}$$

Utilising the second identity in Appendix 9.2.3, the spatial derivative with respect to particle j is given as

$$\frac{\partial \rho_j}{\partial \vec{r}_i} = \sum_q m_q \frac{\phi_j}{\phi_q} \nabla_j W_{jq} \left(\delta_{ji} - \delta_{qi}\right). \tag{3.38}$$

Substituting (3.38) into the second term in the Euler-Lagrange equation (3.28) gives

$$\frac{\partial \mathcal{L}}{\partial \vec{r}_i} = -\sum_j m_j \frac{P_j}{\rho_j^2} \sum_q m_q \frac{\phi_j}{\phi_q} \nabla_j W_{jq} \left(\delta_{ji} - \delta_{iq}\right). \tag{3.39}$$

Rearranging the double sum one gets

$$\frac{\partial \mathcal{L}}{\partial \vec{r}_i} = -\sum_j \sum_q m_j m_q \frac{P_j}{\rho_j^2} \frac{\phi_j}{\phi_q} \nabla_j . W_{jq} \left(\delta_{ji} - \delta_{iq}\right) \tag{3.40}$$

The properties of Kronecker Delta function allows us to partition the above expression into its partial sums

$$\frac{\partial \mathcal{L}}{\partial \vec{r}_i} = -\left[\frac{m_i P_i}{\rho_i^2} \sum_q m_q \frac{\phi_i}{\phi_q} \nabla_i W_{iq} - m_i \sum_j \frac{m_j P_j}{\rho_j^2} \frac{\phi_i}{\phi_q} \nabla_j W_{ji}\right], \tag{3.41}$$

where the first term corresponds to $j = i$ and the second term corresponds to $q = i$. Replacing the dummy index q by j in the first term and utilising the identity in Appendix 9.2.1 (equation (9.24)) gives

$$\frac{\partial \mathcal{L}}{\partial \vec{r}_i} = -\sum_j m_i m_j \left[\frac{P_i}{\rho_i^2} \frac{\phi_i}{\phi_j} + \frac{P_j}{\rho_j^2} \frac{\phi_j}{\phi_i}\right] \nabla_i W_{ij}. \tag{3.42}$$

Substituting equation (3.30), (3.42) into the Euler-Lagrange equation (3.28) results in the generalised momentum equation weighted by an arbitrary scalar function ϕ

$$\frac{D\vec{v}_i}{Dt} = -\sum_j m_j \left[\frac{P_i}{\rho_i^2} \frac{\phi_i}{\phi_j} + \frac{P_j}{\rho_j^2} \frac{\phi_j}{\phi_i}\right] \nabla_i W_{ij}. \tag{3.43}$$

Finally, taking the time derivative of (3.32) gives the SPH internal energy equation

$$\frac{De}{Dt} = \frac{P_i}{\rho_i^2} \sum_j m_j \frac{\phi_i}{\phi_j} \vec{v}_{ij} \nabla_i W_{ij}. \tag{3.44}$$

It can be shown that $\phi = 1$ for standard SPH. Note that the derivation herein focuses on fixed smoothing length, an extension can be easily made for variable smoothing length as shown in Monaghan [140] for standard SPH. The major implication of the results herein is that to achieve a set of consistent SPH equations, it is desirable to utilise the same function ϕ for the discretisation of the spatial derivative, failing to do so may void the conservation of energy and momentum. For completeness, the proof of Galilean invariance and conservation properties of total linear and angular momentum are explicitly shown in Appendix 9.2.4.

3.9 SPH viscosity

The conservation of mass, momentum and energy across a shock region is given by the Rankine-Hugoniot conditions [141, 142, 143, 144, 145] which requires the transformation of kinetic energy into internal energy via viscous heating. However, this is by nature a rapid process occurring at a length scale of the mean free path, which is significantly smaller than the typical resolution scale offered in macroscopic hydrodynamic simulations. It is therefore common to utilise artificial viscosity schemes in numerical hydrodynamic codes.

3.9.1 Standard artificial viscosity

Among the many available artificial viscosity schemes in the literature, the Von Neumann-Richtmyer model [146] and the Landshoff model [147] have gained significant attention due to their simplicity and computational efficiency. Von Neumann [146] introduced: In practice, a linear combination of the Von Neumann-

Richtmyer model [146] and the Landshoff [147] model are usually employed for the artificial viscosity in the mesh-based literature. Similar concept has been adopted in SPH artificial viscosity [60] and it has the particle-wise form of

$$\Pi_{ij} = \begin{cases} \frac{-\alpha_{AV}\bar{c}_{ij}\mu_{ij}+\beta_{AV}\mu_{ij}^2}{\bar{\rho_{ij}}} & \vec{r}_{ij}\cdot\vec{v}_{ij} < 0 \\ 0 & \vec{r}_{ij}\cdot\vec{v}_{ij} > 0 \end{cases}, \tag{3.45}$$

and

$$\mu_{ij} = \frac{\vec{v}_{ij}\cdot\vec{r}_{ij}}{r_{ij}^2+\xi h^2}, \tag{3.46}$$

where $\bar{c}_{ij}$, $\bar{\rho}_{ij}$ are the harmonically averaged speed of sound and density respectively. The numerator $\vec{v}_{ij}\cdot\vec{r}_{ij}$ measures the local divergence of a particle pair $\{i,j\}$. The denominator $r_{ij}^2+\xi h^2$, takes into account the separation between particles, and the softening factor $\xi = 0.01$ is introduced to prevent numerical divergence. The viscosity terms were originally only imposed during compression only; therefore its contribution is always positive. The linear term proportional to the artificial viscosity parameter α_{AV} represents the combination of shear and bulk viscosity. The quadratic term proportional to the β_{AV} term represents the Von Neumann-Richtmyer viscosity and prevents inter-particle penetration [128].

The standard artificial viscosity is Galilean invariant and conserves momentum. It also vanishes for rigid-body rotation ($\vec{v}_{ij}\cdot\vec{r}_{ij} = 0$). The use of a particle-wise measure of the divergence (i.e. $\vec{v}_{ij}\cdot\vec{r}_{ij}$) has both advantages and disadvantages over the mesh-based artificial viscosity model. One advantage is that it takes into account the local particle distribution. A major disadvantage is that the divergence may not vanish even for a pure shear flow when particles are not regularly distributed. The values chosen for artificial viscosity parameters are also problem dependent. For instance, for gravity driven flow of liquids the artificial viscosity parameters are commonly chosen as $\alpha_{AV} = 0.1$, $\beta_{AV} = 0$, whereas the standard choice in astrophysics literature is $\alpha_{AV} = 1$ and $\beta_{AV} = 2\alpha_{AV}$.

3.9.2 Balsara switch

Whilst the purpose of artificial viscosity (3.45) is to inhibit particle interpenetration and damp small scale disordered motion, it is known that the standard SPH artificial viscosity introduces spurious shear viscosity [64, 137, 148, 149]. Thus it is common for modern SPH implementations to utilise the standard SPH artificial viscosity in combination with what is known as a Balsara switch. The Balsara switch [134] is a shear reduction method which takes into account the relative strength between compression $\nabla \cdot \vec{v}_i$ and vorticity $\nabla \times \vec{v}_i$ within the kernel averaged velocity field. The localised velocity divergence and curl are computed via

$$\nabla \cdot \vec{v}_i = -\frac{1}{\rho_i} \sum_j m_j \vec{v}_{ij} \nabla_i W_{ij}, \tag{3.47}$$

and

$$\nabla \times \vec{v}_i = \frac{1}{\rho_i} \sum_j m_j \vec{v}_{ij} \times \nabla_i W_{ij}. \tag{3.48}$$

The Balsara factor is then given as

$$f_i = \frac{|\nabla \cdot \vec{v}_i|}{|\nabla \cdot \vec{v}_i| + |\nabla \times \vec{v}_i| + \xi_f c_i / h}, \tag{3.49}$$

where a softening factor $\xi_f = 0.01$ is introduced to avoid numerical divergence. In the case of strong compression $|\nabla \cdot \vec{v}_i| \gg |\nabla \times \vec{v}_i|$, the Balsara factor approaches unity. On the other hand, the Balsara factor reduces to zero when the particle is subjected to large vorticity $|\nabla \times \vec{v}_i| \gg |\nabla \cdot \vec{v}_i|$. The average Balsara factor between a particle-pair (f_{ij}) is then applied as a multiplicative factor to the standard artificial viscosity model (3.45) to adjust the strength of the actual artificial viscosity applied.

3.9.3 Monaghan real viscosity

The Monaghan real viscosity model [119] is based on the linear part of the standard artificial viscosity term (3.45), except that it is always active regardless the particle pair is undergoing pair-wise compression or not.

$$\Pi_{ij} = -8\frac{(\nu_i + \nu_j)\vec{r}_{ij} \cdot \vec{v}_{ij}}{\bar{\rho}_{ij} + \xi h^2}. \tag{3.50}$$

Furthermore, assuming the fluid particle pair has the same densities and kinematic viscosities, a comparison between (3.50) and (3.45) for $\beta_{AV} = 0$ suggests the relation [120]

$$\nu = \frac{\alpha_{AV} c h}{8}. \tag{3.51}$$

3.9.4 State-of-the-art viscosity models

Time dependent viscosity

Morris and Monaghan [150] introduced the concept of time-varying artificial viscosity coefficients, hereafter called TDV. In this concept, each particle are given its artificial viscosity parameter which evolves according to a simple source and decay equation.

$$\frac{d\alpha_i}{dt} = -\frac{\alpha_i - \alpha_{min}}{\tau_i} + S_i, \tag{3.52}$$

where α_{min} represents the minimum artificial parameter allowed in the simulation, τ_i is the e-folding time which is given by

$$\tau_i = \frac{h_i}{C_1 c_i}, \tag{3.53}$$

where $C_1 = 0.2$ is a parameter to control at decay rate of α_i to α_{min} after a shock have occurred. The source term

$$S_i = \max(-\nabla \cdot \vec{v}_i, 0), \tag{3.54}$$

causes the artificial viscosity parameter to grow when the particle enters a shock and causes it to decay to a small value away from the shock. Rosswog et al. [151] suggested one can also limit the maximum artificial viscosity allowed in the simulation by replacing the source term by $S_i = \max(-\nabla \cdot \vec{v}_i(\alpha_{max} - \alpha_{min}), 0)$, where the typical values are set to be $\alpha_{min} = 0.1$ and $\alpha_{max} = 1.5$.

Inviscid SPH

While the TDV has demonstrated improvements over standard SPH artificial viscosity by lowering undesired effective viscosity, Cullen and Dehnen [152] mentioned that this method still suffer from some limitations. Firstly, they pointed out that $\alpha_{min} > 0$ results in unwanted dissipation. Secondly, there is a time delay between the peak in the viscosity and the shock front. This is because the integration of the differential equation (3.52) does not provide the rapid increase of α_i required for strong shock problems. Thirdly, the source term S_i fails to vanish between pre and post-shock region. More importantly, the authors demonstrated that the source term fails to distinguish between velocity discontinuities within the support of the kernel and converging flows. Having seen the issues of TDV, Cullen and Dehnen [152] proposed a novel shock indicator with two strongly desirable features: able to distinguish shocks from convergent flows, and able to discriminate between the pre- and post-shock regions. Instead of using the SPH estimated divergence, the success of their shock indicator make uses of a second-order derivative of the flow velocity. In particular, the total time-derivative of the velocity divergence (i.e. $\dot{\nabla} \cdot \vec{v} = d(\nabla \cdot \vec{v})/dt$) is computed

by differentiating the continuity equation with respect to time

$$-\dot{\nabla}\cdot\vec{v}=\frac{d^2 ln\rho}{dt^2}, \tag{3.55}$$

where $\dot{\nabla}\cdot\vec{v}<0$ signifies a non-linear increase in density and steepening of flow convergence which typically occurs in the pre-shock region, whereas $\dot{\nabla}\cdot\vec{v}>0$ suggests a post-shock region. Their shock indicator has the form of $A_i=\xi_i\max(-\dot{\nabla}\cdot\vec{v}_i,0)$, where ξ_i is a limiter to suppress false detections. Furthermore, instead of directly solving the artificial viscosity ordinary differential equation, their work relies on the concept of varying the artificial viscosity parameter of a particle from zero to a localised artificial viscosity parameter within the kernel support (α_{loc}) as given by

$$\alpha_{loc,i}=\frac{\alpha_{max}h_i A_i^2}{\vec{v}_{sig,i}^2+h^2A_i}, \tag{3.56}$$

where the signal velocity is given by

$$\vec{v}_{sig,i}=\max_{\vec{r}_{ij}<h_i}(\bar{c}_{ij}-\min(0,\vec{v}_{ij}\cdot\vec{r}_{ij})). \tag{3.57}$$

It is therefore guaranteed that both A and the localised artificial viscosity parameter within the kernel support α_{loc} both decays to zero at the moment of passing through a shock (maximum convergence). Finally, the artificial viscosity parameter of a particle is computed by solving the first order differential equation

$$\frac{d\alpha_i}{dt}=\frac{(\alpha_{loc,i}-\alpha_i)}{\tau_i}, \tag{3.58}$$

where the decay time-scale if defined to be $\tau_i=h_i/0.2\vec{v}_{sig,i}$.

Higher order SPH switch

Motivated by Cullen and Dehnen [152] and the earlier work of Price [110], Read and Hayfield [153] introduced a novel approach based on a second order accurate switch technique to modelling flows with discontinuities which we will called SPHS hereafter. The success of SPHS is based on the high order flow convergence detector and the introduction of appropriate dissipation terms. While the discussion herein focuses on viscosity, this method is very versatile in principle it can be further generalised for all advected fluid quantities such as mass flux, artificial viscosity, and density. Unlike the work of Cullen and Dehnen [152], the authors considered the spatial derivative of the velocity divergence in their dissipation switch, and the dissipation parameter is given by

$$\alpha_{loc,i} = \begin{cases} \frac{\alpha_{max} h_i |\nabla(\nabla\cdot\vec{v}_i)|}{h_i^2 |\nabla(\nabla\cdot\vec{v}_i)| + h_i |\nabla\cdot\vec{v}_i)| + \xi_{loc} c_i} & \nabla\cdot\vec{v}_i < 0 \\ 0 & \nabla\cdot\vec{v}_i \geq 0 \end{cases} \tag{3.59}$$

where $\xi_{loc} = 0.05$ and the $\alpha_{loc,i}$ parameter is a measure of the amount of dissipation for each particle. The dissipation is active when a SPH particle is experiencing a net compression within the support of the kernel $\nabla\cdot\vec{v}_i < 0$, namely in a convergent flow, and the magnitude of dissipation is proportional to the rate of change of the local compression (i.e. $\nabla(\nabla\cdot\vec{v}_i)$) within the kernel. To further improve the accuracy of gradient estimators in equation (3.59), the author propose a second order polynomial to each fluid quantities similar to the earlier work of Maron and Howes [154]. Once $\alpha_{loc,i}$ has been determined, the artificial viscosity parameter α_i is determined by the following conditions:

$$\begin{aligned} \alpha_i &= \alpha_{loc} & \alpha_i &< \alpha_{loc} \\ d\alpha_i/dt &= (\alpha_{loc} - \alpha_i)/\tau_i & \alpha_{min} &< \alpha_{loc,i} < \alpha_i, \\ d\alpha_i/dt &= (\alpha_{min} - \alpha_i)/\tau_i & \alpha_{min} &> \alpha_{loc,i} \end{aligned} \tag{3.60}$$

where the time-scale of the decay is defined as $\tau = h_i/\underset{j}{max}(v_{sig,ij})$. In essence, this guarantees a SPH particle α_{min} to adapt to the localised value within its kernel α_{loc}. In the case of convergent flows, their algorithm is able to detect the rate of change of the localised distribution of the velocity divergence, and therefore introduce the appropriate dissipation in time by changing the artificial viscosity of the particle via equation (3.60).

3.10 Equation of State

The equation-of-state (EoS) determines pressure as a function of state variables such as density or internal energy. The two most commonly employed equation-of-state in SPH are the ideal-gas EoS and the Tait EoS, both of these will be discussed herein. The ideal-gas EoS is commonly used in astrophysical applications

$$P(\rho, e, \gamma) = (\gamma - 1)\rho e. \tag{3.61}$$

It relates the pressure (P) of a particle to its density and internal energy. In astrophysical simulations, the baryons are assumed to be a mono-atomic gas with heat capacity ratio of $\gamma = 5/3$. The ideal-gas EoS can be written in terms of internal energy using the $e = c_v T$, where c_v is the specific heat at constant volume.

For an adiabatic process in ideal-gas, the relationship between temperature, density and pressure, is given by the Poisson's law [155]

$$\frac{T}{T_o} = \left(\frac{P}{P_o}\right)^{\frac{\gamma-1}{\gamma}} = \left(\frac{\rho}{\rho_o}\right)^{\gamma-1}, \tag{3.62}$$

where T_o, P_o and ρ_o are the background temperature, pressure and density re-

spectively. Rearranging (3.62) to obtain the relation for relative pressure gives

$$\Delta P_i(\rho, \rho_o, \gamma) = P - P_o = P_o \left[\left(\frac{\rho}{\rho_o} \right)^{\gamma} - 1 \right]. \tag{3.63}$$

Utilising the definition of the adiabatic speed of sound ($c^2 = \partial P / \partial \rho$), the background pressure has the form of $P_o = \rho c_{SPH}^2 / \gamma$. Note that an artificial speed of sound c_{SPH} is employed instead of the real speed of sound such that the fluid flow remains in the low Mach number regime ($M < 0.1$). Equation (3.63) is the Tait EoS as commonly used within weakly-compressible SPH [62, 128] for terrestrial fluid dynamics applications.

Unlike the ideal-gas EoS, the Tait EoS is a barotropic EoS which considers the relative pressure of a fluid with respect to its initial reference pressure. When temperature effects are significant in a weakly-compressible flow (e.g. natural convection, conduction), one can either apply the Boussinesq approximation or a modified Tait EoS that includes temperature. For small temperature variations, the Boussinesq approximation assumes a linear relationship between density and temperature in the effective gravity term in the momentum equation

$$(\rho - \rho_o)|\vec{g}| \approx -\rho_o \, \beta_{thermal} (T - T_o)|\vec{g}|, \tag{3.64}$$

where $\beta_{thermal}$ is the thermal expansion coefficient defined as

$$\beta_{thermal} = \frac{1}{\rho} \left(\frac{\partial \rho}{\partial T} \right)_p. \tag{3.65}$$

It is obvious that an upward acceleration due to buoyancy is obtained when $\rho < \rho_o$ and $T > T_o$. Alternatively, one can combine the Tait EoS (3.63) and the Poisson's Law (3.62) to obtain a modified Tait EoS (3.66) that encapsulates the

effects of both density and temperature

$$\Delta P_i(\rho, T, \rho_o, T_o, \gamma) = P_o \left(\frac{\rho_i}{\rho_o} \frac{T_i}{T_o} - 1 \right). \tag{3.66}$$

3.11 Multiphase SPH

3.11.1 Survey of multiphase SPH literature

In recent years, some researchers have explored the use of SPH for multiphase flows. Analysing the performance of mesh-based simulation codes and SPH, Agertz et al. [148] pointed out that the conventional SPH formulation is not capable of resolving multiphase flows due to errors in density estimates and discontinuities in internal energies near to fluid interfaces. The combination of biased density estimates and the discontinuity in physical quantities disrupts the dynamic boundary condition and generates an artificial pressure jump near the interface, an effect also known as artificial surface tension in the literature. The multiphase SPH literature in astrophysics and terrestrial fluid dynamics are summarised in following sections.

Astrophysics

The current state-of-the-art multiphase SPH within astrophysics are largely based on three strategies:

i) introduce SPH schemes that ensure a single-valued pressure at the interface by construction. Initially proposed by Ritchie and Thomas [156], smoothed-pressure SPH relies on the concept that fluids on either side of an interface are required to satisfy the dynamic boundary condition. For inviscid fluids, this is given by the equilibrium in pressure at the interface (c.f chapter4, equation (4.3)). Based on this concept, the authors introduced an internal

energy weighted density estimate and an alternative form of the equations of motion which conserves momentum and at the same time guarantees a single-valued pressure.

This approach was extended by Read et al. [109] to resolve mixing problems. The authors discovered standard SPH schemes suffer from two major error sources that suppress mixing, i.e. the leading order term in the momentum equation known as the $\mathbf{E}_{0,i} = 0$ error and the local-mixing error in the pressure gradient approximation. While the $\mathbf{E}_{0,i} = 0$ decreases with increasing number of neighbours, increasing the neighbour count can lead to the pairing instability which causes a decrease in effective resolution. To combat this situation, the authors proposed combining the SPH formulation presented in Ritchie and Thomas [156] with a higher order kernel function would properly remedy mixing problems in SPH. Recently, Saitoh and Makino [157] introduced a density-independent SPH. In contrast to conventional SPH, their SPH scheme is based on smoothing the internal energy density rather than the mass density. The authors demonstrate success in resolving numerous multi-fluid problems, including the KHI between two ideal gases. Inspired by the results of Saitoh and Makino [157], Hopkins [158] proposed a generalised equation of motion for any choice of volume element. The idea behind this concept is that one shall use pressure as a discretisation variable such that the pressure distribution is smoothed by default. In this case, volumes of the particles are estimated from the equation of state once the pressure is known. This can significant reduce the pressure jump which arises from error in the density estimates. Nevertheless, the smoothed-pressure SPH variants are known to break down as the density ratio increase or if the ratio of internal energy increases therefore limiting their capabilities in model high density ratio multiphase flows.

ii) introduce correction terms to artificially smooth out discontinuities in physical quantities (e.g. internal energy, chemical composition). Price [110] introduced an artificial conduction term to smooth out internal energy as SPH particles of different phases approach each other. Recently, Read and Hayfield [153] introduced the SPHS that detects flow convergence, marking regions where the fluid properties are allowed to diffuse discontinuities in all physical quantities. As discussed in section 3.9.4, SPHS is a very versatile method, and the authors have demonstrated the use of this switch for simulating multiphase flows of high density ratios in a multi-mass setup such as a KHI for density ratios up to 8.

iii) Construct higher order solutions of the Euler equation using a local polynomial fit to recover gradient information from a set of disordered SPH particles [154, 159, 160]. A major advantage of this approach is that the corresponding SPH scheme avoid clumping and banding instability as well as reduces the spurious shear viscosity. Nevertheless, the problem due to pressure discontinuity near the interface is not resolved in these higher order SPH schemes unless the $\mathbf{E}_{0,i} = 0$ error is subtracted from the equation of motions. A detailed discussion of these methods is beyond the scope to this, inclined readers are referred to [154, 160].

Terrestrial fluid dynamics

As well as development in the context of astrophysical SPH, multiphase modelling has also been studied in the context of weakly-compressible SPH. Colagrossi and Landrini [161] used a density re-normalization at intermediate time steps, a large artificial surface tension and high wave speed for the low density fluid, and a smoothing of the velocity field. Apart from the non-physical aspects, very small time steps are required in their SPH scheme. Flebbe et al. [162] first introduced the particle number density approach. Hu and Adams [163, 164] applied this

approach in fluid engineering to estimate the density for multiphase flows, where particles of different fluids are both assumed to occupy an equal volume. Although this approach has been widely applied in the weakly-compressible SPH literature, it suffers from severe limitations which need to be properly addressed. (i) In essence, the number density estimate assigns density by spatially-weighted kernel averaging. Nonetheless, this approach is valid only if multi-mass SPH particles are considered, and it is congruent to the standard SPH formulation where equal-mass SPH particles are utilised in the setup of multiphase simulations. This implies if no additional treatment is applied, the number density of the low (high) density fluid will be over(under) estimated hence leading to a spurious pressure gradient near the inference. (ii) Another restriction of this concept is that the particle volume and the change of volume ($\Delta V/V$) due to compression must remain the same for different fluids. The latter means that the choice of the speed of sound ratio is rather limited, usually leading to an un-physical speed of sound ratio between the two fluids (c.f. section 3.11.2) that results in prohibitively small time-steps as the density ratio increases. (iii) Finally, the number density is based on summation density estimate which is not suitable free-surface flow applications within weakly-compressible SPH. Grenier et al. [165] extended the number density approach to model free surface flows. Their approach involves the use of the standard SPH density estimate with a Shepard correction taking into account particles of the same phase. The volume estimate of a particle is made by evolving the continuity equation. In addition a repulsive force between particles of different fluids is introduced to stabilise the interface and prevent artificial surface tension instabilities. Monaghan and Rafiee [166] introduced a SPH method for high density ratios. The model is based on the combined use of an alternative form of the SPH continuity equation and the momentum equation of Ritchie and Thomas [156] as well as a surface stabilisation term that aims to suppress spurious pressure gradient near

the fluid interface. Kruisbrink et al. [167] proposed a quasi-buoyancy correction term to simulate multiphase flow at high density ratios (c.f. section 3.11.3). Their approach demonstrated acceptable results for modelling stratified flow as well as an internal gravity wave for multiphase fluid with a density ratio of 100. Recently, Korzilius et al. [168] proposed a multiphase model based on kinetic collision theory of two incompressible particles (c.f. section 3.11.4). Their model demonstrates success at the simulation of multiphase flows in rapidly rotating circular geometries and a multiphase dam break for density ratios up to three magnitudes.

Fully incompressible analogues of SPH have also gained popularity in the fluid dynamics simulation community, two of the best known examples are the Moving Particle Semi-Implicit method (MPS) and Incompressible SPH (ISPH). Unlike weakly-compressible SPH, these methods are truly incompressible such that both volume and mass of particles remain constant throughout the simulation. The number density approach is used to obtain the local smoothing of physical quantities of neighbour particles, and the pressure of particles are determined by solving the pressure Poisson equation iteratively during each time step. The workings of MPS and ISPH are similar except for the methods used to solve the Poisson equation. A detailed review for these methods is beyond the scope of this thesis, inclined readers are referred to Souto-Iglesias et al. [169].

3.11.2 Pseudo-consistent SPH

The analysis in section 3.8 demonstrates a consistent set of SPH fluid dynamical equations which with the inclusion of any arbitrary scalar function ϕ, can be derived from the Euler-Lagrange equation (3.28) and satisfies the conservation properties of classical mechanics. In search of an appropriate SPH formulation, Read et al. [109] considered an alternative viewpoint where each of the conservation laws has its own arbitrary function ϕ. The authors performed a perturbation

analysis on the SPH fluid dynamical equations and discovered the accuracy of SPH discretisation is directly influenced by the choice of these functions, with the leading order error term in the momentum being the predominate problem. In what follows, we discuss the importance of an appropriate choice for ϕ and demonstrate the concept of smoothed-pressure SPH [109, 156] can be extended to the context of weakly-compressible SPH. Taylor expanding the pressure of a nearby particle j around the particle of interest i gives

$$P_j \approx P_i + \vec{r}_{ij} \cdot \nabla_i P_i + \mathcal{O}(h^2). \tag{3.67}$$

Substituting (3.67) into (3.43) and rearranging the terms yields

$$\frac{D\vec{v}_i}{Dt} \simeq -\sum_j m_j \left[\frac{P_i}{\rho_i^2} \frac{\phi_i}{\phi_j} + \frac{P_i + \vec{r}_{ij} \cdot \nabla_i P_i + \mathcal{O}(h^2)}{\rho_j^2} \frac{\phi_j}{\phi_i} \right] \nabla_i W_{ij}. \tag{3.68}$$

Rearranging the terms with respect to the kernel and the pressure gradient gives

$$\frac{D\vec{v}_i}{Dt} \simeq -\frac{P_i}{\rho_i} \sum_j \frac{m_j}{\rho_j} \left[\frac{\phi_i}{\phi_j} \frac{\rho_j}{\rho_i} + \frac{\phi_j}{\phi_i} \frac{\rho_i}{\rho_j} \right] \nabla_i W_{ij} - \frac{1}{\rho_i} \sum_j \frac{m_j}{\rho_j} \frac{\phi_j}{\phi_i} \frac{\rho_i}{\rho_j} \vec{r}_{ij} \cdot \nabla_i P_i + \mathcal{O}(h), \tag{3.69}$$

where the first term in equation (3.69) is previously known as the $\mathbf{E}_{0,i}$ error [109], and the second term is called $\mathbf{E}_{1,i}$ error herein. The accuracy of the perturbed momentum equation (3.68) and hence (3.43) is given by the extent to which $\mathbf{E}_{0,i} = 0$ and $\mathbf{E}_{1,i} = \mathbf{I}$, with the $\mathbf{E}_{0,i} = 0$ being the dominant factor Read et al. [109]. Analysing these error terms, Read et al. [109] identified three reasons which prevented the $\mathbf{E}_{0,i}$ term from vanishing. Firstly, $\mathbf{E}_{0,i}$ should vanish due to the asymmetry property of the kernel gradient; however, it ceases to vanish when particles are irregularly distributed. Secondly, $\mathbf{E}_{0,i}$ is proportional to the density ratio between the fluids. It is therefore desired to choose $\phi = \rho$ such that the density ratio does not contribute to the amplification of the $\mathbf{E}_{0,i}$ error. Finally, the local mixing instability is responsible for inhibiting mixing at a

kernel level even if the initial setup is at pressure equilibrium [148, 156]. Agertz et al. [148] pointed out that the local mixing instability can be understood as a consequence of the fact that the summation density is computed in every time-step and the internal energy is updated via time-integration. Therefore, as soon as the simulation begins, a low density (high temperature) particle approaching the interface encounters more high density (low temperature) particles, leading to an increase in its density. Whereas a high density (low temperature) particle near the interface encounters more low density (high temperature) particles; therefore its density decreases. This consequently leads to a multi-valued pressure at the interface, resulting in a spurious pressure gradient.

As previously mentioned, the spurious pressure gradient can be remedied by employing artificial conduction schemes [110, 153] or a density estimate that guarantees single-valued pressure by construction [109, 156]. In this thesis, we focus on the latter given its relevance to the multiphase SPH scheme herein.

The concept of the smoothed pressure SPH formulation can be further understood by considering the following: suppose two ideal-gas particles with the same heat capacity ratio are located in the support of the SPH kernel. Pressure equilibrium requires $P_i \approx P_j$. It then follows that

$$\frac{\rho_i}{\rho_j} \approx \frac{e_j}{e_i}. \tag{3.70}$$

Equation (3.70) provides the internal energy weighted density estimate of a single particle pair. Applying the SPH particle estimate(3.36) with $\phi = 1/e$ gives the internal energy density estimate [109, 156]

$$\rho_i \approx \sum_j m_j \frac{e_j}{e_i} W_{ij}. \tag{3.71}$$

It is worth reviewing the underlying assumptions in the derivation of the internal

energy density estimate. Firstly, the particles are assumed to have the same heat capacity ratio. While it is acceptable in astrophysics to assume all SPH particles have $\gamma = 5/3$ for diatomic gas, in general the γ of two fluids need not to be the same (e.g $\gamma = 7.0$ for water and $\gamma = 1.4$ for air). Secondly, the physical argument $P_i \approx P_j$ is only applicable for inviscid fluids. In principle, the dynamic boundary condition requires stress balance across the interface [94]. Thirdly, both fluids are assumed to be ideal-gases. This poses strong limitations on the feasibility of the internal energy density estimate for other EoS because many flow scenarios are modelled by the Tait EoS (3.63) where the pressure of a fluid is not influenced by internal energy (temperature). One can of course utilise the same physical argument based on balancing pressure to reconstruct SPH schemes for barotropic fluids. Replacing the ratio of internal energy in (3.71) by the ratio of the particles densities (ρ_i/ρ_j) gives

$$\rho_i = \sum_j m_j \frac{\rho_i}{\rho_j} W_{ij}. \tag{3.72}$$

However, this density estimate (3.72) requires iterative solvers which can potentially lead to computational overhead. To overcome this challenge, one shall consider the differential form of the continuity equation rather than the summation density estimate. Substituting $\phi = \rho$ and taking the time derivative of (3.36) gives

$$\frac{D\rho_i}{Dt} = \sum_j m_j \frac{\rho_i}{\rho_j} \vec{v}_{ij} \cdot \nabla W_{ij} + \chi_{ij}, \tag{3.73}$$

$$\chi_{ij} = \sum_j m_j \frac{\rho_i}{\rho_j} \left(\frac{1}{\rho_i} \frac{d\rho_i}{dt} - \frac{1}{\rho_j} \frac{d\rho_j}{dt} \right) W_{ij}, \tag{3.74}$$

this is previously known as ϵ in [109]. The error term χ can be further simplified to the difference of velocity divergence at the previous time-step

$$\begin{aligned}\chi_{ij} &= -\sum_j m_j \frac{\rho_i}{\rho_j} \left(\nabla \cdot \vec{v}_i - \nabla \cdot \vec{v}_j\right) W_{ij} \\ &= -\sum_j m_j \frac{\rho_i}{\rho_j} \nabla \cdot \vec{v}_{ij} W_{ij}.\end{aligned} \tag{3.75}$$

We argue that the error term χ_{ij} which arises from the differential form of the continuity equation χ_{ij} is negligible if at least one of the following conditions are satisfied: firstly, if the compressibility of both phases are the same then the divergence of the particle pair offsets each other in equation (3.75). However, as we will demonstrate in the later parts of this section, this requirement imposes strict limitations on choosing the ratio between artificial speed of sound and the heat capacity ratio. Secondly, consider the limiting case of a truly incompressible flow where $\nabla \cdot \vec{v} = 0$ by definition for all particles. While this is generally not true for compressible flows, one should expect similar behaviour for sufficient low Mach number ($M < 0.1$) as considered in weakly-compressible flows. Note that the error term (3.74) should play a significant role as the Mach number increases; however, the investigation of multiphase flows in transonic and supersonic regimes are beyond the scope of this thesis. Thirdly, the *continuity of tangential velocity condition* (c.f. chapter 4, section 4.4.1) requires the tangential velocity component between two fluids to be the same; therefore it is expected the relative velocities of nearby particles decreases with increasing resolution. Hence, it is expected the contribution from the χ_{ij} error term in the differential form of the continuity equation (3.73) should be significantly smaller than the first order term for weakly-compressible flows. Furthermore, since the density ratio factor in equation (3.73) is estimated from the densities at the previous time-step, the use of the differential continuity equation approach does not require the utilisation of iterative solvers.

The inclusion of ϕ in section 3.8 allows one to obtain SPH equations that

are consistent and that conserve mass, momentum and energy. Especially, the SPH equations used in this thesis utilise $\phi = \rho$ for the continuity equation and momentum equation, and $\phi = 1/e$ for the internal energy equation. The derived SPH scheme has numerous advantages over the standard SPH formulation and the internal energy density estimate. The differential continuity equation evolves the density based on the relative velocities of the particles; hence, it allows for the handling of free-surface flow even when a fixed smoothing length is used. This property is highly desirable and is not be possible for the summation density estimates when fixed smoothing length is used. The SPH scheme conserves linear and angular momentum. Finally, the SPH scheme relaxes the assumption in the equation-of-state and the heat capacity ratio between fluids. It is worth addressing the potential limitations of the presented multiphase SPH scheme: that is, because the density ratios is actually replaced by the internal energy ratio in the energy equation, our multiphase SPH can only approximately conserve total energy; hence, it is called a pseudo-consistent SPH hereafter.

The pseudo-consistent SPH scheme discussed above forms the basis of the multiphase method presented in this thesis. It is found that our pseudo-consistent SPH scheme can generate satisfactory results for low density ratio multiphase flows. Nonetheless, there are additional challenges when modelling multiphase flow using weakly-compressible SPH. Bear in mind that weakly-compressible SPH employs a fixed smoothing lengths, and the *multi-mass particle and equal separation* is adopted for the initial conditions setup (c.f. chapter 4, section 4.2). This essentially introduce a mass discontinuity near the interface. More importantly, recall that the Tait EoS (3.63) determines the pressure relative to some background pressure P_o, it can be seen from (3.69) that $\mathbf{E}_{o,i} \propto P_o$ as soon as the density changes from its reference value. Thus, choosing a large background pressure in the Tait EoS (3.63) results in an amplification of the $\mathbf{E}_{o,i}$ error. This naturally leads to a more fundamental question of whether or not the two fluids

should have the same background pressure P_o. To answer this question, we consider a simplified multiphase system consisting of a water and air particle. Figure 3.4 illustrates the pressure computed directly from the Tait EoS (3.63)

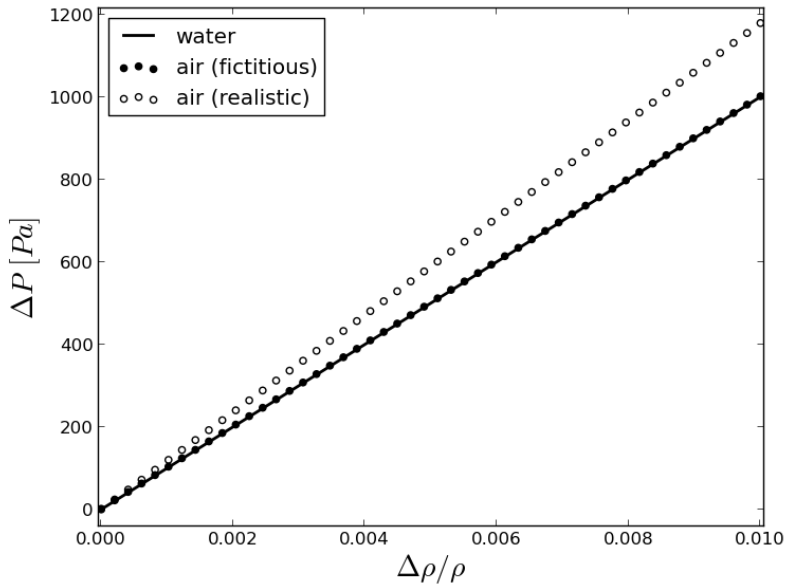

Figure 3.4: Relative pressure determined from Tait EoS (3.63) plotted as a function of the rate of compression. The use of fictitious properties enforces the pressure gradient to vanish. Nonetheless, this leads to non-physical speed of sound ratios and prohibitive time-steps. The use of realistic fluid properties generates a large pressure gradient at the interface proportional to the compression ratio of the fluids.

plotted as a function of the rate of compression ($\Delta\rho/\rho$). The solid line represents the pressure of the water, the black dots correspond to the pressure of air particles computed using fictitious properties (i.e. by satisfying $P_{o,i} = P_{o,j}$) and the open circles correspond to pressure of air particles computed using real properties. Inspecting the results, one can immediately observe that the pressure of the air and water particles coincide when the background pressures are the same $P_{o,air} = P_{o,water}$. Utilising the definition of the background pressure from the Tait EoS (3.63), it is required that

$$\begin{aligned} P_{o,air} &= P_{o,water} \\ \frac{\rho_{air} c^2_{SPH,air}}{\gamma_{air}} &= \frac{\rho_{water} c^2_{SPH,water}}{\gamma_{water}}. \end{aligned} \tag{3.76}$$

Rearranging equation (3.76) for the artificial speed of sound ratio gives

$$\frac{c_{SPH,air}}{c_{SPH,water}} = \sqrt{\frac{\rho_{water}\gamma_{air}}{\rho_{air}\gamma_{water}}}. \tag{3.77}$$

Direct substitution of the state properties of air ($\rho_{air} \approx 1\text{kg/m}^3$, $\gamma_{air} = 1.4$) and water ($\rho_{water} \approx 1000\text{kg/m}^3$,$\gamma_{water} = 7$) into equation (3.77) reveals the artificial speed of sound of an air particle is approximately 14 times larger than the artificial speed of sound of a water particle (i.e. $c_{SPH,air} \approx 14c_{SPH,water}$). This conflicts with reality as the speed of sound in air is significantly lower than the speed of sound in water (i.e. $c_{air} = 343.21\text{m/s}$ and $c_{water} = 1481\text{m/s}$ at 20^oC). This phenomena which we called the *discontinuity in background pressure* hereafter is one of the major challenges in the modelling of multiphase flows using weakly-compressible SPH. Although some literature has employed the same background pressure for both fluids [161, 163, 164], our results is consistent with the claim made by Monaghan and Rafiee [166], Kruisbrink et al. [167] that enforcing the same background pressure leads to physically incorrect (non-physical) speed of sound ratios.

The necessity of correct speed of sound ratios can be further illustrated by an independent study of multiphase systems situated in a confined space and subjected to slight compression via a adiabatic process. Rewriting first law of thermodynamics (3.32) as

$$de = -PdV = \frac{P}{\rho}\frac{d\rho}{\rho}. \tag{3.78}$$

The definition of the adiabatic speed of sound gives the auxiliary relation

$$\frac{dP}{\rho c^2} = \frac{d\rho}{\rho}. \tag{3.79}$$

Substituting (3.79) intro (3.78) gives

$$de = \frac{P}{\rho}\frac{dP}{\rho c^2}. \tag{3.80}$$

In the absence of surface tension and viscous effects, the dynamic boundary condition requires $P_i = P_j$ and $dP_i = dP_j$. Thus, the ratio between the work due to compression for the two fluids is given by

$$\frac{de_i}{de_j} = \left(\frac{\rho_j c_{SPH,j}}{\rho_i c_{SPH,i}}\right)^2. \tag{3.81}$$

Equation (3.81) implies that in order to have an accurate measure between the ratio of the pressure-volume work, it is desirable in weakly-compressible SPH simulations to keep the density and γ of the fluids at their real values, and the ratio of the artificial speed of sound to be the same as the realistic speed of sound ratio (i.e. $c_{SPH,i}/c_{SPH,j} = c_i/c_j$).

Apart from the *mass discontinuity* and the *discontinuity in background pressure*, additional challenge arises when modelling high density ratio stratified flows with SPH. Consider a stagnant flow consisting of two fluids **A** and **B**. The pressure distribution within the two stratified fluid layers is hydrostatic as shown in Figure 3.5. The pressure gradient changes at the interface due to the density difference. The continuum fluid around the interface is at rest due to an equilibrium of surface forces; however, this is not the case when the continuum of fluid is modelled using SPH. It is because a lower density particle i experiences a higher pressure from it neighbour particles j of the high density fluid, resulting in an overall upward movement in the vertical direction. It would stay at rest if its hydrostatic pressure distribution was extrapolated within the kernel scale as shown in Figure 3.5.

It is worth stressing that in a realistic high density ratio multiphase flow subjected to gravitational acceleration, the *mass discontinuity*, the *disconti-*

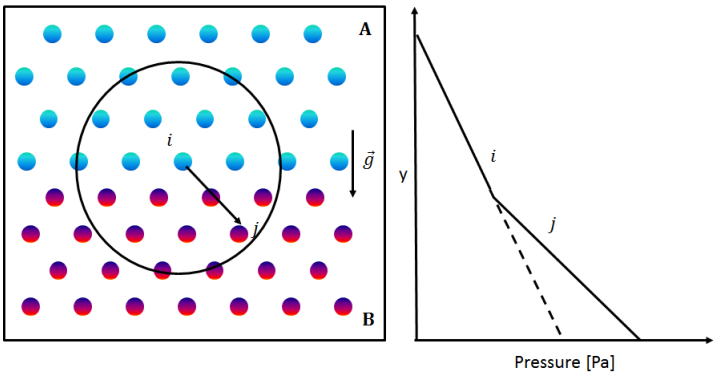

Figure 3.5: Stagnant stratified flow and the piecewise hydrostatic pressure distribution plotted in dots.

nuity in background pressure and the problem with maintaining a hydrostatic pressure profile all contribute to the interface numerical instabilities in weakly-compressible SPH simulations. With the aim to overcome these challenges, two models have been introduced to improve the performance of the pseudo-consistent multiphase SPH scheme for high density ratios: the quasi-buoyancy correction model and the gas repulsion model. The concepts of these models will be discussed in the following subsections.

3.11.3 Quasi-buoyancy correction model

The quasi-buoyancy correction model is based on a buoyancy force acting on a partially submerged particle. It is introduced to stabilise the interface of high density ratio flows subjected to a constant gravitational field. The model has been applied to simulated two phase channel flows, internal gravity waves and RTI for a density ratio of 1.8, where acceptable results were obtained [167]. The model can be derived by taking into consideration of two-phase system {**A**,**B**}, where $\rho_{o,\mathbf{A}} \leq \rho_{o,\mathbf{B}}$. The initial configuration is shown in Figure 3.5. Suppose that a fluid particle i of phase **A** is partially submerged in the bulk of fluid the particles in phase **B**. The force due to buoyancy on particle i is given by

$$\vec{F}_{i,buoyancy} = -(\rho_m - \rho_i)V_i\vec{g}, \tag{3.82}$$

where ρ_m is the mixture density of the surrounding fluid $\mathbf{B}$ within the support of the kernel function. Expressing the mixture density in SPH form gives

$$(\rho_m - \rho_i) = \sum_{j \in \mathbf{B}} (\rho_{m,j} - \rho_i) V_j W_{ij}. \tag{3.83}$$

Replacing the $\rho_m - \rho_i$ term in equation (3.82) by equation (3.83) yields the SPH form of the buoyancy force

$$\vec{F}_{i,buoyancy} = -\sum_{j \in \mathbf{B}} (\rho_{m,j} - \rho_i) V_i V_j \vec{g} W_{ij}. \tag{3.84}$$

This result is formulated as a pressure gradient force correction by taking the opposite sign (i.e. $\vec{F}_{i,buoyancy} = -\vec{F}_{i,correction}$). This concept is applicable to gravity driven flows such as internal gravity waves and stratified channel flows where the effects of viscosity are negligible. Re-writing equation (3.84) in terms of volumes results in a pressure gradient correction force (the negative of the buoyancy force)

$$\vec{F}_{i,correction} = \sum_{j \in \mathbf{B}} (\rho_{m,j} - \rho_i) V_i V_j \vec{g} W_{ij}. \tag{3.85}$$

Consider the limiting case where a low density particle is entirely surrounded by high density neighbour particles. Physically, the buoyancy force should result in an upward motion. Nonetheless, the buoyancy force is entirely suppressed by the pressure gradient force correction (3.84), this leads to the stabilisation of the interface which is un-physical. A reduction factor $C_{i,effective}$ is given to determine the strength of the applied quasi-buoyancy correction, and it is defined as

$$C_{i,effective} = \frac{|S^{eff}_{i,\mathbf{B}}|}{S_{i,\mathbf{A}} + \xi h^2}, \tag{3.86}$$

where a constant $\xi = 0.01$ is introduced to avoid numerical divergence. The numerator is given by the weighted volume of nearby particles of phase **B**,

$$S_{i,\mathbf{B}}^{eff} = \sum_{j \in \mathbf{B}} sign(\vec{g} \cdot \vec{r}_{ij}) V_j W_{ij}. \tag{3.87}$$

The denominator $S_{i,\mathbf{A}}$ accounts for the submergence of particles of interest by comparing the base density of the neighbour particle with the base density of itself, namely $\rho_{o,\mathbf{A}}$.

$$S_{i,\mathbf{A}} = \frac{\rho_m - \rho_{o,\mathbf{A}}}{\rho_{o,\mathbf{B}} - \rho_{o,\mathbf{A}}}. \tag{3.88}$$

Applying the SPH particle approximation of the mixture density (3.87) yields,

$$S_{i,\mathbf{A}} = \sum_j \frac{\rho_{o,j} - \rho_{o,\mathbf{A}}}{\rho_{o,\mathbf{B}} - \rho_{o,\mathbf{A}}} V_j W_{ij}. \tag{3.89}$$

The contribution from nearby particles $j \in \mathbf{A}$ vanishes. Hence, the denominator simplifies to

$$S_{i,\mathbf{A}} = \sum_{j \in \mathbf{B}} V_j W_{ij}. \tag{3.90}$$

The reduction factor ratio (3.86) is essentially the ratio between the effective submergence (3.87) and the SPH evaluation of the mixture density (3.90). Incorporating the reduction factor and applying the volume estimates into equation (3.85) yields the acceleration due to the quasi-buoyancy pressure gradient correction.

$$\vec{a}_{i,correction} = C_{i,effective} \sum_{j \in \mathbf{B}} m_j \left(\frac{1}{\rho_i} - \frac{1}{\rho_j} \right) \vec{g} W_{ij}. \tag{3.91}$$

3.11.4 Gas repulsion model

Although the quasi-buoyancy model proposed in section 3.11.3 successfully recovers the hydrostatic pressure gradient, is not applicable for problems without a gravitational field. Thus, a multiphase SPH model is developed for flow problems

with or without gravity and operates for density ratios up to three magnitudes. The gas repulsion model [170] is motivated by kinetic collision theory. The idea of collisions in SPH is not entirely novel [171, 172], but it has not been applied in the way proposed herein. The model is derived taking into consideration of two boundary cases, namely a fully elastic collision and an inelastic collision.

Consider a fully elastic collision: since no energy is dissipated, the conservation of both momentum and energy is satisfied. The momentum conservation is given by

$$\vec{p}_{i,a} + \vec{p}_{j,a} = \vec{p}_{i,s} + \vec{p}_{j,s}, \tag{3.92}$$

where $\vec{p}_{ij,a}$ and $\vec{p}_{ij,s}$ correspond to the momentum before and after the collision respectively. The energy conservation is given by

$$\frac{\vec{p}_{i,a}^2}{2m_i} + \frac{\vec{p}_{j,a}^2}{2m_j} = \frac{\vec{p}_{i,s}^2}{2m_i} + \frac{\vec{p}_{j,s}^2}{2m_j}, \tag{3.93}$$

The separation velocities of the particles are uniquely determined from equation (3.92)-(3.93) as

$$\vec{v}_{i,s} = \frac{(m_i - m_j)\vec{v}_{i,a} + 2m_j\vec{v}_{j,a}}{m_i + m_j} \quad , \quad \vec{v}_{j,s} = \frac{(m_j - m_i)\vec{v}_{j,a} + 2m_i\vec{v}_{i,a}}{m_i + m_j}. \tag{3.94}$$

In a fully inelastic collision, the post collision velocities of both particles are identical. Since energy is dissipated, there is only conservation of momentum. The post-collision velocity is given by [170]

$$\vec{v}_{i,s} = \frac{\vec{p}_{i,a} + \vec{p}_{j,a}}{m_i + m_j}. \tag{3.95}$$

Defining C_R as the coefficient of restitution and formulating the separation velocities as a linear combination of the elastic (3.94) and inelastic (3.95) collision

gives

$$\vec{v}_{i,s} = \frac{(m_i - C_R m_j)\vec{v}_{i,a} + (1 + C_R)m_j\vec{v}_{j,a}}{m_i + m_j}. \tag{3.96}$$

It can be easily verified that $C_R = 0$ corresponds to an inelastic collision (3.95) and $C_R = 1$ corresponds to an elastic collision (3.94). The change in velocity of a particle i before and after the collision is

$$\Delta v_i = \vec{v}_{i,s} - \vec{v}_{i,a} = \frac{-m_j}{m_i + m_j}(1 + C_R)\vec{v}_{ij,a}. \tag{3.97}$$

The change in velocity should only be applied to the inter-particle direction, as given by the unit vector $\vec{e}_{ij} = \vec{r}_{ij}/|\vec{r}_{ij}|$. The relative velocity along the inter-particle direction is

$$\vec{v}_{ij,a} = (\vec{v}_{ij,a} \cdot \vec{e}_{ij,a})\vec{e}_{ij,a} = \frac{(\vec{v}_{ij,a} \cdot \vec{r}_{ij,a})\vec{r}_{ij,a}}{|\vec{r}_{ij}|^2}. \tag{3.98}$$

Substituting (3.97) into (3.98) yields the velocity of particle i after the collision with particle j

$$\vec{v}_{i,s} = \vec{v}_{i,a} - \sum_j \frac{m_j}{m_i + m_j}(1 + C_R)\frac{(\vec{v}_{ij,a} \cdot \vec{r}_{ij,a})\vec{r}_{ij,a}}{|\vec{r}_{ij}|^2}. \tag{3.99}$$

The particle collision concept is based on velocities. To make the step to forces we assume for the contact time-scale between two particles is $\Delta t_{collision} = |\vec{r}_{ij}|/|\vec{v}_{i,a}|$. Note that $\Delta t_{collision}$ may be much smaller than the time step in the simulation. Combining equation (3.99) with the definition of the contact time-scale gives

$$\frac{\vec{v}_{i,s} - \vec{v}_{i,a}}{\Delta t_{collision}} = -\sum_j \frac{m_j}{m_i + m_j}|\vec{v}_{i,a}|(1 + C_R)\frac{(\vec{v}_{ij,a} \cdot \vec{r}_{ij,a})\vec{r}_{ij,a}}{|\vec{r}_{ij}|^3} \tag{3.100}$$

which is an expression for the acceleration. This suggests the formulation of the force due to a collision closely reassembles the viscous force. In that sense the concept may be considered as a time dependent SPH viscosity model. However,

there is a clear distinction between the standard artificial viscosity model and the gas repulsion model presented herein. The essential difference is that the force may become extremely high, since the collision takes place in very short contact times which is far beyond the resolvable time-scale in traditional viscosity models.

Example 3.11.1. In order to study the performance of different multiphase SPH schemes, we consider a stagnant flow of a liquid-gas system. The density of the top and bottom fluids are $\rho_{air} = 1\text{kg/m}^3$ and $\rho_{liquid} = 10^3\text{kg/m}^3$ respectively. The pressure distribution within the two stratified fluid layers is hydrostatic, where both fluids are modelled by the Tait EoS. The background pressure of the top fluid is $P_{o,gas} = 160.7\text{Pa}$ (i.e. $\gamma_{gas} = 1.4$, $c_{SPH,gas} = 15\text{m/s}$) and the background pressure of the bottom fluid is $P_{o,liquid} = 1.286 \times 10^5\text{Pa}$ (i.e. $\gamma_2 = 7$, $c_{SPH,liquid} = 30\text{m/s}$). The realistic heat capacity ratio of are used for both fluids, and the speed of sound ratio is selected such that $c_{SPH,gas} < c_{SPH,liquid}$.

The numerical results at $t = 1\text{s}$ are plotted in Figure 3.6. Inspecting the results, it is obvious that both the standard SPH and the continuity equation fail to capture a stabilised interface. Similar results are found for the pseudo-consistent SPH scheme when a density ratio of 1000 is considered. Furthermore, the number density (see Figure 3.6 c) fails to maintain a stable interface when the background pressure of the fluids are not the same. Our experiment results suggest the model proposed by Monaghan and Rafiee [166] fails to maintain a stabilised interface as illustrated in Figure 3.6 (d). Moreover, the model contains an artificial coefficient (0.08) that is case dependent; however, no guidelines was provided in their work for the appropriate choice of the coefficient.

It is found that the quasi-buoyancy model (section 3.11.3) and the gas repulsion model (section 3.11.4) out performed the other weakly-compressible SPH models and generated a relatively stable interface. The combination of high density ratios and more realistic speed of sound ratios which has not been presented

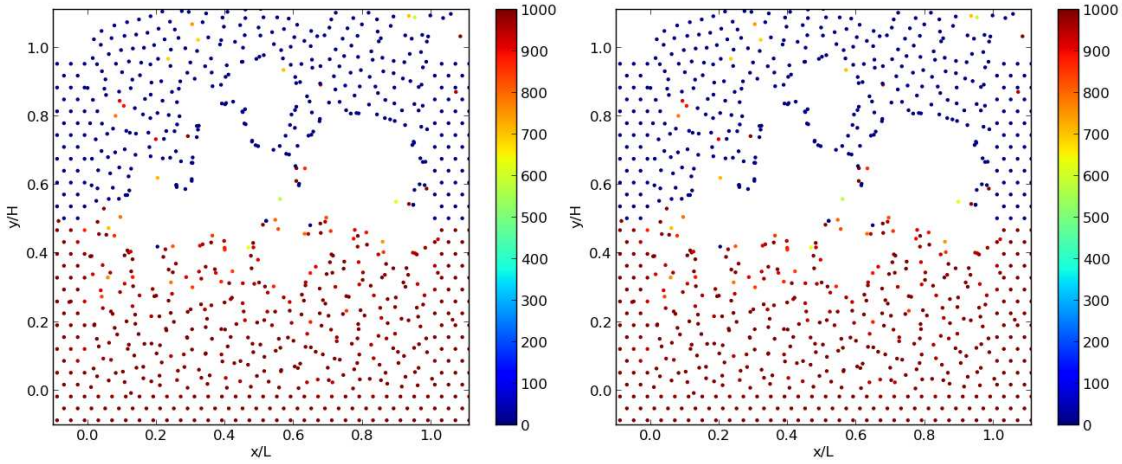

(a) standard SPH

(b) pseudo-consistent SPH

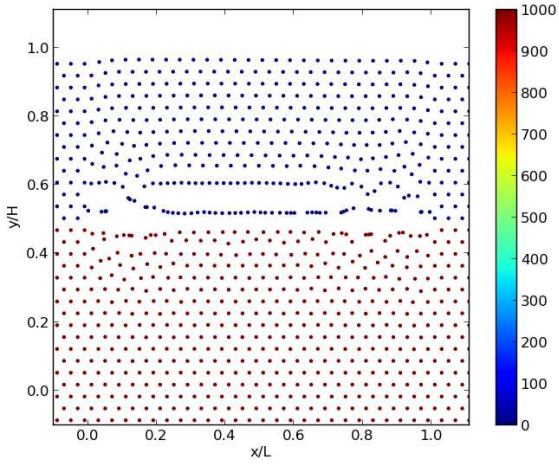

(c) number density [162, 163, 164]

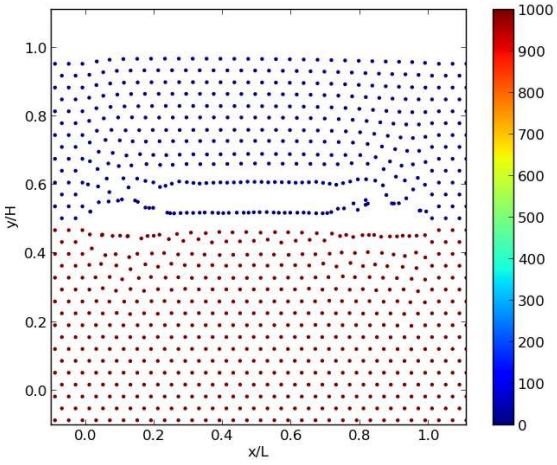

(d) Monaghan interface stabilisation [166]

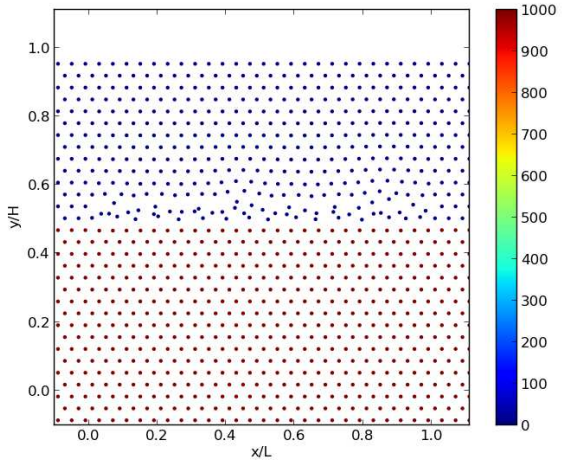

(e) quasi buoyancy model [167]

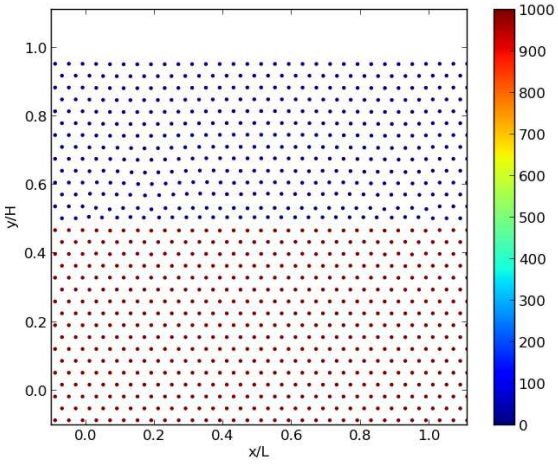

(f) gas repulsion model [170]

Figure 3.6: Numerical results for the stagnant tank example.

in the weakly-compressible SPH literature. More importantly, the presented model does not contain case dependent coefficients which often requires extensive calibrations.

Finally, we would like to point out the implications of this test. Firstly, for high density ratios it is important in weakly-compressible SPH to have correct the speed of sound ratio. Particularly, the modelling pressure-work due to compressibility and temperature effects. It is found that most of the multiphase models in weakly-compressible SPH literature are not capable of resolving a fundamental case like such as stagnant flow when the equal background pressure condition is violated.

3.12 Multiphase pseudo-consistent SPH

To finalise this chapter, we describe the SPH equations used in the subsequent chapters of this thesis. The density and acceleration of a SPH particle are computed from the discretised form of the continuity equation which corresponds to $\phi = \rho$:

$$\frac{D\rho_i}{Dt} = \sum_j m_j \frac{\rho_i}{\rho_j} \vec{v}_{ij} \cdot \nabla_i W_{ij}, \tag{3.101}$$

and the momentum equation:

$$\frac{D\vec{v_i}}{Dt} = -\sum_j m_j \left(\frac{P_i + P_j}{\rho_i \, \rho_j} + \Pi_{ij} \right) \nabla_i W_{ij}. \tag{3.102}$$

In order to keep the formulation generalised, the inclusion of the multiphase models in section 3.11.3 and section 3.11.4 have been omitted. The SPH internal energy equation (3.103) follows from the first law of thermal dynamics and takes into consideration the work done due to compression and the transfer of internal

energy due to viscous heating

$$D_t e_i = -\sum_j m_j \left(\frac{P_i}{\rho_i^2} \frac{e_j}{e_i} + \frac{1}{2}\Pi_{ij} \right) \vec{v}_{ij} \cdot \nabla_i W_{ij}. \tag{3.103}$$

The key features of the multiphase SPH scheme can be summarised as follows:

1. **Artificial speed of sound:** Our gas dynamic simulations employ the real speed of sound that is computed during the simulation, a fixed artificial speed of sound is employed for weakly-compressible SPH. In particular, there are two major restrictions for the choice of the speed of sound. That is, the speed of sound should (i) enforce incompressibility $M < 0.1$ and (ii) allow for practical time-stepping conditions.

2. **Update densities via the $\phi = \rho$ continuity equation and momentum equation:** Particle densities are updated from the multi-fluid flow SPH continuity equation given in equation (3.101). Similarly, the momentum equation in [109, 156] is adopted to improve the stabilisation of the interface for multiphase flows.

3. **Fixed smoothing length for all SPH particles:** With the purpose of modelling weakly-compressible flow, our SPH implementation utilises a constant smoothing length throughout the simulation for all particles.

4. **Density differences are represented by multi-mass SPH particles:** The density differences between fluids are reflected by SPH particles of different masses and equal initial volumes.

3.13 Summary

In this chapter, we reviewed the single and multiphase SPH literature. The first part of this chapter was dedicated to the review of single phase SPH. In particular, the principles of the scattered data approximation and the essential properties of SPH kernel functions were discussed in section 3.3-3.4. An error analysis was performed in section 3.5 to examine the theoretical accuracy of the continuum approximation and particle discretisation used in SPH, followed by a discussion of spatial derivative formulations in the literature in section 3.7. We demonstrated that a consistent set of SPH fluid dynamical equations can be derived from the discretised fluid Lagrangian with the inclusion of arbitrary scalar function ϕ in section 3.8. The artificial viscosity models and equation-of-states employed in SPH simulations were described in section 3.9-3.10.

The second part of the chapter was devoted to multiphase SPH. Starting with a review of the multiphase SPH literature, we discussed the underlying problem faced by standard SPH in handling discontinuities and reviewed the strategies that attempt to solve this matter. Section 3.11.2 introduced a pseudo-consistent formulation of SPH and discussed its advantages and potential limitations. Additional challenges in applying the pseudo-consistent SPH to weakly-compressible multiphase flows systems: mass discontinuity, discontinuity in background pressure, and the difficulty in maintaining a stable interface for high density ratio stratified flows were discussed in detail. It was found that enforcing the same background pressure leads to a physically incorrect speed of sound ratios; hence resulting in prohibitively small time-steps and un-physical pressure-work ratio between fluids. With the aim to overcome these challenges, two interface stabilisation models were presented in section 3.11.3-3.11.4. It was found that these models out performed common multiphase models in the weakly-compressible SPH literature.

Chapter 4

Software Implementation

4.1 Introduction

This chapter is dedicated to the SPH software `Draco` developed for the simulations in this thesis. It is a software project launched and developed by the author, and currently it is made available to research groups at the University of Nottingham, University of Eindhoven, and Tianjin University. The current version of `Draco` supports both single and multiphase fluid dynamics as well as boundary conditions relevant to aerospace engineering applications.

The material in this chapter is organised as follows: section 4.2 provides a survey of existing SPH codes in the research community. Section 4.3 describes the key features of our SPH code. Details regarding the code developmental history are discussed in section 4.3.1. The data structure and the neighbour-list search algorithm used in `Draco` are discussed in section 4.3.2 and 4.3.3. The boundary treatment methods are reviewed in section 4.4. Finally, the time integration scheme is discussed in section 4.5.

4.2 Literature review

A survey of the SPH software in the research community indicates there are generally two types of SPH codes, namely the ones designed for astrophysics and the ones designed for terrestrial fluid dynamics. In astrophysics, SPH is often combined with a gravity solver to model the evolution of astrophysical phenomena that occur in the supersonic regime. Its applications range from cosmology [173], galaxy merging [174], and late-giant impactor problems in planetary astrophysics [175, 176, 177]. In terrestrial fluid dynamics, SPH has been applied to simulate fluid flows in the subsonic regime such as channel flows [178, 179], dam-breaks [180], sediment transport [181] and wave impact problems in coastal structures [182].

Despite the similarities in the SPH concept among these sub-fields, the specific implementations differ in numerous ways. First of all, astrophysical applications usually involve compressible hydrodynamics occurring with a vast dynamical range in density, energies and length-scales. Due to the enormous variation in density, a variable smoothing length is commonly used in astrophysics. Nonetheless, this introduces an additional error which arises from the partial derivative of the kernel function [137, 183]. In contrast, terrestrial fluid dynamics SPH codes model fluid flows with only a small variation of density, such that a constant smoothing length is usually applied throughout except in the shallow water codes when h indicates water depth [184, 185].

Secondly, motivated by tree N-body gravity techniques [186], astrophysical SPH utilises tree algorithms[1] for particle neighbour searching. This approach is generally known as the k-nearest neighbour algorithm, where the tree implementation in SPH is a specific example of the broad family of k-nearest neighbour algorithm [187, 188, 189]. Within terrestrial fluid dynamics applications, a cell-linked list algorithm is usually employed [190]. Note that the cell-linked list is

[1] oct-tree for three-dimensions and quad-tree for two-dimensions

inefficient for variable smoothing length and by default does not reassemble the k-nearest neighbour, unless a sort is implemented to organise the neighbour list based on the inter-particle distance.

The third difference is considered as a consequence of the two differences mentioned above, and it is only relevant for multiphase simulations. In astrophysics, the initial setup usually makes use of the so-called *equal-mass, variable separation* strategy. That is, the higher density fluid is represented by a collection of SPH particles with more particles per unit volume. In terrestrial fluid dynamics, the *multi-mass, equal separation* strategy is employed. In this case, the setup make use of multi-mass SPH particles with equal initial volume. Each strategy has its own advantages and limitations, and often it is controversial to adapt a single strategy. On one hand, the *equal-mass, variable separation* approach does not suffer from a *mass discontinuity*. Yet, it suffers from computational and memory inefficiency for multiphase flows with large density ratios. On the other hand, the *multi-mass, equal separation* approach is both computationally and memory efficient even for large density ratios. Nonetheless, it creates a mass discontinuity between the fluids that requires additional interface stabilisation models such as those discussed in chapter 3.

The popular SPH codes in the research community are summarised below. `Hydra` is a simulation code written in Fortran-77 [4] that combines the standard SPH with inter-particle gravity solver. It was one of the earliest cosmological simulation codes publicly available to the field and has motivated the development of parallel codes for conducting large scale simulations in computational cosmology. `Gadget-2.0` is a MPI parallel SPH implementation written in ASCI-C [133]. It has been applied to simulate many large scale astrophysical phenomena, including the evolution of the cold dark matter model [191], hydrodynamical simulations of cosmological structure formation [192] as well as the evolution of galaxy clusters [193]. `OSPH` is a modification of `Gadget-2.0` targeted for multi-

phase SPH simulations [109]. `SPHysics` is a set of SPH codes co-developed by researchers at the Johns Hopkins University, the University of Vigo, the University of Manchester and the University of Rome La Sapienza. It is designed for free surface flow problems often encountered in civil engineering such as break waves [194], wave impacts on solid boundaries [195], and dam-break [196, 197]. There are three versions distributed within the research community: (i) a serial version written in Fortran-90 for free surface flows, (ii) `parallelSPHysics`, a CPU parallel version written in Fortran-90 and MPI, and (iii) `DualSPHysics`, a GPU thread parallel version written in C++ and CUDA [198, 199]. At the time of writing this thesis, `SPHysics` serves as the major software used by the weakly-compressible SPH research community.

4.3 SPH code - Draco

The primary objective of `Draco` is to facilitate a mesh-free computational tool that aids the research and development of aeroengines with our industry partner Rolls Royce plc. The code is written in ASCI C/C++, and has been tested on multiple operating systems and processors. The SPH implementation `Draco` is designed as a general purpose SPH software with flexibility in mind. Therefore, it supports different SPH formulations, equations-of-state, fluid property and boundary treatments methods, all of which are of relevant to aerospace engineering applications.

4.3.1 Development history

The development of SPH codes within the University of Nottingham's SPH team started from `Hydra` [4]. Hopton [178] modified `Hydra` to simulate open channel flow. Nonetheless, it does not support a graphical user interface for the set-up and visualisation of results. Having seen these limitations, Kruisbrink implemented

a MATLAB version of SPH hereinafter called `MATLAB-Hydra` that aggregates the setup and simulation in a consistent manner. Despite the congruent mathematical SPH formulation, the major differences between these implementations lies in the neighbour search algorithm and time integration scheme. The modified version of `Hydra`[178] utilises the cell-linked-list algorithm for SPH neighbour detection and supports a second order accurate predictor-corrector time integration scheme. Whereas the naive search algorithm $\mathcal{O}(N_p^2)$ and forward Euler scheme are implemented in `MATLAB-Hydra`. The algorithmic differences imply that the contribution from neighbouring particles during the density and momentum evaluation is not taken into account at the same order; this creates additional challenges in code alignment. A series of validation tests were conducted by the author to align the two codes to eight decimal places, when the contributions from particles are sorted to the same order.

With the aim of facilitating a robust SPH software package for the advancement of aerospace engineering research, a new software project `Draco` is launched by combining the advantages of the different versions of `Hydra`. A performance analysis indicates that the use of a compiled programming language is favoured over scripting languages (e.g. MATLAB, Python) for SPH implementations. In addition, given that the neighbour search is the most time consuming part of SPH simulations, an efficient and robust neighbour search algorithm is crucial to the success of running high resolution simulations. The first order accurate forward Euler scheme is chosen for storage efficiency. Finally, unit testing [200, 201] is necessary and should be performed regularly to maintain the code quality.

4.3.2 Software architecture

`Draco` utilises the object oriented programming paradigm where the data structure is organised into the Structure-of-Arrays (SoA). The program consist of seven major classes. The base class `Simulation` stores the physical quantities

of the particle system subjected to investigation. The `SPH` class is responsible for the construction and transversal of the cell-linked list during the simulation. The `TimeIntegration` class implements the adaptive time-stepping integration scheme based on the forward Euler scheme. The `Kernel` class contains different kernel functions and supports both run-time computation and interpolation of kernel values from a pre-computed table. To ensure the consistency of results across different computer platforms, a set of unit tests has been implemented in each of the classes mentioned above.

Additionally, there are three classes responsible for the organisation of the data in `Draco`. The `CaseSpecification` class is responsible for parsing the initial conditions, parameter files generated from case setup scripts in `MATLAB-Hydra` and the checking the correctness of all compiled options in the makefile. It produces the `Log` and `SimulationResults` folders. The former stores the initial conditions, parameters and compilation flags validation file. The latter stores the simulation results. The `Parameter` class contains constants and enumerators used in the simulation (e.g fluid domain, artificial viscosity parameters) and it can be easily extended to more advanced applications. Finally, the `Output` class is responsible for producing the output file in `SimulationResults` folder which stores the simulation results at predefined output time intervals. A class diagram in the Unified Modelling Language (UML) is provided in Figure 4.1 to illustrate the static behaviour of the classes, attributes and methods. The collaboration between sequential function calls is shown in the flow diagram in Figure 4.2.

4.3.3 Cell linked list

The cell-linked-list algorithm proposed in Allen [202] is implemented in `Draco`. During each time-step, the maximum extent of the domain in each direction is first determined. The number of cells in each direction is then given by the ratio between the extent and the kernel scale. The particles are assigned to

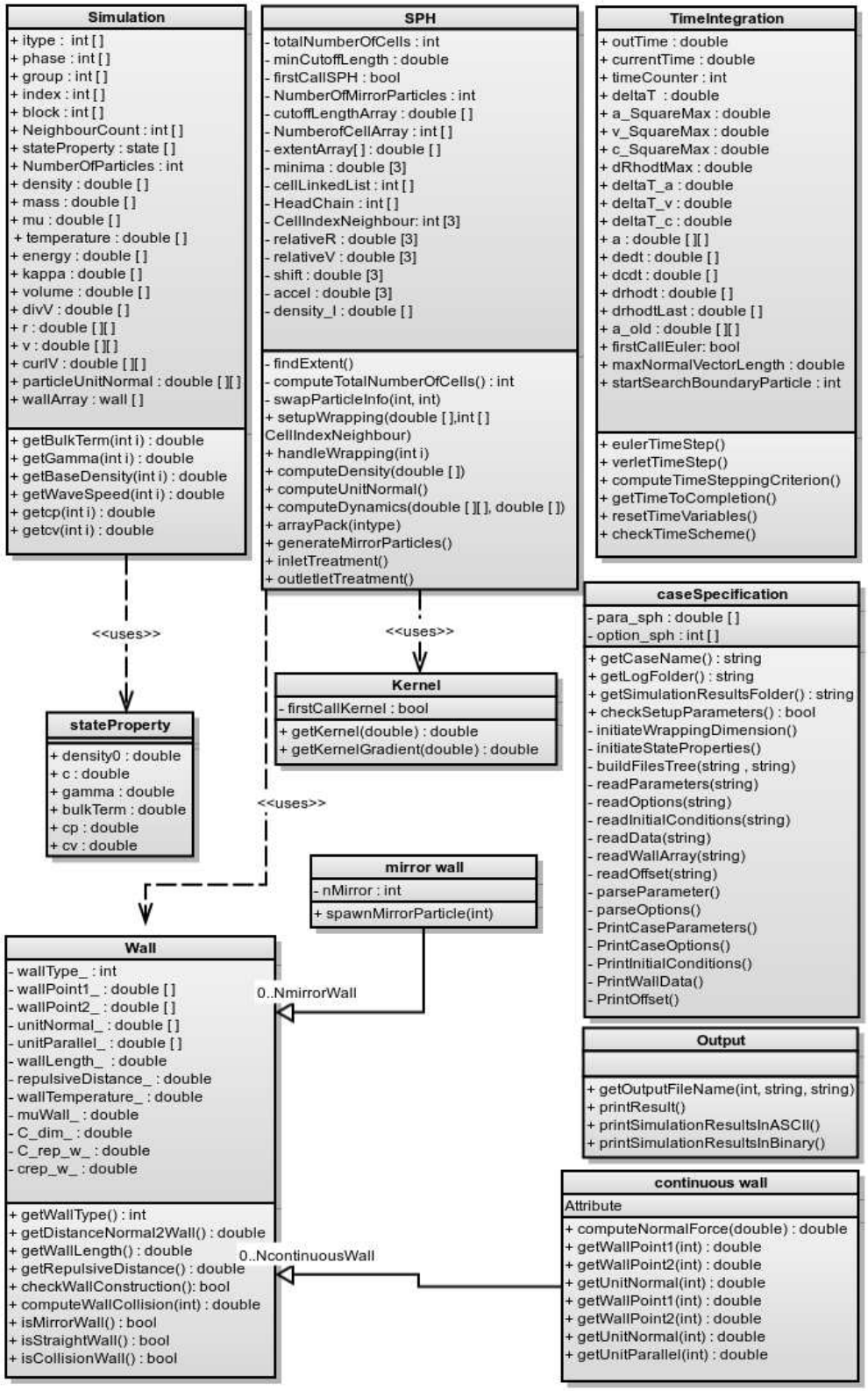

Figure 4.1: UML class diagram of `Draco`.

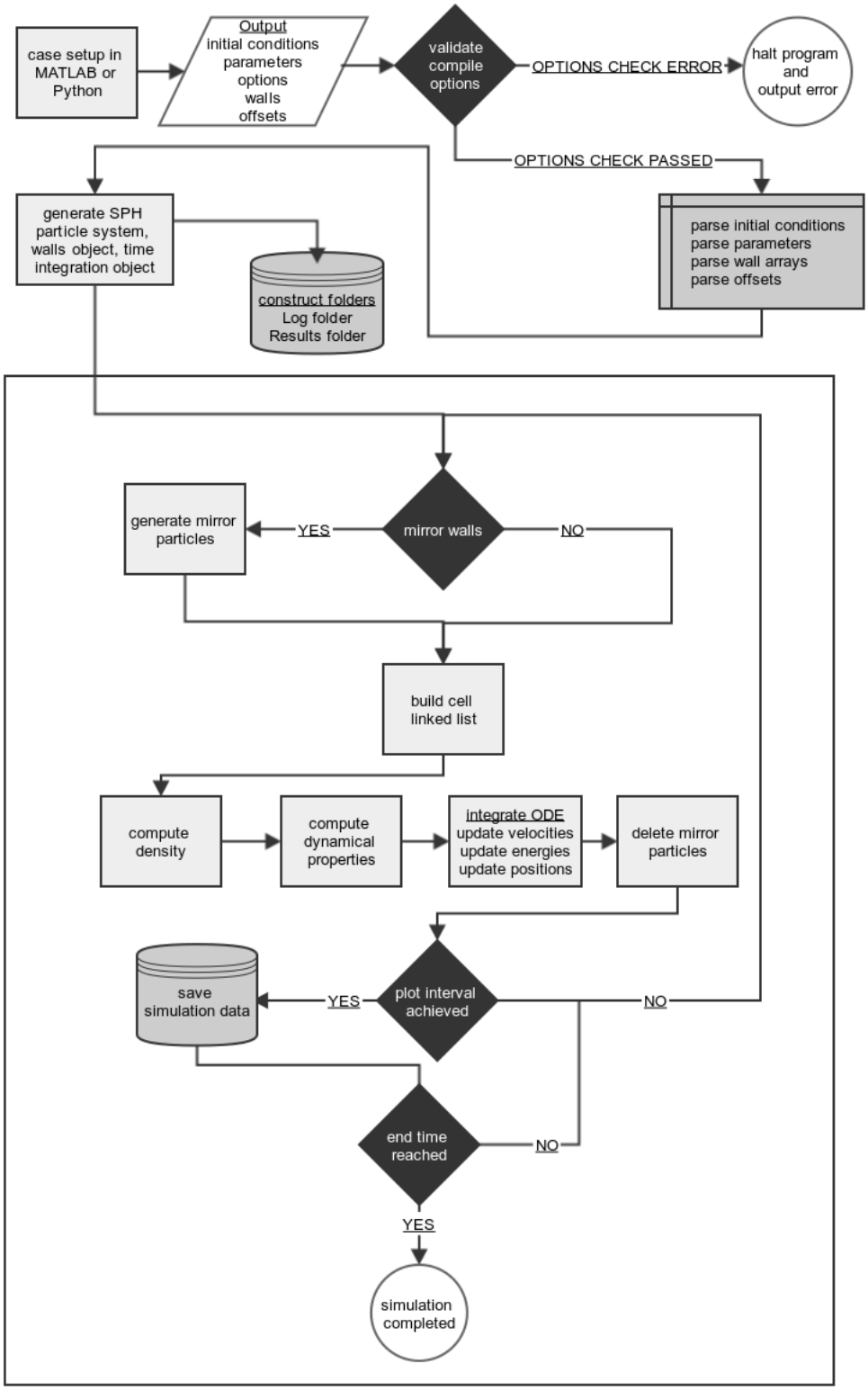

Figure 4.2: UML flow diagram of `Draco`.

the respective cells depending on their positions using a $\mathcal{O}(N_p)$ cell-linked-list construction algorithm (Algorithm 1). This algorithm generates two arrays: (i) the `HeadChain` array stores the first particle in each cell, and (ii) an array of pointers `cellLinkedList` which stores the successive index of particles within the same cell. A pictorial description is provided in Figure 4.3.

Input: The position of a set of particles $\vec{r} = \{\vec{r}_0, \vec{r}_1, \ldots, \vec{r}_{N_p-1}\}$
Input: The minimum position among all particles $\vec{r}_{min}$
Output: The `HeadChain` array that stores the first particle in each cell
Output: The `cellLinkedList` array that stores the index of the successive particle within the same cell

```
1 for i ← 1 to N_p do
2 |   //cast the particle to its appropriate local cell in each direction
3 |     for k ← 0 to N_dim do
4 |     |   cell[k]=min((r_i[k] − r_min[k])/cutoffLength[k],numCell[k]-1)
5 |   //assemble global index
6 |   globalIndex=cell[0]+numCell[0]*cell[1]+numCell[1]*numCell[0]*cell[2]
7 |   //assign new values to cell list and the head chain
  |   cellLinkedList[i]=HeadChain[globalIndex]
8 |   HeadChain[globalIndex]=i
```

Algorithm 1: The cell linked list construction algorithm

Once the cell-linked-list has been constructed, inter-particle operations (e.g. evaluation of densities, accelerations) are computed via the cell-linked-list transversal algorithm (Algorithm 2). The cell-linked-list transversal algorithm checks the adjacent cells[2] to identify potential SPH neighbour particles. The use of a cell-linked-list has the following advantages: (i) it reduces the complexity from $\mathcal{O}(N_p^2)$ into $\mathcal{O}(N_p)$ operations. (ii) the pair-wise fashion ensures the number of computations is further reduced by a factor of two, (iii) it is memory efficient since it does not require the storage space for local neighbour-list on a particle basis [203].

[2] 8 cells in two-dimensions and 26 cells in three-dimensions

```
   Input: The position of a set of particles r⃗ = {r⃗_0, r⃗_1, ..., r⃗_{N_p−1}}
   Input: The HeadChain array that stores the first particle in each cell
   Input: The cellLinkedList array that stores the index of the successive particle within the same cell
1  for cellX ← 0 to numCell[0] − 1 do
2      for cellY ← 0 to numCell[1] − 1 do
3          for cellZ ← 0 to numCell[2] − 1 do
4              // compute globalIndex
               globalIndex=cellX+numCell[0]*cellY+numCell[0]*numCell[1]*cellZ
5              for cellNeighbourX ← cellX − 1 to cellX + 1 do
6                  for cellNeighbourY ← cellY − 1 to cellY + 1 do
7                      for cellNeighbourZ ← cellZ − 1 to cellZ + 1 do
8                          //calculate scalar cell index for neighbour cell
                           globalCellIndexNeighbour=(cellNeighbourX+numCell[0])%numCell[0]+
                           ((cellNeighbourY+numCell[1])%numCell[1])*numCell[0]+
                           ((cellNeighbourZ+numCell[2])%numCell[2])*numCell[0]*numCell[1]
                           i = HeadChain[globalIndex]
9                          // set up periodic boundary condition
                           setupWrapping(shift,globalCellIndexNeighbour)   while i ≠ NULL
                           do
10                             // j is the neighbour particle
                               j = HeadChain[globalCellIndexNeighbour]
11                             while j ≠ NULL do
12                                 if i < j then
13                                     if |r⃗_i − r⃗_j| < 2h then
14                                         //compute pair-wise interactions ···
15                                 j=cellLinkedList[j];
16                             i=cellLinkedList[i];
```

Algorithm 2: The cell linked list transversal algorithm

4.4 Boundary Conditions in SPH

The interaction of a fluid with its boundaries are of crucial importance in terrestrial fluid dynamics. Therefore, extensive research is conducted within the weakly-compressible SPH community on the treatment of boundaries. The physical interpretation and implementation of boundary treatment methods are discussed in the following paragraphs.

4.4.1 Physical interpretation of boundary conditions

There are generally two types of boundary condition, namely the *kinematic boundary condition* and *dynamic boundary condition*. Although there are many variations such as walls, inflow and outflow boundaries in the CFD literature, these are considered specific cases of the kinematic and(or) dynamic boundary conditions.

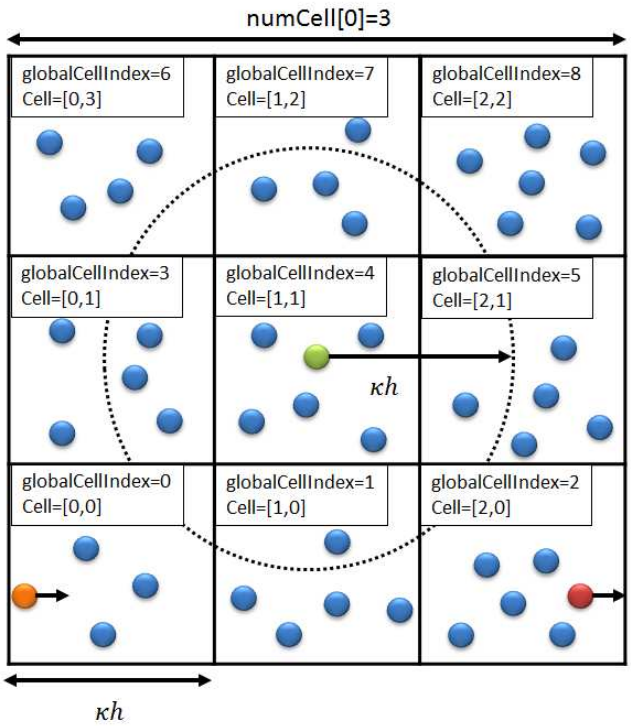

Figure 4.3: Cell-linked list structure in two-dimensional case. The cell index array in each direction is utilised to compute the unique global cell index that defines a cell value.

Consider two fluid particles of different phases in the configuration shown in Figure 4.4, their velocity components tangential and normal to the interface are described by $v_{\parallel}$ and $v_{\perp}$. On a particle basis, the *kinematic boundary condition* requires that the velocity component normal to the interface of particle i is of equal magnitude but opposite sign to that of particle j

$$v_{i\perp} = -v_{j\perp} \quad \vec{r}_j, \vec{r}_j \in \partial\Omega_s. \tag{4.1}$$

At the fluid interface it is required that the tangential velocity components are the same. This is known as the *continuity of tangential velocity condition* and is a good approximation for immiscible Newtonian fluids [94, 96, 107].

$$v_{i\parallel} = v_{j\parallel} \quad \vec{r}_j, \vec{r}_j \in \partial\Omega_s. \tag{4.2}$$

For viscous fluid where surface tension is insignificant, the *dynamic boundary*

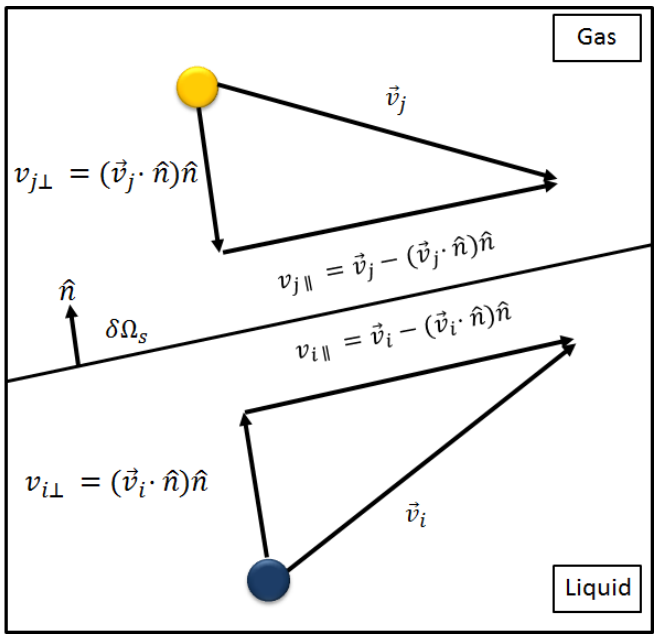

Figure 4.4: Generalised boundary between two particles.

condition simplifies to the stress balance

$$\left\{ \begin{array}{l} P_i = P_j \\ \tau_i = \tau_j \end{array} \right\} \quad \vec{r}_i, \vec{r}_j \in \partial\Omega_s, \tag{4.3}$$

where τ represents the viscous stress tensor [94].

Fluid-fluid and fluid-solid boundaries

Generally speaking, the fluids on the respective sides of the interface must satisfy the *kinematic boundary condition* (4.1), *continuity of tangential velocity condition* (4.2) and the *dynamic boundary condition* (4.3). These condition constrain particles at either side of the interface are expected to remain on their respective side of the interface without penetrating through to the other side. Similarly, for a rigid wall moving at a constant velocity V_{rigid}, nearby fluid particles should adapt the tangential velocity of the wall $V_{rigid\,\parallel}$, whereas the normal velocity

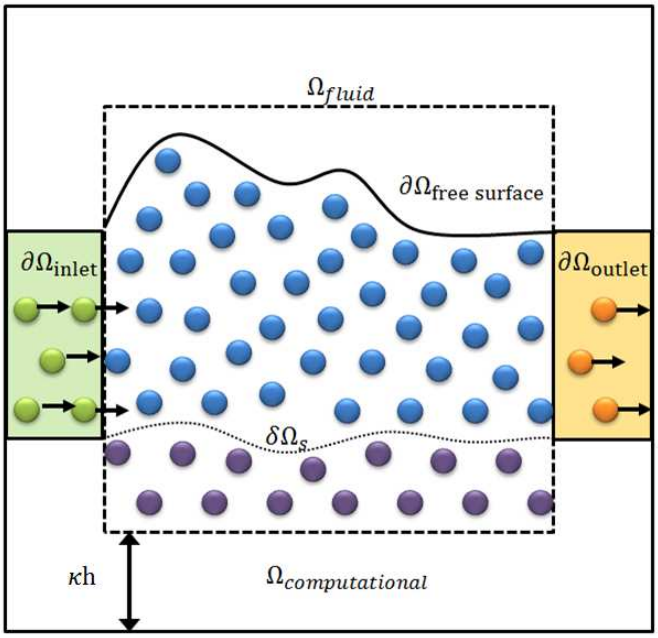

Figure 4.5: The fluid domain convention used in `Draco`. The inlet sub-domain is coloured in green, the outlet sub-domain is coloured in orange. The particles residing in the fluid domain are coloured in blue and purple, where the interface is give by $\delta\Omega_s$. Similarly, the free surface is given by $\delta\Omega_{freesurface}$. The computational domain has a width of κh such that it ensures the support of the kernel is properly filled for all fluid particles.

component must be zero in order to obtain a *non-permeable* wall.

$$v_{i\parallel} = V_{rigid\parallel} \quad \text{and} \quad v_{i\perp} = 0 \qquad \vec{r}_i \in \Omega_{fluid}. \tag{4.4}$$

Free-surface boundaries

For free-surface flow, the *kinematic boundary condition* (4.1) implies that fluid particles initially on the free surface shall remain part of the free-surface and the *dynamic boundary condition* (4.3) enforces the momentum balance across the interface such that the pressure at the interface is equivalent to the atmospheric pressure. Since the ambient pressure is set to be the background pressure P_o in a free-surface flow in the absence of surface tension and viscous effects, the dynamic condition is

$$P(\vec{r}_i, t) = P_o \qquad \vec{r}_i \in \partial\Omega_{free\,surface}. \tag{4.5}$$

Inflow/Outflow boundaries

An inflow boundary allows for spatially dependent initial velocity profiles as well as different fluid properties.

$$v_{i\,\perp} = v_{inlet\,\perp} \quad \text{and} \quad v_{i\,\parallel} = v_{inlet\,\parallel} \qquad \vec{r}_i \in \partial\Omega_{inlet}. \tag{4.6}$$

In `Draco`, an inflow boundary is represented by a block of inlet particles selected prior to run-time. In order to have a properly filled kernel, the dimension of the inlet block is required to be larger than the radius of the kernel function κh. During the course of the simulation, a new inlet particle is generated once its precursor inlet particle has entered the fluid domain. The new inlet particle has the same properties as its precursor inlet particle and it is placed at the rear end of the inlet particle block as marked green in Figure 4.5.

An outflow boundary is employed when fluids exit the fluid domain, where both the tangential and normal velocities of the outflow remain constant in the direction normal to the boundary

$$\frac{\partial v_{outlet\,\perp}}{\partial \hat{n}} = 0 \quad \text{and} \quad \frac{\partial v_{outlet\,\parallel}}{\partial \hat{n}} = 0 \qquad \vec{r}_i \in \partial\Omega_{outlet}. \tag{4.7}$$

The particle domains in `Draco` are shown in Figure 4.5. The domain treatment is applicable to external and internal flows. In addition, the inlet/outlet boundaries allow the number of SPH particles to dynamically increase during the simulation. Another aspect is that the width of the computational domain $\partial\Omega_{computational}$ is typically set to κh, such that all fluid particles have a properly filled kernel.

Periodic boundaries

Periodic boundaries are implemented to simulate periodic flows. SPH particles in a boundary cell contribute to the density and dynamical evaluations of fluid

particles located in cells at the opposite side. In addition, fluid particles exiting the fluid domain are placed in the opposite side of the domain as illustrated by the red particle and the orange particle in Figure 4.3.

4.4.2 Wall boundaries

Within SPH, walls are typically modelled by wall particles, ghost particles and mirror particles. A distinction can be made between frozen wall particles at the wall, ghost particles behind the wall, or mirror particles dynamically generated behind the wall, as introduced by Monaghan [62, 204]. In these concepts, the force exerted by the wall onto a fluid particle is modelled by force in the inter-particle direction, which should enforce *non-permeable* wall boundary via pressure gradient and impose a no-slip wall condition via viscous force due to artificial viscosity.

Ghost Particles

Ghost particles are used to simulate the behaviour of static or virtually moving walls. During the simulation, the positions, densities and velocities of the ghost particles remain constant. Hence, when a ghost particle j resides in the support of the kernel of a fluid particle i, it contributes to the pressure gradient and viscous force evaluation of particle i; hence, it is consistent with the *dynamic boundary condition* and the *continuity of tangential velocity condition*.

Wall Particles

Wall particles were introduced by Monaghan [62] as a non-penetration boundary condition in free surface flows. In this concept, a wall is represented by an array of particles. A wall particle exerts a repulsive force along the inter-particle

direction similar to the Lennard-Jones potential in molecular dynamics [205].

$$F(|\vec{r}_{i,wall}|) = \begin{cases} C_{rep,LJ}\left[\left(\frac{d_{nat}}{|\vec{r}_{i\,wall}|}\right)^{q_o} - \left(\frac{d_{nat}}{|\vec{r}_{i\,wall}|}\right)^{q_1}\right]\frac{\vec{r}_{i,wall}}{|\vec{r}_{i,wall}|} & |\vec{r}_{i,wall}| \leq d_{nat} \\ 0 & |\vec{r}_{i,wall}| > d_{nat} \end{cases}, \quad (4.8)$$

where q_o, q_1 are dimensionless parameters and $C_{rep,LJ}$ is a calibration factor. This formulation of the Lennard-Jones potential is strictly repulsive as $F(|\vec{r}_{i,wall}|)$ vanishes for particles located outside the influence zone of the wall $|\vec{r}_{i,wall}| > d_{nat}$. The wall particle force depends on three parameters, with the condition $q_o > q_1$. The conventional choice suggested by the literature [62] is $q_o = 4$, $q_1 = 2$. These values are obtained from on a series of numerical experiments performed for free-surface flows. Nevertheless, it is unclear how the choice of these parameters may influence the flow field in other applications. More importantly, the utilisation of wall particles does not provide sufficient neighbour particles behind the wall and results in a *truncated kernel* as discussed in chapter 3.

Mirror Particles

Mirror particles model the behaviour of a solid wall by copying the properties of their parent fluid particles. Their velocities have the following form

$$\vec{v}_{mirror\,\parallel} = \alpha_{mirror}\vec{v}_{i\,\parallel} \quad \text{and} \quad \vec{v}_{mirror\,\perp} = -\vec{v}_{i\,\perp}, \quad (4.9)$$

where the constant α_{mirror} controls slip behaviour at the wall, namely $\alpha_{mirror} = 1$ for a free-slip condition and $\alpha_{mirror} = -1$ for a no-slip condition. In addition, their velocity component normal to the wall is of equal magnitude and opposite direction, such that the *non-permeable* behaviour of a wall is ensured.

$$\vec{v}_{mirror\,\parallel} = -\vec{v}_{i\,\parallel} \quad \text{and} \quad \vec{v}_{mirror\,\perp} = -\vec{v}_{i\,\perp}. \quad (4.10)$$

In the beginning of each time-step, the mirror particles are generated prior to the construction of the cell-linked list. This ensures fluid particles near the virtual wall $|\vec{r}_{i,wall}| < \kappa h$ has a fully filled kernel and a symmetric pressure distribution across the wall. The mirror particle contributes to the density and dynamical evaluation of neighbouring fluid particles, except that they are deleted from the particle system prior the execution of the time integration subroutines.

Continuous Wall Boundary

This concept is based on continuous modelling by introducing a boundary surface force rather than an inter-particle force. A repulsive force normal to the wall is exerted when fluid particles are in close proximity to the wall boundary. The wall repulsion is modelled as a reaction force due to fluid compression as described by Hooke's law. For an adiabatic process, this is proportional to the bulk modulus of elasticity of the fluid $K = \rho c^2$. The radial force on a fluid particle is proportional to the pressure increase due to its compressibility and the assumed contact area. The compression is described by the ratio between the change of the volume of a particle with respect to its initial volume ($\Delta V/V$). Assuming the initial volume of the particles are the same, a dimensional analysis suggests the force due to compression has the form $\vec{F}_{n,i} \propto -mc^2 \Delta V/V (\vec{e}_i \cdot \hat{n}_{wall})\hat{n}_{wall}$. The repulsive force normal to the wall is given by

$$\vec{F}_{n,i} = -m_i N_{dim} C_{rep} c_i^2 \frac{|\vec{r}_{i,wall}| - r_{rep}}{|\vec{r}_{i,wall}|^2} (\vec{e}_i \cdot \hat{n}_{wall})\hat{n}_{wall} \quad |\vec{r}_{i,wall}| < r_{rep}, \tag{4.11}$$

where $C_{rep} \sim \mathcal{O}((c_{SPH}/c)^2)$ is a scaling coefficient between the real speed of sound and the artificial speed of sound in SPH. Thus, the continuous wall force is active when the distance between the wall and fluid particle is closer than the pre-defined activation distance r_{rep} which is typically set to $0.5 d_{nat}$.

Remark on wall boundaries

While different boundary handling methods have been implemented in `Draco`, each of the these methods suffered from certain limitations. In practice, the choice of a suitable boundary condition depends on the situation and requires the critical judgement by the researcher. For instance, the ghost particles suffer from particle penetration for large impact velocities. The mirror particle requires dynamic memory allocation/deallocation in each time step incurs computational cost. Additionally, its current implementation is only suitable for straight walls. Finally, the wall particles and continuous wall suffer from the *truncated kernel* and requires case specific parameter tuning. More importantly, these concept can only enforce a *non-permeable* wall which does not correctly account for the physical effects due to the wall shear.

4.5 Time integration

The spatial operators in the fluid dynamical equations are written in the SPH formulation, resulting in a system of ordinary differential equations in time. Although implicit numerical integration schemes allow for the utilisation of larger time-steps and improved stability, it requires solving a linear system at each time-step which can potentially be computationally expensive. Hence, explicit time integration schemes are commonly employed in SPH. The forward Euler numerical integration scheme is implemented in `Draco`. This scheme is chosen for storage efficiency [206]. During each time-step, the density is first evaluated

$$\rho_i^{n+1} = \rho_i^n + \frac{D\rho_i^n}{Dt}\Delta t, \tag{4.12}$$

where Δt represents the time-step, and the $D\rho_i^n/Dt$ is the change in the density of a particle with respect to time. After the pressure is evaluated from the updated

density, and the forces on a particle are evaluated, the velocity of a particle is updated via

$$\vec{v}_i^{n+1} = \vec{v}_i^n + \frac{D\vec{v}_i^n}{Dt}\Delta t. \tag{4.13}$$

Similarly, the internal energy of a particle is updated according to

$$e_i^{n+1} = e^n + \frac{De_i^n}{Dt}\Delta t. \tag{4.14}$$

Finally, the position of the particle is updated according to

$$\vec{r}_i^{n+1} = \vec{r}_i^n + (\vec{v}_i^n + \vec{v}_{i,XPSH}^n)\Delta t. \tag{4.15}$$

The XSPH velocity correction [119, 204] is computed via

$$\vec{v}_{i,XSPH}^n = \epsilon_{XSPH} \sum_j \frac{\vec{v}_{ij}}{\rho_{ij}} W_i j, \tag{4.16}$$

and $\epsilon_{XSPH} = 0.01$ is employed. The numerical integration scheme is first order accurate and conditionally stable. The adaptive time stepping is based on three Courant-Friedrichs-Levy (CFL) conditions for the velocity, acceleration and change of density

$$\Delta t_v = \frac{h}{\sqrt{|\vec{v}|^2_{\max}}} \quad , \quad \Delta t_a = \frac{\sqrt{h}}{\sqrt[4]{|\vec{a}|^2_{\max}}} \quad , \quad \Delta t_\rho = \frac{\rho_o}{(D\rho/Dt)_{\max}}. \tag{4.17}$$

The time step is then obtained from

$$\Delta t = \min(\omega_v \Delta t_v, \omega_a \Delta t_a, \omega_\rho \Delta t_\rho), \tag{4.18}$$

where the coefficients ω_v, ω_a, ω_ρ are predefined by the user at compile time. The default values are $\omega_{v,a} = 0.01$ and $\omega_\rho = 1$. Although other time-stepping conditions such as conditions for viscous force and pressure gradient force exist in

literature [4, 137, 138, 183], in most cases the CFL conditions above are sufficient for the simulations considered herein.

4.6 Summary

The features of the SPH software used in this thesis - `Draco` were discussed in this chapter. A survey of literature was presented to identity the popular SPH codes in the research community. It was found that the major difference between SPH codes in astrophysics and engineering were the utilisation of a variable smoothing length and different neighbour search algorithms.

After reviewing the precursor versions of `Hydra` [4, 178] and `MATLAB-Hydra`, the decision was made to implement `Draco` in C++ using the object oriented programming paradigm. The combined use of the object oriented programming paradigm and test driven development approach [200, 201] successfully reduced the code alignment and debugging processes. To optimise computational speed, a cell-linked-list algorithm was implemented for SPH neighbour searching and an adaptive time-stepping scheme based on the forward euler method was implemented for the time integration of the dynamical system.

`Draco` offers numerous boundary treatment methods including inflow/outflow, solid walls and periodic boundaries for terrestrial fluid dynamics applications. It is worth mentioning that at the time of writing this thesis, an appropriate treatment of solid wall boundary that strictly satisfies the no-slip condition and wall shear remains an open topic in the weakly-compressible SPH community. However, in many cases we found the ghost particles gives acceptable results for *non-permeable* walls provided that the effects due to wall shear are insignificant.

Chapter 5

Kelvin-Helmholtz Instability

5.1 Introduction

The growth of the Kelvin-Helmholtz instability generated at the interface between two ideal gases is studied by means of SPH. A series of simulations is performed to investigate the influence of viscosity, smoothing, the thickness of density and velocity transition layers.

In order to conduct a systematic study, the analysis in this chapter are divided into two parts. The first part of the chapter concentrates on the idealised KHI test in literature for density ratio of two (section 5.3-5.4). The idealised test-case serves as an excellent bench-mark case which allows for a fundamental study of the performance of a multiphase SPH scheme. The second part of the chapter focusses on the stratified shear instability (SSI) results from the growth of perturbations at the shearing interface between two fluids via the KHI in the presence of a constant gravitational field (section 5.5-5.6).

The rest of this chapter is organised as follows: section 5.2 presents a survey of literature regarding the experimental and numerical work. section 5.3 outlines the initial conditions. The numerical results for the idealised KHI will be first presented in section 5.4. The numerical results of a fiducial model will be first

illustrated in section 5.4.1. The influences of the following aspects are then investigated: (i) section 5.4.2 discusses the influence of artificial viscosity, (ii) section 5.4.3 studies the dependence of local resolution (κ), which governs the number of SPH neighbours (N_n). (iii) Section 5.4.4 discusses the influence of the thickness of the velocity and density transition layer.

Based on the knowledge acquired from the idealised KHI test, we conduct an elaborated study on the stratified shear instability that is relevant to terrestrial fluid dynamics. Section 5.5 outlines the initial conditions of the SSI. The numerical results of a fiducial model of SSI are presented in section 5.6.1 before considering the effects of resolution, Reynolds number, Richardson number and Atwood number. Finally, the major research findings will be summarised in section 5.7.

5.2 Literature review

Kelvin [76] and Helmholtz [77] pioneered the investigation of shear instabilities by studying the relative motion between two adjacent fluids subjected to tangential velocity difference. This phenomenon has subsequently become known as the Kelvin-Helmholtz instability. Given its crucial importance in a wide range of applications [7, 63, 82, 83, 84, 85, 86], the KHI has been study experimentally and numerically since the 18^{th} century.

Most of the KHI experiments were carried out under terrestrial conditions where the fluids are subjected to a gravitational acceleration. In particular, if the denser fluid initially lies underneath the less dense one, the KHI manifests into the so called stratified shear instability [63]. The instability is characterised by the Richardson number (Ri), which determines the dominant factor of the instability. For example, $Ri > 1$ implies buoyancy forces are important as the potential energy is dominant, whereas $Ri < 1$ implies the kinetic energy is dominant

and buoyancy forces are unimportant. The shear instability has been actively researched since the 19^{th} century. Miles [88] and Howard [207] introduced the celebrated Miles-Howard theorem for the stratified instability. The authors reported a critical Richardson number of $Ri = 0.25$ for incompressible fluids, above which the instability remains stable. The experimental work has also facilitated better understanding of the shear instability. Thorpe [208] conducted the well known tilted-tank experiments to investigate the onset of turbulence between two immiscible fluids and found good agreement between the experimental measurements and the analytical prediction. Linden [209] investigated the mixing of stratified flows for numerous Richardson numbers and noted that the boarder the thickness of the velocity interface results in a lower kinetic energy and equivalently stronger buoyancy effects which lead to a less pronounced growth of the instability.

Advances in computer technologies equipped modern day researchers with the tools to investigate fluid flow numerically, with many research groups developing numerical methods to simulate the KHI. For example, Patnaik et al. [210] applied the finite difference method to simulate the KHI between two stratified fluids by applying the Boussinesq approximation. The authors studied the minimum Richardson number required for the onset of KHI at Reynolds number (Re) of 100 and found good agreement with linear stability analysis. Whereas other research groups have focussed on the long-term evolution of the instability: Klaassen and Peltier [211] studied the long-term evolution of the KHI between two stratified viscous fluids using a mesh-based method and concluded that the two-dimensional KHI does not lead to secondary instabilities in the transition to three-dimensional motion. Caulfield and Peltier [212] compared the evolution of two-dimensional and three-dimensional stratified mixing layer results simulated by means of DNS and concluded that the three-dimensional KHI is dominated by the convective instability at the central core of the KHI billow. Brüggen

and Hillebrandt [63] simulated the two-dimensional and three-dimensional SSI between two ideal gases using the finite difference code `Zeus`. In contrast to the simple linear stability criterion, their results indicate efficient mixing can occur for Richardson numbers substantially higher than $Ri = 0.25$. The authors reported that the dimensionality of the problem did not affect the steady state behaviour of the simulation, but did alter the dynamics of the onset of the instability. Hazel [213] studied the effects of the initial velocity (density) profiles perpendicular to the interface and pointed out that in reality the development of a SSI not only depends on the Richardson number, but also on other parameters such as the formulation of the initial velocity and density profiles. Similarly, Miczek [214] constructed semi-analytical solutions and conducted FVM simulations for various initial velocity (density) profiles and concluded that the ratio between the density gradient and the velocity gradient plays a crucial role in the growth of stratified shear instability. Summarising the above, the current literature suggests that the idealisation of the linear stability analysis has lead to some ambiguity in the critical Richardson number which describes the necessary condition for the onset of the instability. In many cases, the onset of the instability was found to be dependent on the exact form of the initial profiles used in the setup [63, 213, 214].

There has been a concerted effort to compare the performance of mesh-based methods with SPH. Junk et al. [64] investigated the evolution of both inviscid and viscous KHI and compared numerical results between mesh-based codes and SPH in conjunction with the artificial conduction scheme introduced by Price [110]. Similarly, McNally et al. [108] examined the performance of various mesh-based codes and SPH (with artificial conduction) for smoothed velocity and density profiles, and reported that the mesh-based simulation and SPH are both in good agreement with the analytical predictions. Hubber et al. [215] compared the convergence properties between SPH and various mesh-based codes. Their

results suggested that a higher order smoothing kernel and larger number of neighbours improves the performance of SPH when simulating the KHI.

There has also been some development in the weakly-compressible SPH community to model KHI. Shadloo and Yildiz [149] studied the evolution of a KHI subjected to surface tension and gravity by means of the number density approach. The authors reported that the SPH results are sensitive to the artificial viscosity parameter prescribed. However, because their simulations terminated before the non-linear development had occurred and the initially perturbation only correspond to a single; hence more advance phenomena such as the generation of shearing layer and vortex pairing were not presented in their work. Shakibaeinia and Jin [216] studied the KHI using the MPS method and claimed that spurious fluctuations in pressure are responsible for the disruption of the growth of KHI. In addition, their numerical method failed to model the core of the cat-eye vortices and generated a spurious vacuum layer at the vortex cores.

5.3 Initial Conditions

The fluid domain is constrained within $x \in [0, L], y \in [0, H]$, where the aspect ratio is normally set to unity (i.e. $L/H = 1$). Periodic boundaries are applied in both directions. The initial perturbation of the fluid interface is given by the horizontal velocity profile

$$u(y) = \begin{cases} u_1 - \frac{\Delta u}{2} e^{-\frac{|y-0.25|}{L_u}} & 0 \leq y < 0.25 \\ u_2 + \frac{\Delta u}{2} e^{-\frac{|y-0.25|}{L_u}} & 0.25 \leq y < 0.5 \\ u_2 + \frac{\Delta u}{2} e^{-\frac{|(1-y)-0.25|}{L_u}} & 0.50 \leq y < 0.75 \\ u_1 - \frac{\Delta u}{2} e^{-\frac{|(1-y)-0.25|}{L_u}} & 0.75 \leq y \leq 1 \end{cases}, \tag{5.1}$$

where u_1 and u_2 are the far-field horizontal velocities and $\Delta u = u_1 - u_2$. The far-field velocities are defined to be $u_1 = 0.5\text{m/s}$ and $u_2 = -u_1$. In order to perturb the fluid system, an initial velocity perturbation function

$$v\left(x,y\right) = \delta v \sin\left(kx\right) \begin{cases} e^{-|y-0.25|} & 0 \leq y < 0.5 \\ e^{-|(1-y)-0.25|} & 0.5 \leq y \leq 1 \end{cases}, \tag{5.2}$$

is applied to prescribe the vertical velocities of the particles, where the amplitude is $\delta v = 0.01\Delta u$. The exponential factor ensures the magnitude of initial vertical perturbation decays rapidly away from the interface. The perturbation wave number is defined to be $k = 2\pi/\lambda$, where the wavelength $\lambda = L/2$ corresponds to the initialisation of two KHI modes along the horizontal direction. Similarly, the initial density profile is given by

$$\rho\left(y\right) = \begin{cases} \rho_1 - \frac{\Delta\rho}{2} e^{-\frac{|y-0.25|}{L_\rho}} & 0 \leq y < 0.25 \\ \rho_2 + \frac{\Delta\rho}{2} e^{-\frac{|y-0.25|}{L_\rho}} & 0.25 \leq y < 0.5 \\ \rho_2 + \frac{\Delta\rho}{2} e^{-\frac{|(1-y)-0.25|}{L_\rho}} & 0.5 \leq y < 0.75 \\ \rho_1 - \frac{\Delta\rho}{2} e^{-\frac{|(1-y)-0.25|}{L_\rho}} & 0.75 \leq y \leq 1 \end{cases}, \tag{5.3}$$

where ρ_1 and ρ_2 denote the densities of the two fluids. For the particular setup considered herein, the higher density fluid is initially situated in the central band of the vertical domain $0.25 < y < 0.75$. Unless otherwise mentioned, the time (t) quoted herein is given in terms of the inviscid sharp interface Kelvin-Helmholtz time-scale, namely $\tau_{KH} = (\rho_1 + \rho_2)/(k\Delta u\sqrt{\rho_1\rho_2})$ [5]. In all cases, multi-mass SPH particles all with equal initial separation distance are utilised to setup the simulations, where both fluids are modelled with the ideal-gas equation-of-state with the heat capacity ratio $\gamma_{1,2} = 5/3$.

5.4 Results and Discussion

The instability resulting from the initial conditions presented in section 5.3. The four major parameters that influence the numerical solution are the viscosity, the local resolution parameter (or equivalently the number of neighbours), and the thickness of the density and velocity transition layers. Each of these will be investigated in the subsequent sections and compared against our fiducial reference model.

In order to validate the numerical results, we compare the absolute error (Δn_c) and the relative error (η) with the analytical expectations in the literature. In particular, the results are compared against three dispersion relations: first of all, the classical growth rate (i.e. $n_{c,classical} = {\tau_{KH}}^{-1}$) refers to the inviscid growth rate derived from sharp initial distributions [5]. Secondly, in section 5.4.2 the extracted growth rates are compared against the viscous growth rate derived in [64] for sharp velocity and density initial distributions. Finally, we compare the measured growth rate, $n_{c,smooth}$, to the inviscid analytical growth rate presented in [7, 65, 66] for more physically realistic initial distributions.

5.4.1 Fiducial Model

The fiducial simulation utilises a total of $N_p = 65536$ particles organised in uniform grid, where the initial particle separation distance is $d_{nat} = L/256$. The smoothing length is defined as $h = \kappa d_{nat}$, where $\kappa = 2.33$ ($N_n = 68$). The KHI is simulated up to $t = 7$ which enables a detailed investigation of both the linear and the non-linear evolution of the instability. In order to remedy the jump condition to physical quantities, the initial density and velocity gradient are specified to be $L_{u,\rho} = 2d_{dnat}$. This results in smoothing of the physical properties over four layers of particles either side of the interfaces at $y = 0.25$ and $y = 0.75$. The standard artificial viscosity parameters ($\alpha_{AV} = 1$, $\beta_{AV} = 2$) are utilised in conjunction with

the Balsara switch to avoid particle interpenetration. The density and internal

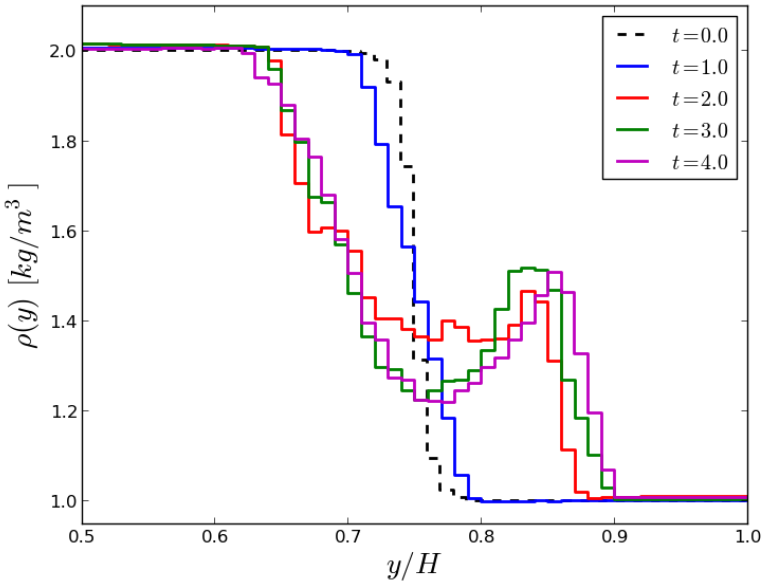

Figure 5.1: The density distribution in the top half of the vertical domain plotted at the times indicated. The initial density discontinuity is smoothed out as the KHI evolves into the non-linear regime.

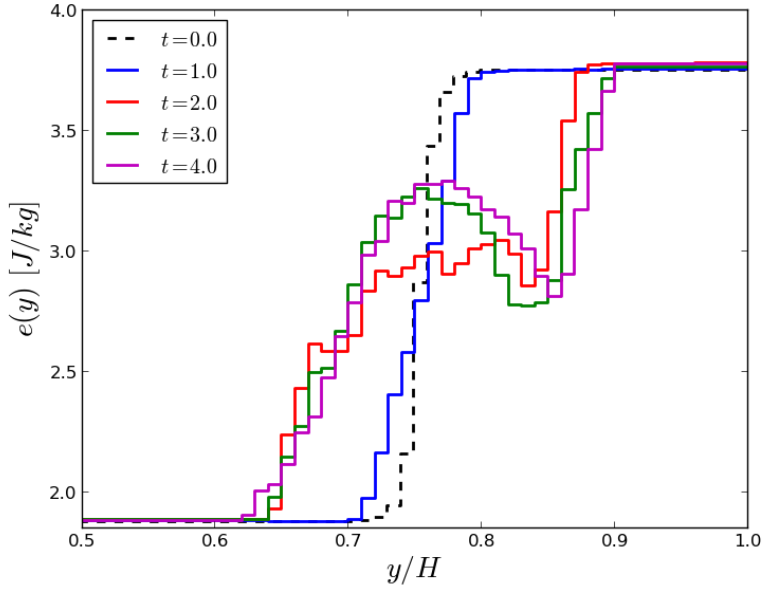

Figure 5.2: The energy distribution in the top half of the vertical domain plotted at the times indicated. The initial energy discontinuity is smoothed out as the KHI evolves into the non-linear regime.

energy at various indicated times are plotted in Figure 5.1-5.2. As expected, the density and energy distribution becomes increasingly diffused as the instability evolves into the non-linear regime. Figure 5.3 plots the relative error in pressure along the vertical direction at various times, with the maximum measured error of 7% near the interfaces. As the instability emerges into the non-linear regime physical quantities such as density and energy become further smoothed out, thus reducing the associated error in pressure from 7% to 5%.

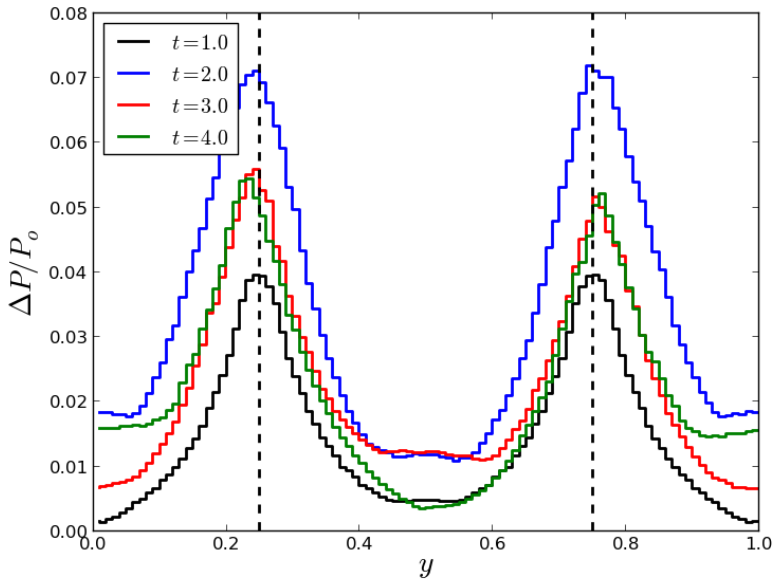

Figure 5.3: Fractional error in the pressure relative to the initial pressure in the vertical direction at the times indicated. The maximum measured relative error of 7% is observed near both interfaces at time $t = 2$. The location of the initial interface at $y = 0.25$, and $y = 0.75$ is indicated by dotted vertical lines.

The numerical results at different times are shown in Figure 5.4, with a fixed time increment of $\Delta t = 0.2$ between each panel. During the early stage $0 \lesssim t \lesssim 1$, the vertical perturbation generates a small amplitude wave-like structure near the fluid interface. At this stage, the instability is in the linear regime at which the amplitude of the perturbation follows an exponential growth. The instability continues to evolve into the non-linear regime as the destabilising effects of the horizontal shearing motion further amplifies the initial perturbation. By $t \approx 1.2$

the instability has emerged into the non-linear regime and the formation of the KHI billows are clearly observed. In the absence of dissipative mechanisms, the amplitude of the KHI billows continue to roll-up and eventually lead to the formation of the well known cat-eye vortex at $t \approx 1.7$. At $t \approx 2$ the cat-eye vortex has fully developed, and secondary instabilities begin to appear at the edges of the vortices. Nevertheless, it is very likely that these secondary KHI billows are dominated by numerical noise in the kernel density estimate. In addition, the secondary KHI billows occur at length-scales that are far beyond the resolution scale considered in our simulations.

The post billow development stage of the instability reveals additional features which have been omitted in previous work [64, 149, 216, 217]. From $3 \lesssim t \lesssim 4$, the fully developed KHI billows which have the form of cat-eye vortices are driven by the horizontal shearing motion between the fluid layers. This results in the collapse of the finite amplitude KHI billows. The evolution of the instability then enters a transition period where the collapsed billows generate a shearing layer near the interface. This transition is however short lived, $4 \lesssim t \lesssim 5$, as the rotating fluid particles situated inside the cat-eye vortices experience a centrifugal force which then leads to the retardation of the upper right billow and the bottom left billow. The retarded movement of the billow eventually disrupts the evolution of the horizontal shearing layer, and the force imbalance between the vortices consequently leads to the onset of the so called vortex pairing process at $t \approx 6$. During the pairing process in $t = 6.2 - 6.4$, the billows coalesce to form a larger billow at both interfaces. Finally, the merging processes is complete by $t \approx 7$ which results in the formation of two single KHI vortices that dominate the entire fluid domain.

5.4.2 Dependence on artificial viscosity parameters

α_{AV}: In order to understand the influence of artificial viscosity, a series of stimu-

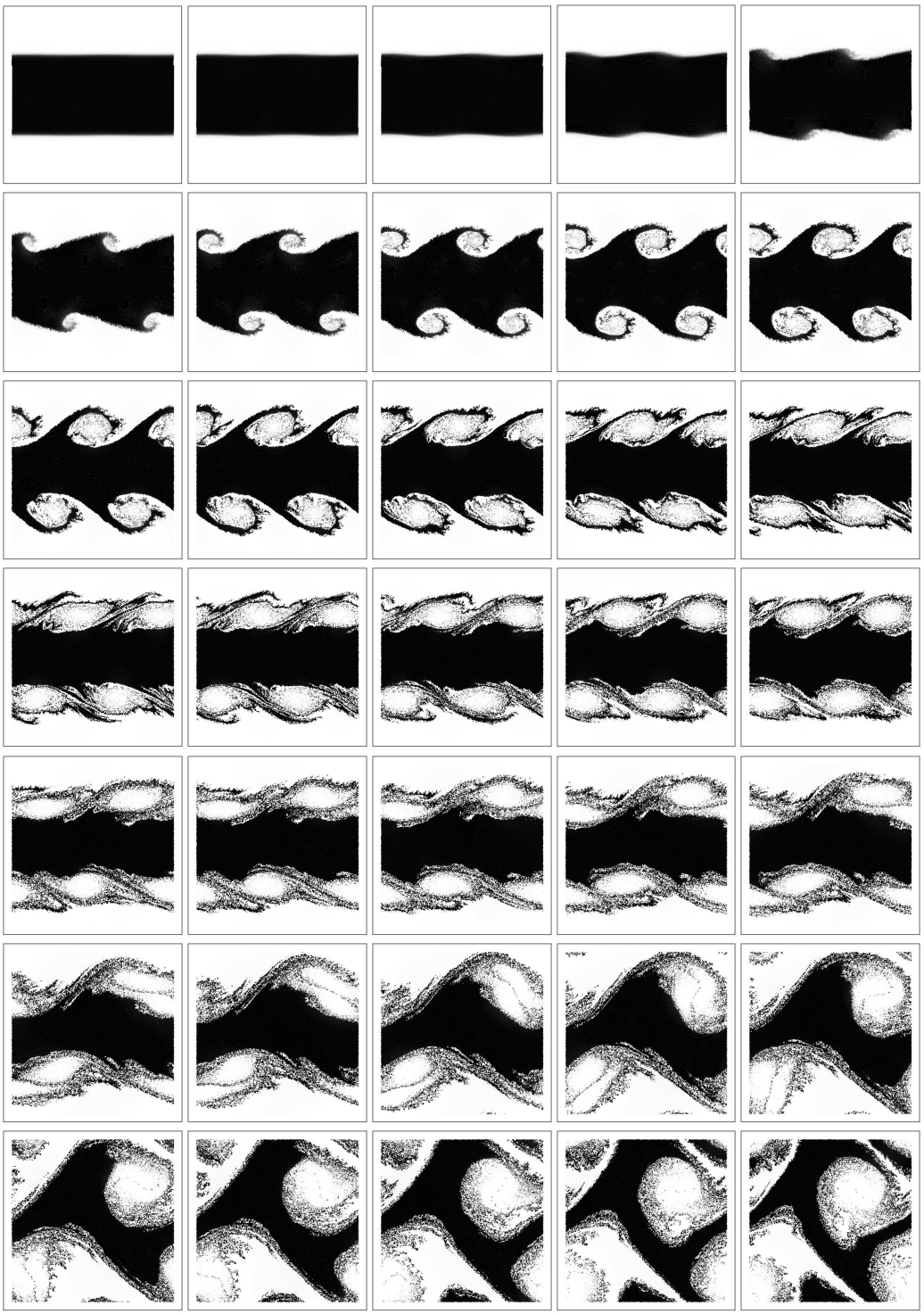

Figure 5.4: Numerical results of the fiducial model plotted at times between $t = 0.2 - 7$, with a fixed increment of $\Delta t = 0.2$ plotted from left to right, top to bottom.

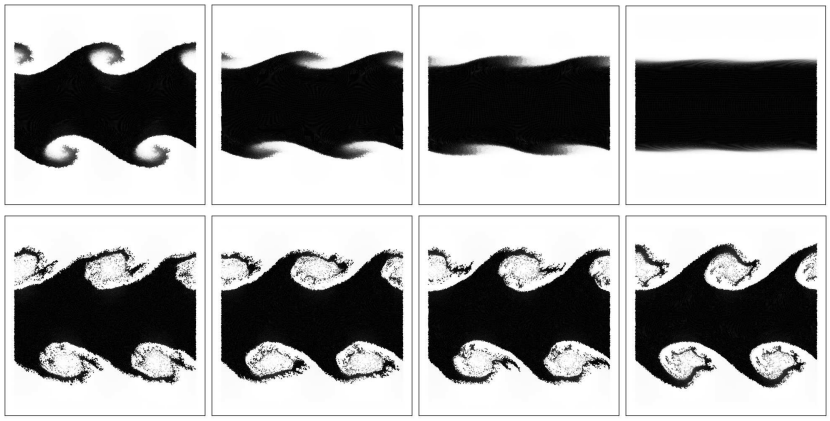

Figure 5.5: Numerical results generated by different indicated artificial viscosity parameter α_{AV} plotted at $t = 2$. The top row corresponds to results that utilised the conventional artificial viscosity, and the bottom row corresponds to the results generated with the combined use of a Balsara switch and conventional artificial viscosity.

lations is conducted for the sharp interface KHI using different artificial viscosity parameters. The utilisation of initial conditions with a sharp interface enables a direct comparison between our numerical results and the analytical growth rates including viscosity presented in Junk et al. [64]. Two sets of simulations are carried out: the first set of simulations utilise the standard artificial viscosity while the second set studies the combination of the standard artificial viscosity and a Balsara switch.

The numerical results corresponding to the different viscosity parameters are plotted in Figure 5.5, where the top (bottom) row corresponds to the results without (with) the utilisation of a Balsara switch. Even a cursory visual inspection of the numerical results reveals the influence of the Balsara switch. Without the Balsara term we found that, for the conventional artificial viscosity, the numerical results are strongly dependent on the prescribed artificial viscosity parameter α_{AV}. For example, focussing on $\alpha_{AV} = 2$ (see Figure 5.5, top) the utilisation of the standard artificial viscosity results in the suppression of the initial perturbation modes. The introduction of the Balsara switch largely reduces the suppression and the development of a full rotation of the billow is

clearly observed at all the tested values of α_{AV} (see Figure 5.5, bottom row).

In order to validate the results quantitatively, a discrete Fourier transform introduced in McNally et al. [108] is conducted to filter out the vertical velocity amplitudes corresponding to the initial perturbation at each output time interval $\Delta t = 0.2$. A selection of these vertical velocity amplitudes for different values of α_{AV} are shown in Figure 5.6. The slope of the velocity amplitude data is fitted during the linear regime between $t = 0.2$ and $t = 0.8$ to estimate the growth rate of the imposed perturbation in each SPH simulation. These fitted growth rates are used as input for the dispersion relation [64] to determine the SPH effective kinematic viscosity ν_{sph}. Afterwards, a linear interpolation is applied to determine the relationship between the effective viscosity and the SPH viscosity parameter α_{AV} as shown in Figure 5.7.

Inspecting Figure 5.6, it is clear that the velocity amplitude exhibits an initial decay prior to the expected linear growth of the instability being established. We suspect this decay is caused by the interaction of the high frequency noise seeded by the initial particle distribution, which is rapidly damped out by the artificial viscosity. The seeded growing perturbation mode corresponding to $\lambda = L/2$ becomes dominant as the instability emerges into the linear regime. Analysing the data for conventional artificial viscosity, a linear relationship is found between the effective viscosity and α_{AV} with a slope of 0.147 and an intercept of 0.017. The intercept indicates the intrinsic SPH viscosity which is inherited from the numerical discretisation (see Figure 5.7). The extracted growth rate, the effective viscosity, and the absolute and relative error between the extracted growth and classical inviscid growth rate [5] are reported in Table 5.1. A comparison of the data in Table 5.1 allows the quantification of the earlier observations regarding the suppression of the growth rate caused by the conventional artificial viscosity. For instance, the simulation for $\alpha_{AV} = 1$ corresponds to an effective viscosity of $\nu_{sph} = 0.17\text{m}^2/\text{s}$ and a relative error of $\eta_{classical} = 62\%$ when compared against

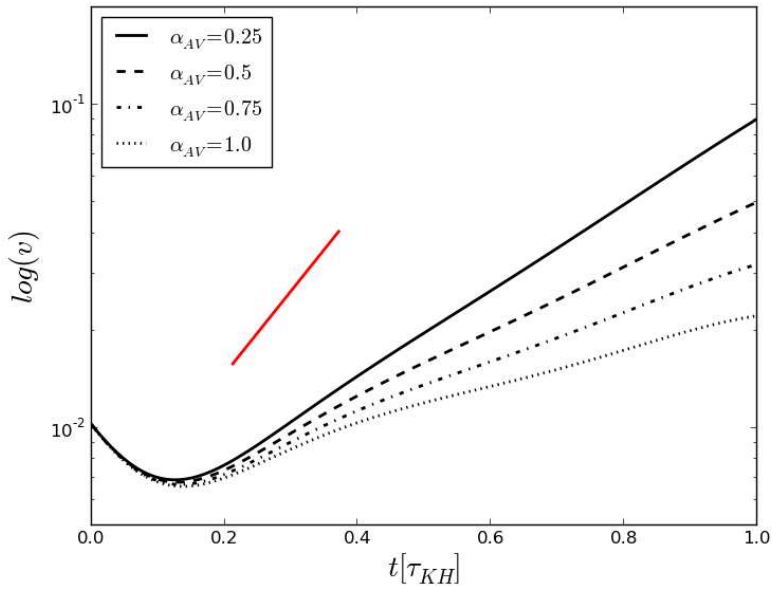

Figure 5.6: Vertical velocity amplitude for the conventional Monaghan artificial viscosity (as indicated) without a Balsara switch. The classical inviscid solution presented in [5] is plotted in red.

the classical inviscid growth rate. The utilisation of a Balsara switch significantly reduces the effective viscosity to $\nu_{sph} = 0.06\text{m}^2/\text{s}$, with the corresponding relative error of $\eta_{classical} = 12\%$. Similar results are observed for other viscosity parameters. The fitted curve between α_{AV} and effective viscosity ν_{BAL} has a slope of 1.68×10^{-4} and an intercept of 0.06 (see Figure 5.7). It is also worth pointing out that the reported effective viscosity is significantly higher than the values given in [183] (see [183] equation 100), namely $\nu_{sph,theory} = \alpha_{AV} c_i h_i / 8$. For the fiducial model $\nu_{sph,theory} \approx 0.0018\text{m}^2/\text{s}$, however the estimated viscosity from the fitted growth rate indicates a viscosity of $\nu_{sph} \approx 0.06\text{m}^2/\text{s}$. Furthermore, if one utilises the definition of the Reynold's number, $Re = \lambda u / \nu_{sph}$, the effective Reynold's number in the presented simulation is $Re \sim \mathcal{O}(10^1)$, suggesting the simulations herein are well within the laminar regime.

β_{AV}: The influence of the second artificial viscosity parameter β_{AV} is studied following the same procedures described above. In order to avoid particle pen-

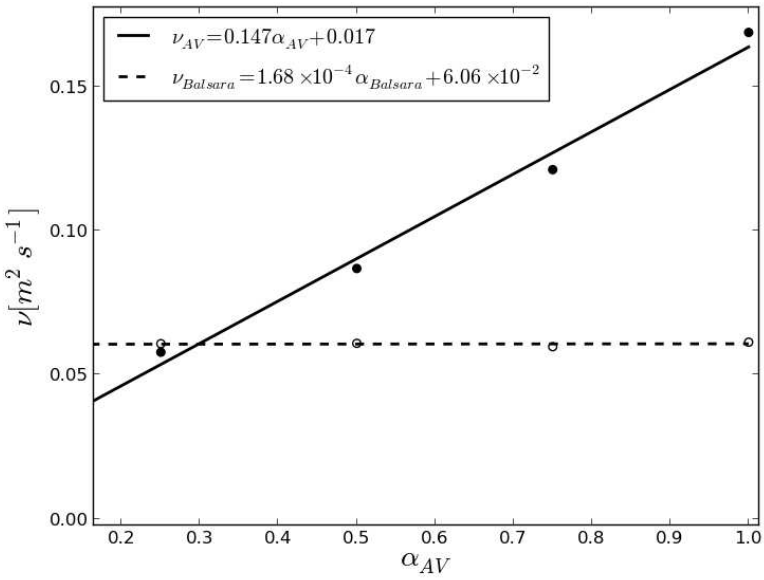

Figure 5.7: The interpolated effective viscosity between the Monaghan artificial viscosity parameter α_{AV} with the corresponding viscosity ν_{AV}. The interpolated effective viscosity ν_{BAL} for the combined use of artificial viscosity and Balsara switch are plotted as dotted lines.

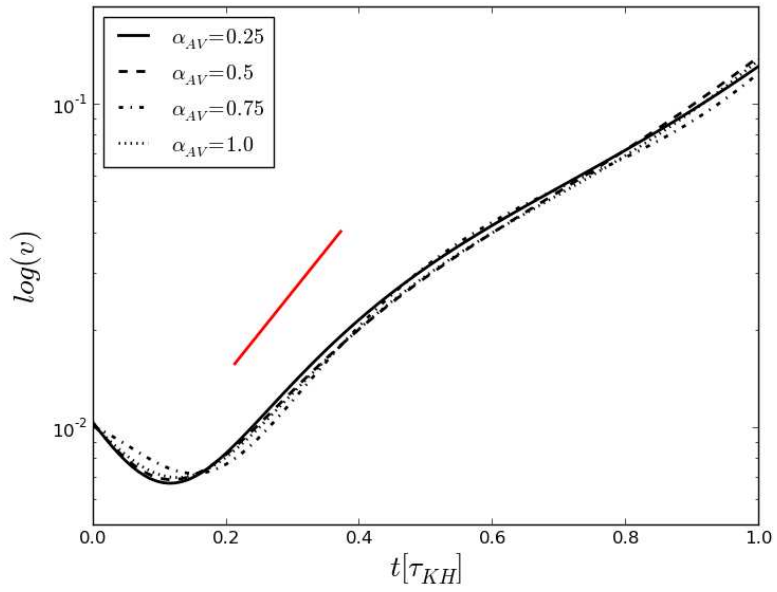

Figure 5.8: Vertical velocity amplitude for the conventional standard artificial viscosity (as indicated) and the Balsara switch. The slope of the classical inviscid solution presented in Chandrasekhar [5] is plotted in red.

standard AV						
α	ν_{sph}	n_c	$\Delta n_{c,classical}$	$\eta_{classical}$	$\Delta n_{c,smooth}$	η_{smooth}
0.25	0.07	4.7	1.2	20	0.85	15
0.50	0.09	4.0	2.0	33	1.59	29
0.75	0.12	3.0	2.9	49	2.51	45
1.00	0.17	2.3	3.7	62	3.31	59
Balsara switch						
α	ν_{sph}	n_c	$\Delta n_{c,classical}$	$\eta_{classical}$	$\Delta n_{c,smooth}$	η_{smooth}
0.25	0.06	5.1	0.84	14	0.48	9
0.50	0.06	5.1	0.85	14	0.49	8
0.75	0.08	5.1	0.78	13	0.43	8
1.00	0.06	5.1	0.87	15	0.51	9

Table 5.1: Fitted growth during the initial linear stages development for different viscosity parameters. The first set of data corresponds to the simulations with standard artificial viscosity(rows 1-4), and the second set of data corresponds to simulations where the combination of standard SPH viscosity and Balsara switch were utilised (row 5-8) . The artificial viscosity parameter (1^{st} column), kinematic viscosity (ν_{sph}) (2^{nd} column), extracted growth rate (n_c) (3^{rd} column), the absolute error ($\Delta n_{c,classical}$, $\Delta n_{c,smooth}$) (4^{th}-6^{th} column) and relative error given in % ($\eta_{classical}$,η_{smooth}) (5^{th}-7^{th} column).

etration, the first parameter is fixed at $\alpha_{AV} = 0.25$ and the parameter β_{AV} is varied between $\beta_{AV} = 1 - 4$. The results for different values of β_{AV} at $t = 2$ are shown in Figure 5.9. A visual inspection of the results indicates that the evolution of the KHI is weakly dependent on the value of the prescribed β_{AV}. The vertical amplitude for various values of β_{AV} as indicated are plotted in Figure 5.10. A linear relation is also recovered between the viscosity parameter β_{AV} and the effective kinematic viscosity, with a slope of 5.2×10^{-3} and an intercept of 0.057 as shown in Figure 5.11. The extracted growth rate, the effective viscosity and the absolute and relative error between the SPH results and classical inviscid theory [5] are reported in Table 5.2. It is apparent that the growth rates and the viscosities are remarkably similar between different rows. Nonetheless, because the standard artificial viscosity model with $\alpha_{AV} = 0.25$ is utilised in these cases, the additional viscosity from the first order viscosity parameter α_{AV} is therefore responsible for the discrepancy between the extracted and classical growth rate.

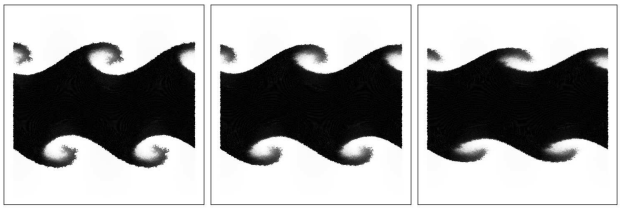

$\beta_{AV} = 1.0$ $\beta_{AV} = 2.0$ $\beta_{AV} = 4.0$

Figure 5.9: Numerical results generated by different artificial viscosity parameters β_{AV}, with fixed $\alpha_{AV} = 0.25$ plotted at $t = 2$.

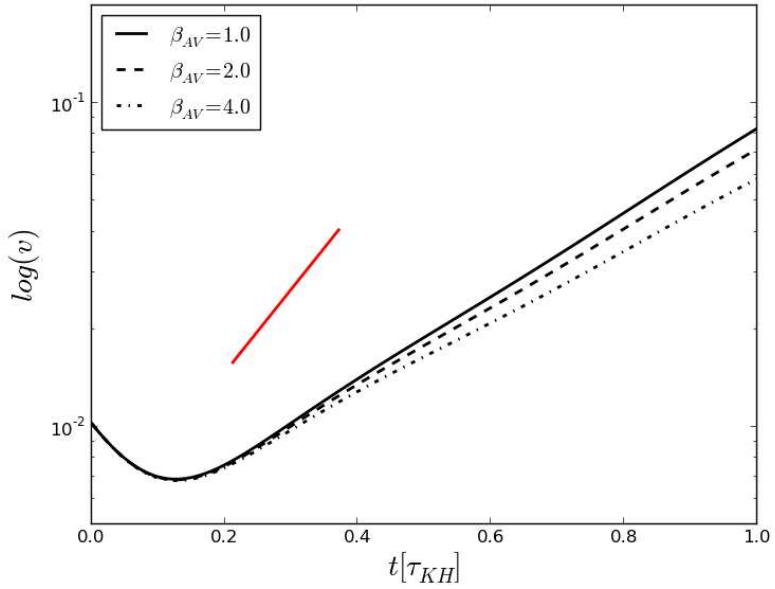

Figure 5.10: Vertical velocity amplitude for various values of β_{AV} as indicated for a conventional Monaghan artificial viscosity with $\alpha_{AV} = 0.25$. The slope of the classical inviscid solution of [5] is plotted in red.

β_{AV}	ν_{SPH}	n_c	$\Delta n_{c,classical}$	$\eta_{classical}$	$\Delta n_{c,smooth}$	η_{smooth}
1	0.06	5.1	0.81	14	0.45	8
2	0.07	4.8	1.1	19	0.75	12
4	0.08	4.4	1.5	26	1.18	21

Table 5.2: The fitted growth rates for different values of β_{AV}. The effective viscosity (ν_{SPH})(2^{nd} column), the fitted growth rate (n_c) (3^{rd} column), the absolute error ($\Delta n_{c,classical}$, $\Delta n_{c,smooth}$) (4^{th}-6^{th} column) and relative error ($\eta_{classical}$, η_{smooth}) (5^{th}-7^{th} column).

5.4.3 Dependence on local resolution κ

The fiducial model is simulated with everything else being fixed except the local resolution parameter, κ, which is varied between $\kappa = 1.25 - 2.33$ while fixing

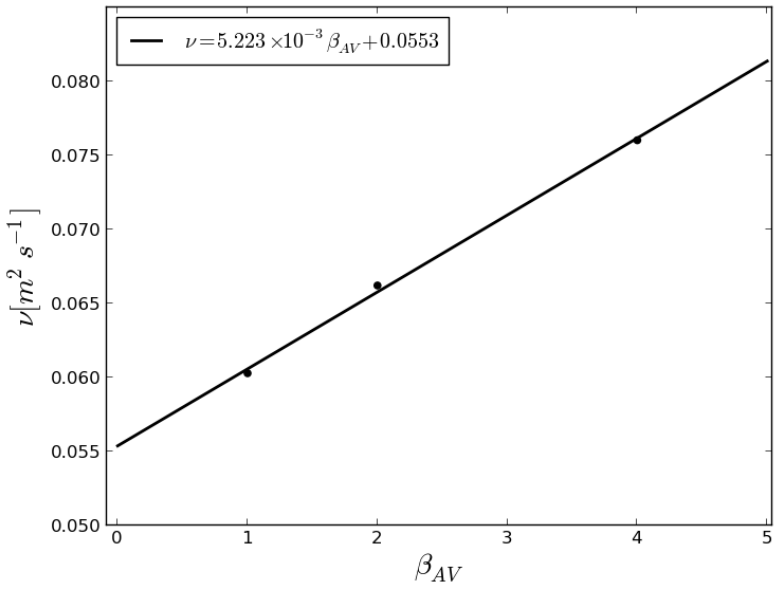

Figure 5.11: The fitted relation between the artificial viscosity parameter β_{AV} and the interpolated kinematic viscosity.

the global resolution (i.e. total number of SPH particles the same as our fiducial model). As previously mentioned in chapter 2, the sharp interface initial conditions are pathological cases. In practice, the interface is better described using the smoothed initial condition approach [7, 65, 66]. The dependence of local and global resolution are deferred until section 5.6.2 for the stratified shear instability. Recall that weakly-compressible SPH formulation employs a fixed smoothing length for all SPH particles, and the parameter κ controls the support of the kernel function (larger values of κ imply more neighbours on average). An alternative approach is to allow the smoothing length to vary while the number of neighbours is kept fixed. The numerical results corresponding to different values of κs are shown in Figure 5.12. Although the simulation terminates during the linear regime, a visual inspection of Figure 5.12 clearly suggests the local resolution parameter can significantly alter the numerical results even at the initial stage of the instability. This is because when multi-mass SPH particles are utilised in conjunction with a fixed smoothing length, the kernel weighted

density estimate of physical variables will be biased against the higher density fluid particles once the volume of the SPH particles departs from its initial volume, resulting in noise at the interface where the fluid properties such as density and velocity varied rapidly. Inspecting Figure 5.12, one can clearly observe that the interface layer between fluids appears to be more regularised for larger values of κ. While an increase in κ suppresses the noise problem at the interface during the linear regime, one should pay attention to the implied consequence of choosing a large smoothing length in weakly-compressible SPH simulations. That is, by employing a large smoothing factor which is fixed throughout the simulation one automatically commits oneself to the limited kernel resolution. The smallest scale motion that can be followed is of order the SPH kernel size. In other words, any motion smaller than the size of the kernel should be regarded as noise. Furthermore, since the higher density fluid is represented by particles of higher mass, during the simulation the number of interpolation points that can describe the small-scale motion are effectively reduced. Although these limitations are irrelevant during the linear regime, but as the growth of the KHI billow emerges into the cat-eye vortex a fixed smoothing length approach would be limited by its resolution scale to accurately resolve the dynamics within the cat-eye vortex. More importantly, as mentioned in Read et al. [109], one should be aware that the utilisation of a large smoothing length can lead to a more devastating consequence, namely the pairing instability.

Figure 5.13 illustrates the vertical velocity amplitudes for different local resolution parameters during the linear regime. Inspecting the results, it is found that an increase in κ results in an increased growth rate which converges to the analytical expectation given in [7, 65, 66]. The extracted growth rates and their errors compared to the classical and smoothed interface solution are reported in Table 5.3. Note that the convergence to the analytical growth rate [7] is clearly observed as κ increases. For example, for $\kappa = 1.25$ a relative error of 56% is

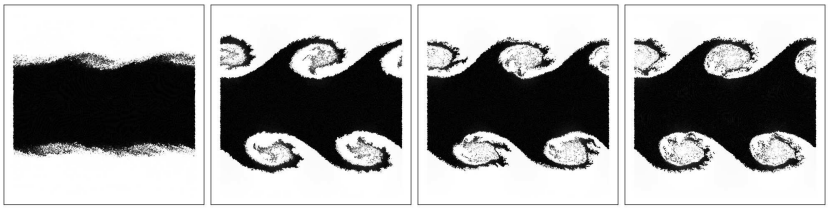

$\kappa = 1.25$ $\kappa = 1.50$ $\kappa = 1.95$ $\kappa = 2.33$

Figure 5.12: Numerical results of the fiducial model simulated with different values of the resolution parameter κ plotted at $t = 2$.

reported, whereas the relative error of the growth rate decreases to 10% for $\kappa = 2.33$.

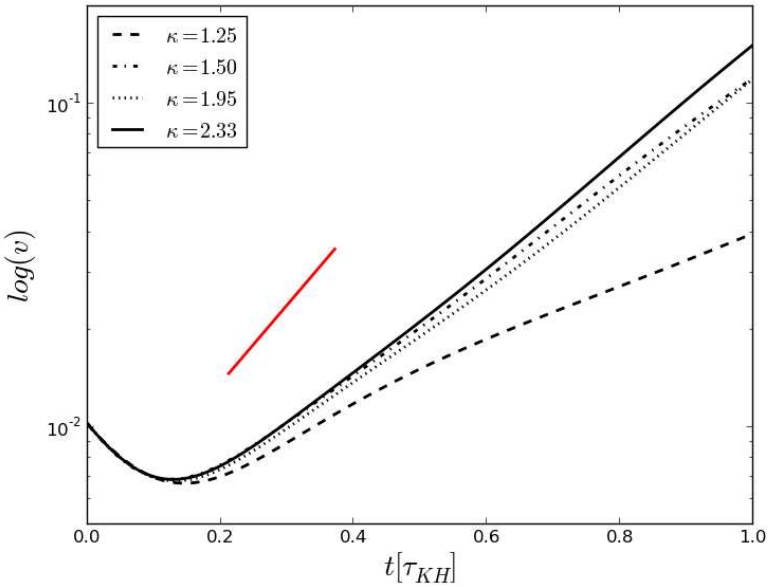

Figure 5.13: Vertical velocity amplitude for the local resolution parameters (as indicated). The slope of the classical growth rate [5] is plotted in red.

κ	N_n	n_c	$\Delta n_{c,classical}$	$\Delta n_{c,smooth}$	$\eta_{classical}$	η_{smooth}
1.25	20	2.4	3.5	3.1	59	56
1.50	28	4.2	1.7	1.3	29	24
1.95	47	4.2	1.7	1.3	28	24
2.33	68	5.0	0.9	0.5	15	10

Table 5.3: The fitted growth rates for various smoothing scales as indicated. The number of neighbour particles (2^{nd} column), the extracted growth rate (n_c) (3^{rd} column), the absolute error ($\Delta n_{c,classical}$, $\Delta n_{c,smooth}$) (4^{th}-5^{th} column) and relative error ($\eta_{classical}$,η_{smooth}) (6^{th}-7^{th} column).

5.4.4 Dependence on the thickness of the velocity and density transition layers

While it has been reported in the literature [58, 108, 109] that smoothed initial conditions are better suited for SPH simulations, a comprehensive study of the influence of the depth of the initial interface has not been attempted in the literature. To finalise our study, we investigate the role of the width of the initial velocity and density transition layer. In order to formulate a systematic analysis, the density and velocity gradient are varied independently from $L_{u,\rho} = 2d_{nat} - 6d_{nat}$ and simulated up to $t = 2$. Figure 5.14 illustrates the vertical velocity amplitude for different initial velocity gradients. Inspecting the velocity amplitudes, it is found an increase in the initial velocity gradient results in a less pronounced KHI. The extracted growth data and the associated difference between the classical (sharp transition) and smoothed analytical growth rates are reported in Table 5.4 (see also Table 5.4, rows 1-3). The SPH results are in good agreement with the analytical expectation of [7], with an average relative error of $\langle \eta_{smooth} \rangle = 12\%$ and depart from the classical growth rate [5], with an average relative error of $\langle \eta_{smooth} \rangle = 22\%$.

The influence of the density gradient is also studied in a similar fashion. Figure 5.15 illustrates the vertical velocity amplitude for different initial smoothed density interface widths. As we have shown in chapter 2, for a sharp velocity interface ($L_u = 0$) an increase in initial density gradient leads to a decrease in the local Atwood number between each differential horizontal layer which consequently results in a more pronounced KHI growth than the classical values. In contrast, we find an increase in initial density gradient results in a smaller growth rate than the classical expectation (Table 5.4 row 4-6) and results in an average relative error of $\langle \eta_{smooth} \rangle = 17\%$.

Finally, we study the scenario where both the initial velocity and density

L_u	n_c	$n_{c,smooth}$	$\Delta n_{c,classical}$	$\Delta n_{c,smooth}$	$\eta_{classical}$	η_{smooth}
2	5.0	5.51	0.89	0.51	15	9
4	4.8	5.22	1.10	0.37	19	7
6	3.9	4.92	1.98	0.95	33	19
L_ρ	n_c	$n_{c,smooth}$	$\Delta n_{c,classical}$	$\Delta n_{c,smooth}$	$\eta_{classical}$	η_{smooth}
2	5.1	5.99	0.83	0.89	14	15
4	4.7	6.03	1.22	1.33	21	22
6	5.2	6.07	0.68	0.83	11	14
D	n_c	$n_{c,smooth}$	$\Delta n_{c,classical}$	$\Delta n_{c,smooth}$	$\eta_{classical}$	η_{smooth}
10	5.1	5.76	0.81	0.65	14	11
20	5.1	5.81	0.77	0.66	13	11
40	5.2	5.84	0.77	0.69	13	12

Table 5.4: The fitted growth rates for various initial velocity gradient (top) and density gradient (bottom) values as indicated. The extracted growth rate (n_c) (2^{nd} column), the analytical growth rate presented in [7] (3^{rd} column), the absolute error ($\Delta n_{c,classical}$, $\Delta n_{c,smooth}$) (4^{th}-5^{th} column) and relative error ($\eta_{classical}$,η_{smooth}) (6^{th}-7^{th} column).

transition layers are of finite width (i.e. $L_{u,\rho} > 0$). In this case, the velocity gradient $L_u = 2d_{nat}$ is chosen as the base parameter and the ratio between the density and velocity gradient, namely $D = L_\rho/L_u$ is varied from $D = 10 - 40$ in order to study how the initially smoothed distribution effects the evolution of the KHI in SPH simulations.

The numerical results and the extracted vertical amplitudes are plotted in Figure 5.16-5.17 respectively. As expected, the combined smoothing of the velocity and the density transition layers leads to an overall suppression of the KHI compared to its classical analytical growth rate. In addition, the extracted growth rates are found to be in acceptable agreement with the linear growth rate in chapter 2 with an average relative error of $\langle \eta_{smooth} \rangle = 11\%$.

Further comparison of the errors corresponding to the three different sets of simulations in Table 5.4 suggests that the finite velocity and density gradient simulations are always in better agreement with the smoothed linear growth rates [7, 65, 66] than the sharp velocity and density transition simulations. Note that in theory it is possible to prescribe sharp discontinuous initial conditions, but the inherent smoothing properties of SPH smooth out the initial condition as soon

as the simulation begins. This explains the inconsistency between SPH results and sharp interface linear growth rate [5]. Furthermore, when the width of the density transition layer exceeds the width of the velocity transition layer, the concept of a sharp interface is no longer relevant and the instability is expected to behave similar to a localised single phase KHI.

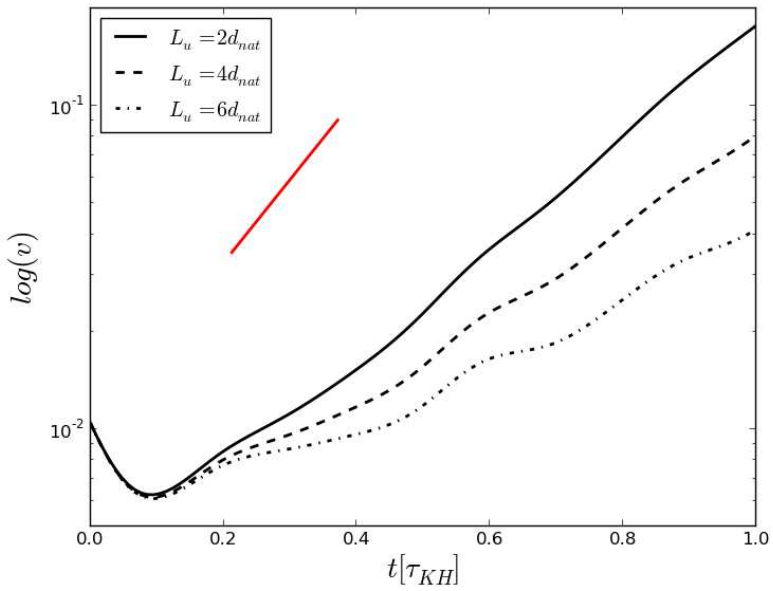

Figure 5.14: The extracted vertical velocity amplitude for different velocity gradients L_u. The increase in velocity gradient suppresses the growth of the KHI.

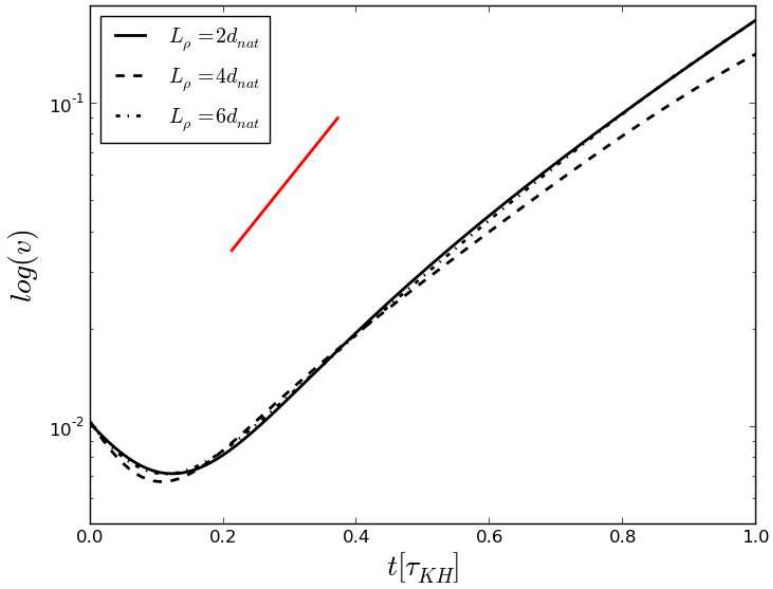

Figure 5.15: The extracted vertical velocity amplitude for different density gradients L_ρ. The increase in velocity gradient suppresses the growth of the KHI.

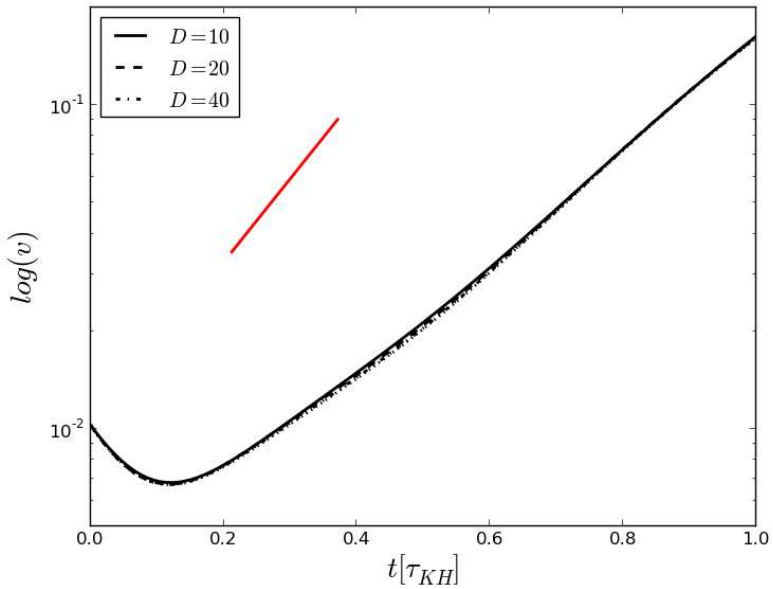

Figure 5.16: The vertical velocity amplitude growth for different length scale ratios D (as defined in the text).

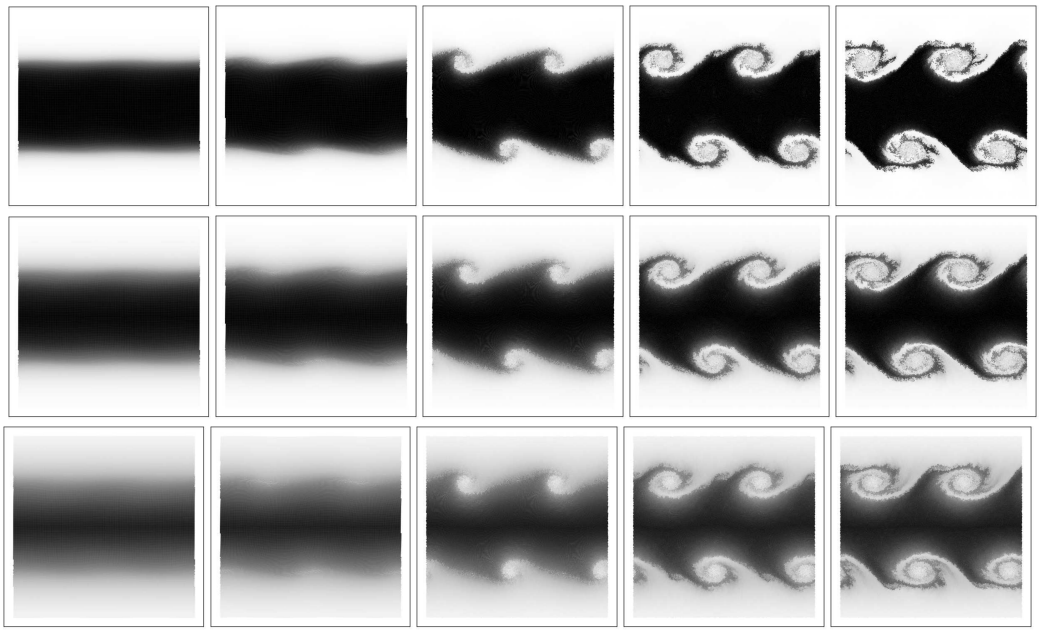

Figure 5.17: Numerical results of the fiducial model simulated with ratios of density and velocity gradients $D = 10$ (top), $D = 20$ (middle) $D = 40$ (bottom) plotted at various time-steps.

Stratified shear instability

5.5 Initial Conditions

The two-dimensional stratified shear instability is confined in a semi-infinite parallel plane $x \in [0, L], y \in [0, H]$, where the aspect ratio is normally set to unity. The initial conditions are similar to the ones in section 5.3, except ghost particles with constant velocities are placed at the top and bottom of the vertical computational domain to simulate the behaviour of moving walls. The initial density profile is given by

$$\rho(y) = \begin{cases} \rho_1 - \frac{\Delta\rho}{2} e^{-\frac{|y-y_o|}{L_\rho}} & 0 \leq y < y_o \\ \rho_2 + \frac{\Delta\rho}{2} e^{-\frac{|y-y_o|}{L_\rho}} & y_o \leq y < H \end{cases}. \tag{5.4}$$

The horizontal velocity profile

$$u(y) = \begin{cases} u_1 - \frac{\Delta U}{2} e^{-\frac{|y-y_o|}{L_u}} & 0 \leq y < y_o \\ u_2 + \frac{\Delta U}{2} e^{-\frac{|y-y_o|}{L_u}} & y_o \leq y \leq H \end{cases}. \tag{5.5}$$

is utilised to prescribe the horizontal velocities of the particles. The density (5.4) and velocity (5.5) profiles define the interface at $y_o = H/2$, at which the density and horizontal velocity are $\rho(y_o) = (\rho_1 + \rho_2)/2$ and $u(y_o) = (u_1 + u_2)/2$. In order

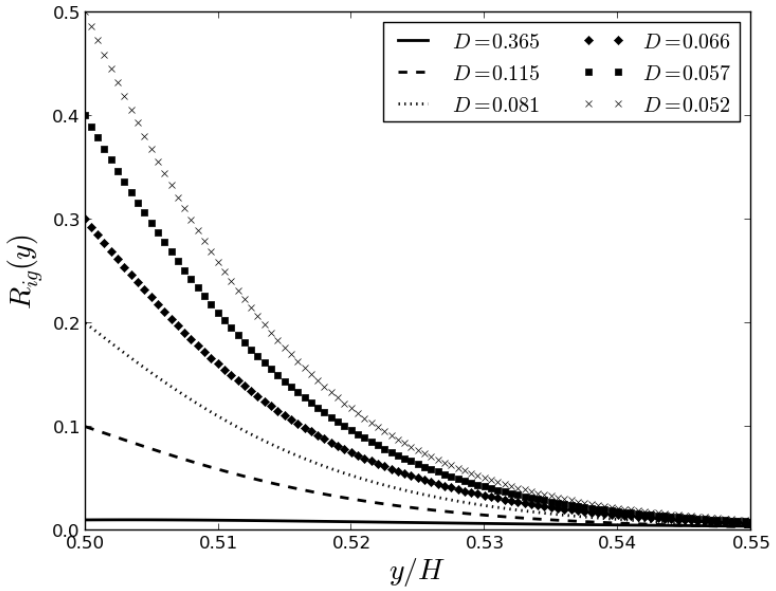

Figure 5.18: The initial gradient Richardson number for different length scale ratios $D = L_\rho/L_u$ along the top half of the vertical computational domain for $g = -0.1\text{m/s}^2$ and $L_\rho = 0.01L$.

to perturb the fluid system, an initial seed vertical velocity perturbation function

$$v\,(x, y) = \delta v_y \sin(kx) e^{-k|y-y_o|}, \tag{5.6}$$

is applied with an amplitude $\delta v_y = 0.01\Delta u$. The exponential factor in (5.6) ensures the vertical velocity perturbation vanishes away from the interface. The gradient Richardson number Ri_g is defined as the ratio between the square of the Brunt-Väisälä frequency and the velocity shear. For small vertical velocity perturbation, the gradient Richardson number is given by

$$Ri_g = \frac{|\vec{g}|}{\rho} \frac{\partial\rho/\partial y}{(\partial u/\partial y)^2} \tag{5.7}$$

The local gradient Richardson number in the vertical direction for the indicated length scale ratios are plotted in Figure 5.18. The gradient Richardson number

reported here follows from equation (5.7) evaluated at the interface y_o,

$$Ri_g(y_o) = \frac{4|g|\, L_u^2\, A_T}{\Delta u^2\, L_\rho}. \tag{5.8}$$

For a fixed density ratio, gravitational acceleration and velocity shear, the gradient Richardson number essentially indicates how much broader the smoothing of the velocity is than that employed for the density. As the velocity smoothing is extended further than the density smoothing the effective kinetic energy in this region is reduced and so the Richardson number increases.

Furthermore, it is necessary to distinguish the gradient Richardson number (Ri_g) reported here and the conventional Richardson number in classical hydrodynamics literature [88, 207, 208]. The gradient Richardson number Ri_g accounts for the effects of velocity and density boundary layers. In contrast, the conventional Richardson number is only suitable for fluid system: (i) with discontinuous initial velocity profile and (ii) small density differences such that the Boussinesq approximation applies.

The shear instability is described by a set of dimensionless parameters, namely the Atwood number (A_T), the gradient Richardson number (Ri_g), the ratio of widths of the velocity transition layer and the density transition layer (D) and the Reynolds number ($Re = \lambda u_1/\nu_{sph}$ [218]). The kinematic viscosity reported herein is given by the relation $\nu_{sph} \approx \alpha_{AV} ch/8$ (Price [183] equation 100). With the aim of quantitative comparison in mind, the extracted growth rates are compared against the classical growth rate [5] and the linear growth rate for smoothed initial profiles presented in chapter 2, both of these can be found in chapter 2. The error metrics for reported in this section are defined in the same fashion as the ones in section 5.3.

5.6 Results and Discussion

The stratified shear instability that evolves from the initial conditions set-up as described in section 5.5 is simulated. The instability is characterised by seven parameters, five of which are physical and the remaining two are numerical. The physical parameters are the Reynolds number, which sets the relative speed of the shearing layers, the viscosity of the fluids (α_{AV}), the width of the density transition layer (L_ρ) the gradient Richardson number (Ri_g), which sets the relative widths of the initial density and velocity transition layers and the Atwood number (A_T), which defines the density ratio of the two fluids. The numerical parameters are N, the number of particles across the simulation box of width, L, which defines the mean inter-particle separation: $d_{nat} = L/N$. Note that for the particular geometry described herein the ratio $L : H = 1$, so $N^2 = N_p$ as well as the local smoothing parameter κ. The dependence of the simulated outcome on each of these parameters will be investigated in the following sections by comparing against a fiducial reference model defined below.

5.6.1 Fiducial Model

The fiducial simulation contains a total of $N_p = 4 \times 10^4$ particles, with 3.5×10^4 fluid particles and 5×10^3 ghost particles. The initial particle separation distance is $d_{nat} = L/N$, where each horizontal row consist of $N = 200$ particles and the local resolution parameter is $\kappa = 1.95$ in this case. The standard artificial viscosity [204] is used in conjunction with the Balsara switch, with artificial viscosity parameters chosen to be ($\alpha_{AV} = 0.5$, $\beta_{AV} = 0$). Furthermore, the Balsara switch is not active for ghost particles such that SPH fluid particles near the lateral boundaries adapt to the shearing velocity of static ghost particles. The initial density gradient is $L_\rho = 0.01L$, and the ratio between the velocity and density gradient is $D = 0.365$, a choice that sets the Richardson number

to $Ri_g = 0.01$ as illustrated in Figure 5.18. The density ratio between fluids is 2, which corresponds to an Atwood number of $A_T = 0.\bar{3}$. The instability is simulated up to $t = 10$ which enables a detailed investigation of both the linear as well as the non-linear evolution of the instability.

The numerical results are shown in Figure 5.19, with a fixed time increment of $\Delta t = 0.5$ between each panels. During the early stage $0 \lesssim t \lesssim 1.0$, the vertical generates a small amplitude wave-like structure near the interface. Particles that were initially above (below) the interface are marked in red (green) so that there evolution can be easily tracked. At this stage, the SPH results can be compared against the linear analytical predictions to examine the accuracy of the presented SPH method. By $t \approx 1.5$, the instability has emerged into the non-linear regime. The perturbation continues to grow in time $1.5 \lesssim t \lesssim 2.5$ as the de-stabilising effects of velocity shearing overcome the stabilising effect due to gravity, and the roll-up behaviour of the KHI billows generate the well known cat-eye vortices at $t \lesssim 2.5$.

During the post billow development stage $t \geq 2.5$, the fluid particles situated at the edge of the KHI billows are unstable against the KHI and RTI. The secondary instability causes the upper fluid to sink towards the bottom of the interface due to gravity, which suppresses the growth of the instability. The competition between gravity and shearing motion can be seen during $3.0 \lesssim t \lesssim 3.5$. This eventually stops the KHI billow to grow further, and lead to the transformation into a shearing layer at $t \approx 4.0$. During the transformation, the cat-eye vortices are heavily suppressed $4.0 \lesssim t \lesssim 4.5$, and eventually the two vortices merge into each other at $t \approx 5.0$. This marks the beginning of the vortex pairing process, which lasts between $5.0 \lesssim t \lesssim 7.0$. During the vortex pairing process, the fluid particles in the inner region of the original cat-eye vortices remain in the inner core region of the paired vortex. Moreover, additional instabilities can be seen at the edges of the merged vortex (see Figure 5.19, $t =$

7.5). Finally, the pairing process completes at $t \approx 7.5$, resulting in a single vortex at the center of the computational domain. The numerical results are in good qualitative agreement with the $Re = 500$ simulations in Klaassen and Peltier [211].

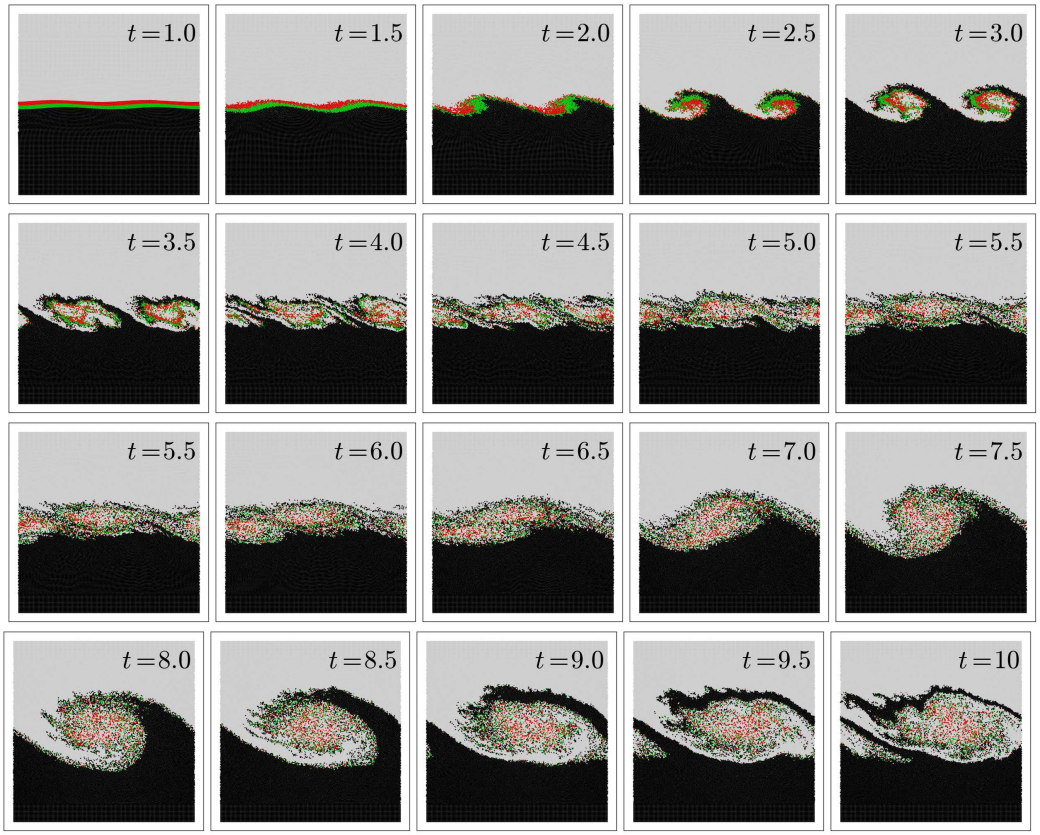

Figure 5.19: Numerical results of the fiducial model plotted at the times indicated. Particles with initial vertical positions above (below) the interface marked in red (green).

5.6.2 Resolution Dependence

For an SPH simulation there are two relevant length scales that influence resolution. The global resolution is set by the number of particles (N_p), as this defines the mean inter-particle separation (i.e. $d_{nat} = L/N$), where $N = \sqrt{N_p}$ for the test cases herein. The local resolution refers to the number of particles within in the support of the kernel function which smooths quantities represented by the smoothing length $h = \kappa d_{nat}$.

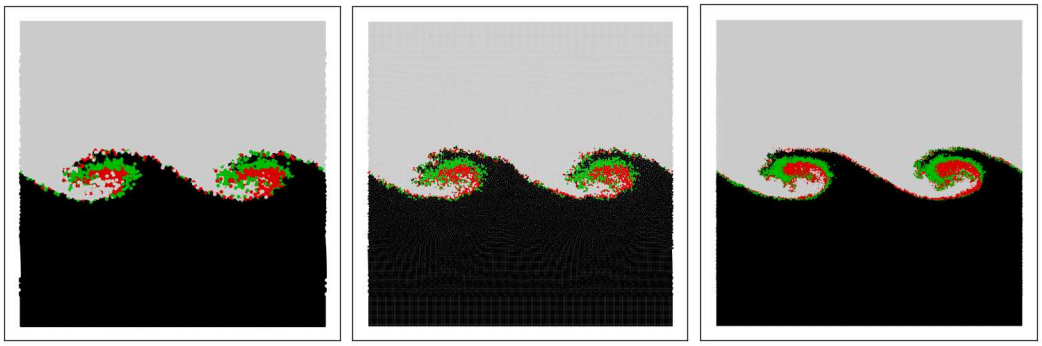

$N = 100$ $N = 200$ $N = 400$

Figure 5.20: Density plot for different global resolutions at $t = 2.5$. The low resolution simulation is shown on the left side, the fiducial resolution is shown in the middle, and the high resolution simulation is shown on the right hand side. The scatter plot marker size are scaled with respect to the number of particles per row.

In order to study the effects of global resolution, the fiducial model is simulated with the same set of parameters except with the global resolution varying from $N = 100$ to $N = 400$ while keeping other parameters unchanged. The numerical results at $t = 2.5$ are shown in Figure 5.22 (top row). Qualitatively we note: (i) despite the resolution change the amplitude of the KHI billows appear to be remarkably similar, and (ii) the dynamics occurring at the inner region of the KHI vortices are better resolved with a higher global resolution. Figure 5.20 further illustrates the qualitative behaviour for the low $N = 100$, medium $N = 200$ and high $N = 400$ resolution simulations considered herein. Note that, despite the similarities in the general structure, a comparison between the results plotted in Figure 5.20 indicates that a deficiency in global resolution results in poor resolution within the inner core region. The vertical velocity amplitudes corresponding to various global resolutions are plotted in Figure 5.21. We confirm that the velocity amplitudes are weakly dependent upon the global resolution.

As the qualitative results suggest the amplitude of the vertical velocity is weakly dependent on the number of SPH particles employed, one should expect the roll-up behaviour should occur earlier in the higher resolution simulations.

This is because as the resolution increases, the intrinsic error due to the discretisation of a fluid continuum into a discrete set particles decreases; therefore resulting in a more rapid growth rate as predicted by analytical theory. To quantify the effects of global resolution, the extracted growth rates are compared against the analytical predictions in a similar manner to section (5.4.2). The extracted growth rate as well as the absolute and relative errors are reported in Table 5.5. As expected, an increase in global resolution results in an increased growth rate (see Table 5.5, column 3). Finally, we would like to point out that while the results herein confirm the findings of Shadloo and Yildiz [149], the improvements due to increasing global resolution is hardly observable via visual inspection Figure 5.20. In fact, our studies suggest that one should rather rely on the numerically extracted growth rates.

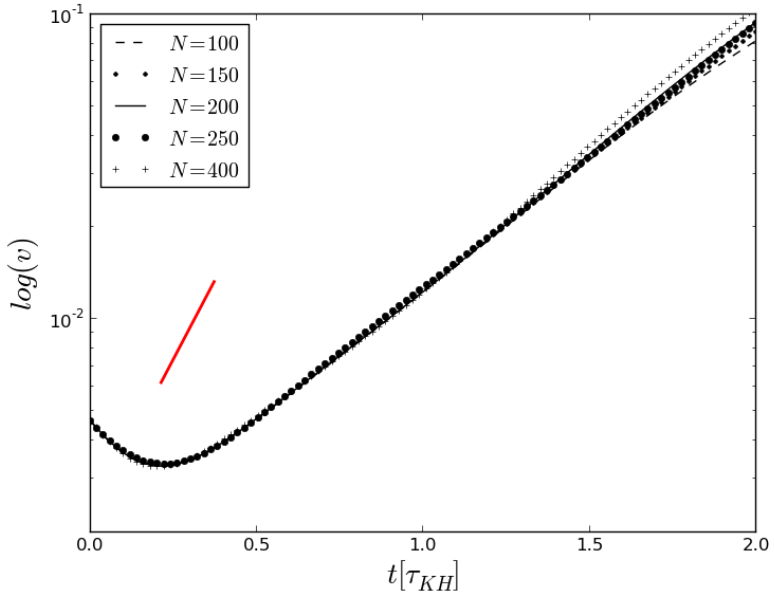

Figure 5.21: Vertical velocity amplitude for the different global resolutions. The classical growth rate [5] is plotted in red.

The local resolution scale in SPH is controlled by the smoothing length, which defines the region over which local quantities are smoothed. Detailed dynamics occurring on length-scales smaller than the smoothing length cannot

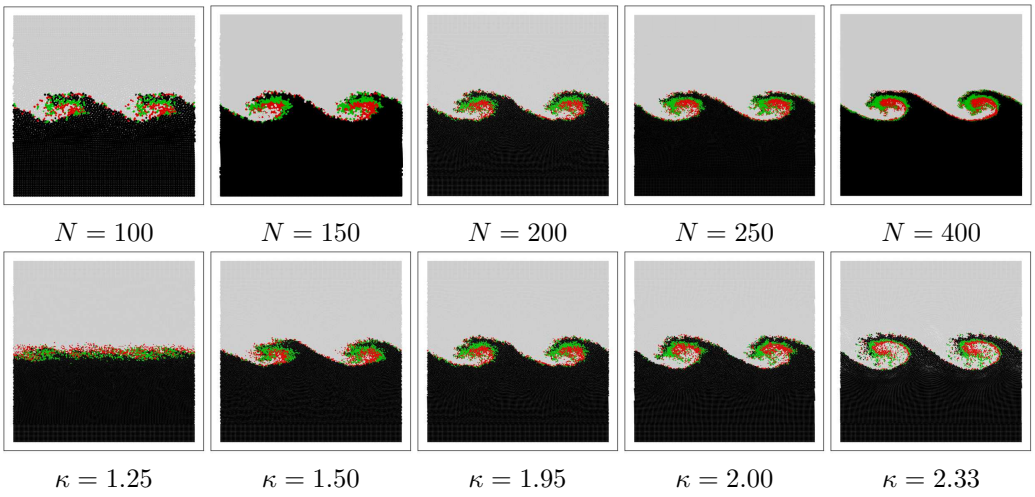

Figure 5.22: Numerical results at $t = 2.5$ simulated with global resolutions between $N = 100$ and $N = 400$ (top row) and local resolutions between $\kappa = 1.25 - 2.33$ (bottom row).

N	n_c	$\Delta n_{c,classical}$	$\Delta n_{c,smooth}$	$\eta_{classical}$	η_{smooth}
100	3.7	2.3	1.1	38	238
150	3.7	2.2	1.0	38	22
200	3.8	2.2	1.0	37	21
250	3.9	2.0	0.9	34	18
400	4.1	1.8	0.6	30	13

Table 5.5: The fitted growth rates during the initial stages of KHI growth for different global resolutions as indicated in the 1^{st} column. The extracted growth rate (n_c) (2^{nd} column), the absolute errors ($\Delta n_{c,classical}$, $\Delta n_{c,smooth}$) ($3^{rd} - 4^{th}$ column) and the relative errors ($\eta_{classical}$,η_{smooth}) given as percentages ($5^{th} - 6^{th}$ column).

be accurately resolved. Larger smoothing lengths include more particles under the SPH kernel, improving the stability of the implementation at the expense of reducing the effective number of resolution elements. Generally a balance is sought between having enough SPH neighbours to limit numerical issues while keeping as large a number of independently resolved regions as possible.

For the purpose of comparison, we simulated the fiducial model with the local resolution parameter varying between $\kappa = 1.25$ and $\kappa = 2.33$. The numerical results at $t = 2.5$ are plotted in Figure 5.22 (bottom row). Unlike the subtle difference seen for global resolution, it is found that the $\kappa = 1.25$ results significantly deviate from the larger κ runs in the following aspects: firstly, the roll-up

κ	N_n	n_c	$\Delta n_{c,classical}$	$\Delta n_{c,smooth}$	$\eta_{classical}$	η_{smooth}
1.25	20	2.3	3.7	2.52	62	53
1.50	28	3.2	2.8	1.6	47	33
1.95	47	3.8	2.2	1.0	37	21
2.33	68	4.0	1.9	0.7	32	16

Table 5.6: The fitted growth rates during the initial stages of the KHI growth for different local resolutions. The local resolution parameter, κ (1^{st} column), the number of neighbour particles (2^{nd} column), the extracted growth rate (n_c) (3^{rd} column), the absolute errors ($\Delta n_{c,classical}$, $\Delta n_{c,smooth}$) (4^{th}-5^{th} column) and the relative errors ($\eta_{classical}$,η_{smooth}) given as percentages ($6^{th} - 7^{th}$ column).

behaviour is completely absent. Secondly, particles near the interface have been driven away from the interface. Moreover, a comparison of the velocity amplitudes in Figure 5.23 suggests an increase in κ generally results in a larger growth rate (see Figure 5.23, $\kappa = 1.25$). This is attributed to an insufficient number of particles within the SPH smoothing kernel; hence significantly reducing the effective velocity shear between each vertical layer. In general the lack of sufficient local resolution to encapsulate the dynamics causes serious problems in regions where the physical properties such as velocity and density change steeply. The extracted growth rates are compared against the analytical predictions in Table 5.6. It is found that at fixed global resolution (here $N = 200$), both the absolute and relative error decrease with increasing local resolution. The absolute error $\Delta n_{c,smooth}$ decreases from 2.5 to 0.7, and the relative error η_{smooth} decreases from 53% to 16% as κ increases from 1.25 to 2.33.

5.6.3 Dependence on Reynolds number

In order to understand the role of the SPH artificial viscosity, the fiducial model is repeated until $t = 2.5$ using viscosity parameters between $\alpha_{AV} = 0.125$ and $\alpha_{AV} = 2.0$. For the purpose of comparison, two sets of simulations were conducted, namely with and without the Balsara switch. The numerical results corresponding to the different viscosity parameters are shown in Figure 5.25, where

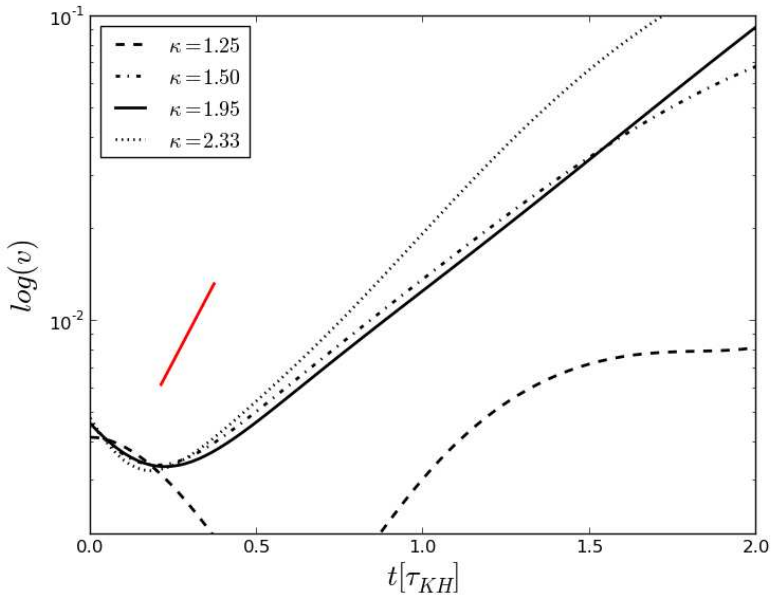

Figure 5.23: Vertical velocity amplitude for the different smoothing factors κ applied to the simulation of the fiducial model. The classical inviscid growth rate [5] is plotted in red.

the top (bottom) row corresponds to the results without (with) Balsara switch. Even a cursory visual inspection of the numerical results the clear influence of the Balsara switch. Without the Balsara switch, the numerical results are strongly dependent on the artificial viscosity parameter α_{AV}. For example, focussing on $\alpha_{AV} = 2$ (see Figure 5.25, top right) the standard artificial viscosity results in the suppression of the initial perturbation modes. The Balsara switch largely reduces the suppression and the development of a full rotation of the billow is clearly observed at all the tested values of α_{AV} (see Figure 5.25, bottom right).

Inspecting the vertical velocity amplitudes for the simulations without Balsara switch (see Figure 5.24, thin lines), it is found that while the growth of the initial perturbation can be seen for the low viscosity (i.e. $\alpha_{AV} = 0.125$) simulation, the amplitude decreases with increasing α_{AV}. In contrast, the vertical velocity amplitudes of the second series of simulations utilising the Balsara switch show little dependence on α_{AV} (see Figure 5.24, thick lines) and are always above the set of thin lines corresponding to the simulations performed with

Balsara switch.

In order to quantify our findings, the effective viscosity (ν_{sph}), Reynold's number (Re), extracted growth rates (n_c), and the corresponding errors are reported in Table 5.7. We confirm that without a Balsara switch the growth rate is sensitive to α_{AV}. In particular, a negative growth rate (i.e. decay) is observed for $\alpha_{AV} \geq 0.5$. A comparison of data in Table 5.8 indicates that the utilisation of a Balsara switch generates growth rates that are essentially independent of the choice of α_{AV}. In order to understand this behaviour, we examine the Balsara factor f_i in the context of the initial velocity profiles. Firstly, recall the Balsara switch f_{ij} measures the relative strength of compression versus vorticity for each SPH particle pair. Secondly, the initial velocities profile (5.5)-(5.6) is constructed such that particles away from the interface $y_o = H/2$ have similar horizontal and vertical velocities. During the linear regime, the relative velocities are approximately zero everywhere except near the interface. Hence, the Balsara switch as well as the viscosity term Π_{ij} diminish outside the velocity transition layer $|y_i - y_o| > L_u$. At this point the flow behaves as inviscid everywhere, except near the interface where the artificial viscosity is active to prevent particle interpenetration. Therefore it is not surprising that the expected growth rates are in better agreement with analytical predictions based on the assumption of inviscid and incompressible fluids [5, 7]. For example, comparing the extracted growth rates for standard artificial viscosity simulations (see Table 5.7) with the smoothed profile growth rate $n_{c,smooth} = 4.8$ gives an average absolute error of $\langle \Delta n_{c,smooth} \rangle = 5.8$, and average relative error of $\langle \eta_{smooth} \rangle = 121\%$. However, with the utilisation of a Balsara switch (see Table 5.8), the average absolute error $\langle \Delta n_{c,smooth} \rangle$ reduces from 5.8 to 1.3. Similarly, the average relative error $\langle \eta_{smooth} \rangle$ reduces from 121% to 27%.

The results with Balsara switch (see Table 5.8) further suggest that the extracted growth rates are in better overall agreement with the smoothed profiles

in Wang et al. [7] ($n_{c,smooth} = 4.8$) than the classical growth rate given in [5] ($n_{c,classical} = 6.0$). In addition, we would like to point out that previous articles [64, 109, 138, 153] compared the extracted growth rates for sharp interface profiles although smoothed initial conditions are used to setup the simulations. As we have illustrated, the presence of thickness velocity and density transition layers (i.e. $L_{\rho,u} > 0$) reduces the relative velocity between vertical layers, resulting in a smaller growth rate. Therefore we do not advise comparing SPH results obtained with smoothed initial profiles with the analytical growth rate for sharp initial profiles. Instead, a more sensible comparison can be made by comparing the extracted growth rate with the linear growth rate for smoothed initial profiles obtained from equation (2.33) in chapter 2.

α_{AV}	ν_{sph}	Re	n_c	$\Delta n_{c,classical}$	$\Delta n_{c,smooth}$	$\eta_{classical}$	η_{smooth}
0.125	3.10×10^{-4}	803	2.2	3.8	2.6	63	54
0.25	6.21×10^{-4}	401	1.0	5.0	3.8	84	80
0.5	1.24×10^{-3}	200	-1.5	7.5	6.3	125	132
1.0	2.42×10^{-3}	100	-2.8	8.8	7.7	148	160
2.0	4.97×10^{-3}	50	-3.8	9.7	8.6	164	179

Table 5.7: The fitted growth rates during the initial linear stages development for different viscosity parameters for simulations with standard artificial viscosity and no Balsara switch. The artificial viscosity parameters α_{AV} (1^{st} column), the kinematic viscosities (ν_{sph}) (2^{nd} column), the Reynold's number (Re) (3^{rd} column), the extracted growth rates (n_c) (4^{th} column), the absolute errors ($\Delta n_{c,classical}$, $\Delta n_{c,smooth}$) ($5^{th} - 6^{th}$ column) and the relative errors ($\eta_{classical}$, η_{smooth}) [%] ($7^{th} - 8^{th}$ column).

α_{AV}	n_c	$\Delta n_{c,classical}$	$\Delta n_{c,smooth}$	$\eta_{classical}$	η_{smooth}
0.125	3.5	2.5	1.3	41	27
0.25	3.5	2.4	1.3	41	26
0.5	3.5	2.4	1.3	41	26
1.0	3.5	2.5	1.3	42	27
2.0	3.4	2.6	1.4	43	29

Table 5.8: The fitted growth rates during the initial linear stages development for different viscosity parameters for simulations with standard artificial viscosity and Balsara switch. The artificial viscosity parameters α_{AV} (1^{st} column), the extracted growth rates (n_c) (2^{nd} column), the absolute errors ($\Delta n_{c,classical}$, $\Delta n_{c,smooth}$) ($3^{rd} - 4^{th}$ column) and the relative errors ($\eta_{classical}$, η_{smooth}) [%] ($5^{th} - 6^{th}$ column). The kinematic viscosity and Reynold's number are the same as those listed in Table 5.7.

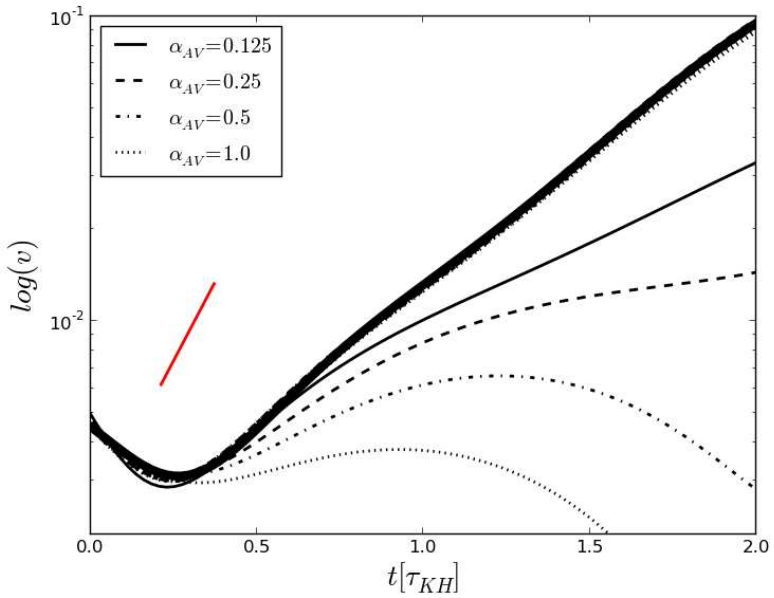

Figure 5.24: Vertical velocity amplitude for different values of the conventional Monaghan artificial viscosity (as indicated) and with/without the Balsara switch (thick/thin lines). The slope of the classical inviscid solution presented in [5] is plotted in red.

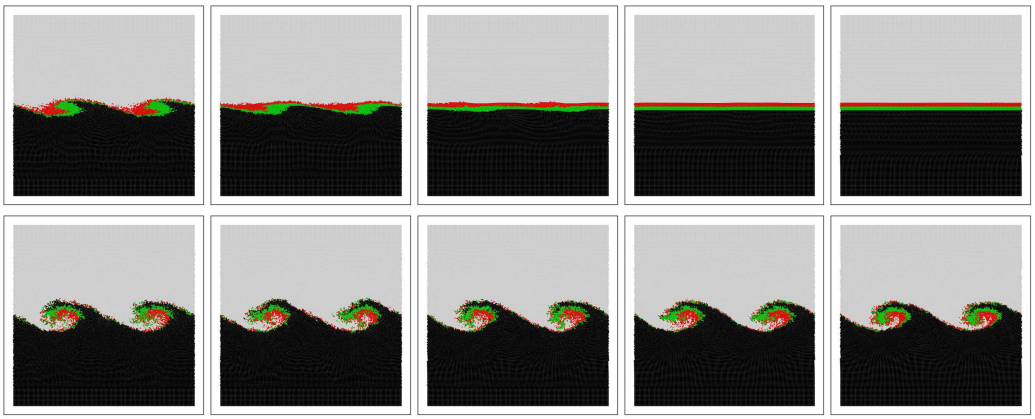

Figure 5.25: Numerical results generated by different indicated artificial viscosity parameters, α_{AV}, plotted at $t = 2.5$. The top row corresponds to results that utilised the conventional artificial viscosity without a Balsara switch, and the bottom row corresponds to the results generated with the combined use of a Balsara switch and conventional artificial viscosity.

5.6.4 Dependence on Gradient Richardson number

The gradient Richardson number is a useful way of quantifying the influence of buoyancy in a stratified shear flow simulation. In order to study the gradient Richardson number dependence, we simulate the stratified instability for $Ri_g =$

$0.1 - 0.5$ measured as illustrated in Figure 5.18. The width of the smoothed density interface is fixed at $L_\rho = 0.01L$, with other parameters such as the α_{AV}, global resolution N and local smoothing parameter κ being same as the fiducial model. The numerical results corresponding to different gradient Richardson numbers are plotted in Figure 5.26. A visual inspection of the numerical results suggests an increase in Ri_g corresponds to a less pronounced instability. Recall that the larger the gradient Richardson number Ri_g, the stronger the influence of gravity (which is damping the system), and the weaker the kinetic energy which is acting to destabilise the system. The extracted vertical velocity amplitude during the linear regime are plotted in Figure 5.27. Inspecting the results, we found that the fluid system remains stable for $Ri_g > 0.3$ where a negative growth rate (i.e. decay) is obtained (see Table 5.9, column 3). Although the critical growth rate are in general agreement with the inviscid sharp-interface hydrodynamic theory (i.e. $R_{ig,c} \sim 0.3$ herein, whereas $R_{i,c} = 0.25$ [88],[207]), the SPH growth rates are found to be heavily suppressed for large gradient Richardson number compared to analytical growth rates in [5, 7] (see Table 5.9, column 5-8).

Ri_g	D	n_c	$n_{c,smooth}$	$\Delta n_{c,classical}$	$\Delta n_{c,smooth}$	$\eta_{classical}$	η_{smooth}
0.1	0.115	3.5	3.4	2.5	0.09	42	3
0.2	0.081	1.7	2.9	4.2	1.1	71	40
0.3	0.066	0.67	2.6	5.3	1.9	88	73
0.4	0.057	−0.09	2.4	6.1	2.5	101	103
0.5	0.052	−0.51	2.2	6.5	2.7	108	123

Table 5.9: The fitted SSI growth rates during the initial stages for simulations with different Richardson numbers. Listed are the gradient Richardson number parameter (1^{st} column), the length scale ratio (D) (2^{nd} column), the extracted growth rate (n_c) (3^{rd} column), the analytical growth rate for smoothed initial conditions ($n_{c,smooth}$)(4^{th} column), the absolute errors ($\Delta n_{c,classical}$, $\Delta n_{c,smooth}$) (5^{th}-6^{th} column) and the relative errors ($\eta_{classical}$,η_{smooth}) given as percentages (7^{th}-8^{th} column).

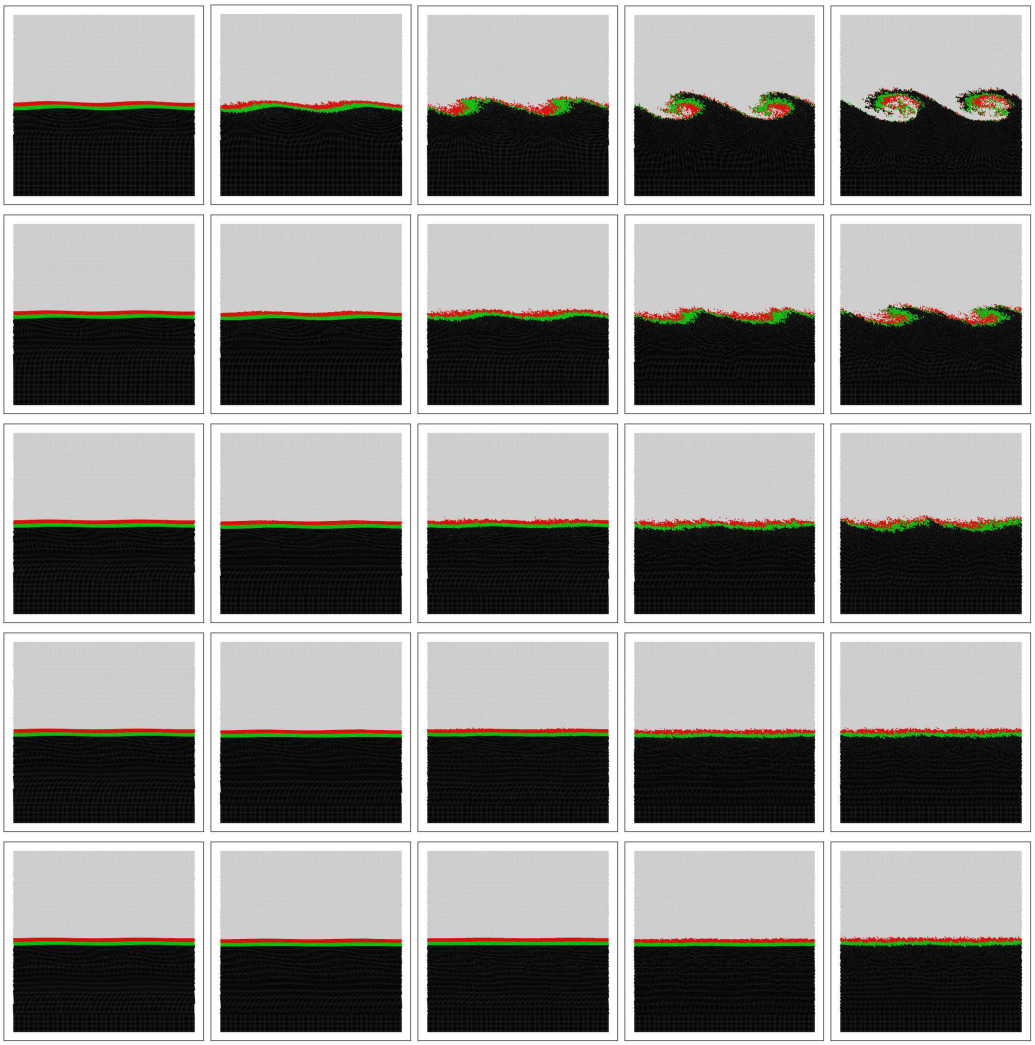

Figure 5.26: Numerical results for different initial gradient Richardson numbers from $Ri_g = 0.1 - 0.5$ (top to bottom) within the time interval $t = 1 - 3$, with a fixed increment of $\Delta t = 0.5$ plotted from left to right. Particles correspond to the initial vertical positions near the interface ($|y_i - y_o| \leq 4d_{nat}$) are coloured to illustrate the evolution of inter-facial particles during the instability.

5.6.5 Dependence on Atwood number

To finalise our study, we consider a case study to investigate the influence of the Atwood number, focussing on the simulation of three Atwood numbers, namely $A_T = 0.\bar{3}, 0.\bar{6}, 0.\bar{8}$ for $Ri_g = 0.1$ and $Re = 200$. These Atwood numbers correspond to density ratios of 2, 5 and 8 respectively. The numerical results are plotted in Figure 5.28, and the single-phase ($A_T = 0$) results are also presented for completeness. As expected, the growth rate of the induced KHI decreases

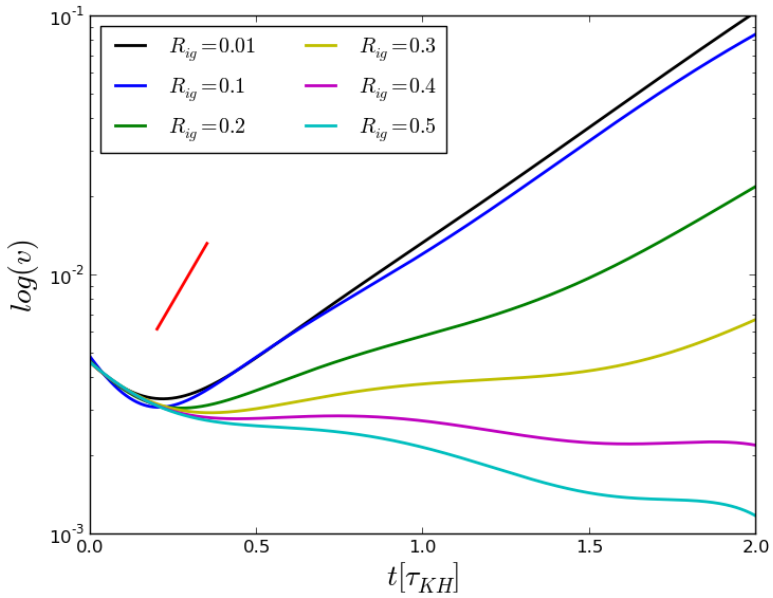

Figure 5.27: Vertical velocity amplitude for different Richardson numbers as indicated.

with increasing density ratio between the two fluid layers. In addition, we found the result exhibit remarkable qualitative differences: firstly, the roll-up behaviour of the instability is more pronounced for low Atwood number (i.e. $A_T = 0.\bar{3}$) than for the larger Atwood number simulations. Secondly, in the large Atwood number simulations the destabilising effects of velocity shear cannot successfully overcome the stabilising effect caused by gravity. Hence, the bulk movement of the fluid did not result in the conventional roll-up behaviour observed in the $A_T = 0.\bar{3}$ simulation. Instead, the velocity shearing between the fluid layers manifested itself by stripping of heavier fluid particles away from the interface (see Figure 5.28, $A_T = 0.\bar{8}$), resulting in the formation of ligaments as the up-rising heavier fluid penetrates into the lighter ambient fluid. However, we think it is likely that the ligaments in the high density ratio $A_T = 0.\bar{8}$ simulation are caused by the spurious pressure gradient. It is because for the multi-mass initial conditions, the mass ratio is proportional to the density ratio; therefore, an increase in density ratio introduces a mass discontinuity which lead to the error

in the density estimate for the smoothed-pressure SPH variants [109, 156, 157]. In fact, our results indicate pseudo-consistent SPH suffers from similar problems for resolving high density ratio shear flows. However, the mass discontinuity can be resolved using mass flux switching technique introduced in Read and Hayfield [153].

Comparison of the growth data in Table 5.10 indicates both the absolute (6th column) and relative error (8th column) decreases for higher Atwood number. We suspect this is primarily due to the overall decrease in growth rate for large Atwood number. Note that both sharp and smoothed linear growth rates decrease for larger Atwood number, as the kinetic energy from velocity shear becomes significantly smaller than the potential energy which stabilises the fluid system.

A_T	n_c	$n_{c,smooth}$	$n_{c,classical}$	$\Delta n_{c,classical}$	$\Delta n_{c,smooth}$	$\eta_{classical}$	η_{smooth}
$0.\bar{3}$	3.8	3.4	6.0	2.1	0.46	36	13.6
$0.\bar{6}$	3.4	3.3	4.8	2.00	0.080	29	2.41
$0.\bar{8}$	3.0	2.9	3.8	0.78	0.0088	21	0.31

Table 5.10: The fitted growth rates during the initial stages of the KHI for different Atwood number. Given are the Atwood number (1^{st} column), the extracted growth rate (n_c) (2^{nd} column), the analytical growth rate for smoothed initial conditions ($n_{c,smooth}$) (3^{rd} column), the classical growth rate ($n_{c,classical}$) (4^{th} column), the absolute errors ($\Delta n_{c,classical}$, $\Delta n_{c,smooth}$) (5^{th}-6^{th} column) and the relative errors ($\eta_{classical}$,η_{smooth}) given as percentages (7^{th}-8^{th} column).

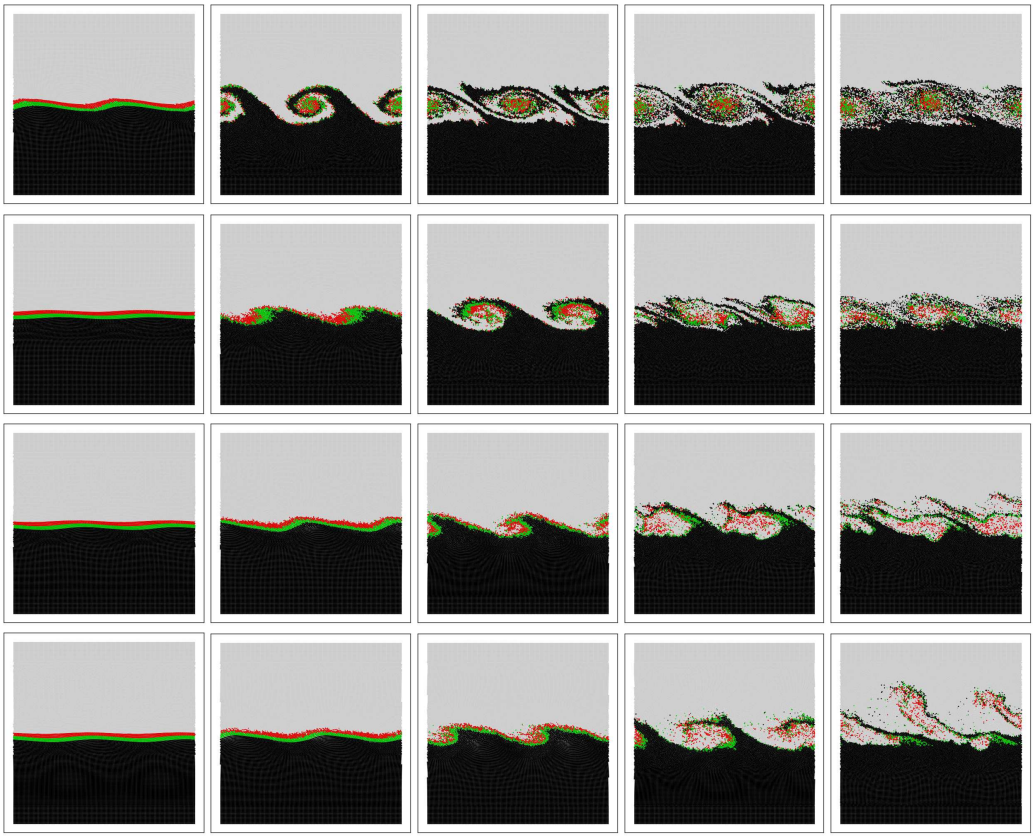

Figure 5.28: Numerical results for different Atwood numbers plotted at times between $t = 1\text{s} - 5\text{s}$, where $Ri_g = 0.1, Re = 200$. From top to bottom, $A_T = 0.0$ (1st row), $A_T = 0.\bar{3}$ (2nd row), $A_T = 0.\bar{6}$ (3rd row) and $A_T = 0.\bar{8}$ (4th row).

5.7 Summary

The Kelvin-Helmholtz instability between two superposed fluids was simulated by means of the pseudo-consistent multiphase scheme. The analysis conducted was divided into two parts, the first part studies the idealised KHI without taken into consideration the damping effects of gravity, and the second part focusses on the evolution of KHI subjected to gravitational effects, known as the stratified shear instability.

A series of numerical simulations was carried out to investigate the effective viscosity in the SPH simulations. Despite the differences in the kernel function, multiphase treatment and momentum equation employed, our findings are in good agreement with previous research [64, 149]. That is, the growth of the KHI is strongly dependent on the artificial viscosity parameter utilised. In addition, a linear relationship was found between the artificial viscosity parameter α_{AV} and the effective viscosity with a slope of 0.147. The use of Balsara switch reduces the slope from 0.147 to 1.68×10^{-4}. Furthermore, the growth of the KHI exhibits a very weak dependence on artificial viscosity parameter β_{AV}, with the linear dependence between β_{AV} and effective viscosity found to be 5.22×10^{-3}. The maximum Reynold's number estimated herein is $Re \sim \mathcal{O}(10^1)$ suggesting the flow problems considered are well within the laminar regime. Therefore, we conclude that the utilisation of a Balsara switch is crucial to the success of modelling inviscid KHI in SPH. Furthermore we would encourage further comparison on shear flows such as KHI using modern switch techniques available literature [152, 153, 219].

In the first part of this chapter we focussed on the KHI for a density ratio of two, there are two potential limitations for the present pseudo-consistent weakly-compressible multiphase method. Firstly, the differential form density estimate based on the SPH continuity equation is suitable for low Mach number problems

[62, 166, 167]. Secondly, the multi-mass approach is not suitable to high density ratios. It is because in a multi-mass approach, the density ratio is proportional to the mass ratio of the particles. Hence, the kernel density estimate are biased against the heavier particles which may potentially affects the accuracy of kernel density estimates in SPH. In fact, we would advise the use of either a switch technique [110, 153] or interface stabilisation model [167, 170] for high density ratio shear flows.

The effects of the local resolution parameter κ were also investigated numerically. It was found that during the linear regime, a larger local resolution parameter results in a more accurate growth rate [7] as well as a regularised interface. Nonetheless, the utilisation of large κ in combination with multi-mass SPH particles limits the capability of resolving fine scale structures that are less than $\sim 2h$. For example, the occurrences of instabilities within the core region of the cat-eye vortices are not well resolved in the presented simulations. Finally, the evolution of the KHI for different velocity and density gradients was studied systematically. For the sharp density, finite velocity gradient cases ($L_u = 0, L_\rho > 0$), the simulations are in good agreement with the analytical prediction, with the average relative error of $\langle \eta_{smooth} \rangle = 12\%$. Similarly, the sharp velocity, finite density gradient cases ($L_\rho = 0, L_u > 0$) had an average relative error of $\langle \eta_{smooth} \rangle = 17\%$. The generalised scenario where both velocity and density transition layers are of finite width ($L_{u,\rho} > 0$) was also studied. The smoothed initial density distribution reduces the local density ratio between each successive layer, where the simulation results were found to have an average relative error of $\langle \eta_{smooth} \rangle = 11\%$.

Based on the knowledge acquired from the idealised KHI simulations, we investigated the development of a multiphase stratified shear instability (a KHI between two fluids of different densities under the influence of a gravitational field). Motivated by recent analytical theory [7, 65, 66] and numerical simu-

lations [58, 108], smoothed initial velocity and density profiles were utilised to study the SSI. The influence of numerical resolution, kinematic viscosity (effective Reynold's number), gradient Richardson number, and Atwood number were studied systematically. Similar to the results from the idealised KHI, we found that the growth rate of the SSI is largely independent of the SPH viscosity parameter α_{AV} when a rotation preserving Balsara switch is used. The numerical results also suggest both the global and the local resolution play a role in the growth of the shear instability. At the highest global resolution considered (i.e. $N = 400$), the extracted growth rate is $n_c = 4.2$ with an relative error of $\eta_{smooth} = 13\%$. Whereas for a fixed global resolution of $N = 200$, the highest local resolution simulation (i.e. $\kappa = 2.33$) yields a growth rate of $n_c = 4.0$, with the corresponding relative error of $\eta_{smooth} = 16\%$. We conclude that the convergence of SPH to the expected analytical result for a smoothed initial density and velocity profile is achieved with increasing resolution.

A series of simulations was conducted to investigate the influence of Richardson number. As expected, the growth rate decreases with increasing gradient Richardson number, as the higher velocity gradient L_u corresponds to less kinetic energy to overcome the stabilisation effects of stratification. For the particular set of parameters considered herein, the growth of the instability was observed for Richardson number up to $Ri = 0.3$. It is worthwhile mentioning that the growth of the instability depends not only on the Richardson number, but also depends on the velocity and density distribution of the base-flow [63, 214]. As a final remark, we suggest an in depth study of the thickness of the initial transition layers and their influence in the non-linear evolution of the stratified shear instability. Finally, we undertook a case study into the effect of varying the Atwood number, which quantifies the density contrast between the two fluids. It was found that for density contrasts of 10 (and Atwood number of $0.\bar{8}$) the development of the KHI is qualitatively different with ligatures of the high density fluid forming.

Even so, the growth rate of the instability is broadly in line with the analytic prediction which also slows with increasing Atwood number due to the relatively increased influence of gravity.

We conclude that a carefully constructed implementation of SPH can be readily used to model the onset and late-time development of the KHI instability in the presence of a gravitational field and between fluids of somewhat different densities. The growth rate of the instability is close to that predicted by analytical theory that includes the effect of a smoothed density transition in both density and velocity between the two layers. While the presented computational algorithm is implemented in a cell-linked list SPH code, in theory the numerical scheme proposed is also suitable for a tree-SPH code implementation. In fact, we would suggest a comparison between the multi-mass approach utilised herein and the alternative equal-mass (constant number of neighbours) setup employed elsewhere in the literature as it is unclear which SPH scheme is best suited to multiphase problems. For example, at room temperature the density ratio of water-air is of $\mathcal{O}(10^3)$. The equal-mass SPH setup therefore requires approximately 1000 water particles for each air particle. Whereas, the multi-mass SPH setup requires the mass ratio between the particles of the different phases, $m_{water}/m_{air} = 1000$. Nonetheless, this implies the small-scale motions occurring near the interface will be encapsulated into the motion of a single water particle. Thus, the utilisation of multi-mass SPH particles may suffer from the limitations of deficient resolution scale for fine-scale motions.

Chapter 6

Rayleigh-Taylor Instability

6.1 Introduction

The proper modelling of Rayleigh-Taylor instability is important in many fluid dynamical simulations. Previous work on RTI with mesh-based methods encountered problems in modelling the vast morphological variations of the interface in the non-linear regime and, hence, several research groups have started exploring alternative methods. This chapter presents the simulation results of single and multi-mode RTI. Single-mode RTI is used to validate the SPH model against the analytical growth rate in the early linear stage and against the drag-buoyancy model at the non-linear stages of the RTI.

This chapter is organised as follows: section 6.2 provides a survey of literature regarding to the numerical simulation and experiential work of RTI. Section 6.3 discusses the physical models from literature used in our validation cases. The numerical results for single and multi-mode SPH, including comparison with analytical and experimental results are presented in section 6.5. The major research findings are summarised in section 6.6.

6.2 Literature review

Rayleigh [78] and Taylor [79] were the first to study the instability of two immiscible and incompressible fluids subjected to acceleration, therefore the Rayleigh-Taylor instability (RTI) is named after them. Following Sharp [220], the evolution of a single-mode RTI can be divided into three stages: during the first stage, the dynamic amplitude of the perturbation is small compared to its wavelength, and its growth is accurately modelled by linear stability theory. In the second stage, the formation of the bubbles due to the uprising light fluid and a jet-like spike caused by the sinking heavy fluid occurs as the two fluids interchange position (c.f. Figure 6.1). When the amplitude becomes comparable to the perturbation wavelength, linear growth rate given in chapter 2 is no longer valid. In the third stage, the RTI can be described by the drag-buoyancy model [68, 69, 70], where the bubbles and spike are considered as separate entities. The balance between drag and buoyancy force then provides an estimate of the terminal velocities of the bubbles and spike. During this stage additional fine structures appear. In the absence of ablative effects, material diffusion, and surface tension, the bubble and spike evolution is characterised by two parameters namely, the Atwood number and the Reynolds number $Re = \sqrt{Lg}L/\nu$ [221], where L is the width of the domain. Recent experimental work [222] suggests that for low Atwood numbers and high Reynolds numbers the shear motion between the fluids leads to secondary KHIs. Whereas the RTI for large Atwood numbers is dominated by buoyancy effects.

While the single-mode RTI serves as a simplified model and benchmark test, more realistic RTI scenarios may involve a spectrum of superimposed waves. In multi-mode RTI, each perturbation frequency has an unique growth rate, leading to a multiple of RTI bubbles and spikes. Recent work suggests that the interaction between different RTI modes may be responsible for transition

into turbulence, which is one of the frontier topics in fluid dynamics that is currently under active investigation [223, 224, 225]. However, finding an analytical solution that encapsulates the coupling between RTI modes is extremely mathematical challenging [226]. Therefore, direct comparison of experiments, simulations and analytical solutions is uncommon in the literature. Instead, the comparison between experiments and simulations is made using the self-similar scaling relationship of the bubble-front $h_b = \Theta A_T g t^2$, where Θ is a constant of proportionality.

Apart from the theoretical developments discussed in chapter 2, the RTI has also been investigated experimentally. Cole and Tankin [227] studied the single-mode RTI at a water-air interface by means of acoustic perturbation of the fluid interface. To circumvent the difficulties in measuring the initial perturbation height in experiments, the authors proposed a fitted curve method that compares the dispersion relation for the experimental data with analytical theory and found good agreement with linearised theory up to second order perturbation. Andrews and Spalding [73] conducted experiments on two-dimensional RTI at $A_T = 0.08$. The experiments included multi-mode RTI, where the fluids are placed in a vertical tank with a horizontal axle placed at the middle of the tank, and the instability is triggered by tilting the tank. The authors studied the effects from different tilt angles and Rayleigh-Taylor induced mixing between fluids. Their experimental results confirm the self-similar scaling law of the bubble front by Youngs [71, 72] with the measured constant of proportionality of $\Theta = 0.04$.

The RTI has also been investigated by means of numerical simulations. For conventional numerical methods, RTI poses serious challenges due to the vast morphological variations in the non-linear regime. Glimm et al. [74] reviewed mesh-based methods and showed that in many cases, extensive use of mesh refinement and interface tracking routines lead to additional computational complexity for resolving RTI. Further, the authors pointed out that the discrepan-

cies between reported simulation results from various research groups originate from the mass and viscosity diffusion properties in mesh-based methods. Thus, some researchers migrated towards mesh-free methods for simulating RTI. For instance, Moscinski et al. [228] conducted molecular dynamics simulations for RTI, whereas Nie et al. [229] proposed a multiphase Lattice Boltzmann method to simulate the two-dimensional RTI.

There have been numerous attempts to simulate RTI with mesh-free methods. Cheng et al. [230] introduced the MPS method to simulate RTI between two fully incompressible fluids and reported a good agreement between their simulations results and the linear growth rates. Furthermore, features observed in experiments such as formation the of bubbles and the stripping of particles at the edges of the spike are also presented in their work. Shadloo et al. [231] simulated the single-mode RTI using ISPH with primary attention to the role of surface tension, which has been implemented using a SPH version of the continuum surface force [232]. They conducted a parametric study to evaluate the damping effects of surface tension and found that (i) surface tension suppresses the growth of RTI, and (ii) the initial particle distribution significantly influences the symmetry of the instability along the vertical direction and (iii) their surface tension model accurately recovers the Young-Laplace pressure of a droplet. Furthermore, while focussing on the effects of surface tension and initial particle distribution, their work did not investigate the effects of density ratios, viscosity and how the inherent smoothing properties from SPH may potentially influence the final numerical solution.

6.3 Validation models from literature

This section focusses on the models in the literature which describes the later stages of the RTI, namely the drag-buoyancy model for single-mode RTI and

the self-similar scaling law for the more realistic multi-mode RTI. These models will be used in conjunction with the linear analytical growth rate presented in chapter 2 as benchmarks in their respective regimes for the simulation results presented in section 6.5.

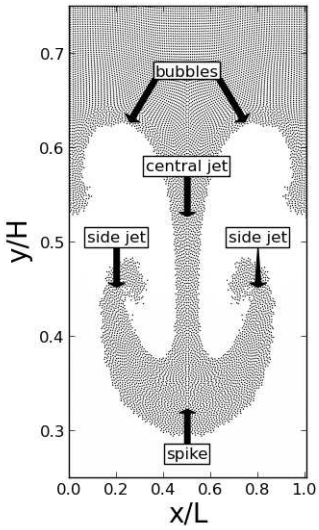

Figure 6.1: Features of single-mode RTI instability. The development during the nonlinear stage results in two bubbles, a down-falling spike which comprises of three jets. The left and right jets are caused by the secondary KHI roll-up, and the central jet is by the down-falling of the heavy fluid due to gravity.

6.3.1 Non-linear regime: Drag-Buoyancy Model

When the dynamic amplitude of the same order to the perturbation wavelength, the RTI enters the nonlinear regime where the stability theory is no longer valid. Figure 6.1 shows the structure of a single-mode RTI during the nonlinear regime. The RTI has developed into a mushroom shape, with the formation of two bubbles and one spike in the axis of symmetry at $x = 0.5L$. The onset of KHI causes the edges of the heavy fluid spike to roll-up and form two jets at the sides of the spike.

To capture the late-time behaviour of the RTI, researchers have devised the drag-buoyancy model [68, 70, 71]. The model considers the bubbles and spike as

separate entities. The equation of motion of the bubble has the form,

$$(\rho_2 + C_A\rho_1)\,\Lambda\frac{dv}{dt} = -\rho_1 v^2 C_D\lambda + (\rho_1 - \rho_2)\,\Lambda|\vec{g}|. \tag{6.1}$$

Similarly, the equation of motion of the spike has the form

$$(\rho_1 + C_A\rho_2)\,\Lambda\frac{dv}{dt} = -\rho_2 v^2 C_D\lambda + (\rho_1 - \rho_2)\,\Lambda|\vec{g}|, \tag{6.2}$$

where $\rho_1 > \rho_2$, C_A and C_D are the added mass coefficient and drag coefficient, v is the vertical velocity, λ is the perturbation wavelength, and Λ is the volume. Starting from the left hand side of the equation (6.1) and (6.2), the first term represents the fluid inertia of the corresponding feature, the second term represents the added mass of the surrounding fluid. The third and fourth terms represent the Newtonian drag and buoyancy force. Assuming the bubbles and spike have the same added mass coefficient and drag coefficient, the terminal velocities of the bubble (v_b) and spike (v_s) are then explicitly given by

$$v_b = \sqrt{\frac{2A_T}{1+A_T}\frac{|\vec{g}|\lambda}{C_D}} \quad , \quad v_s = \sqrt{\frac{2A_T}{1-A_T}\frac{|\vec{g}|\lambda}{C_D}}. \tag{6.3}$$

The average velocity of the bubble and spike velocity then follows the relation

$$v_{ave} = \Gamma\left[\sqrt{\frac{\pi|\vec{g}|}{k}\frac{A_T}{1+A_T}} + \sqrt{\frac{\pi|\vec{g}|}{k}\frac{A_T}{1-A_T}}\right], \tag{6.4}$$

where $\Gamma = C_D^{-1/2}$ is a constant of proportionality. The drag-buoyancy model has received significant attention and validation in the literature. In particular, the constant of proportionality Γ is often reported in comparisons between simulation and experiments. Alon et al. [67] found the constant of proportionality of the average velocity to be $\Gamma = 0.22$ independent of A_T. Layzer [68] analysed the limiting case $A_T = 1$ using potential flow analysis and showed that the drag coef-

ficient in two-dimensions is $C_D = 6\pi$ or equivalently $\Gamma = 0.23$. Their results were later confirmed by Ramaprabhu et al. [233] using various mesh-based codes. Furthermore, Waddell et al. [234] reported the estimated constant of proportionality for the average velocity from empirical experiments to be $\Gamma = 0.217 \pm 6.0 \times 10^{-3}$.

6.3.2 Multi-mode RTI scaling

Parallel to the developments in single-mode RTI, the multi-mode RTIs has received significant attention in the late 20^{th} century. In multi-mode RTI, the bubbles of different sizes undergo complex interactions, such as competition and merging during the nonlinear regime. Youngs [72] found the dynamic height of the multi-mode RTI bubble can be described by a self-similar relation

$$h_b(t) = \Theta A_T |\vec{g}| t^2, \tag{6.5}$$

where $h_b(t)$ defined as the dynamic height of the bubble and Θ is a constant of proportionality. The self-similarity relation is motivated by both experiments and numerical simulations: using mesh-based simulations, Youngs [71, 72] found $\Theta = 0.04 - 0.05$. Glimm et al. [74] compared the reported Θ in the literature and argued the numerical diffusion effects in mesh-based simulations are responsible for the discrepancies between the Θs obtained by different research groups. Andrews and Spalding [73] conducted a series of two-dimensional experiments and found $\Theta = 0.04$. The constant of proportionality extracted from SPH results will be compared against the values reported in the literature in section 6.5.3.

6.4 Initial Conditions

The single-mode RTI is simulated in a semi-confined geometry. The fluid domain is $x \in [0, L], y \in [0, H]$, where the aspect ratio is $L/H = 1 : 4$. The initial

perturbation of the fluid interface is given by

$$\eta(x) = \epsilon_o \cos(kx) + \frac{H}{2}, \tag{6.6}$$

with initial amplitude $\epsilon_o = 0.1L$ and wave number $k = 2\pi/L$. The dynamic amplitude $a(t)$ is given by the half distance between the crest and trough of the perturbed mode that grows with time. To impose a no-slip condition, static ghost particles are introduced at the left, right and bottom of the domain. The initial pressure is prescribed by the piecewise pressure profile

$$P(x,y) = \begin{cases} \rho_2\, g\, [\eta(x) - y] + \rho_1\, g[H - \eta(x)] & y < \eta(x) \\ \rho_1\, g\, (H - y) & y \geq \eta(x) \end{cases}. \tag{6.7}$$

The initial density of the fluid particles is computed from the Tait equation of state. Finally, the mass of SPH particles is then given by product of the initial densities and the initial volume of the particles. The single-mode RTI is simulated for three Atwood numbers: $A_T = 0.\bar{3}$, $0.\bar{6}$ and $0.\bar{8}$, where the base density of the heavier fluid is kept at $\rho_{o,1} = 10^3 \text{kg/m}^3$ in all cases.

6.5 Results and Discussion

The simulation results for both the single-mode and multi-mode Rayleigh-Taylor instability are presented in this section. To validate the SPH model, the simulation results are subjected to quantitative comparison against the models in literature discussed in chapter 2 and section 6.3. In particular for the single-mode, we compare the early-stage results with linear stability theory and the late-stage results with the drag-buoyancy model [68, 70, 71]. For the multi-mode RTI, we compare our results with the bubble front predictions from Youngs [71, 72] and those reported in Andrews and Spalding [73].

6.5.1 Data Extraction and Analysis

In order to validate the results quantitatively, we extract the growth rate (n_c) and the terminal vertical velocities of bubble (v_b) and spike (v_s) from the RTI simulation data. The extraction of growth rate is a three-step process:

1. The dynamic amplitude $a(t)$ is extracted from the simulation data by taking half the distance from the peak to trough positions at each time-snapshot.

2. The extracted amplitudes are fitted to the bi-exponential function (Equation (2.30) in chapter 2) using a least-squares algorithm to obtain the growth rates (n_c).

3. The growth rates are then substituted into the dispersion relation (Equation (2.28) in chapter 2) to determine the effective kinematic viscosity in each SPH simulation.

The comparison between fitted viscous growth rates and inviscid growth rates then shows how the SPH viscosity suppresses the growth of the RTI. Furthermore, two methods are introduced to evaluate the terminal velocities of the bubbles and spikes. The *direct extraction method* determines the velocity for the corresponding features from the positions of the SPH particles that represents at the frontal area. That is, the bubble (spike) velocity is defined by the vertical velocity of the low (high) density SPH particle which has the maximum (minimum) y-component during each time-step. In contrast, the *fitted amplitude slope method* extracts the velocity from the linear fit of the positions of the intermediate stage of the corresponding feature. The slope of the linear fit then provides a measure for the terminal velocity of bubble (spike) in each SPH simulation.

6.5.2 Single-mode Rayleigh-Taylor Instability

Three major parameters may influence the RTI simulation results: the density ratio (Atwood number), the artificial viscosity (Reynolds number), and the numerical resolution (i.e. global resolution N_p, and the local resolution κ). Each of these will be investigated in the following sections in comparison to our fiducial reference model.

Fiducial Model

Our fiducial model for Atwood number $A_T = 0.\bar{3}$, $\alpha_{AV} = 0.1$, $Re = 100$, $\kappa = 2.33$ and $d_{nat} = 0.01$, with a total of $N_p = 4.92 \times 10^4$ particles. Figure 6.2 shows the time evolution of the RTI. The perturbed interface starts growing as soon as the simulation begins. The numerical solution then departs from the linear regime at $t \sim 1.2$ as the heavy and light fluid interchange position. At later times $t \gtrsim 1.5$, the development of bubbles become more apparent as the light density fluid gradually rises towards the top of the vertical domain due to buoyancy. A spike is formed around the plane of symmetry at $x = 0.5L$ the heavy fluid sinks towards the bottom of the domain. During $3.0 \lesssim t \lesssim 4.5$, the spike evolves into a mushroom shape, as the onset of KHI at the side jets results in two secondary vortices. During $4.5 \lesssim t \lesssim 6.0$, the RTI has emerged into the fully non-linear regime, where the vortices at the sides of the spike evolve into elongated jet-like structures. At $t \gtrsim 6.0$, additional KHI modes appear at the edges of the spike, leading to additional vortices at the sides of the RTI spike. Finally, at $t \sim 7.5$ the RTI spike has fully developed, resulting in three jets: the central jet at $x = 0.5L$ which remains well collimated and two side jets spike dominated by the shear between fluid layers.

The development of the RTI is in qualitative agreement with the time evolution reported in the particle simulation literature such as Figure 7 in Shadloo et al. [231] obtained using ISPH and Figure 4 in Jeong et al. [217] obtained by

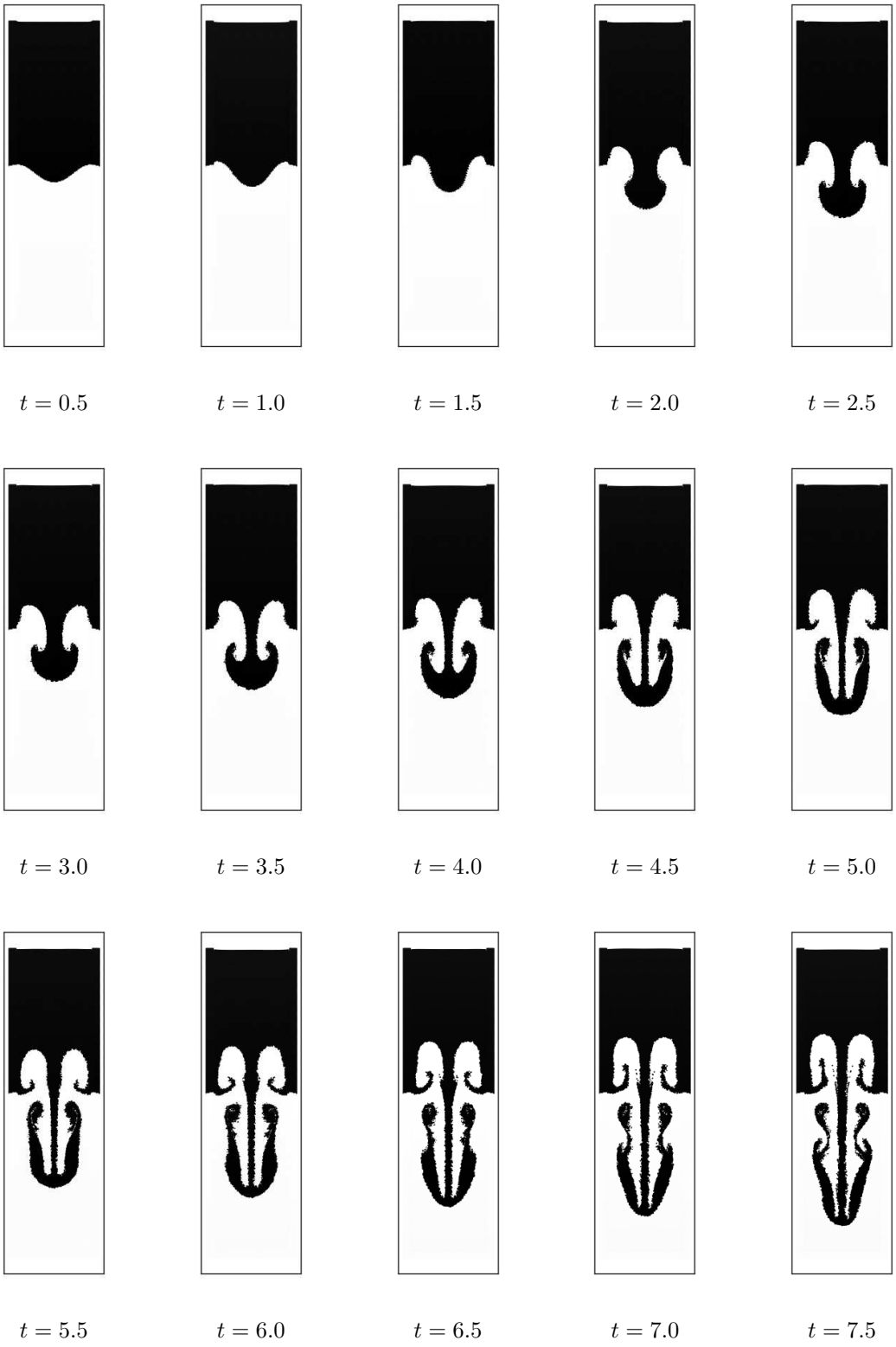

Figure 6.2: The evolution of single-mode RTI for our fiducial model plotted at the times indicated. The time is measured in units of $\sqrt{L/g}$.

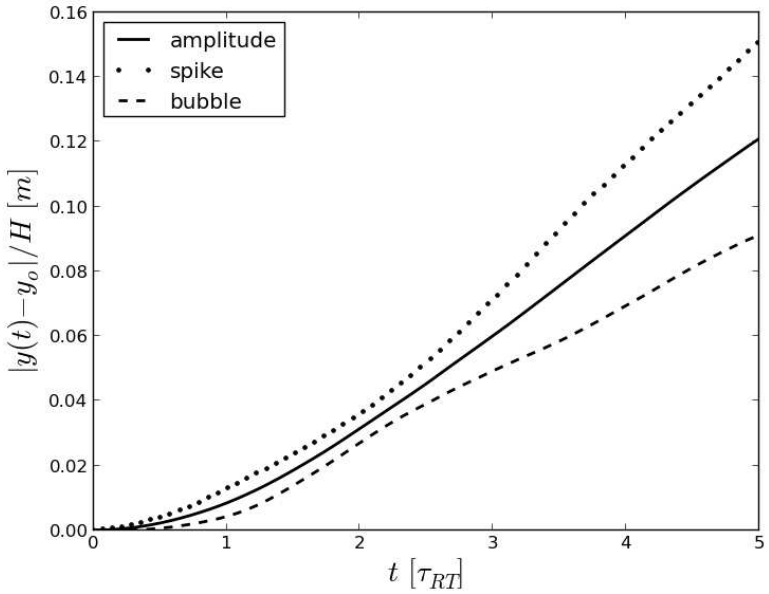

Figure 6.3: Time evolution of the amplitude, spike and bubble relative to their original position for $A_T = 0.\bar{3}$. The overall increase in amplitude is caused by the formation of spike as the heavier fluid accelerated towards the bottom of the computational domain.

means of MPS. Though with the current resolution ($d_{nat} = 0.01$), our method resolves the secondary KHIs much better than Jeong et al. [217] ($d_{nat} = 0.02$). However, some differences are observed when comparing SPH and mesh-based simulations (see Sahu and Vanka [221], Figure 2-4) as the evolution of KHI in the mesh-based simulations appears to be much more pronounced. We suspect these differences are caused by the combination of different resolution (49200 SPH particles vs. 169092 grid cells) and artificial viscosity ($Re_{\text{eff}} = 100$ vs. $Re = 256 - 2048$ in [221, 235]). As we will discuss in section 6.5.2, the SPH standard artificial viscosity translates into a much higher effective viscosity than the viscosity in mesh-based simulations; thus, limiting the Reynolds number achieved in the present SPH simulation.

Figure 6.3 shows the dynamic amplitude, spike and bubble evolution. The overall increase in the dynamic amplitude is dominated by the down-falling spike position. Focussing on the linear regime, we show that the evolution of the

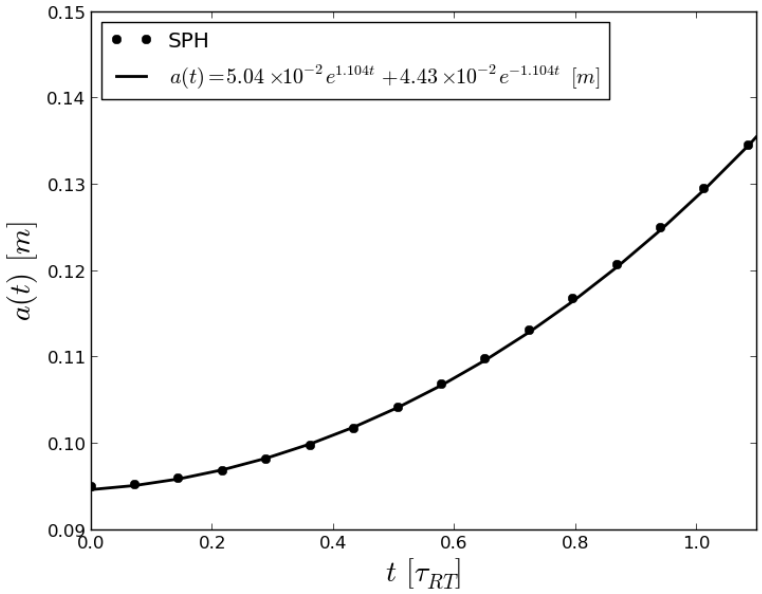

Figure 6.4: The amplitude of RTI growth for $A_T = 0.\bar{3}$ case with artificial viscosity parameter $\alpha_{AV} = 0.1$ at the early stage of the RTI.

dynamic amplitude $a(t)$ and the corresponding curve predicted from linear theory (equation (2.30) in chapter 2 or [90]) are in good agreement with each other in Figure 6.4. Note that the theoretical growth rate for inviscid fluid is $n_{c,inviscid} = 1.37\,[\mathrm{s}^{-1}]$. Yet, this inviscid growth rate cannot be compared with the SPH growth rate, due to the inherent SPH artificial viscosity (see Figure 6.8).

Finally, the constant of proportionality corresponding to the average terminal velocities of the bubble and spike (see Equation (6.4)) is estimated to be $\Gamma_{\mathrm{direct}} = 0.222$ for the direct extraction method and $\Gamma_{\mathrm{fitted}} = 0.216$ for the fitted amplitude slope method. In both cases, the estimated Γ for our fiducial model is consistent with the values reported in the literature [68, 233, 234, 236].

Dependence on Atwood number

To study the influence of density ratios, we compare two simulations with Atwood numbers $A_T = 0.\bar{6}$ and $0.\bar{8}$, with our $A_T = 0.\bar{3}$ fiducial model described in section 7.7.1. Figure 6.5 shows the time evolution of the two simulations, though only

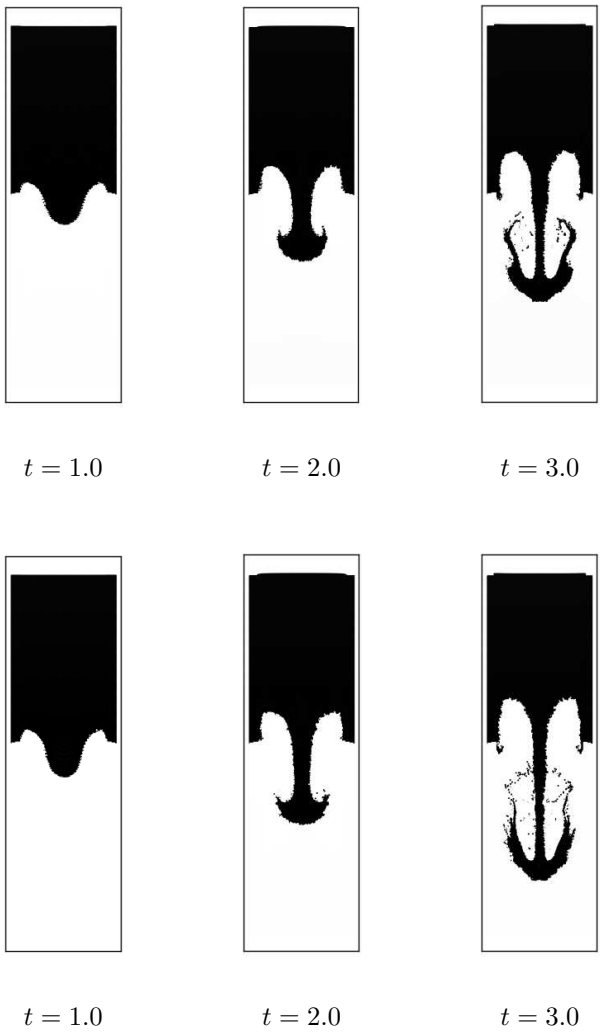

Figure 6.5: Time evolution of single mode RTI for Atwood number $A_T = 0.\bar{6}$ (top) and $A_T = 0.\bar{8}$ (bottom) at the different time measured in units of $\sqrt{L/g}$.

focussing on three distinctive time steps i.e. $t\,[\sqrt{L/g}] = 1, 2, 3$. The time-steps are chosen to illustrate the difference in the RTI morphology for different Atwood numbers. It is found that during the nonlinear regime the asymmetric behaviour between the spike and bubble is more pronounced for large Atwood numbers. Furthermore, the shearing motion in large Atwood number simulations strips SPH particles away from the edges of the heavy fluid spike rather than generating the KHI vortices. Figure 6.6 illustrates the dynamic amplitude, bubble and spikes evolution at different Atwood numbers. The development of RTI is also

A_T	n_c	ν_{eff}	$v_{b,\text{direct}}$	$v_{b,\text{fitted}}$	$v_{s,\text{direct}}$	$v_{s,\text{fitted}}$	Γ_{direct}	Γ_{fitted}
$0.\bar{3}$	1.10	1.00×10^{-2}	0.13	0.12	-0.23	-0.22	0.22	0.21
$0.\bar{6}$	1.59	1.29×10^{-2}	0.17	0.17	-0.46	-0.47	0.22	0.22
$0.\bar{8}$	1.78	1.24×10^{-2}	0.18	0.17	-0.63	-0.64	0.22	0.22

Table 6.1: Simulation results for different density ratios. The columns show the respective Atwood number A_T, the fitted growth rate (n_c), the effective viscosity (ν_{eff}), the terminal velocities of bubble and spike derived from either direct extraction or fitted slope method ($v_{b,s}$) (c.f. section 6.5.1), and the constant of proportionality for the average terminal velocity (Γ).

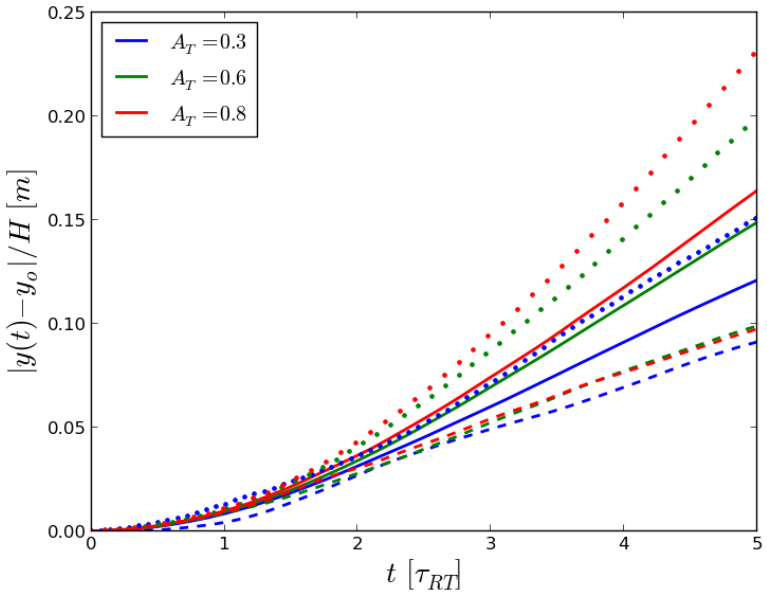

Figure 6.6: Time evolution of the amplitude (solid line), spike (dotted line) and bubble (dashed line) relative to their original position for different Atwood numbers. The large Atwood number $A_T = 0.\bar{8}$ grows more rapidly than the lower Atwood number simulations $A_T = 0.\bar{3}$ and $A_T = 0.\bar{6}$.

more pronounced for larger Atwood number and resulting in larger growth rates. Table 6.1 summarises our results for these simulations: the Atwood numbers, density ratios, the fitted growth rate n_c, effective kinematic viscosity ν_{eff} and the terminal velocities of bubble and spike from both direct extraction and the fitted amplitude slope method. Similar to the results for the $A_T = 0.\bar{3}$ case, the estimated growth rates for $A_T = 0.\bar{6}$ and $A_T = 0.\bar{8}$ are lower than the classical growth rate [5] due to the influence of artificial viscosity.

As the constant of proportionality of the terminal velocity in the drag-

buoyancy model is independent of the density ratio of the two fluids, we obtained the average of it for all three simulations with different Atwood number A_T. Based on the data in Table 6.1, we found $\langle \Gamma = 0.221 \rangle$ for both the direct extraction and fitted slope method, which is in good agreement with the results in the literature [68, 233, 234, 236].

Dependence on artificial viscosity parameter

In order to understand the role of damping due to the standard artificial viscosity, we compare our fiducial simulation with $\alpha_{AV} = 0.1$ ($Re = 100$) with simulations performed using artificial viscosity parameters $\alpha_{AV} = 0.05 - 0.25$. Figure 6.7 shows the results of two simulations with $\alpha_{AV} = 0.15$ and $\alpha_{AV} = 0.25$. The corresponding Reynolds numbers are $Re = 85$ and $Re = 70$, respectively. It is found that the shape of the central region jet remains highly collimated and show little dependence on the artificial viscosity parameter (Reynolds number), while the interface of the side jets of the lower Reynolds number simulations is smoother than that in the fiducial model as shown in Figure 6.2. Moreover, the secondary KHI vortices at the edges of the spike are completely absent at $\alpha_{AV} \gtrsim 0.15$ ($Re \lesssim 85$). This suggests the increase in α_{AV} significantly suppresses the growth of shear instabilities at the edges of the spike. More importantly, the artificial viscosity not only suppresses the secondary KHIs, but also damps the growth of RTI. Figure 6.8 shows the amplitude of the $A_T = 0.\bar{3}$ RTI simulation at different artificial viscosity parameters. A comparison between the amplitude data with the inviscid growth amplitude function confirms our earlier claim in section 7.7.1 and illustrates that the deviation between the SPH solution and inviscid theory is due to the effects of artificial viscosity.

In Figure 6.9, we investigate the time evolution of the bubble/spike positions for different artificial viscosities more closely and confirm the growth rate decays with increasing viscosity. Figure 6.10 shows the corresponding velocity evolu-

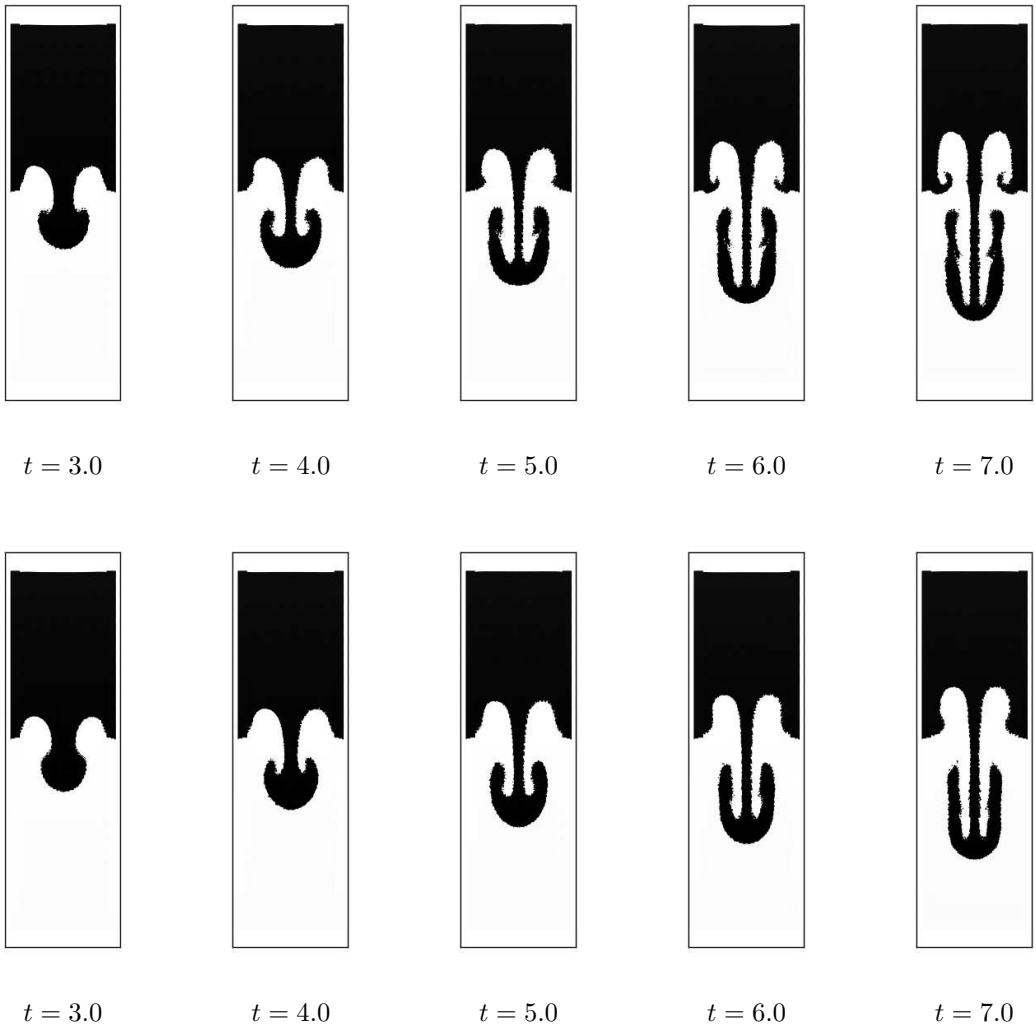

Figure 6.7: Time evolution of our single-mode RTI simulation with different viscosities $\alpha_{AV} = 0.15$ i.e. $Re = 85$ (top) and $\alpha_{AV} = 0.25$ i.e. $Re = 70$ (bottom), respectively. The time is measured in units of $\sqrt{L/g}$.

tion of the bubble and spike. The boxed region highlights the evolution during $1.0 \leq t \leq 2.0$, where re-acceleration of the spike occurs. Until $t \sim 1.5$ the spike slows down, before it then re-accelerates until it has reached its terminal velocity. This re-acceleration occurs earlier for lower viscosity simulations. We suspect the increase of viscosity delays re-acceleration of the spike by damping out two mechanisms: (i) small scale numerical noise in SPH simulations that grows faster than the dominating mode and (ii) the interaction between secondary vortices at the fluid interface. Note that while the damping of small scale noise is a desired

α_{AV}	n_c	ν_{eff}	Re	$v_{b,\text{direct}}$	$v_{b,\text{fitted}}$	$v_{s,\text{direct}}$	$v_{s,\text{fitted}}$
0.05	1.16	8.11×10^{-3}	123	0.14	0.15	-0.24	-0.24
0.10	1.10	1.00×10^{-2}	100	0.12	0.12	-0.22	-0.22
0.15	1.06	1.17×10^{-2}	85	0.12	0.12	-0.20	-0.20
0.20	1.02	1.31×10^{-2}	77	0.11	0.11	-0.20	-0.19
0.25	0.99	1.43×10^{-2}	70	0.10	0.10	-0.18	-0.19

Table 6.2: Simulation results for different artificial viscosity parameters. The columns show the respective artificial viscosity (α_{AV}), the growth rate (n_c), the kinematic viscosity (ν_{eff}), the effective Reynolds number (Re), as well as the terminal velocities of bubble and spike derived from either direct extraction or fitted slope method ($v_{b,s}$).

behaviour, the damping of secondary vortices undesired, since the SPH viscosity decreases the growth of the bubble/spike as shown in Figure 6.9. Table 6.2 summarises the growth and velocity data at different artificial viscosity parameters. As expected, the RTI growth rate n_c decreases with increasing viscosity (lower Reynolds number). Furthermore, a linear relationship is found between the artificial viscosity parameter (α_{AV}) and the effective viscosity (ν_{eff}), with a slope of 3.08×10^{-2} and an intercept of 6.82×10^{-3}. The source of intrinsic viscosity is primarily due to insufficient particle resolution, which will be further discussed in the next section. Note that while it is acceptable to interpret the slope as an indication of the relationship between the artificial viscosity and effective viscosity, one shall not infer $\alpha_{AV} = 0$ simply corresponds to an intrinsic viscosity of $\nu_{\text{eff}} = 6.824 \times 10^{-3}[\text{m}^2/\text{s}]$. This is because SPH simulations can easily suffer from particle interpenetration in lieu of artificial viscosity models.

Resolution Dependence

To study the global resolution dependence of our simulation, two additional fiducial simulations with coarse-grained resolutions corresponding to the initial inter particle separations $d_{nat} = 0.04$ and $d_{nat} = 0.02$ are simulated. The amplitudes for different global resolutions are shown in Figure 6.11. Inspecting the growth data for different resolutions in Table 6.3, it appears the low resolution

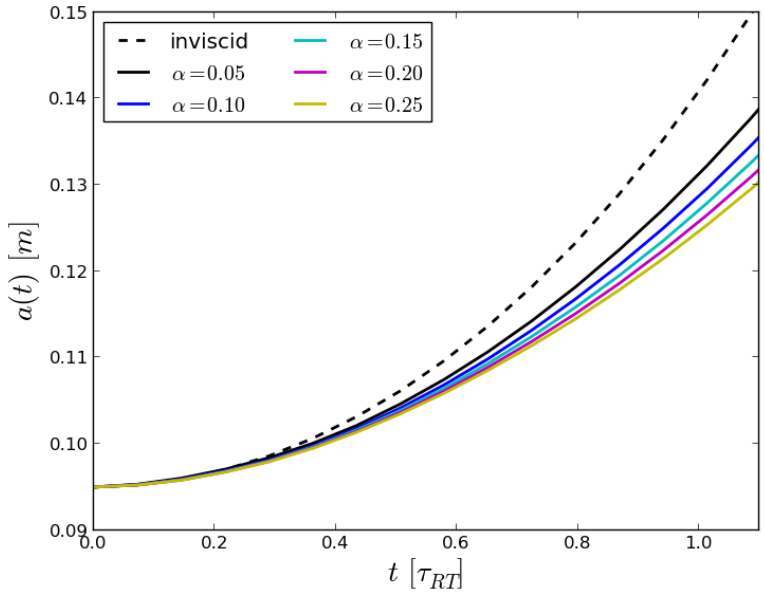

Figure 6.8: The amplitude of RTI growth for $A_T = 0.3$ case simulated using different artificial parameters α_{AV}. The growth of RTI is suppressed compared to the inviscid growth due to the influence of increasing artificial viscosity parameters.

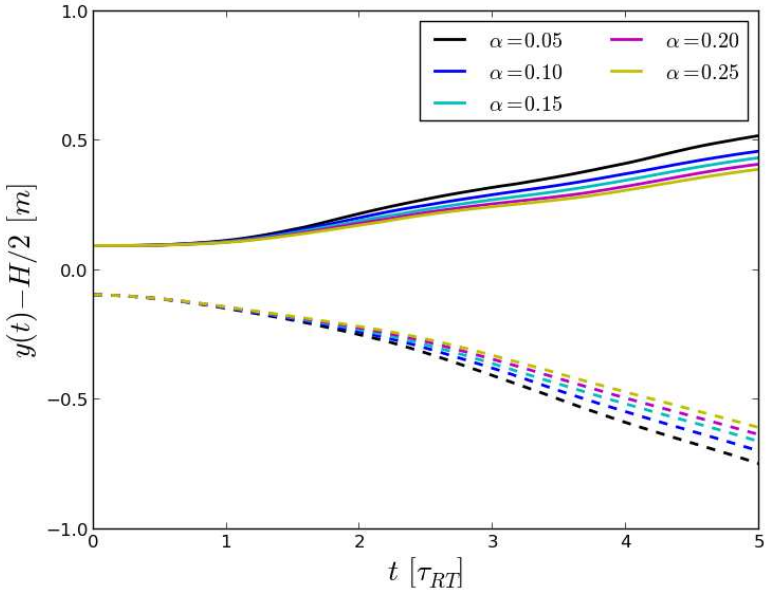

Figure 6.9: Positions of bubble (solid line) and spike (dashed line) as a function of time for different artificial viscosity parameters relative to the initial interface at $y = H/2$.

simulations have a more dissipative effect than the high resolutions simulations. Consequently, for the low resolution presented herein, SPH is not capable of

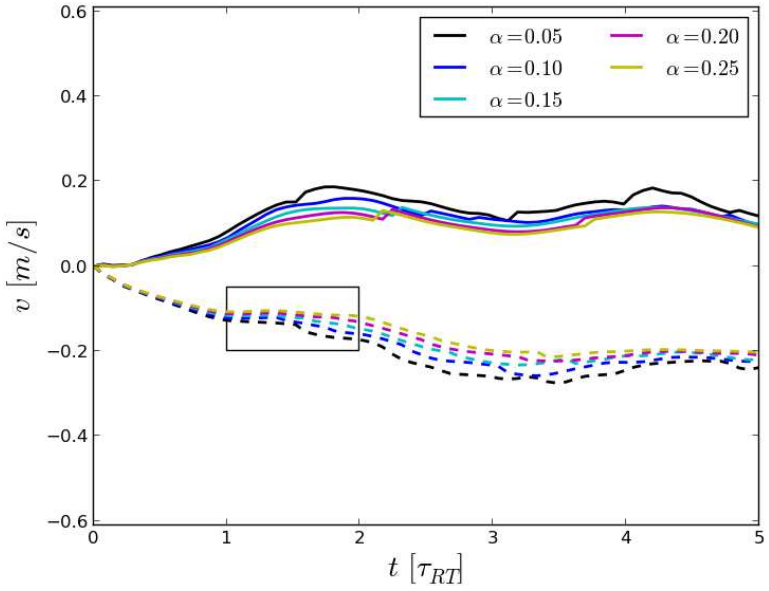

Figure 6.10: Vertical velocities of bubble (solid line) and spike (dashed line) front as a function of time for artificial viscosity parameters. The boxed region indicates the time period of re-acceleration that is delayed with increasing viscosity.

resolving the shear motion accurately. Note that while the difference is subtle during the early stage of the instability, the growth of KHI plays a crucial role to the break-up of the spike during the later stages.

d_{nat}	N_{fluid}	n_c	ν_{eff}	$v_{b,\text{direct}}$	$v_{b,\text{fitted}}$	$v_{s,\text{direct}}$	$v_{s,\text{fitted}}$
0.04	2500	0.94	1.63×10^{-2}	0.08	0.09	-0.15	-0.15
0.02	10000	0.94	1.62×10^{-2}	0.10	0.11	-0.21	-0.20
0.01	40000	1.10	1.00×10^{-2}	0.12	0.12	-0.23	-0.22

Table 6.3: Illustration of fitted growth during initial stages of different resolutions for Atwood number $A_T = 0.3$. The growth rate (n_c) (1st column), the number of fluid particles (N_{fluid}) (2nd column), effective viscosity (ν_{eff}) (3rd column), velocity of bubble, spike computed via direct extraction: (4th, 6th column) and velocity of bubble and spike computed via fitted slope method: (5th, 7th column).

The kernel smoothing factor κ is varied from $\kappa = 1.50$ to $\kappa = 2.33$ to study the effects of local resolution. For a constant global resolution, a larger smoothing factor accounts for more neighbours within the kernel function. Therefore, additional smoothing is applied to smear our the interface discontinuity. The RTI amplitudes for different κ values plotted in Figure 6.12 suggests the early

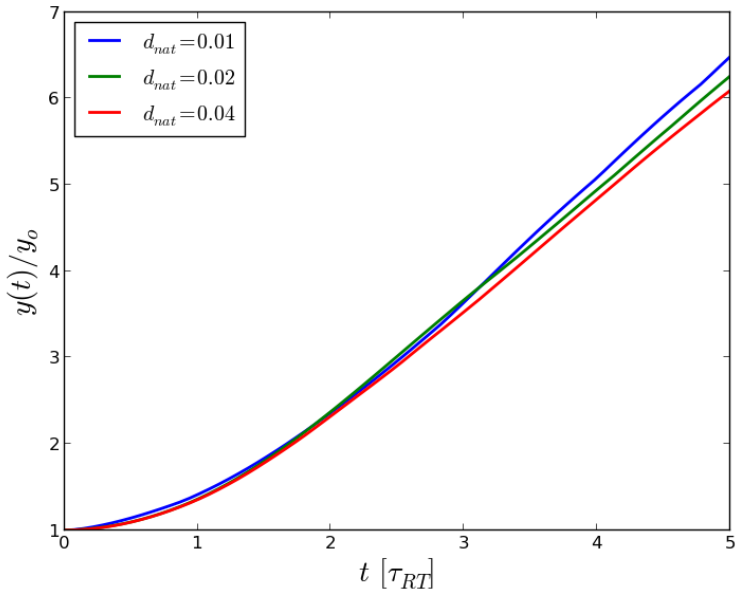

Figure 6.11: Growth amplitude of RTI with Atwood number $A_T = 0.3$ for various global resolutions.

κ	N_n	n_c	ν_{eff}	$v_{b,\text{direct}}$	$v_{b,\text{fitted}}$	$v_{s,\text{direct}}$	$v_{s,\text{fitted}}$
1.50	28	0.94	1.64×10^{-2}	0.13	0.12	-0.18	-0.17
1.75	36	0.99	1.41×10^{-2}	0.15	0.14	-0.23	-0.22
1.95	47	1.01	1.35×10^{-2}	0.14	0.13	-0.23	-0.22
2.33	68	1.10	1.00×10^{-2}	0.12	0.12	-0.23	-0.22

Table 6.4: Illustration of fitted growth during linear regime generated by different smoothing factors (κ) for the $A_T = 0.\bar{3}$ simulation. The number of neighbours within the kernel support (N_n) (2^{nd} column), the growth rate (n_c) (3^{rd} column), effective viscosity (ν_{eff}) (4^{th} column), velocity of bubble, spike computed via method 1: (5^{th}, 7^{th} column) and velocity of bubble and spike computed via method 2: (6^{th}, 8^{th} column). The growth data (n_c) and effective kinematic viscosity (ν_{eff}) exhibits a decreasing relationship with increasing κ.

evolution of RTI is weakly dependent upon κ provided sufficient neighbour particles resides within the support of the kernel function. Table 6.4 summarises number of neighbours, interpolated growth rate, the effective kinematic viscosity for different smoothing factors in the $d_{nat} = 0.01$ simulation. Note that the effective viscosity decreases with increasing smoothing factor, resulting in an overall increase in the growth rate of RTI. Upon closer inspection of Figure 6.13, we observed that the fine scale structure of the KHI roll-up at the edges of the

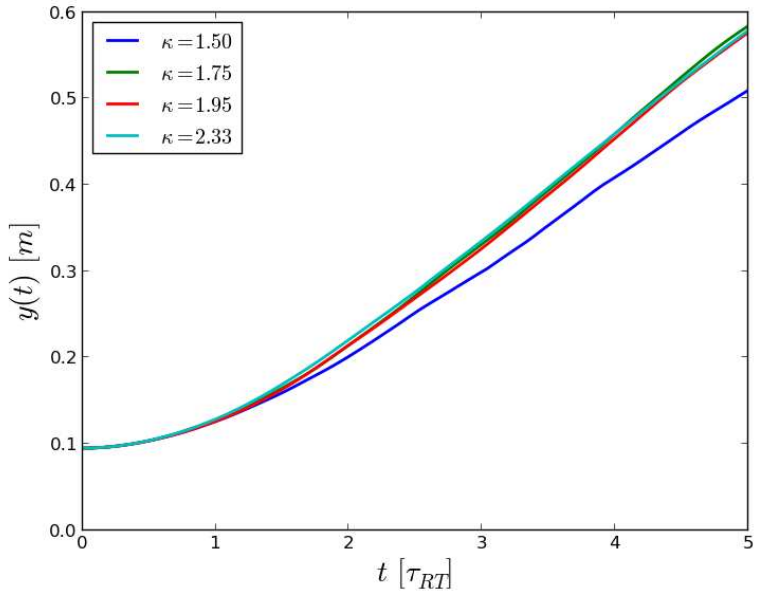

Figure 6.12: Growth amplitude of RTI with Atwood number $A_T = 0.\bar{3}$ for various kernel smoothing parameters (κ).

spike are much better resolved for large κ, although the position of the spike and bubble are similar for $\kappa > 1.5$. Moreover, the RTI simulations for large κ behave more symmetrically along the vertical line at $x = 0.5L$. This is primarily due to the fact that for small κ, the contribution from a high mass particle is significantly larger than the contribution from the low mass particles. Therefore, a slight offset in particle distribution would lead to a bias in density estimate, consequently effecting the symmetry at $y = L/2$ in later stages of the instability. In contrast, using a large smoothing length has the effect of smoothing out the density jump at the interface and therefore aids to maintain the symmetry of the instability for single-mode RTI.

6.5.3 Multi-mode Rayleigh-Taylor Instability

In real fluid systems, the initial perturbation consists of a spectrum of different frequencies. The interaction between different RTI modes may then give rise to turbulence. For completeness, we simulate the multi-mode RTI subjected to

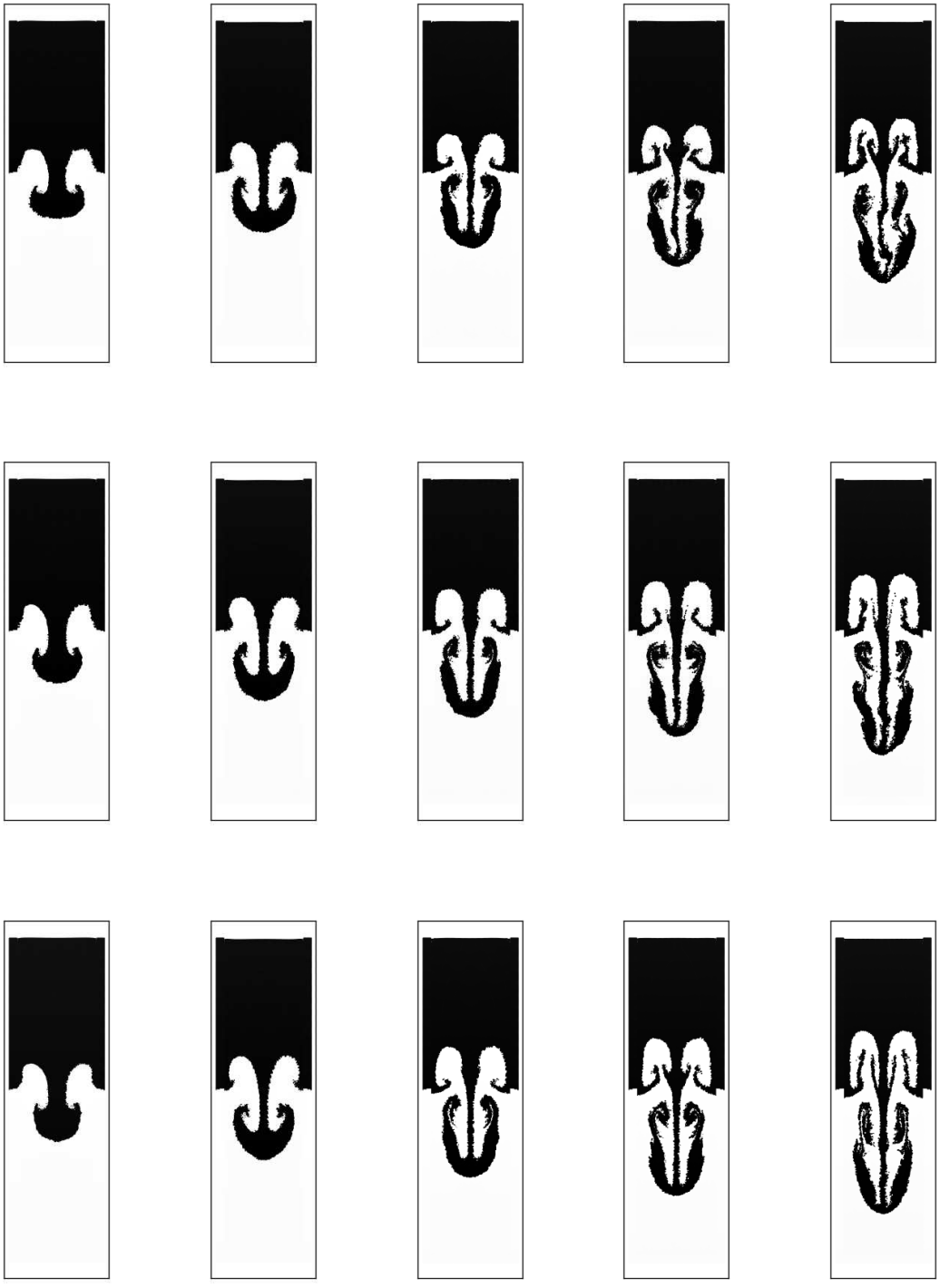

$t = 3.0$ $t = 4.0$ $t = 5.0$ $t = 6.0$ $t = 7.0$

Figure 6.13: Time evolution of $A_T = 0.\bar{3}$ RTI for numerous smoothing factors κ at times between 3.0-7.0 in units of $\sqrt{L/g}$. Top $\kappa = 1.5$, middle $\kappa = 1.75$, bottom $\kappa = 1.95$. Difference in both the symmetry and morphology of the KHI vortices can be clearly observed.

random perturbation for $A_T = 0.\bar{3}$ with the aspect ratio of $L/H = 2:1$. The simulation domain is $x \in [0, L]$ and $y \in [0, H]$ with no-slip boundary condition applied at the sides and bottom of the simulation domain. The initial conditions are similar to that in section 7.6, except that the fluid interface is described by

$$g(x) = \sum_{m'=m'_{min}}^{m'_{max}} A_{m'} \cos\left(\frac{2\pi\, m'}{L} x\right) + B_{m'} \sin\left(\frac{2\pi\, m'}{L} x\right), \tag{6.8}$$

where $m'_{min} = 20$, and $m'_{max} = 40$, and the coefficients $A_{m'}, B_{m'} \in [0 - 1 \times 10^{-3}]$ are generated randomly from a Gaussian distribution.

The numerical results at times $t = 0 - 5$ are plotted in Figure 6.14. During the early stage ($t \lesssim 1.0$), the small wave-number modes grow fastest. The associated bubbles and spikes are generated as the heavy and light fluid interchange positions ($t \sim 1.0$). This results in a mixing layer where the thickness of the layer increases with time ($t \sim 2.0$). At later times ($t \sim 3.0$), the interaction between different modes leads to the merging of bubbles. The merged bubbles with larger volume grow faster than the smaller bubbles due to buoyancy. As the merging of bubbles and spikes occurs ($t \sim 4.0$), the onset of KHI at the respective edges can be seen. By ($t \sim 5.0$) the merged spikes reach the bottom of the domain. Similarly the merged bubbles reached the top of the domain.

In order to understand the effects of mixing in our simulation, we define the mixing layer as the horizontal layer where the average density lies in between those of the two fluids. The average density is computed by partitioning the simulation data across the vertical direction into 100 equal width bins. Figure 6.15 plots the average density along the vertical direction, where the height of the merged bubble increases with time. Figure 6.16 plots the evolution of the multi-mode bubble and spike. The estimated coefficient for the multi-mode bubble is found to be $\Theta = 0.048$, which is within the range reported in the literature [71, 72, 73, 74].

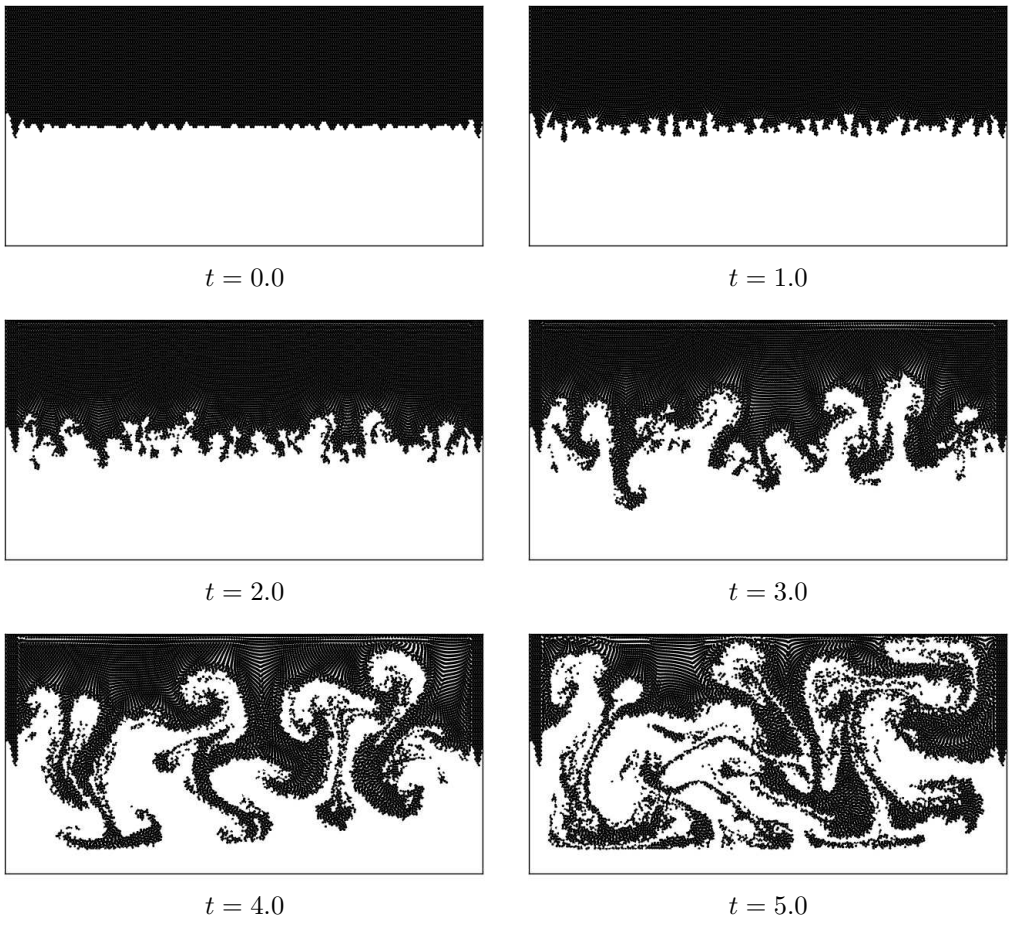

Figure 6.14: Numerical results for $A_T = 0.\bar{3}$ RTI subjected to multi-mode random perturbations. The time is measured in $\sqrt{L/g}$.

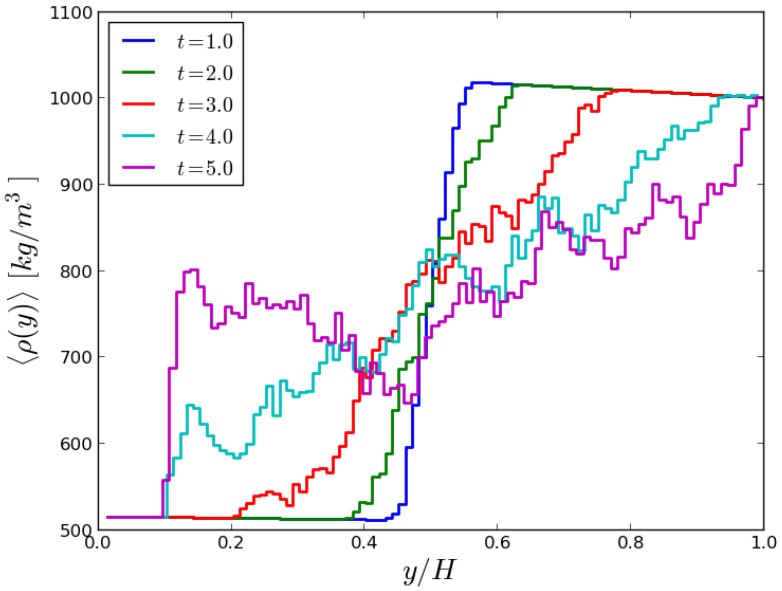

Figure 6.15: Average fluid density of the mixing layer plotted against the vertical direction for multi-mode RTI subjected to random perturbation. The time is measured in $\sqrt{L/g}$.

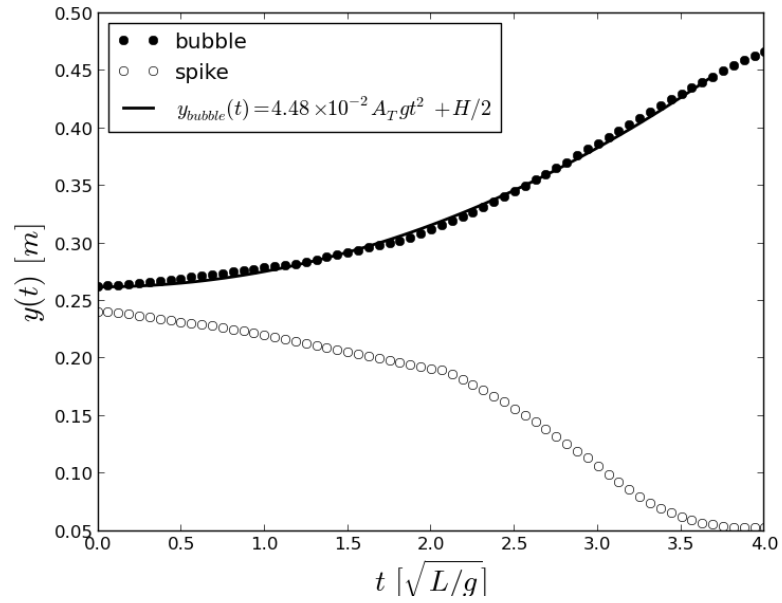

Figure 6.16: Position of bubble and spike for the multi-mode RTI plotted against time. The time is measured in $\sqrt{L/g}$.

6.6 Summary

The two-dimensional single- and multi-mode Rayleigh-Taylor instability between two immiscible fluids were simulated in this chapter. The Lagrangian nature of SPH serves as a powerful alternative to mesh-based numerical methods as it is capable of resolving multi-fluid flow phenomena without the use of interface tracking routines. The effects of Atwood number, Reynolds number and resolution were investigated. It was found that the development of low Atwood number RTI can be influenced by the KHI, whereas for large Atwood number, the shear motion results in the stripping of SPH particles at the edges of the spike. Furthermore, we found that the artificial viscosity suppresses both the RTI growth rate and the development of secondary KHI vortices. For $Re = 100$, the KHI roll-up was clearly observed. Whereas, the KHI vortices are absent at lower Reynolds numbers ($Re \lesssim 85$). The maximum Reynolds number considered in this chapter was $Re = \mathcal{O}(10^2)$, which was well within the laminar regime. Furthermore, a linear relation between artificial viscosity and effective viscosity was found, with the slope of 3.08×10^{-2} and intercept of 6.82×10^{-3}.

Two methods of extracting the vertical terminal velocities were introduced: direct extraction and fitted amplitude slope extraction method. The extracted constant of proportionality was found to be $\Gamma = 0.221$ for both the fitted slope method and the direct extraction method, and agrees well with previous experimental results [68, 233, 234, 236].

A series of numerical simulations was also carried out to study the dissipative effects due to global resolution. As expected, the effective viscosity decreases with increasing global resolution (more SPH particles). Furthermore, the low resolution also led to the suppression of the KHI hence the simulation has a higher effective viscosity.

The multi-mode Rayleigh-Taylor instability was also examined. The numer-

ical results indicate the mixing layer generated by the merging of bubbles and spikes tends to grow in time, and the time evolution of the merged bubble front follows the scaling relation (see equation (6.5)) with the constant of proportionality estimated to be $\Theta = 0.048$.

Summarising, weakly-compressible SPH was found to be a powerful alternative to other particle methods [217, 230, 231] and mesh-based methods [74, 221, 235]. It is superior to the incompressible SPH variants [217, 231] because it does not require the use of iterative solvers to enforce incompressibility; hence, reducing the total computation time. The Lagrangian particle-nature of SPH automatically handles stripping and fragmentation without using interface tracking routines as required by meshed-based methods. However, the major shortcoming of SPH is that the artificial viscosity model damps out the shear motion between fluids, resulting in the suppression of both the growth rate and the increase of effective viscosity. This behaviour is crucial for small Atwood number RTI. The presence of viscosity in the flow problem makes the comparison between the SPH solution with inviscid analytical prediction difficult. However, our results are consistent with the viscous analytical prediction. We would also like to point out that for large Atwood number $A_T \to 1$, the RTI is dominated by buoyancy, and the effects of viscosity are expected to be negligible. However, there is a need improve the existing SPH viscosity model as well as a suitable turbulence model, such that realistic flow conditions can be properly handled in high Reynolds number regimes.

Chapter 7

Rayleigh-Plateau Instability

7.1 Introduction

This chapter presents the simulation results for the three-dimensional Rayleigh-Plateau instability (RPI) conducted using multiphase weakly-compressible SPH. The instability governs the fragmentation of a low Weber number hydrodynamic jet in the presence of low density ambient medium. Thus, the SPH simulation of a hydrodynamic jet at high density ratio requires a multiphase model and a surface tension model that is capable of handling the necking behaviour which is responsible for the break-up of a jet into droplets.

We apply the surface tension model of Adami et al. [75] motivated by continuum surface force (CSF) model. In addition, a Neumann boundary condition near the interface is applied to allow for the discontinuous pressure jump due to surface tension. The combination of surface tension model and multiphase SPH scheme successfully demonstrates the break-up of a hydrodynamic jet, where the density of the jet fluid and its surround ambient fluid differs up to three magnitudes. Three validation cases are presented to evaluate the combination of these models: (i) the square box test, (ii) the static droplet pressure comparison with the Young-Laplace pressure, and (iii) the oscillation of a liquid droplet

suspended in a gas.

The rest of this chapter is organised as follows: section 7.3 discusses the theoretical aspects of the RPI. Section 7.4 describes the surface tension model introduced by Adami et al. [75]. Section 7.5 presents the results for three test cases employed to validate the combination of surface tension model with our multiphase SPH scheme. The SPH results of the RPI are presented in section 7.7. Finally, we summarise our findings in section 7.8.

7.2 Literature review

The RPI is crucial to the understanding of jet break-up and atomisation processes that are drive by the effects of surface tension. In its simplest form, an initially cylindrical liquid column is subjected to a surface perturbation. Due to the difference in curvature, surface tension acts to minimize the area of the liquid column, eventually leading to the break-up of the liquid column and the generation of droplets. Plateau [237] pioneered the study of the jet break-up experimentally and found that the break-up occurs provided that the length of the liquid column exceeded the diameter of the jet by a factor of 3.13. His work was later extended by Rayleigh [6], who conducted a linear stability analysis to study the break-up of a liquid jet.

Since the work of Plateau [237] and Rayleigh [6], there has been a series of theoretical studies that aim to encapsulate additional physical effects in the jet break-up process. Weber [238] derived the analytical growth rate of a viscous liquid jet and demonstrated convergence to the growth rate for an inviscid fluid [6]. Lafrance [239] conducted a third order perturbation analysis of an inviscid liquid jet, and found that interaction among the non-linear terms is responsible for the generation of satellite droplets.

Advances in numerical analysis has motivated the study of RPI using numer-

ical techniques. Mead-Hunter et al. [240] simulated the RPI occurring around an optical fiber with FVM. Choi et al. [241] simulated the capillary instability of a nano-scale surface tension driven flow of a Lennard-Jones fluid by means of molecular dynamics. The authors reported good agreement with classical theories and claimed that thermal fluctuations are responsible for the break-up of nano-scale jets.

The past decade has also witnessed increased use of particle methods in jet simulations. Shibata et al. [242] simulated the jet break-up using MPS. After studying the effects of Weber number and Froude number, the authors reported the break-up length deviated from the experimental data by 70%-80%, with a relative error of 25% in the absence of gravity. Takashima et al. [243] simulated the break-up process by means of ISPH and reported good qualitative agreement with the experimental results, except for the pinch-off length. Sirotkin and Yoh [244] introduced the corrected smoothed particle hydrodynamics method for simulating surface tension driven flow. Their numerical scheme is based on the combined use of the continuity equation approach (for density evaluation) and the surface tension model of Morris [245]. They simulated the two-dimensional jet break-up without taking into account the ambient fluid and found acceptable agreement for the critical Weber number, which governs the transition from jetting to dripping.

7.3 Theory of Rayleigh-Plateau Instability

This section discusses the theoretical aspects of the RPI. Firstly, we present the analytical theory of the RPI. While the single-fluid linear growth rate have been proposed, this work fills the gap in the literature to derive a linear growth rate for a multiphase RPI where the presence of ambient fluid is taken into consideration. Secondly, we summarise the major results in the literature that will be used in

the later sections for the comparison with SPH results.

7.3.1 Multiphase RPI growth rate

The linearised growth rate of the RPI for a jet fluid suspended in an ambient fluid is presented. Our derivation is based on the assumption that the flow is axis-symmetric, where the jet (inner) and ambient (outer) medium are both initially static, and influence due to gravity is negligible. These assumptions allow the RPI to be the dominant process. The continuity equation for incompressible, axis-symmetric flow in cylindrical coordinates is given by [94, 96, 107]

$$\frac{1}{r}\frac{\partial}{\partial r}(ru_r) + \frac{\partial u_z}{\partial z} = 0. \tag{7.1}$$

The momentum equations in $\hat{r}$ and $\hat{z}$ are

$$\rho\left(\frac{\partial u_r}{\partial t} + u_r\frac{\partial u_r}{\partial r} + u_z\frac{\partial u_r}{\partial z}\right) = -\frac{\partial P}{\partial r}, \tag{7.2}$$

$$\rho\left(\frac{\partial u_z}{\partial t} + u_r\frac{\partial u_z}{\partial r} + u_z\frac{\partial u_z}{\partial z}\right) = -\frac{\partial P}{\partial z}. \tag{7.3}$$

Applying the position, velocity and pressure perturbation

$$\begin{aligned} u_r &\approx u_{r0} + \epsilon u_{r1} + O(\epsilon^2) \\ u_z &\approx \epsilon u_{z1} + O(\epsilon^2) \\ P &\approx P_0 + \epsilon P_1 + O(\epsilon^2) \\ R &\approx R_0 + \epsilon R_1 + O(\epsilon^2) \end{aligned}, \tag{7.4}$$

to equation (7.1)-(7.3) results in a system of linearised differential equations

$$\frac{\partial u_{r1}}{\partial r} + \frac{u_{r1}}{r} + \frac{\partial u_{z1}}{\partial z} = 0 \tag{7.5}$$

$$\rho \frac{\partial u_{r1}}{\partial t} = -\frac{1}{\rho}\frac{\partial P_1}{\partial r} \tag{7.6}$$

$$\rho \frac{\partial u_{z1}}{\partial t} = -\frac{1}{\rho}\frac{\partial P_1}{\partial z}. \tag{7.7}$$

Finally applying the following perturbation quantities

$$\begin{Bmatrix} u_{r1}(r,z,t) \\ u_{z1}(r,z,t) \\ P_1(r,z,t) \\ R_1(r,z,t) \end{Bmatrix} = \begin{Bmatrix} \hat{u}_{r1}(r) \\ \hat{u}_{z1}(r) \\ \hat{P}_1(r) \\ \hat{R}_1(r) \end{Bmatrix} e^{ikz+nt} \tag{7.8}$$

to equation (7.5)-(7.7) and eliminating the pressure gradient term results in the following second order ordinary differential equation

$$r^2 \frac{\mathrm{d}\hat{u}_{r1}^2}{\mathrm{d}r^2} + r\frac{\mathrm{d}\hat{u}_{r1}}{\mathrm{d}r} - [1 + (kr)^2]\hat{u}_{r1} = 0. \tag{7.9}$$

The solution of equation (7.9) is given by the piecewise function

$$\hat{u}_{r1}(r) = \begin{cases} C_1\, I_1(kr) & r \le r_o \\ C_2\, K_1(kr) & r \ge r_o \end{cases} \tag{7.10}$$

where I_1, K_1 are the modified Bessel functions of the first and second kind, and C_1, C_2 are the constants of integration to be determined. Substituting equation (7.10) into equation (7.6) and integrating with respect to r gives

$$\begin{aligned} -nC_1\,\rho_1\, I_0(kr) &= kP_1(r) \quad r \le r_o, \\ C_2\,\rho_2\, K_0(kr) &= kP_1(r) \quad r \ge r_o. \end{aligned} \tag{7.11}$$

The constant of integrations C_1 and C_2 are determined by applying the linearised kinematic boundary condition at the interface $r = r_o$

$$\frac{\partial R_1}{\partial t} = \hat{u}_{r1}. \tag{7.12}$$

Substituting (7.8) and (7.10) into equation (7.12) and evaluating at the interface yields the constants

$$C_1 = \frac{n}{I_1(kr_o)} \quad , \quad C_2 = \frac{n}{K_1(kr_o)}. \tag{7.13}$$

Finally, the dynamic boundary condition for inviscid fluids requires the pressure difference at the interface to be equivalent to the Young-Laplace pressure

$$\Delta P = \sigma \nabla \cdot \hat{n} = \sigma \left(\frac{1}{R_1} + \frac{1}{R_2} \right), \tag{7.14}$$

where the R_1, R_2 are the two principle radii of curvature. Since the cylinder is subjected to a radial perturbation, the outside radius of curvature is

$$\frac{1}{R_1} = \frac{1}{R_o + \epsilon e^{nt+ikz}} \approx \frac{1}{R_o} - \frac{\epsilon}{R_o^2} e^{nt+ikz}, \tag{7.15}$$

whereas the innter radius of curvature is

$$\frac{1}{R_2} = \epsilon k^2 e^{nt+ikz}. \tag{7.16}$$

Substituting (7.11), (7.15)-(7.16) into (7.14) and collecting the $\mathcal{O}(\epsilon)$ terms gives the linear growth rate of the RPI between two inviscid and incompressible fluids

$$n^2 = \frac{k\sigma}{r_o^2 \rho_1} \frac{[1 - (kr_o)^2] \frac{I_1(kr_o)}{I_o(kr_o)}}{\left(1 + \frac{\rho_2}{\rho_1} \frac{K_o(kr_o)}{K_1(kr_o)} \frac{I_1(kr_o)}{I_o(kr_o)} \right)}. \tag{7.17}$$

Inspecting equation (7.17), it is found that the derived linear growth rate for two fluids recovers the free-surface flow growth rate presented in Rayleigh [6] for large density between jet and ambient medium as illustrated in Figure 7.1. The theoretical break-up time (t_{break}) is defined as the time at which the perturbed cylinder breaks into droplets, and it is given by the inverse of the theoretical growth rate (n) (i.e. $t_{break} = n^{-1}\,[s]$). For the free surface case, the break-up time is given by Rayleigh [6]

$$t_{break,theory} \approx 2.91\sqrt{\frac{\rho_1 r_o^3}{\sigma}}. \tag{7.18}$$

While the work of Rayleigh [6] applies to inviscid fluids, Weber [238] developed the dispersion relation for a viscous fluid and reported that the growth rate as well as break-up time not only depends on the wave number and the initial radius, but also on the relative importance of the viscosity and surface tension as measured by the Ohnesorge number ($Oh = \sqrt{We}/Re$)

$$n_{viscous} = \sqrt{\frac{\sigma}{\rho_1 r_o^3}}\left[\sqrt{\frac{r_o^2}{2}(k^2 - k^4 r_o^2) + \frac{9}{4}Oh^2\,(kr_o)^4} - \frac{3}{2}Oh\,(k\,r_o)^2\right]. \tag{7.19}$$

As for the multiphase finite viscosity case, the growth rate is expected to dependent an additional parameter, namely the Atwood number. However, the derivation of an analytical growth rate for a multiphase viscous RPI is beyond the scope of this thesis.

7.4 Surface tension model

The surface tension model is based on the continuum surface force (CSF) introduced by Brackbill et al. [246]. Morris [245] applied the CSF model to SPH and proposed SPH representations of the normal vector and curvature. The surface tension force is smoothed across the interface using a delta-function. The SPH

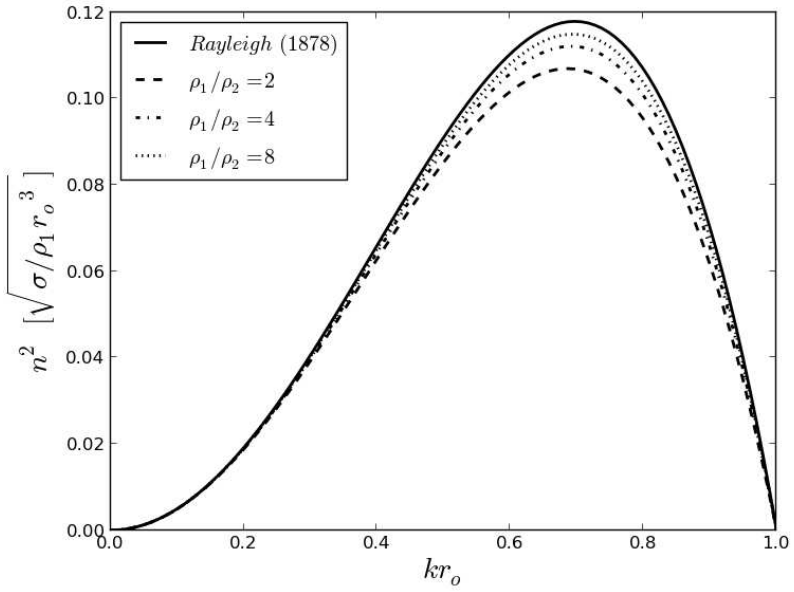

Figure 7.1: The square of the analytical growth rate plotted for numerous density ratios. The classical growth rate given in [6] is plotted as solid line.

version of the CSF method has been reviewed, aiming for a better evaluation of the curvature, while the delta-function is only defined in the interface band. The model of Adami et al. [75] is used with some modifications to allow for a better scaling with droplet size and high density ratios. The CSF is applied as a particle-wise force

$$\vec{F}_{st} = -\sigma\,\mathrm{curv}\,\hat{n}\,\delta_s, \tag{7.20}$$

where σ is the surface tension coefficient, curv is the local curvature of the interface, $\hat{n}$ is the unit vector normal to the interface and δ_s is a interface delta function. Following Adami et al. [75], the unit normal vector is evaluated from a color variable

$$\nabla \mathbf{c}_i = \frac{1}{V_i}\sum_j (V_i^2 + V_j^2)\mathbf{c}_{ij}\frac{\partial W}{\partial r_{ij}}\vec{e}_{ij} \quad \hat{n}_{ij} = \frac{\nabla \mathbf{c}}{|\nabla \mathbf{c}|}. \tag{7.21}$$

The density weighted color defined as

$$\mathbf{c}_{ij} = \frac{\rho_j}{\rho_i + \rho_j}\,\mathbf{c}_i + \frac{\rho_i}{\rho_i + \rho_j}\,\mathbf{c}_j, \tag{7.22}$$

where $\mathbf{c}_{i,j}$ are the color marker variable. During the simulation, the colour variable is $\mathbf{c} = 1$ provided there exists a neighbour particle of the other fluid within the support of the kernel function, otherwise the colour variable is assigned $\mathbf{c} = 0$. The curvature is evaluated under the kernel gradient as

$$\text{curv}_i = \nabla \hat{n}_i = N_{dim} \frac{\sum_j \hat{n}_{ij} \cdot \vec{e}_{ij} \frac{\partial W}{\partial r_{ij}} V_j}{\sum_j r_{ij} \frac{\partial W}{\partial r_{ij}} V_j}. \tag{7.23}$$

The term in the denominator is the kernel gradient correction. Finally, the delta function is defined as gradient of the color function $\delta_{s,i} = |\nabla \mathbf{c}_i|$. In practice, the delta function is non-zero only in the interface band, and zero everywhere else where the color function is zero. In the simulations, an effective surface tension coefficient is employed to allow for a scaling with droplet size and correct Young-Laplace pressure. That is, the real surface tension coefficient ($\sigma = 0.073$N/m at 20^oC) is multiplied by the initial particle volume. To improve numerical stability, we apply the Neumann boundary condition near the interface as follows: the jet fluid particle experiences the pressure of its low density ambient neighbour particles. A similar approach has been employed in the MPS scheme Shakibaeinia and Jin [216] to allow for better numerical stability for surface tension driven flow.

7.5 Validation cases

The surface tension model is validated in three test cases relevant to the RPI. The first test case examines the capability of the SPH scheme to simulate multiphase flow. The second test case studies the steady-state behaviour of static droplets

suspended in an ambient fluid. A calibration curve provides the relation between the actual surface tension coefficient and the numerical surface tension coefficient. The third test case studies the oscillation of a high density elongated droplet suspended in a low density medium. Unless otherwise mentioned, the following parameters are utilised throughout this section: $\rho_1 = 1000\text{kg/m}^3$, $\rho_2 = 1\text{kg/m}^3$. The speed of sound is $c_{1,2} = 10\text{m/s}$ and $\gamma_{1,2} = 1$. Finally, the fluid domain is constrained within $x \in [0, L], y \in [0, H]$, where the aspect ratio is normally set to unity (i.e. $L/H = 1$, and $L = 1\text{mm}$).

7.5.1 Square box test

The square box test in the literature [75] is conducted with and without surface tension to demonstrate the capability of the weakly-compressible SPH scheme in terms of (i) handling multi-phase flow, (ii) to tackle large deformations, (iii) modelling the physical behaviour of surface tension. Three simulations assess the performance of the multiphase SPH scheme. The first simulation utilised standard SPH, the second simulation used a multiphase scheme. Both simulations are performed in the absence of surface tension. The third simulation used the multiphase SPH scheme and surface tension. The results are shown in Figure 7.2. It is found that standard SPH based on the summation density approach suffers from the so-called artificial surface tension (see Figure 7.2, top row). That is, the initially square fluid block turned into an ellipse even without surface tension. Whereas the square box remains static in the multiphase simulation (see Figure 7.2, middle row). Furthermore, the results with surface tension (see Figure 7.2, bottom row) demonstrate the expected behaviour by generating a stable interface and the deformation from a square into a circular droplet.

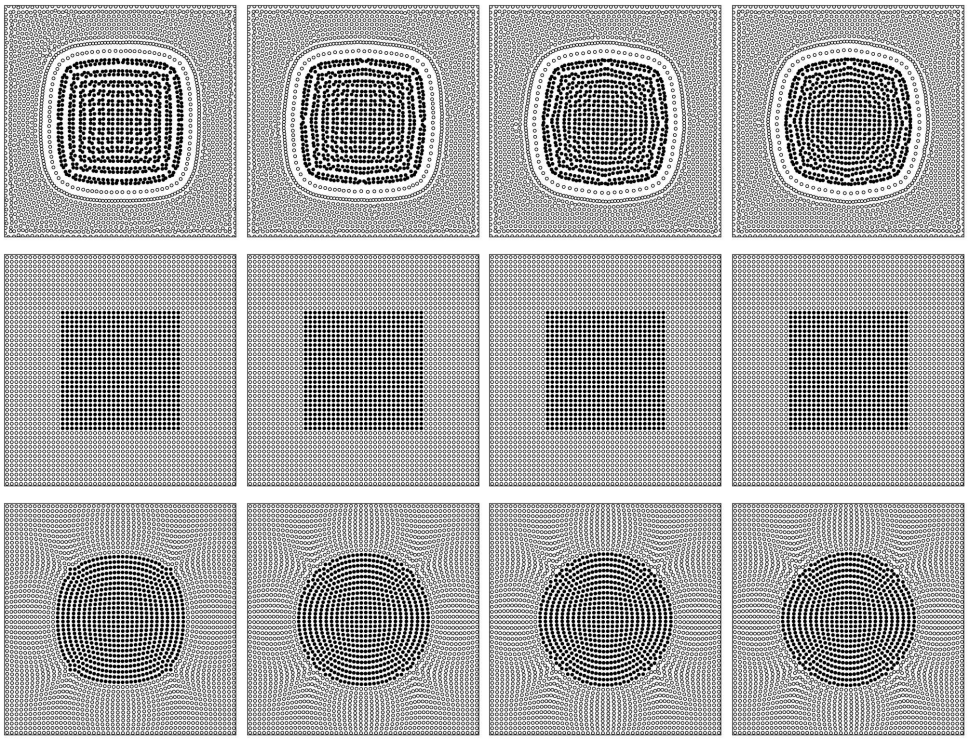

Figure 7.2: Numerical results of the square droplet test in the time interval $t = 0 - 0.2$s. Standard SPH without surface tension (top), multiphase weakly-compressible SPH scheme without surface tension (middle), and SPH scheme with surface tension (bottom).

7.5.2 Static droplet

The pressure within a static droplet obtained with the multiphase weakly-compressible SPH scheme is compared with the Young-Laplace pressure. A parameter study is conducted to investigate the role played by the local resolution parameter (κ), the dimensions of the problem (N_{dim}) and the density ratio (ρ_1/ρ_2). For a three dimensional droplet of radius $r_o = 2.5$mm, $\sigma = 0.073$N/m, the Young-Laplace pressure is $P_{YL} = 58.4$Pa, whereas in our case the droplet pressure is estimated to be $P_{SPH} = 65$Pa. Thus, the absolute and relative error are $\Delta P_{droplet} = 6.6$Pa and 11% respectively. The ratio of the pressure obtained from SPH and the Young-Laplace pressure is plotted as a function of density ratio as shown in Figure 7.3. The calibration curves depends on the density ratio, the

local resolution and the number of dimensions of the droplet

$$P_{SPH} = -AB^{log(\rho_1/\rho_2)} + C, \tag{7.24}$$

the values of the fitted curve are given in Table 7.1. A series of out-of-sample test are also conducted to assess the predictability of the fitted curves. In all cases, the out-of-sample tests are consistent with the fitted curves.

κ	N_{dim}	A	B	C
1.5	2	0.81	0.23	1.93
1.95	2	0.64	0.18	1.71
1.5	3	0.39	0.17	1.54
1.95	3	0.34	0.16	1.49

Table 7.1: Fitted coefficients for the droplet pressure calibration curves.

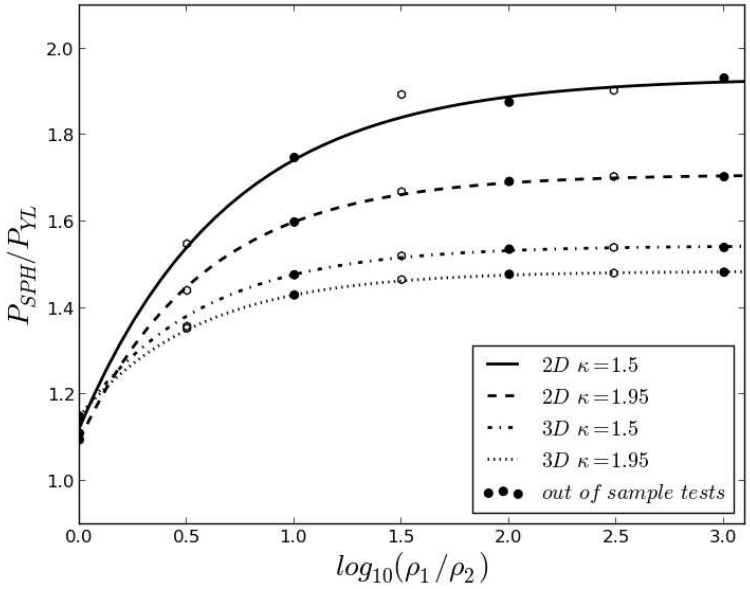

Figure 7.3: Calibration curves for static droplet plotted for density ratios. The fitted curves for two and three dimensional cases are indicated by the dotted (solid) lines.

7.5.3 Droplet oscillation

The oscillation of a droplet surrounded by an ambient fluid is simulated. The oscillation frequency of an inviscid droplet is described by the Rayleigh equation [247]. In two-dimensions it is given by

$$\omega^2 = m(m^2 - 1)\frac{\sigma}{\rho R_o^3}, \tag{7.25}$$

where m is an oscillation mode, and R_o is the radius of the droplet. The principal mode for two-dimensional case is $m = 2$, where the corresponding period is

$$t_{osc,theory} = 2\pi\sqrt{\frac{\rho R_o^3}{6\sigma}}. \tag{7.26}$$

The oscillation of a two-dimensional droplet is simulated. The oscillation period and pressure are compared against the analytical theory. The initial droplet has the shape of an ellipse, with major axis $a = L/2.5$ and $b = H/5$. Some typical results of an oscillating droplet are shown in Figure 7.4. The initial relative pressure is zero, as if there is no surface tension. The surface tension then quickly deforms the droplet by contracting the initially elongated ellipse into a circular droplet. The droplet then recovers the approximated elliptical shape; however, the major axis length decreased to 85% of its initial value due to viscous dissipation. The history of the average droplet pressure is shown in Figure 7.5. The pressure of the particles near the interface increases as soon as the simulation starts. It is found that the pressure within the droplet is overestimated by a factor of 2.13 ($P_{SPH} = 550$Pa, $P_{YL} = 258$Pa). Similarly, the oscillation period is overestimated by a factor of 1.5 ($t_{osc,SPH} = 1.49$ms, $t_{osc,theory} = 1.01$ms). Since the relation (7.26) is derived for inviscid fluids, it is reasonable to expect that the increase in oscillation period is caused by the combination of viscous damping, the presence of an ambient fluid, domain size and inertia.

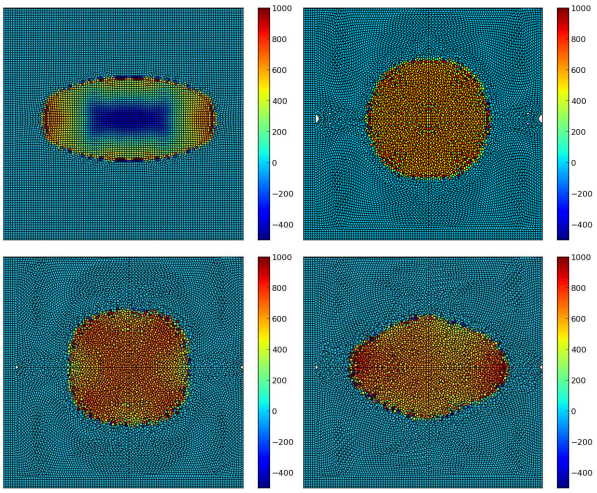

Figure 7.4: Numerical results of the two-dimensional droplet oscillation plotted at the times indicated, with the colour indicated as pressure.

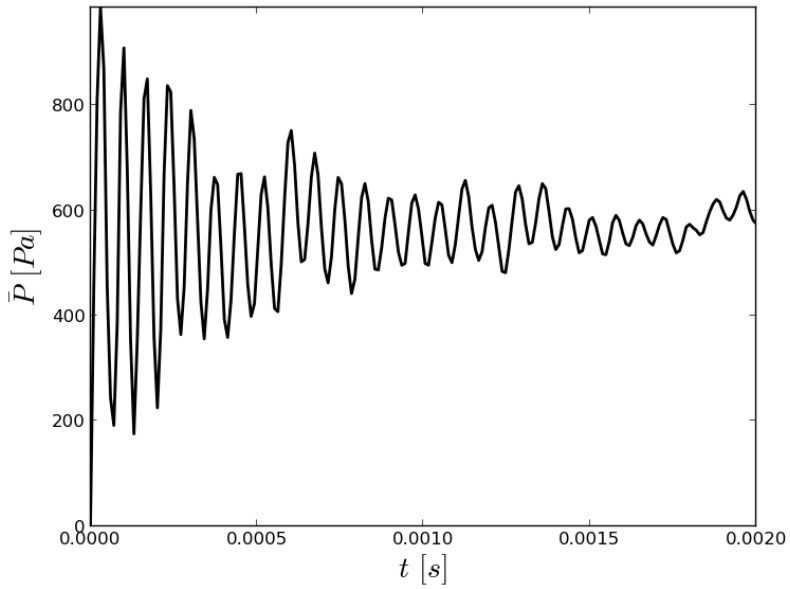

Figure 7.5: Average pressure of the oscillating droplet.

7.6 Initial Conditions

The three-dimensional Rayleigh-Plateau instability is considered, where the fluid domain is $x \in [0, L]$, $y \in [0, W]$, $z \in [0, H]$, where $L/W = 1$, $L = 1$cm and $H = 6.8$cm. For simplicity, periodic boundary conditions are applied in all directions. The initially cylindrical fluid column of radius $r_o = 2.5$mm travels at constant velocity $V_z = -0.01$m/s and is subjected to a radial perturbation $\delta_r(z) = \delta_a d_{dnat} \cos(kz)$, where δ_a is the initial perturbation amplitude given in terms of d_{nat}. The perturbation $\delta_r(z)$ is applied to excite the initial system such that the necking behaviour due to surface tension dominates the fluid flow as shown in Figure 7.6.

We simulated the wavelength corresponding to the maximum growth given by inviscid analytical theory $\lambda_{max} \approx 9.02 r_o$. The set-up is designed to generate three primary droplets after the break-up has occurred. In all cases, the density of the jet medium (ρ_1) is larger than the density of the ambient medium (ρ_2). In a multiphase set-up, the RPI can be characterised by the following set of dimensionless parameters: the Atwood number, the Weber number ($We = \rho_1 r_o {V_z}^2/\sigma$), the Reynold's number ($Re = r_o V_z/\nu$), and the shear viscosity relative to the surface tension is represented by the Ohnesorge number.

7.7 Results and Discussion

The simulation results for the Rayleigh-Plateau instability using is presented. The influence of three parameters are examined: the initial perturbation amplitude (δ_a), the Atwood number, and the Ohnesorge number (Oh). Each of these will be investigated in the following sections in comparison to the fiducial model.

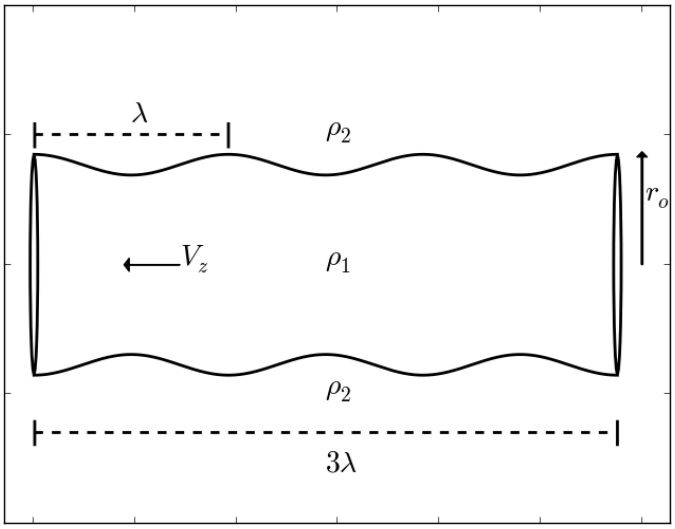

Figure 7.6: Initial set-up of the Rayleigh Plateau Instability simulation.

7.7.1 Fiducial model ($A_T = 0.998$, $Re = 0.0128$, $We = 0.003$, $Oh = 4.572$)

The RPI with the initial condition described in section 7.6 is simulated until $t = 0.15$s. The initial particle distribution is organised as a uniform grid, with separation distance $d_{nat} = 6.25 \times 10^{-4}$m. The simulation consists of $N_p = 27648$ particles (6456 jet and 21192 ambient particles), where a local smoothing factor $\kappa = 1.5$ is assigned. The SPH artificial viscosity parameter $\alpha_{AV} = 2.0$ is used. This corresponds to an effective kinematic viscosity of $\nu_{sph,theory} = 1.953 \times 10^{-3}\text{m}^2/\text{s}$. The surface tension coefficient is $\sigma = 0.073\,\text{N/m}$.

The results of the fiducial model are shown in Figure 7.7. During the early stage of the instability, the surface tension dominates the fluid flow $t \lesssim 0.8$s. The onset of the instability soon leads to the break-up of the jet, resulting in three droplets that span the vertical domain ($t \approx 0.12$s). The droplets become increasingly spherical as the surface tension acts to minimise the surface area of a droplet ($0.12\text{s} \lesssim \text{t} \lesssim 0.16\text{s}$). The break-up time is observed to be $t_{break,SPH} \approx 0.12$s, which is delayed by a factor of 2.6 when compared against theoretical break-up. We suspect the combination of artificial viscosity and the presence

of an ambient fluid may be responsible for causing the delay. Therefore, the influence of these parameters will be investigated in the following sub-sections.

7.7.2 Dependence on Ohnesorge number

To investigate the influence of artificial viscosity, we simulated the RPI utilising artificial viscosity parameters $\alpha_{AV} = 2-4$ with $\kappa = 1.5$ while keeping the Weber number fixed at $We = 0.003$. A selection of the numerical results are shown in Figure 7.9. Inspecting the results, we found that the break-up time increases with the viscosity parameter α_{AV}. In addition, a comparison with the post-break up results of the reference case indicates the use of a large viscosity parameter results in the scatter near the interface between the two fluids. For example, the droplet in the reference case $\alpha_{AV} = 2$ appears to form tightly bounded droplets after $t = 0.15$s, whereas for the highest viscosity simulation considered ($\alpha_{AV} = 4$) the droplet interface exhibits a large scatter. Despite the scatter at the interface, the particles near the center of the droplet have already formed the major portion of the droplet by the time the steady state is reached at $t \approx 0.3$s. We suspect the interface scattering with increasing α_{AV} is caused by the inertia between the jet and ambient fluids. A linear relation is recovered between the break-up time and α_{AV}, with a slope of 0.049 and an offset of 0.038. One may extrapolate that $\alpha_{AV} = 0$ corresponds to the break-up time $t_{break} = 0.038$s, which deviates from the analytical break-up time for inviscid fluid by $\sim 10.81\%$. Although such extrapolation gives an indication of the inviscid break-up time, we found that the utilisation of $\alpha_{AV} < 2.0$ results in inter-particle penetration during the simulations.

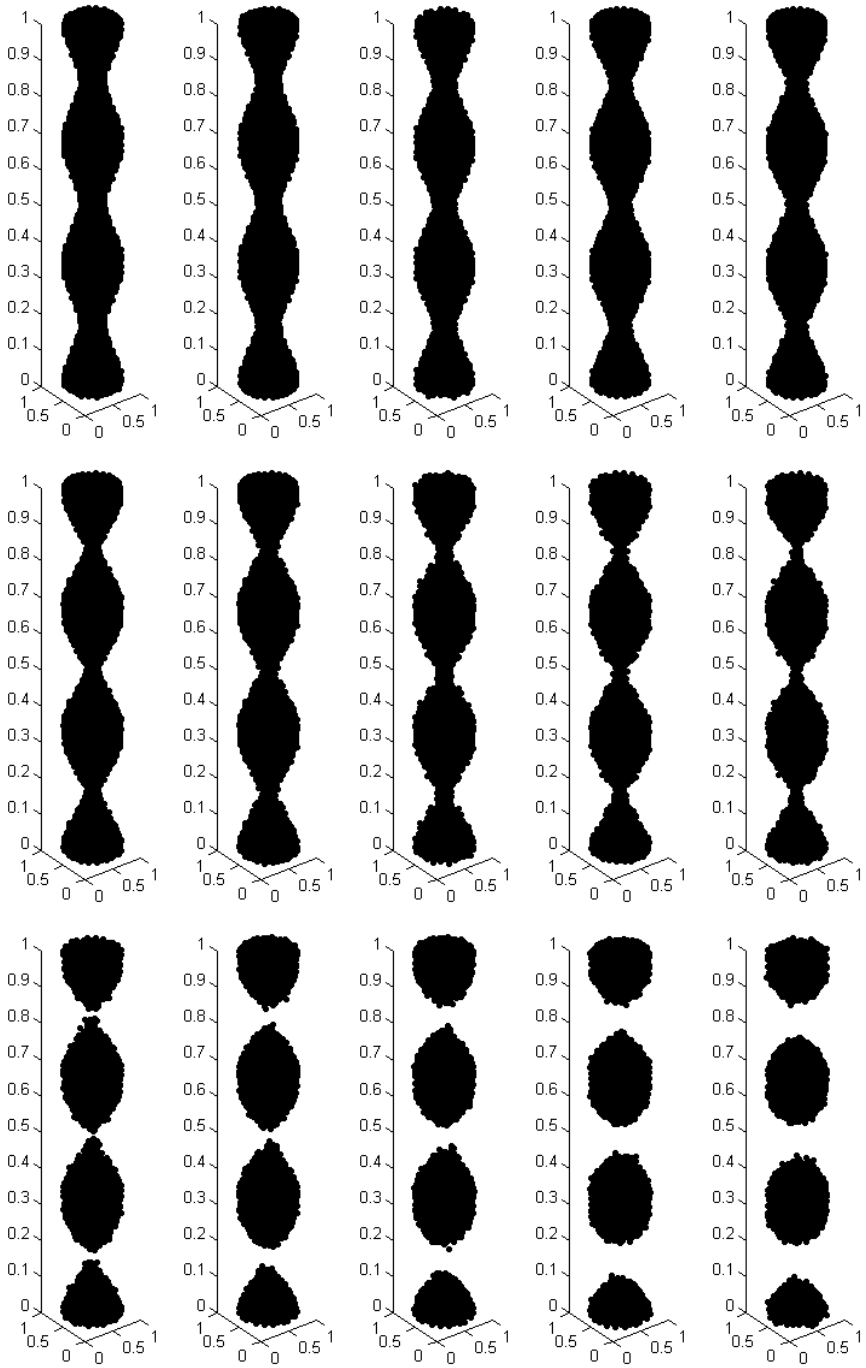

Figure 7.7: Numerical results of the fiducial model normalised with respect to the domain size and plotted from $t = 0.01$s to $t = 0.15$s with a fixed increment of $\Delta t = 0.01$s plotted from left to right, top to bottom.

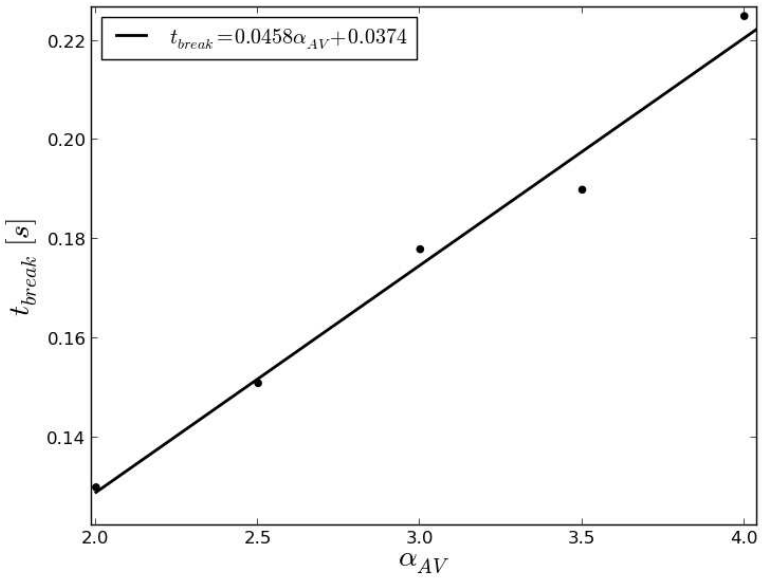

Figure 7.8: Break-up time dependence of RPI plotted as a function of artificial coefficients α_{AV}.

7.7.3 Dependence on initial perturbation

It is reasonable to expect the break-up characteristics such as the break-up time and the distance between droplets are dependent on the amplitude of the initial perturbation. A series of simulations is conducted with $\delta_a = 0.5 - 2.5$ to study the influence of initial perturbation amplitude. The numerical results are shown in Figure 7.10. Inspecting the results, it is found an increase in the perturbation decreases the break-up time of the droplet. In addition, we observed that the utilisation of a small perturbation ($\delta_a = 0.5$) results in an asymmetric necking process where the break-up has already occurred in the bottom half of the domain, whereas the break-up between the top-most and middle droplet remains in progress (see Figure 7.10 first row third column). Similar results can be found in the $\delta_a = 1$ results. Although it is possible for antisymmetric break-up to occur in nature, we suspect the asymmetry observed in our result is due to the limited resolution. For the resolution considered herein, each vertical slice has a total of 256 particles (16 particles in each direction) organised in a uniform grid. Note

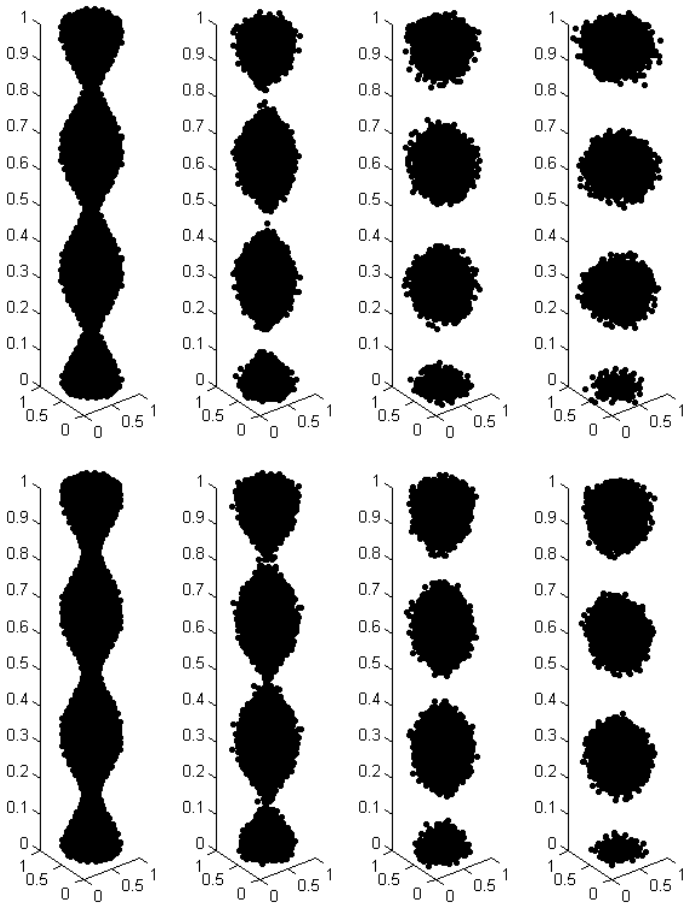

Figure 7.9: Numerical results correspond to artificial viscosity parameters $\alpha_{AV} = 3$ (top row), $\alpha_{AV} = 4$ (middle row) at times between $t = 0.1\text{s} - 0.4\text{s}$ with a fixed increment of $\Delta t = 0.1\text{s}$ plotted from left to right.

that while the setup considered here does fulfil a fundamental requirement for the linear perturbation analysis, nevertheless, this small perturbation $\delta_a = 0.5$ is beyond the resolvable scale given that each direction only has limited number of particles. In practice, the unresolved perturbation maybe responsible for the asymmetric break-up as seen in Figure 7.10.

7.7.4 Dependence on Atwood number

Since the classical solution presented in Rayleigh [6] is based on the free-surface assumption, the influence due to the ambient fluid has not been taken into account. It is therefore interesting to study the dependence on the Atwood number.

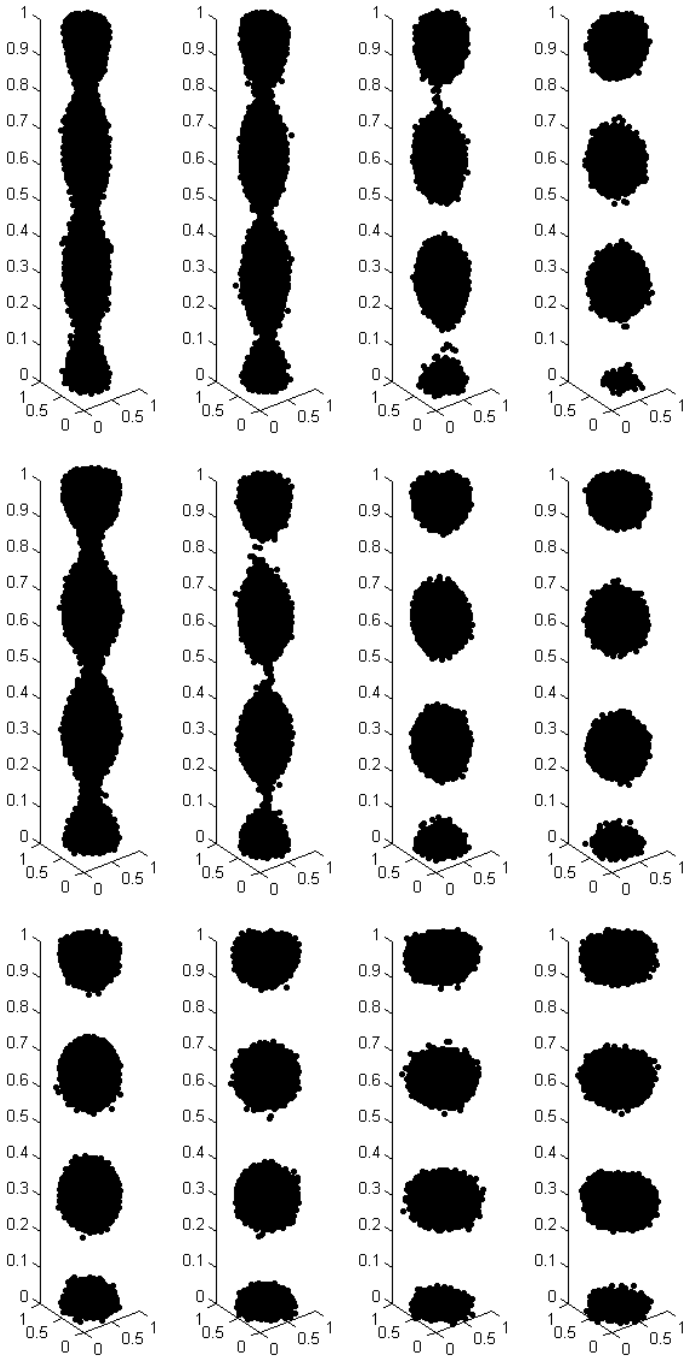

Figure 7.10: Numerical results of correspond to different initial perturbations $\delta_a = 0.5$ (top row) $\delta_a = 1$ (middle row), $\delta_a = 2$ (bottom row) plotted at $t = 0.15\text{s} - 0.3\text{s}$, with fixed increment of $\Delta t = 0.05\text{s}$ plotted from left to right.

A series of simulations were conducted by varying the density of the ambient fluid (ρ_2), while fixing the density of the jet fluid at $\rho_1 = 1000\text{kg/m}^3$. Some typical results are shown in Figure 7.11. It is found that even though the break-up occurred in all cases, the collection of SPH particles representing the droplets

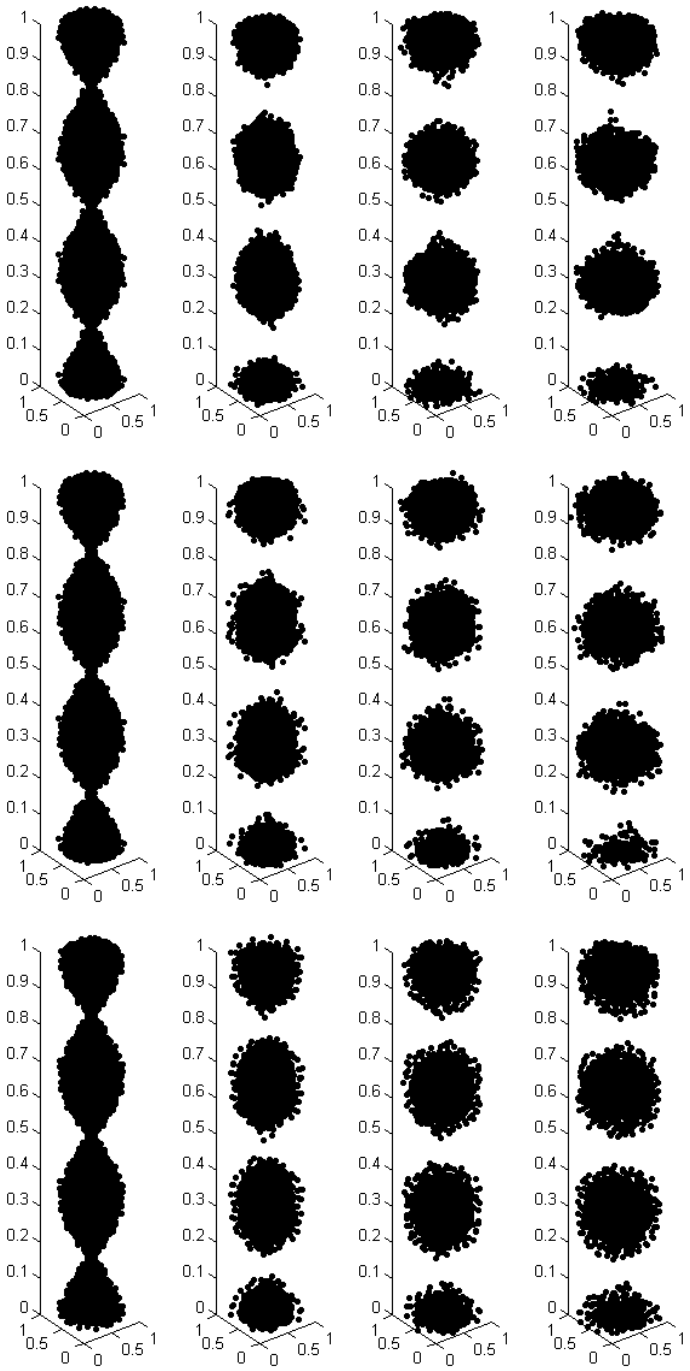

Figure 7.11: Numerical results correspond to density ratios: $\rho_1/\rho_2 = 200$ ($A_T = 0.99$) (top row), $\rho_1/\rho_2 = 100$ ($A_T = 0.98$) (middle row), and $\rho_1/\rho_2 = 20$ ($A_T = 0.96$) (bottom row) at times between $t = 0.1\text{s} - 0.4\text{s}$ with a fixed increment of $\Delta t = 0.1\text{s}$ plotted from left to right.

are strongly influenced by its surrounding ambient fluids. This is because for decreasing density ratio, the shearing motion between the jet fluid and the initially static ambient fluid becomes increasing significant. According to the multiphase

analytical growth rate presented in section 7.3, the presence of an ambient fluid should lead to a delayed break-up time compared to the free-surface case. Similar behaviour is observed in our simulations. A comparison between the extracted break-up times and the multiphase analytical growth equation (7.17) suggests the break-up time is delayed by a factor of two. This observation is consistent with our earlier findings in section 7.7.2 which suggests the delay in break-up is attributed to the viscous damping.

7.8 Summary

In this chapter, the three-dimensional Rayleigh-Plateau instability was simulated by means of multiphase SPH in conjunction with a surface tension model motivated by Adami et al. [75]. Three cases were carried out to asses the performance of the surface tension model. In the square box case, we demonstrated that in the absence of surface tension, the square droplet remains stable. In addition, the expected deformation from square to droplet is observed when surface tension is active. In the static droplet case, the surface tension was validated against the Young-Laplace pressure. The accuracy of the droplet pressure was found to be dependent on the density ratio between the fluids and the local smoothing parameter. In the oscillating droplet case, the model is validated against the Rayleigh equation [247], where the droplet pressure is overestimated by a factor of 2.13.

The three-dimensional RPI was simulated, where the effects of Ohnesorge number, initial perturbation, the Atwood number were investigated. It was found that that the break-up time increases with the artificial viscosity parameter. A linear relation between artificial viscosity and break-up time was found, with a slope of 0.046. Extrapolation to $\alpha_{AV} = 0$ corresponds to $t_{break,SPH} = 0.038$s, which deviates from the analytical break-up time by 11%. In addition, it was

found that the break-up time is linearly dependent on the amplitude of the initial perturbation, with a slope of -0.12 and an intercept of 0.33.

Our results suggest that the inertia between the jet and ambient medium in combination with the viscous effects is responsible for causing a larger scatter in low Atwood number simulations. Whereas with increasing Atwood number, the influence of the ambient fluid becomes insignificant and the break-up time approaches the analytical solution derived from the inviscid single-fluid free-surface flow approach.

While the implementation of the CSF surface model provided acceptable agreement with theoretical results, a systematic investigation is necessary to gain further quantitative understanding of the behaviour of the surface tension model. At the current development stage, `Draco` suffers from performing high resolution simulations in three-dimensions which hinders the quantitative analysis performed herein. Finally, we would like to point out that the current surface tension model is formulated for multiphase and as such requires the filling entire kernel domain with particles. As we have shown for density ratios of 100 and above, the influence of the ambient fluid is negligible. In practice, this would significantly increase the computational resources in three-dimensional simulations. Instead, we suggest surface tension models which do not require the introduction of an ambient fluid such as Kruisbrink et al. [248].

Chapter 8

Jet fragmentation

8.1 Introduction

This chapter concentrates on the numerical simulation of a hydrodynamic jet using SPH. Based upon the results presented in the earlier chapters, we investigate the fragmentation of hydrodynamic jets driven by the Kelvin-Helmholtz instability, Rayleigh-Taylor instability and Rayleigh-Plateau instability in combination with gravity. This chapter is organised as follows: section 8.3 presents the results of a KHI driven jet fragmentation, section 8.4 presents the results of a RTI driven jet fragmentation, section 8.5 presents the results of a jet fragmentation process driven by the RPI. Finally, the major research findings are summarised in section 8.6.

8.2 Literature review

Jets, collimated streams of matter that carries higher momentum than their surroundings are found in many scientific and technological applications. In astrophysics, jets plays a significant role to young stellar objects, proto-planetary nebulae as well as active galactic nuclei. In technological applications, jets are

important in precision cutting machinery, ink-jet printing technologies, combustion process of jet engine propulsion systems.

The SPH literature regarding to the simulation of jet flows can be subdivided into two categories. The first category simulates the propagation of liquid jets in a free surface flow setting where the influence of the ambient medium is not taken into account. For example, Monaghan [62] simulated jet flow under gravity and found acceptable agreement with steady and unsteady problems involving free-surfaces and moving boundaries. Hou et al. [249] simulated the impingement of a water jet onto a wall by means of single phase SPH. Although the results are in good agreement with analytical theory, the authors reported the free surface profile is heavily influenced by the artificial viscosity parameters. The second category aims to simulate the interaction of astrophysical jets [250, 251, 252, 253]; however these articles utilise the conventional SPH scheme, which is known to suffer for multiphase flow problems. At the time of writing this thesis the fragmentation of multiphase jets has not been attempted. This work presented in this chapter therefore files the gap in the current SPH literature by simulating multiphase jet fragmentation processes driven my multitude hydrodynamic instabilities that would otherwise be impossible without an appropriate multiphase scheme.

8.3 Jet fragmentation driven by Kelvin-Helmholtz Instability

This section focusses on the fragmentation of a hydrodynamic jet driven by Kelvin-Helmholtz instability. We consider the injection of a high density jet medium (ρ_1) into a low density ambient medium (ρ_2). The fluid domain is $x \in [0, L]$, $y \in [0, H]$ with an aspect ratio of $L/H = 4$. A jet of diameter $L_{jet} = 0.5H$ is injected from the inflow boundary at $x = 0$ and $0.25H \leq y \leq 0.75H$.

Its horizontal velocity profile is given by a Gaussian distribution centered at $y = 0.5H$ with a mean of $u = 1\text{m/s}$ and standard deviation of $5d_{nat}$.

In real jet systems, it is common for the initial perturbation to consist of a spectrum of frequencies which arises from the imperfection of the nozzle geometries or acoustic noise propagation within the ambient medium. To model multi-mode behaviour, an initial vertical velocity perturbation of the following form

$$f(x,y) = \left\{ \sum_{n=1}^{n=40} = \left[A_n \sin\left(\frac{2\pi n}{H} y\right) + B_n \cos\left(\frac{2\pi n}{H} y\right) \right] \right\} \frac{x}{L}, \tag{8.1}$$

is assigned to the ambient fluid particles, and the coefficients $A_n, B_n \in (0 - 10^{-4})$ are generated randomly. The perturbation function is designed such that the ambient fluid particles located downstream side experience a larger velocity perturbation than the particles located upstream side. Figure 8.1 shows the setup for the KHI driven jet fragmentation. Static ghost particles are placed at the top and bottom of the domain to allow for two outlets at $0 \leq x \leq L - 0.5L_{jet}$. The jet fragmentation is simulated with an 167456 initial particles ($d_{nat} = L/200$). The gas repulsion model is applied for interface stabilisation. The Monaghan artificial viscosity ($\alpha_{AV} = 1$, $\beta_{AV} = 2$) is used to inhabit particle interpenetration between the two gases. The viscosity model is used in combination with a Balsara switch to resolve the shearing motion near the interface.

8.3.1 Fiducial model

The KHI driven jet fragmentation setup described above is simulated for a density ratio of 5 (i.e. $\rho_1 = 5\,\text{kg/m}^3$, $\rho_2 = 1\,\text{kg/m}^3$) up to $t = 4\text{s}$. The numerical results at different times are shown in Figure 8.2, with a fixed time increment of $\Delta t = 0.25\,\text{s}$ between each panel. During the early stage of simulation $0\text{s} \lesssim \text{t} \lesssim 1\text{s}$, the shear motion between the jet and ambient fluid leads to the onset of KHI as soon as the jet particles are injected from the nozzle into the fluid domain. As expected, the

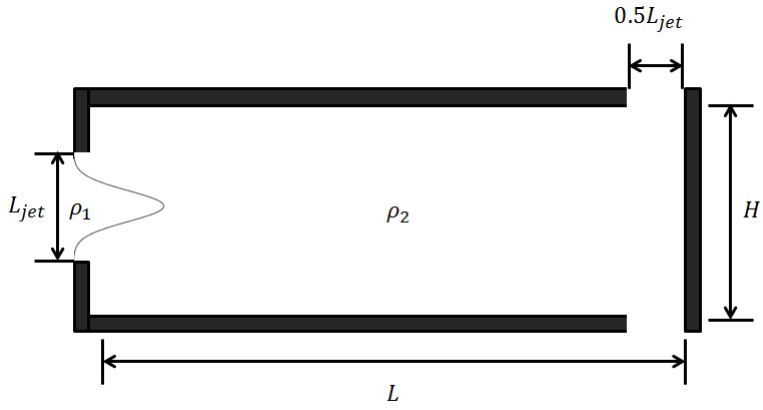

Figure 8.1: Initial setup for the KHI jet fragmentation case.

KHI grows fastest at the tip of the jet. This is because for fixed wave number and density ratio, the inviscid growth rate of the KHI is proportional to the relative velocity between fluid layers ($n_c \propto \sqrt{\Delta U}$), at which its maxima is given by the velocity at the front of the jet.

For $1.25 \lesssim t \lesssim 2$s, the KHI continues to amplify around the front of the jet. However, a full rotation of the KHI similar to those reported in chapter 5 for a density ratio of 2 is not observed. Instead, the KHI manifests to the stripping of particles near the edges of the jet (see Figure 8.2, $t = 1.25\text{s} - 1.5\text{s}$). The stripped particles then reconnect to the central body of the jet by $t = 2$s, causing the central portion of the jet $0.2L \leq x \leq 0.3L$ to undergo slight contraction.

As the jet propagates further downstream, it experiences additional perturbations from the ambient fluid. This marks the beginning of the intermediate stage of the simulation where the influence of the random perturbation becomes important. Inspecting the results at $t = 2.25$s, it is observed that the excitation of these random perturbation disrupts the symmetry at the jet front. The random perturbation begins to dominate the flow for $t \geq 2.75$s, where the asymmetric nature can be seen near the jet front and the central body of the jet at $0.3L \leq x \leq 0.4L$ (see Figure 8.2 $t \approx 3$s). During the late stage of the simulation $3.25\text{s} \lesssim \text{t} \lesssim 4$s, the random perturbation generates a body wave motion that

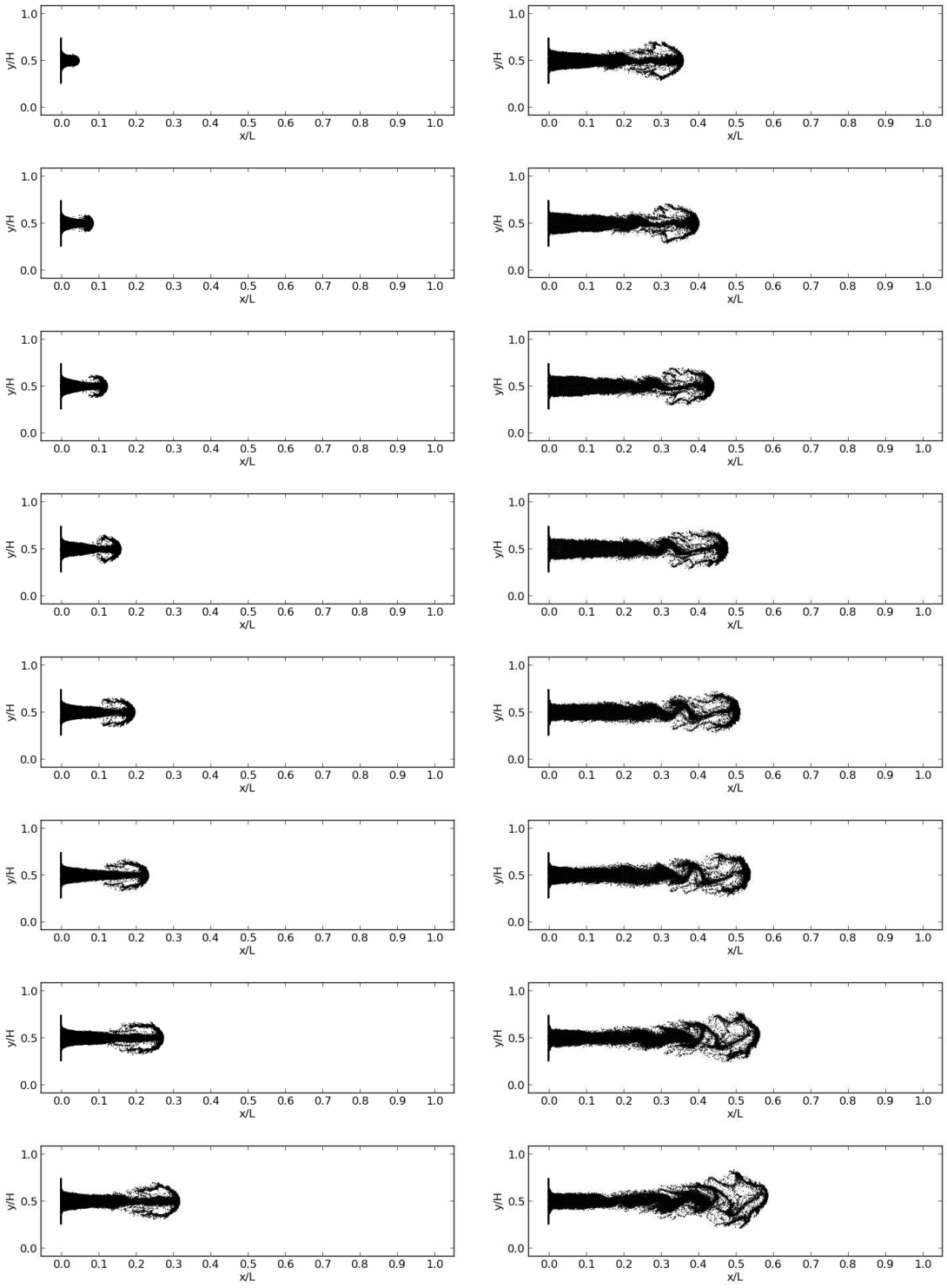

Figure 8.2: Numerical results of the fiducial model simulated up to $t = 4$s plotted with fixed time interval $\Delta t = 0.25$s from left to right, top to bottom. The left column corresponds to $0.25\text{s} \leq \text{t} \leq 2\text{s}$ and the right column corresponds to $2.25\text{s} \leq \text{t} \leq 4\text{s}$.

further distorts the symmetry of the jet. The body wave leads to the growth of secondary instabilities at the sides of the jet $0.1L \leq x \leq 0.25L$ as it continues to propagate downstream.

8.3.2 Dependence on density ratio

The influence of the density ratio is investigated by simulating the same case setup for three different inlet densities $\rho_1 = 1, 2, 10\text{kg/m}^3$ while keeping the density of the ambient fluid at $\rho_2 = 1\text{kg/m}^3$. The density ratio is denoted as $\rho_r := \rho_1/\rho_2$ hereinafter. The numerical results are shown in Figure 8.3, with a fixed time increment of $\Delta t = 0.5\text{s}$.

Inspecting the results, we found that the development of jet flow differs even at a very early stage (see Figure 8.3, $t = 0.5\text{s}$). For the $\rho_r = 1, 2$ cases, the jet front evolves into a circular shape, whereas the corresponding structure remains relatively static for the $\rho_r = 5, 10$ cases. Furthermore, the jet remains symmetric during $1\text{s} \lesssim \text{t} \lesssim 1.5\text{s}$, with the development of the KHI roll-up being most apparent at $t \approx 1.5\text{s}$ for $\rho_r = 1$. In contrast, for the higher density simulations $\rho_r \geq 5$, the shearing motion near the interface leads to the stripping of particles near the edges of the jet.

As the jet propagates further into the fluid domain, the random perturbation eventually leads to asymmetric development for the $\rho_r = 5, 10$ cases at $t \approx 3\text{s}$. Note that while the same perturbation is applied to all cases, the asymmetric behaviour of the jet arises at an earlier time for the high density ratio simulation. It is because the KHI is more pronounced for low density ratio simulations and its development dominates the jet flow, causing a delay in the excitations of random perturbations. This behaviour is best illustrated by the results at $2.5\text{s} \lesssim \text{t} \lesssim 3\text{s}$ in Figure 8.3 for the high density ratio simulation.

During the later stages $3\text{s} \lesssim \text{t} \lesssim 4\text{s}$, the growth of the random perturbations becomes obvious even in the $\rho_r = 1$ simulation. This generate a body wave

motion that further distorts the symmetry of the jet. However, the influence of the random perturbations is more important for the high density ratio simulations than that of the low density simulations (see Figure 8.3, $t = 4$s for $\rho_r = 1, 10$). Our results demonstrate in a qualitative manner that the simulation of KHI driven jet fragmentation can be achieved with an appropriate choice of multiphase scheme, artificial viscosity mode (i.e. a Balsara switch) and boundary conditions. Nonetheless, a direct comparison of our results and those reported in the mesh-based simulation literature is not possible. This is because the cases considered in the literature concern the development of a turbulent jet, whereas we focus on the development of a laminar jet injected to an ambient fluid with perturbed velocity field. In practice, the modelling of turbulent flow requires either a high resolution DNS [53, 54] or the utilisation of a turbulence model [140]. The modelling of turbulent flow is beyond the scope of this thesis.

8.4 Jet fragmentation driven by Rayleigh-Taylor Instability

This section focusses on the fragmentation of a hydrodynamic jet driven by Rayleigh-Taylor instability. The simulation setup is similar to the one used in chapter 6, except for the initial vertical position of the perturbation function. We simulate the RTI driven jet fragmentation in a two-dimensional semi-confined fluid domain $x \in [0, L]$, $y \in [0, H]$, with an aspect ratio of $L/H = 1 : 5$. A initial perturbation of the form $f(x) = 0.75H + 0.1\cos(kx)$, where $k = 2\pi/L$ is used to assign the initial fluid interface. This setup ensures the dominant RTI mode has a wavelength corresponding to the size of the horizontal domain. Static ghost particles are introduced at the sides and bottom of the fluid domain. The gas repulsion model is applied to maintain the stability of the interface. The fluid system is described by a total of $N_p = 54432$ particles, out of which 50000 are

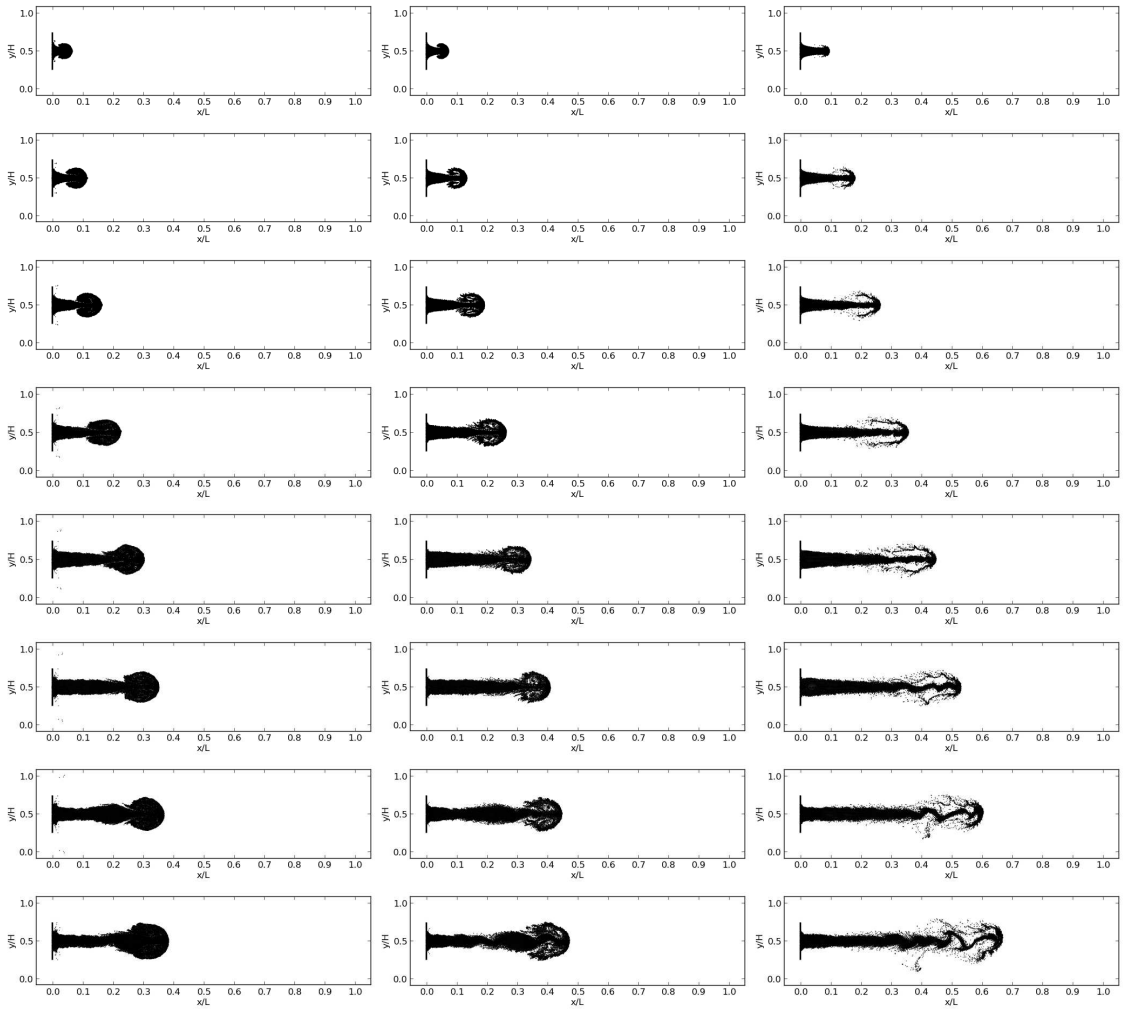

Figure 8.3: Numerical results for the KHI driven jet fragmentation of a density ratio of 1 (1^{st} column), 2 (2^{nd} column) and 10 (3^{th} column) simulated up to $t = 4$s and plotted at fixed time increment of $\Delta t = 0.5$s from top to down.

fluid particles (16670 high density particles and 33330 low density particles) and 4432 ghost particles.

8.4.1 Fiducial model

We simulate the case setup described above with the density of the top and bottom fluid being $\rho_1 = 100\text{kg/m}^3$ and $\rho_2 = 10\text{kg/m}^3$ respectively ($\rho_r = 10$). Figure 8.4 plots the simulation results at fixed time interval of $\Delta t = 0.5$s. During the initial stage $0 \lesssim t \lesssim 1[\sqrt{L/g}]$, the amplitude grows as the heavy and light fluid exchange positions. The interface remains symmetric along the vertical direction. At later times $t \geqslant 1[\sqrt{L/g}]$, the development of the bubble becomes increasing apparent as the light fluid rises toward the top of the fluid domain due to buoyancy. Similarly, the down falling jet (spike) is observed as the heavy fluid sinks towards the bottom of the fluid domain. At time $1.5 \lesssim t \lesssim 2[\sqrt{L/g}]$, the development of the RTI jet (spike) can be clearly observed. For a density ratio of 10, a full rotation which generates sides jets due to KHI is not observed. Instead, the stripping of particles near the edges of the RTI jet is clearly observed $1.5 \lesssim t \lesssim 2[\sqrt{L/g}]$. This is consistent with our earlier findings in section 8.3.

During the intermediate stage of the simulation $2.25 \lesssim t \lesssim 2.5[\sqrt{L/g}]$, the RTI jet has emerged into the fully non-linear regime, where particles near the edges of jet continue to elongate into jet-like structures. Furthermore, additional KHI modes appear both at the edges as well as the bottom of the jet (see $t \lesssim 2.5[\sqrt{L/g}]$). Finally at $t \sim 3$ the RTI jet has fully developed, with a single spike at the center and two jets one on each side of the center jet.

8.4.2 Dependence on density ratio

The influence of the density ratio is investigated by simulating the RTI jet fragmentation at three different densities ratios $\rho_1 = 20, 50, 100\text{kg/m}^3$, where the

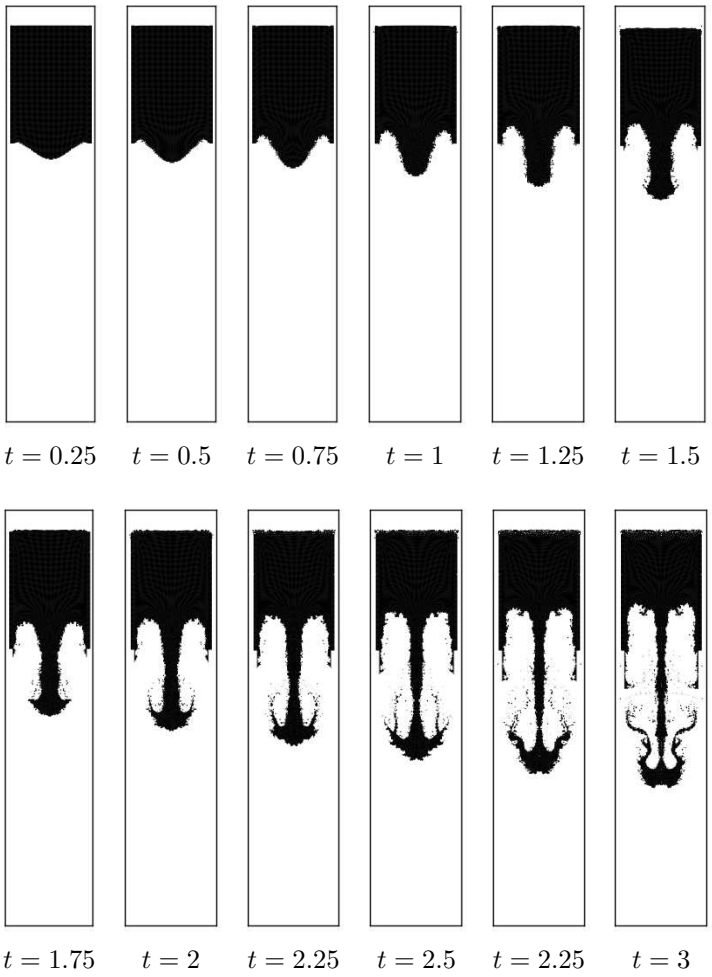

Figure 8.4: Results for RTI driven jet fragmentation of density ratio $\rho_r = 10$ plotted at fixed time-interval $\Delta t = 0.25[\sqrt{\mathrm{L/g}}]$ between $t = 0$ to $t = 3[\sqrt{\mathrm{L/g}}]$

lower density fluid is assigned to be $\rho_2 = 10\mathrm{kg/m}^3$ in all cases. The numerical results are shown in Figure 8.5. It is found that despite the density ratios, the numerical results are remarkably similar during the initial stage of the simulation $0 \lesssim t \lesssim 1[\sqrt{\mathrm{L/g}}]$. However, the results begin to deviate from each other as the development of the RTI occurs. For the lower density simulations $\rho_r = 10, 20$ the bottom of the RTI jet reassembles a circular shape. For the highest density ratio simulation considered ($\rho_r = 100$) the expansion at the bottom of the jet is completely absent. This is because the growth rate of the KHI at the jet front decreases with the density ratio. Thus, when the density ratio between the heavy and light fluid is sufficiently large, the growth of KHI becomes less relevant. The

same phenomenon applies when a solid (i.e. stone) falls under gravity in a tank of water. In this case, the water level rises due to Archimedes principle and the stone sinks towards the bottom of the tank without fragmenting into pieces.

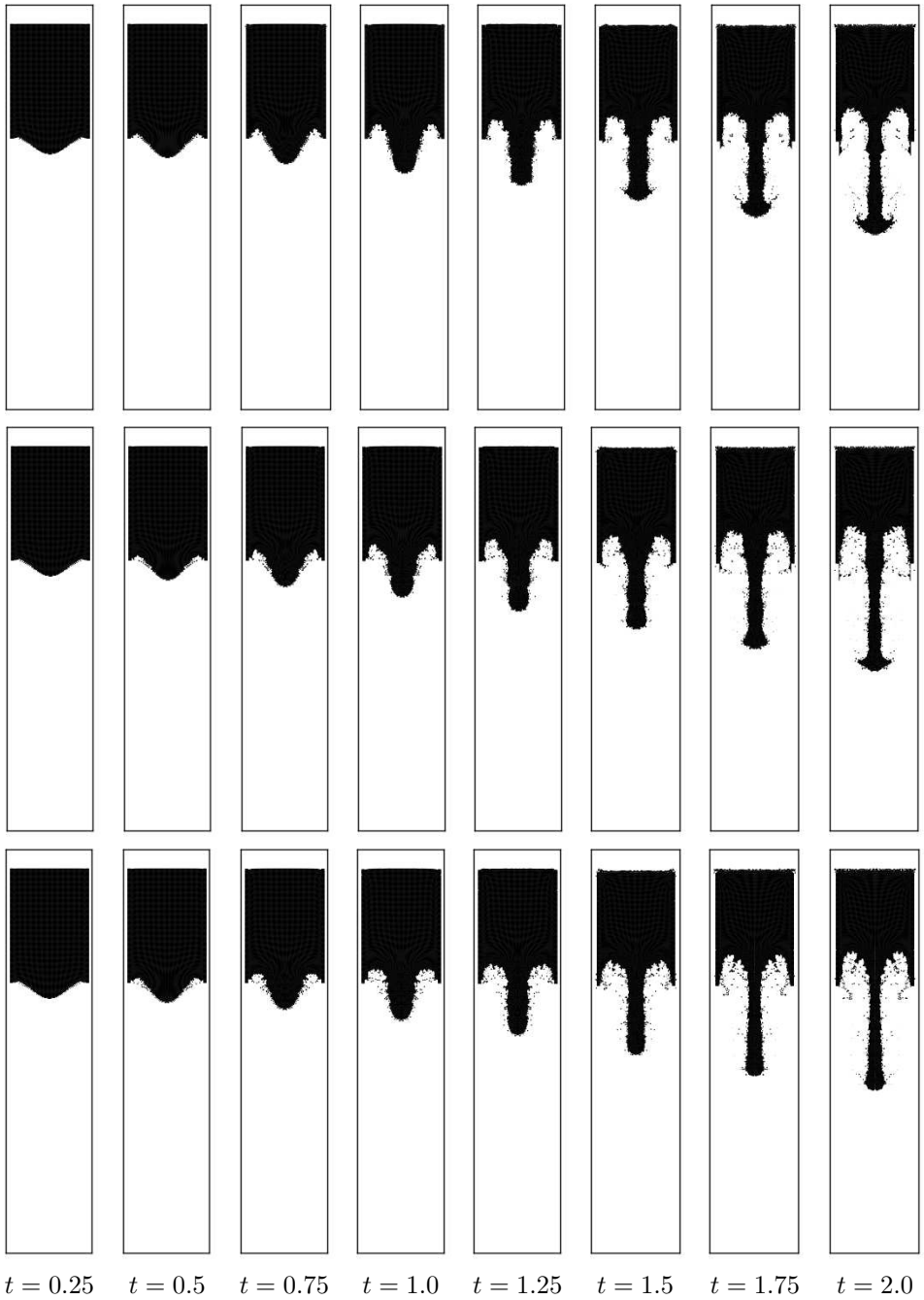

Figure 8.5: Numerical results for RTI driven jet fragmentation corresponding to different density ratios. From top to bottom the density ratios are $\rho_r = 20, 50, 100$ plotted at fixed time-interval $\Delta t = 0.25[\sqrt{\mathrm{L/g}}]$ between $t = 0$ to $t = 2[\sqrt{\mathrm{L/g}}]$.

8.5 Jet fragmentation driven by Rayleigh-Plateau Instability

This section focusses on the fragmentation of a hydrodynamic jet driven by the Rayleigh-Plateau instability, which is more commonly known as jet break-up in the engineering literature. We consider the primary break-up of an initially static jet which is suspended from the top of a vertical domain. The initial density of the jet and ambient fluid are $\rho_1 = 10^3 \text{kg/m}^3$ and $\rho_2 = 10 \text{kg/m}^3$. The dimension of the fluid domain is $x \in [0, L]$, $y \in [0, W]$, $z \in [0, H]$, where $L = 2\text{cm}$, $W = 2\text{cm}$, and $H = 3\text{cm}$. The dimension is specified such that the flow problem is dominated by surface tension. To ensure a properly filled kernel for particles near the boundaries, four layers of ghost particles are placed on each side of the domain. The particle system is described by 26136 particles ($d_{nat} = L/16$), out of which 13848 are static ghost particles and 12288 are fluid particles (1564 jet particles and 10724 ambient fluid particles).

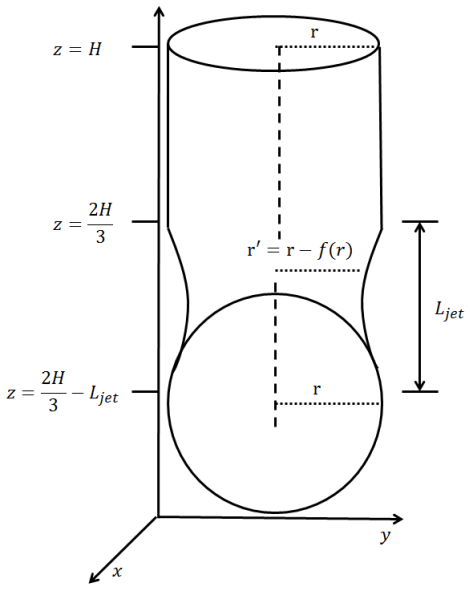

Figure 8.6: Initial setup for the RPI jet break-up.

The jet has a radius of $r_{jet} = 0.25L$ and it is centered at $(x, y) = (0.5L, 0.5W)$.

It has a length of $L_{jet} = 2L$ as measured from the top of the fluid domain. Two perturbations are applied to the initially cylindrical jet. Firstly, the initial interface of the jet in the vertical direction is prescribed by the function

$$f(z) = r_{jet} - 1.5d_{nat} \sin\left(\pi \frac{z - 0.75H + L_{jet}}{L_{jet}}\right) (0.75H - L_{jet}) \leq z \leq 0.75H, \tag{8.2}$$

which modifies the curvature of the initial cylinder to a sinusoidal shape. Secondly, a spherical shape with radius $r_{droplet} = 0.25L$ is initialised at the bottom part of the jet to ensure a smoothly varying curvature at the bottom of the jet as shown in Figure 8.6. The initial densities of the fluid jet particles are also varied accordingly to account for the pressure rise due to the surface tension. The conventional artificial viscosity model is used. We would like to point out that the Balsara switch is not used in the RPI jet simulation since the estimation of the velocity curl used in the Balsara switch is computationally expensive in three dimensions. Therefore a decision was made to apply a smaller artificial viscosity parameter $\alpha_{AV} = 0.1$, and $\beta_{AV} = 0$ throughout.

The jet break-up is simulated until $t = 0.24$s. The CFL condition recommended condition in the work of Adami et al. [75] is $\Delta t \leq 0.25\sqrt{\rho_{jet} h^3/(2\pi\sigma)}$. However, our experience suggests that this CFL condition is too relaxed, leading to the oscillation in position/velocity for particles experience surface tension force. Instead, we employ the default time-stepping criterion in `Draco`, and define the minimum and maximum allowed time-steps to be 10^{-6}s and 10^{-5}s. Since the jet is initially static, conventional dimensionless ratios such as the Weber number We and Froude number $Fr := V_z^2/(gr_o)$ are both nullity. Instead, the fluid problem is characterised by the ratio between the Weber number and Froude number $We/Fr := \rho g r_o^2/\sigma$, where the gravitational acceleration is $\vec{g} = -0.1\text{m/s}^2\hat{\text{z}}$.

8.5.1 Fiducial model

We simulate the case setup described above using the real surface tension coefficient of water $\sigma_o = 0.073$N/m at 20^oC. This corresponds to a Weber-Froude number ratio of $We/Fr \approx 0.034$, so that surface tension effects dominates. Figure 8.7 plots the simulation results for the fiducial model. The initial perturbation amplifies as soon as the simulation begins ($0 \lesssim t \lesssim 0.08$s). At the region with smallest radius $z \approx 0.4H$, the positive curvature due to the convex interface dominates the negative curvature due the concave interface. In this case, the surface tension force manifests into a necking behaviour that causes particles to migrate towards the unperturbed region of the cylinder.

The necking behaviour continues during $0.08 \lesssim t \lesssim 0.16$s, where the top part of the fluid jet contracts and the bottom part of the jet becomes increasing spherical. The formation of a spike can be observed at $t \approx 0.14$s. The jet eventually breaks at $t \approx 0.16$s, resulting in a droplet at the bottom part of the fluid domain and a patch of fluid at the upper part of the fluid domain that adheres onto the top walls represented by ghost particles. Upon closer inspection, it is found that there exist a single particle at $z \approx 0.5H$ which does not belong to either the patch of fluid at the top nor the droplet. Although similar results have been reported in both the simulation and experimental literature, we do not advocate the presence of satellite droplets due to the limited resolution used herein. We suspect the generation of satellite drops may occur if higher global resolution is considered.

8.5.2 Influence of surface tension coefficient

The influence of the surface tension coefficient is investigated by simulating the RPI for several surface tension coefficients $\sigma = 0.5\sigma_o, 2\sigma_o, 4\sigma_o$. The results are shown in Figure 8.8. As expected, the break-up occurs earlier in time as the

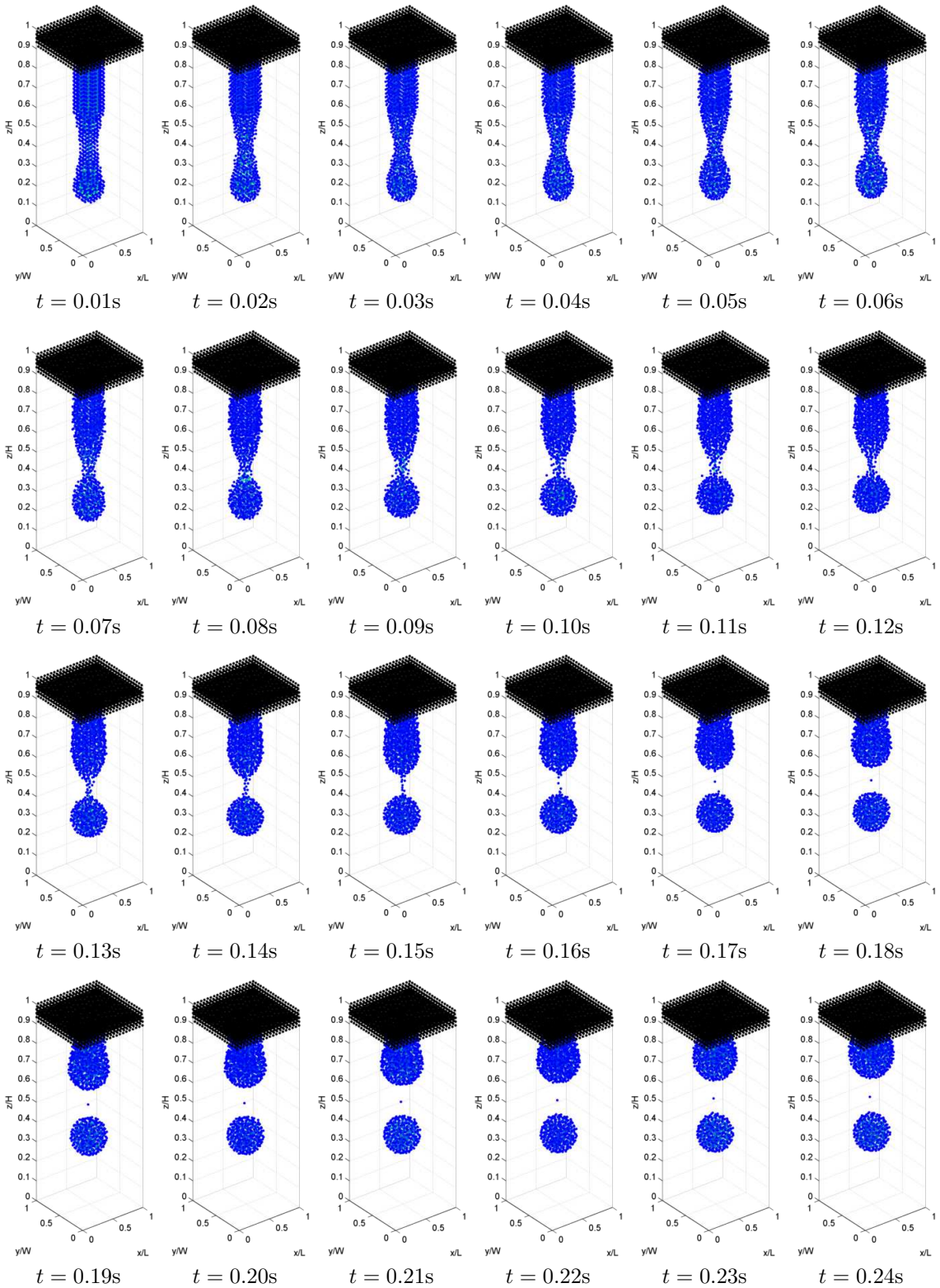

Figure 8.7: Numerical results for the fiducial simulation of the RPI driven jet break-up, with $|\vec{g}| = 0.1\text{m/s}^2$ and $\sigma_o = 0.073\text{N/m}$.

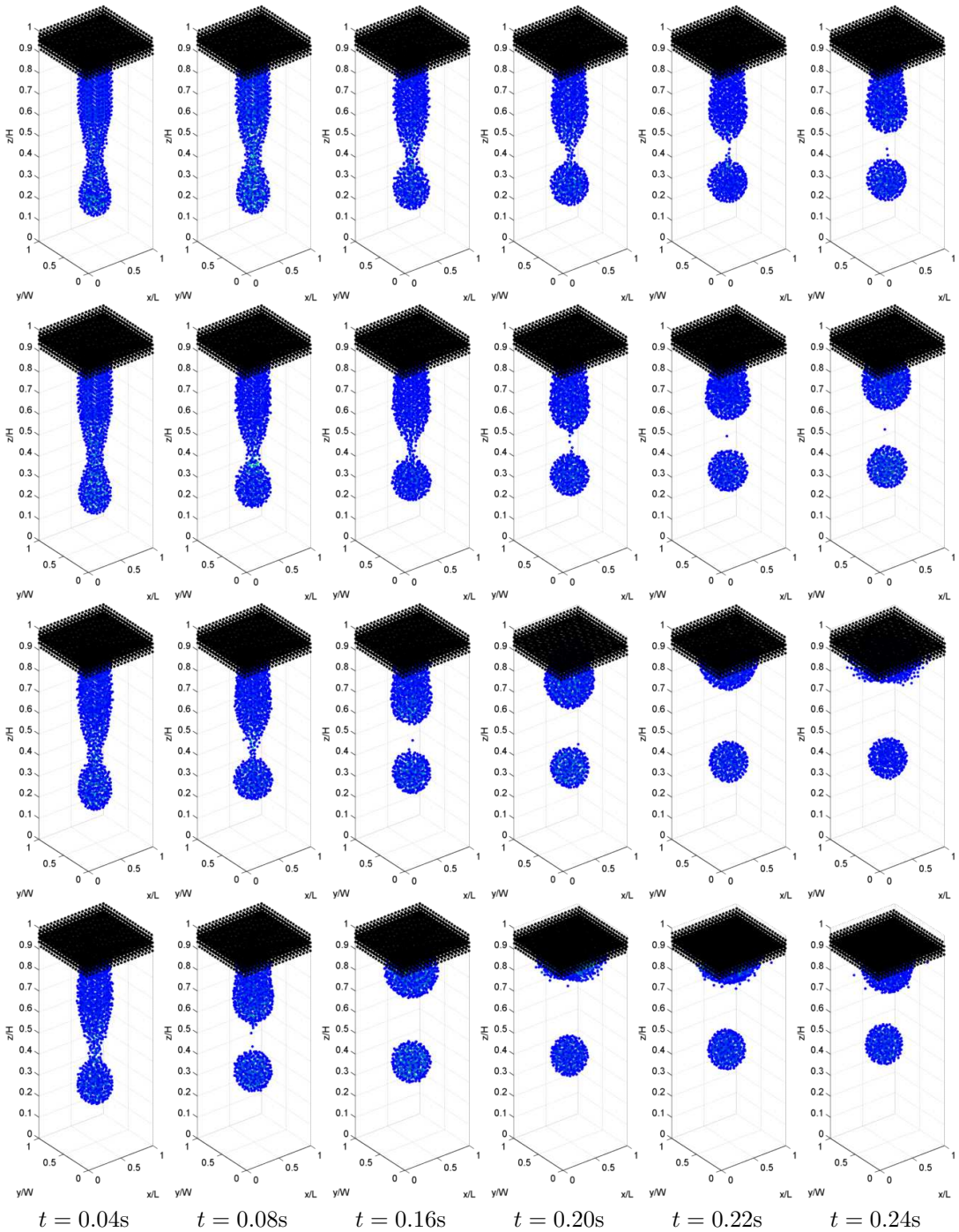

Figure 8.8: Numerical results for different surface tension coefficients plotted at fixed time instance, with a time interval $\Delta t = 0.01$s between plots. From top to bottom, $\sigma = 0.5\sigma_o$, $1\sigma_o$, $2\sigma_o$, $4\sigma_o$ and $|\vec{g}| = 0.1\text{m/s}^2$ in all cases.

surface tension coefficient increases. The extracted and theoretical break-up times are shown in Figure 8.9. It is found that the two curves exhibit the same decaying trend. In particular, a constant of 3.72 is obtained from the fitted curve and the theoretical expectation has a leading constant of 2.91. We would like to point out the discrepancy between the results and theory is primarily caused by the difference in the perturbation wave number. That is, the theoretical break-up time is derived for the wave number which gives rise to the maximum growth of the RPI applied to the entire vertical domain. Whereas the perturbation herein corresponds to a wave number of $k = \pi/L$, which is applied only to the bottom part of the cylindrical jet $(0.75H - L_{jet}) \leq z \leq 0.75H$.

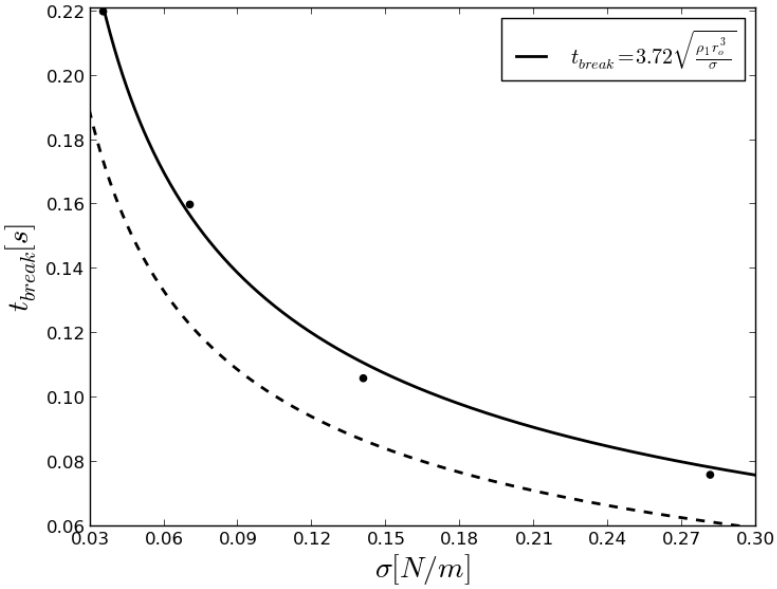

Figure 8.9: Break-up time of RPI plotted as a function of surface tension coefficient. The theoretical(numerical) break-up time is plotted as dashed line, where a slope of 2.91 is expected from theory and 3.72 is obtained from our SPH results.

8.6 Summary

In this chapter, we simulated the jet fragmentation driven by three hydrodynamical instabilities: the Kelvin-Helmholtz instability, the Rayleigh-Taylor instability

and the Rayleigh-Plateau instability. The conditions considered in our work are summarised in Table 8.1. In the fiducial model of the KHI driven jet fragmenta-

		KHI jet	RTI jet	RPI jet
initial setup	N_{dim}	2	2	3
	fluid domain scale $[m]$	1	1	0.01
	highest density ratio ρ_r	10	100	100
	inflow/outflow	✓	✓	×
	free surface	×	✓	×
physical effects	surface tension	×	×	✓
	gravitational acceleration	×	✓	✓
numerical model	Balsara switch	✓	✓	×
	Gas repulsion model	✓	✓	✓

Table 8.1: Summary of the conditions for jet fragmentations simulations considered herein.

tion ($\rho_r = 5$), we found that the KHI manifests itself by stripping off particles near the edges of the jet which excite the random perturbations near the interface and the frontal area of the jet. The excitation further disrupts the symmetry of the jet and generated a body wave motion that deflects the central portion of the jet. A series of simulations was performed to investigate the influence of the density ratio where the asymmetric behaviour of the jet was found to increases with density ratio.

The KHI driven jet simulations demonstrated the fragmentation in a qualitative manner. However, a direct comparison between our results with those reported in the mesh-based simulation literature cannot be done without an appropriate turbulence model. This is because the cases considered in the literature focus on the development of a turbulent jet whereas the flow condition herein aims to model jet flows in laminar regime. In experiments, the perturbation can be caused by the imperfection of the nozzle and the propagation of sound waves within the ambient fluid. The fragmentation of a jet is driven by the turbulence generated at the inflow boundary rather than the perturbation of the ambient fluid. As previously mentioned, a detailed model of the behaviour of turbulence

requires either a high resolution direct numerical simulation or an appropriate turbulence model [140].

The RTI jet fragmentation was simulated for four different densities ratios $\rho_r = 10, 20, 50, 100$. Similar to the KHI jet fragmentation results, it was found that the qualitative results deviate from each other as the development of the RTI occurs. For the $\rho_r = 10, 20$ simulations, the development of the center RTI jet (spike) leads to two subsequent jets one on each side of the central jet. However, these jets were completely absent in the high density ratio simulation. Furthermore, our results in previous chapters 5-6 suggest that the simulation of KHI driven flows requires high resolution $d_{nat} = L/200$. Nevertheless, at the current level of development `Draco` suffers from limited resolution such that a fully three dimensional simulation of KHI and is not possible.

The RPI driven jet fragmentation (break-up) process of an initially static liquid jet falling under gravity was simulated. The numerical results successfully demonstrate the break-up of a liquid jet submerged in a low density ambient medium. A series of simulations were performed to investigate the influence of the surface tension coefficient. As expected, the break-up time decreases with increasing surface tension, where the fitted coefficient of the break-up time dependence on surface tension coefficient was found to be greater than that of the theoretical expectation (3.72 in SPH, 2.91 in theory). This is because the perturbation herein corresponds to the wave number $k = \pi/L$ and it was applied to the bottom part of the cylindrical jet, whereas the theoretical break-up time is derived for the wave number ($k = 0.697/r_{jet}$).

Based on our experience, we suggest that a realistic simulation of a jet under gravity with inlet particles requires the modification of the current inflow boundary to take into account the acceleration due to gravity (see Table 8.1 row 1 and 4). Furthermore, the utilisation of a surface tension model that requires filling the entire domain with ambient fluid particles requires high resolution

simulation. Depending on the nature of the flow problem, in many cases the influence of the ambient medium can be ignored. For instance, in water wave modelling the presence of air is usually not taken into account, and the flow problem is modelled as a free-surface flow problem. This is however not true some applications such as high speed shear driven flow due to rapid air currents are relevant.

The SPH jet simulations carried out in this chapter provide features at the interface that would typically require additional refinement in a mesh-based CFD code. Nonetheless, due to the limited resolution we are unable to study the jet fragmentation process driven by the combination of KHI, RTI and RPI. Our experience shows a typical two-dimensional KHI driven jet fragmentation requires approximately $160K$ fluid particles, the two-dimensional RTI jet fragmentation simulation requires $50K$ fluid particles, and the three dimension RPI jet break-up requires $12K$ particles. A rough estimate indicates a three-dimensional simulation that encapsulate the effects of KHI, RTI and RPI requires approximately $75200K$ particles, which is far beyond the computational resolution offered by our current SPH code. However, we think SPH would be is good candidate for the sub-grid inter-facial models for mesh-based simulation of jet flows. In essence, SPH can be used for resolving the dynamics only at the interface whenever needed. This strategy allows researchers to benefit from the adaptive refinement capabilities of a mesh-based simulation, as well as the Lagrangian nature of SPH to resolve small scale hydrodynamic instabilities near the interface.

We would like to point out that while the initial conditions considered in this chapter are based on idealised geometries, further research on jet flows can be carried out by studying simulation conditions relevant to aero-engines such as: the jet impingement on moving walls and rapidly rotating geometries, the atomisation of jet into droplets subject to different nozzle geometries, and the control of jets in cross-flows for lubrication and cooling purposes.

Chapter 9

Conclusion and recommendations

In this thesis, we presented the results of multiphase Smoothed Particle Hydrodynamics applied to jet fragmentation driven by three hydrodynamic instabilities, namely the Kelvin-Helmholtz instability, the Rayleigh-Taylor instability, and the Rayleigh-Plateau instability. The hydrodynamic instabilities have been studied theoretically by means of linear stability analysis and numerically using our new general purpose SPH software `Draco`, developed during the course of this thesis.

9.1 Concluding remarks

The Lagrangian nature of SPH does not require the utilisation of interface tracking routines. Nevertheless, conventional SPH suffers from problems when utilised to simulate multiphase flow which have been studied extensively in this thesis. The major research findings regarding the SPH simulation of these hydrodynamic instabilities are summarised below:

- The linear stability analysis presented in chapter 2 allows for a systematic investigation of the combined Kelvin-Helmholtz instability and Rayleigh-Taylor instability occurring between two fluids. It was found that both viscosity and gravity suppress the growth of a sharp interface Kelvin-

Helmholtz instability. Whereas viscosity was found to suppress the growth of the Rayleigh-Taylor instability, gravity was found to amplify it. For an inviscid smoothed interface Kelvin-Helmholtz instability, increasing the smoothed density gradient led to more pronounced growth. In contrast, increasing the smoothed velocity gradient suppressed the linear growth rate. Finally, the growth rate of a smoothed initial interface stratified shear instability was found to be significantly smaller than the classical expectation.

- A generalised purpose SPH software `Draco` was developed to simulate multiphase flows. Prior to the development of `Draco`, significant effort was spent on the alignment between existing SPH codes `Hydra` and `MATLAB-Hydra`. The current version of `Draco` aggregated the basic components for modelling multiphase fluid dynamics problems occurring in aero-engines.

- A type of boundary condition known as a continuous wall was developed to model a non-permeable wall. We found that similar to other solid boundary concepts, fluid particles near the wall suffered from *truncated kernel* behaviour that destroyed the accuracy of SPH. In practice, it is necessary to initiate a pack of ghost particles behind the continuous wall to avoid the undesired *truncated kernel* behaviour.

- A new multiphase model based on the quasi-buoyancy correction [167] was proposed for interface stabilisation. The model was easy to implement, and yielded the expected buoyant behaviour. The model did not require calibration and demonstrated significant improvement over some multiphase schemes in the literature. However, a major disadvantage of this model was that it was only applicable to flow problems under the influence of gravity.

- A new multiphase model motivated by kinetic collision theory called the gas-repulsion model [170] was presented to model multiphase flow scenar-

ios with and without the influence of gravity. The model considers two boundary cases of particle collision, namely the elastic and inelastic cases. In the elastic case, conservation of momentum was guaranteed. Whereas for the inelastic case, a colliding particle pair obtained the same velocity. The linear combination of the two cases were then written in SPH particle form, where a constant coefficient of restitution was pre-defined to determine the elasticity of the fluid. This model demonstrated successes in many test-cases [170]. However, an extensive study would need to be carried out to quantify the actual viscosity represented by this model as well as the dependence of the inherited viscosity as a function of C_R.

- The standard SPH artificial viscosity [60] introduced spurious viscosity. This hindered the comparison between SPH and the inviscid analytical solution in the literature. The influence of spurious viscosity was found to be case dependent. In shear dominated flow problems such as the Kelvin-Helmholtz instability, the use of the standard SPH artificial viscosity was partially responsible for the suppression of the linear growth rate. Similar results were found in the small Atwood number Rayleigh-Taylor instability. In this case, the spurious viscosity causes significant suppression of the development of subsequent jets at the edge of the central region Rayleigh-Taylor instability spike. Our numerical experiments showed the issue of spurious viscosity can be remedied with the utilisation of a viscosity switch such as that introduced by Balsara [134].

- The evolution of the Kelvin-Helmholtz instability was studied systematically for different velocity and density gradients. For the sharp density, finite velocity gradient cases, the simulations were in good agreement with the analytical prediction, with the average relative error being $\langle \eta_{smooth} \rangle = 12\%$. The sharp velocity, finite density gradient cases had an

average relative error of $\langle \eta_{smooth} \rangle = 17\%$. The generalised scenario for finite width velocity and density transition layers was also studied, with an average relative error of $\langle \eta_{smooth} \rangle = 11\%$.

- The evolution of a multiphase stratified shear instability (a Kelvin-Helmholtz instability between two fluids of different densities under the influence of a gravitational field) for initial velocity and density profiles was simulated. As expected, the growth rate decreased with increasing gradient Richardson number. The growth of the instability was observed for the gradient Richardson number up to $Ri_{g,c} = 0.3$, whereas the critical Richardson number of $Ri_c = 0.25$ was reported in classical hydrodynamics for sharp interfaces.

- For the single-mode Rayleigh-Taylor instability, the SPH simulation results were consistent with the sharp interface viscous growth rate. In particular, the constant of proportionality of the terminal velocity $\Psi_{SPH} = 0.22$ was in good agreement with the predictions from the drag buoyancy model [68, 233, 234, 236]. For the multi-mode Rayleigh-Taylor instability subjected to random perturbations, the thickness of the mixing layer generated by the merging bubbles and spikes was consistent with the self-similar relation in the literature with $\Theta = 0.048$ in the SPH simulation, as opposed to $\Theta = 0.04 - 0.05$ in the literature [71, 72].

- The three-dimensional Rayleigh-Plateau instability was simulated up to a density ratio of 1000. It was found that the break-up time increased with the artificial viscosity parameter, with a slope of 0.046. Extrapolation of the break-up time to no artificial viscosity case led to $t_{break,SPH} = 0.038$s, which deviated from analytical break-up time by 11%. A major disadvantage of the multiphase surface tension model proposed by Adami et al. [75] was the requirement of filling the entire domain with SPH particles. This

was however impractical as certain real-life applications of surface tension driven flows (e.g. droplets merging, droplet impingement onto a solid wall) are usually treated as free-surface flows.

9.2 Recommendations for future work

- The software code `Draco` utilised in this thesis is implemented as a serial CPU code. Given the limitations of running high resolution simulations, a parallel version of the code `Draco-GPU` is currently under development for our industrial partner. However, it is worth pointing out that parallel SPH implementations (e.g. `Gadget-2.0`, `SPHysics`) are already publicly available. In particular, very often modification of SPH scheme are distributed among the astrophysics community for `Gadget-2.0` [109, 153] so that researchers can focus on further advancing the numerical methodology. We strongly encourage the adoption of these open-source codes rather than developing a parallel implementation from scratch unless there is a clear advantage from a commercial point of view.

- At the current stage, there is no turbulence model implemented in `Draco`. In order to model the effects of turbulence, one can either make use of a turbulence model or direct numerical simulation which simulates the dynamics of the entire range of spatial and temporal turbulence scales [125, 126, 254]. The commonly used turbulence model in SPH is a Large Eddy Simulation model used in conjunction with a Smagorinsky model for the sub-particle turbulence [255]. It is also worth commenting that SPH loses consistency whenever particles are irregularly distributed within the kernel. However, in a turbulent flow, particles would be naturally irregularly distributed. In this case, the SPH kernel density estimate would be inaccurate. Therefore, we recommend further research in combining consistency restoration

schemes [129, 256] and turbulence modelling in SPH.

- The standard SPH viscosity and its variants have been widely applied in the weakly-compressible SPH community. However, it is found that viscosity switches are rarely used in weakly-compressible SPH literature. We suspect that this is because the majority of investigations carried out by the weakly-compressible SPH community aim to model gravity driven flows (e.g. dam break, ocean wave propagation) where viscosity plays a less significant role than topics considered in this thesis. Nevertheless, our experience suggests the use of standard artificial viscosity in SPH introduces spurious shear viscosity which makes the comparison between SPH results and the analytical solution extremely difficult. In many cases, this results in fine tuning of the artificial viscosity parameters to obtain the desired solution. Therefore, we strongly encourage the weakly-compressible SPH community to adopt the use of a viscosity switch similar to the Balsara switch [134] considered in this thesis and the ones presented in the literature [152, 153].

- For multiphase fluid problems with rapid change of gradient in the physical quantities (e.g. density, velocity), it may be useful to consider the utilisation of adaptive particle splitting and merging schemes [257, 258] to enable resolution refinement near the interface.

- While the multi-mass setup approach used in this thesis compromise for resolution, it introduces a mass discontinuity which requires further investigation. In particular, we would encourage the utilisation of the switch introduced by Read and Hayfield [153].

- Given the success in resolving the Kelvin-Helmholtz instability, stratified shear instability and the Rayleigh-Taylor instability, it is interesting to extend the research to study the combined Rayleigh-Taylor instability and

Kelvin-Helmholtz instability and compare the extracted growth rate from SPH with the linear growth rate presented in chapter 2.

- We think the work presented in this thesis (numerical methods and the software `Draco`) opens a new avenue of research topics for simulating low Mach number astrophysical and geophysical flows with SPH. For instance, the buoyancy and gas-repulsion model can be used to study the multiphase Rayleigh-Benard convection (RBC), which is responsible for the heat transport from the planetary core to the outer layers of terrestrial bodies. In particular, the weakly-compressible SPH approach herein offers the choice of temperature dependent equation of state (modified Tait EoS) or the classical Boussinesq approximation, which is uncommon in existing mesh-based CFD software. Therefore, we think it is interesting to conduct further exploration studies of the multiphase RBC by means of SPH. A problem that is closely related to the multiphase RBC is the double-diffusive convection (a.k.a semi-convection). The double-diffusive convection is driven by two density gradients with different rates of diffusion such as the salinity and temperature. Recently, there has been speculation that the double-diffusive convection may play a role in the formation of subsurface ice pockets in Jupiter's moon Europa, a particular geophysical environment that might lead to conditions that harvest life [259]. Similarly, our work can be further utilised to conduct numerical simulation of hydrothermal vent activities, which is another plausible candidate that provides the chemical and biological conditions of origin of life [260].

Appendix 1

9.2.1 Derivation of spatio-temporal RTI

Suppose a two initially static fluid system with densities ρ_1 and ρ_2, where $\rho_1 > \rho_2$ is subjected to a constant gravitational acceleration, and the fluid is separated by an spatio-temporal moving interface $y = y_o + \eta(x,t)$. If the fluids are both incompressible, irrotational and the growth of the initial perturbation satisfies the Laplace equation

$$\nabla^2 \Phi_{1,2}(x,y,t) = 0, \tag{9.1}$$

where Φ_1 and Φ_2 are the scalar velocity potentials for the corresponding fluids. The kinematic boundary condition (2.21) simplifies to

$$\hat{v} = \frac{\partial \eta}{\partial t} \quad y = y_o + \eta(x,t). \tag{9.2}$$

Substituting the velocity potential into (9.2) and eliminating all quadratic terms gives

$$\frac{\partial \eta}{\partial t} - \frac{\partial \Phi_{1,2}}{\partial y} = 0 \quad y = y_o + \eta(x,t). \tag{9.3}$$

Given the Bernoulli equation[94]

$$\frac{\partial \Phi}{\partial t} + \frac{1}{2} \left\| \nabla \Phi \right\|^2 + g\eta + \frac{P}{\rho} = 0, \tag{9.4}$$

and omitting the second order term gives

$$\frac{\partial \Phi}{\partial t} + g\eta + \frac{P}{\rho} = 0. \tag{9.5}$$

Rearranging (9.5) and equating the pressure across the interface (i.e. $P_1 = P_2$) yields

$$\rho_1 \frac{\partial \Phi_1}{\partial t} + \rho_1 g\eta = \rho_2 \frac{\partial \Phi_2}{\partial t} + \rho_2 g\eta \quad y = y_o + \eta(x,t). \tag{9.6}$$

Assuming the initial perturbation has the form $\eta(x,0) = \epsilon_o \cos(kx)$. The Laplace equation (9.1) subjected to the boundary conditions (9.3) and (9.6) is an initial boundary value problem that can be solved using separation of variables. The proposed eigenfunctions are

$$\Phi_i(x,y,t) = \phi(y,t)\cos(kx), \tag{9.7}$$

$$\eta(x,t) = a(t)\cos(kx), \tag{9.8}$$

where $a(t)$ is defined as the dynamic amplitude of the perturbation. The initial condition requires $a(0) = \epsilon_o$ and $a_t|_{t=0} = 0$. Substituting (9.7) into (9.1) leads to a second order ordinary differential equation.

$$\frac{\partial^2 \phi_i}{\partial y^2} - k^2 \phi_i = 0 \qquad i \in 1,2 \tag{9.9}$$

The general solution of (9.9) has the form

$$\phi_i = a_i(t)\left(\Lambda_1 e^{ky} + \Lambda_2 e^{-ky}\right) \qquad i \in 1,2. \tag{9.10}$$

To ensure boundedness of the solution, it is required that $\phi_i \to 0$ as $y \to \pm\infty$. Therefore, the velocity potentials have the form

$$\Phi_1(x,y,t) = A_1(t)e^{-ky}\cos(kx) \quad y > y_o \tag{9.11}$$

$$\Phi_2(x,y,t) = A_2(t)e^{ky}\cos(kx) \quad y < y_o. \tag{9.12}$$

Applying the kinematic boundary condition (9.3) and dynamic boundary condition (9.6) at the interface yields a second order homogeneous ordinary differential equation for $a(t)$,

$$\frac{d^2a(t)}{dt^2} - kA_T g a(t) = 0. \tag{9.13}$$

Its general solution is

$$a(t) = C_1 e^{n_c t} + C_2 e^{-n_c t}, \tag{9.14}$$

where the constants C_1 and C_2 depend on the initial and boundary conditions, and the inviscid growth rate is given by $n_c = \sqrt{A_T g k}$.

Appendix 2

9.2.2 SPH spatial discretisation error

Proof. The spatial discretisation error $|\langle f(\vec{r})\rangle - f(r)|$ is bounded by $\mathcal{O}(h^2)$.

$$
\begin{aligned}
|\langle f(\vec{r})\rangle - f(r)| &= \left|\frac{1}{2}\frac{d^2 f}{d\vec{r}^2}\int_\Omega (r-r')^2 W(\vec{r}-\vec{r}',h)d\vec{r}\right| && (9.15)\\
&\leq \left|\frac{1}{2}\frac{d^2 f}{d\vec{r}^2}\right|\left|\int_\Omega (r-r')^2 W(\vec{r}-\vec{r}',h)|d\vec{r}\right| && (9.16)\\
&\leq \left|\frac{1}{2}\frac{d^2 f}{d\vec{r}^2}\right|\left|\int_\Omega (\kappa h)^2 W(\vec{r}-\vec{r}',h)|d\vec{r}\right| && (9.17)\\
&\leq (\kappa h)^2\left|\frac{1}{2}\frac{d^2 f}{d\vec{r}^2}\right|\left|\int_\Omega W(\vec{r}-\vec{r}',h)|d\vec{r}\right| && (9.18)\\
&\leq \frac{\kappa^2}{2}\left|\frac{d^2 f}{d\vec{r}^2}\right| h^2 && (9.19)\\
&\leq C_o h^2 && (9.20)\\
&\approx \mathcal{O}(h^2). && (9.21)
\end{aligned}
$$

9.2.3 Spatial derivatives of radially symmetric kernels

The proof of three important identities useful for the construction of SPH fluid dynamical equations in section 3.8 are shown here. The identities concerns the spatial derivatives of kernel functions of two particles $\{j,k\}$ with respect to the position of the particle of interest i.

Proof. Spatial derivative property of distance between two particles with respect

to the particle of interest

$$\begin{aligned}
\frac{\partial|\vec{r}_j-\vec{r}_k|}{\partial\vec{r}_i} &= \frac{\partial[(\vec{r}_j-\vec{r}_k)\cdot(\vec{r}_j-\vec{r}_k)]^{\frac{1}{2}}}{\partial\vec{r}_i} \\
&= \left(\frac{\partial\vec{r}_j}{\partial\vec{r}_i}-\frac{\partial\vec{r}_k}{\partial\vec{r}_i}\right)\frac{(\vec{r}_i-\vec{r}_k)}{[(\vec{r}_j-\vec{r}_k)\cdot(\vec{r}_j-\vec{r}_k)]^{\frac{1}{2}}} \\
&= \frac{(\delta_{ji}-\delta_{ki})(\vec{r}_j-\vec{r}_k)}{|\vec{r}_j-\vec{r}_k|} \\
\therefore \frac{\partial|\vec{r}_j-\vec{r}_k|}{\partial\vec{r}_i} &= \frac{(\delta_{ji}-\delta_{ki})(\vec{r}_j-\vec{r}_k)}{|\vec{r}_j-\vec{r}_k|}
\end{aligned} \tag{9.22}$$

Proof. Transitive property for SPH kernel gradient with respect to the position of the particle of interest

$$\begin{aligned}
\nabla_i W_{jk} &= \frac{\partial W_{jk}}{\partial\vec{r}_i} \\
&= \frac{\partial W_{jk}}{\partial|\vec{r}_{jk}|}\frac{\partial|\vec{r}_j-\vec{r}_k|}{\partial\vec{r}_i} \\
&= \frac{\partial W_{jk}}{\partial|\vec{r}_{jk}|}\frac{(\vec{r}_j-\vec{r}_k)}{|\vec{r}_j-\vec{r}_k|}(\delta_{ji}-\delta_{ki}) \\
&= \nabla_j W_{jk}(\delta_{ji}-\delta_{ki}) \\
\therefore \nabla_i W_{jk} &= \nabla_j W_{jk}(\delta_{ji}-\delta_{ki})
\end{aligned} \tag{9.23}$$

Proof. Asymmetric property of SPH kernel gradient

$$\begin{aligned}
\nabla_i W_{ij} &= \frac{\partial W_{ij}}{\partial\vec{r}_i} \\
&= \frac{\partial W_{jk}}{\partial|\vec{r}_{ij}|}\frac{\partial|\vec{r}_{ij}|}{\partial\vec{r}_i} \\
&= \frac{\partial W_{jk}}{\partial|\vec{r}_{ij}|}\frac{\partial\vec{r}_{ij}}{\partial|\vec{r}_i|} \\
&= -\frac{\partial W_{jk}}{\partial|\vec{r}_{ij}|}\frac{\partial\vec{r}_{ij}}{\partial|\vec{r}_j|} \\
&= -\nabla_j W_{ij} \\
\therefore \nabla_i W_{ij} &= -\nabla_j W_{ij}
\end{aligned} \tag{9.24}$$

9.2.4 Galilean invariance and conservation properties

In the section, we show mathematically that SPH is strictly Galilean invariant and satisfy conservation properties in classical mechanics provided that the same scalar function ϕ is used throughout. The proofs shown herein closely reassembles earlier works for standard SPH [118, 137]. To simplify the derivations, a new variable Ψ is introduced to account for the partial contribution of a particle to the pressure gradient term

$$\Psi_i = \frac{P_i}{\rho_i^2}\frac{\phi_i}{\phi_j}. \tag{9.25}$$

Furthermore, the inter-particle pressure gradient term as given by $\Psi_{ij} = \Psi_i + \Psi_j$ is symmetric (i.e. $\Psi_{ij} = \Psi_{ji}$).

Galilean invariance

A major advantage that SPH has over Eulerian mesh-based hydrodynamic code is being Galilean invariant [58, 118, 137]. To demonstrate this property, one can consider expressing a particle initially residing in a reference from $\{0\}$ undergoes the following coordinate transform

$$\begin{aligned} \vec{r}_i^{\{1\}} &= \vec{r}_i^{\{0\}} + \vec{V}_o t \\ \vec{v}_i^{\{1\}} &= \vec{v}_i^{\{0\}} + \vec{V}_o. \end{aligned} \tag{9.26}$$

For illustration purpose, we only consider the momentum equation (3.43). The Galilean invariance of continuity equation(3.101) and energy equation (3.103)

can be shown in the same fashion. Substituting ($\vec{r}_i^{\,1}$, $\vec{v}_i^{\,1}$) into equation (3.43)

$$\begin{aligned}
\frac{D\vec{v}_i^{\{1\}}}{Dt} &= -\sum_j m_j(v_i^{\{1\}} - v_j^{\{1\}})\Psi_{ij}\nabla_i W_{ij} \\
&= -\sum_j m_j(\vec{v}_i^{\{0\}} + \vec{V}_o - \vec{v}_j^{\{0\}} - \vec{V}_o)\Psi_{ij}\nabla_i W_{ij} \\
&= -\sum_j m_j(\vec{v}_i^{\{0\}} - \vec{v}_j^{\{0\}})\Psi_{ij}\nabla_i W_{ij} \\
&= \frac{D\vec{v}_i^{\{0\}}}{Dt}.
\end{aligned} \tag{9.27}$$

Conservation of momentum

To validate the conservation of momentum, we consider a particle system comprises of N_p particles. The total linear momentum is given by the sum of the linear momentum of individual particles $\vec{P} = \sum_i^{N_p} m_i\vec{v}_i$. Assuming the mass is independent of time, the change in total momentum ($\vec{P}$) with respect to time is

$$\begin{aligned}
\frac{d\vec{P}}{dt} &= \sum_i^{N_p} m_i \frac{D\vec{v}_i}{Dt} \\
&= \sum_i^{N_p}\sum_j^{N_p} -m_i m_i \Psi_{ij}\nabla_j W_{jq} \\
&= -\frac{1}{2}\left(\sum_i^{N_p}\sum_j^{N_p} m_i m_i \Psi_{ij}\nabla_i W_{ij} + \sum_i^{N_p}\sum_j^{N_p} m_i m_i \Psi_{ij}\nabla_i W_{ji}\right) \\
&= -\frac{1}{2}\left(\sum_i^{N_p}\sum_j^{N_p} m_i m_j \Psi_{ij}\nabla_i W_{ij} + \sum_j^{N_p}\sum_i^{N_p} m_j m_i \Psi_{ji}\nabla_j W_{ji}\right) \\
&= -\frac{1}{2}\sum_{ij}^{N_p} m_i m_j \Psi_{ij}(\nabla_i W_{ij} + \nabla_j W_{ji}) \\
&= 0.
\end{aligned} \tag{9.28}$$

Conservation of angular momentum

For a system of N_p particles, the total angular momentum is given by $\vec{L} = \sum_i^{N_p} m_i \vec{p}_i$.

$$
\begin{aligned}
\frac{d\vec{L}}{dt} &= \sum_i^{N_p} m_i \vec{r}_i \times \frac{D\vec{v}_i}{Dt} \\
&= -\sum_i^{N_p} m_i \vec{r}_i \times \sum_j^{N_p} m_j \Psi_{ij} \nabla_i W_{ij} \\
&= -\frac{1}{2}\left(\sum_i^{N_p} \sum_j^{N_p} m_i m_j \Psi_{ij} \vec{r}_i \times \frac{\partial W_{ij}}{\partial |\vec{r}_{ij}|} \frac{\vec{r}_{ij}}{|\vec{r}_{ij}|} + \sum_i^{N_p} \sum_j^{N_p} m_i m_j \Psi_{ij} \vec{r}_i \times \frac{\partial W_{ij}}{\partial |\vec{r}_{ij}|} \frac{\vec{r}_{ij}}{|\vec{r}_{ij}|} \right) \\
&= -\frac{1}{2}\left(\sum_i^{N_p} \sum_j^{N_p} m_i m_j \Psi_{ij} \vec{r}_i \times \frac{\partial W_{ij}}{\partial |\vec{r}_{ij}|} \frac{\vec{r}_{ij}}{|\vec{r}_{ij}|} + \sum_j^{N_p} \sum_i^{N_p} m_j m_i \Psi_{ji} \vec{r}_j \times \frac{\partial W_{ij}}{\partial |\vec{r}_{ij}|} \frac{\vec{r}_{ji}}{|\vec{r}_{ij}|} \right) \\
&= -\frac{1}{2}\left(\sum_{ij}^{N_p} m_i m_j \Psi_{ij} (\vec{r}_i - \vec{r}_j) \times \frac{\partial W_{ij}}{\partial |\vec{r}_{ij}|} \frac{\vec{r}_{ij}}{|\vec{r}_{ij}|} \right) \\
&= -\frac{1}{2}\left(\sum_{ij}^{N_p} \frac{m_i m_j \Psi_{ij}}{|\vec{r}_{ij}|} \frac{\partial W_{ij}}{\partial |\vec{r}_{ij}|} \vec{r}_{ij} \times \vec{r}_{ij} \right) \\
&= 0.
\end{aligned}
\tag{9.29}
$$

Conservation of energy

For a system of N_p particles, the total energy is given by $E = \sum_i^{N_p} m_i \left(e_i + \frac{1}{2}\vec{v}_i \cdot \vec{v}_i\right)$. The change in total energy with respect to time is therefore

$$\begin{aligned}
\frac{dE}{dt} &= \sum_i^{N_p} m_i \left(\frac{De_i}{Dt} + \vec{v}_i \cdot \frac{D\vec{v}_i}{Dt}\right) \\
&= \sum_i^{N_p} m_i \left[\sum_j^{N_p} m_j \Psi_i \vec{v}_{ij} \cdot \nabla_i W_{ij} - \vec{v}_i \cdot \sum_j^{N_p} m_j \Psi_{ij} \nabla_i W_{ij}\right] \\
&= -\sum_i^{N_p}\sum_j^{N_p} m_i m_j \Psi_i \vec{v}_j \cdot \nabla_i W_{ij} - \sum_i^{N_p}\sum_j^{N_p} m_i m_j \Psi_j \vec{v}_i \cdot \nabla_i W_{ij} \\
&= -\sum_i^{N_p}\sum_j^{N_p} m_i m_j \Psi_i \vec{v}_j \cdot \nabla_i W_{ij} - \sum_j^{N_p}\sum_i^{N_p} m_j m_i \Psi_i \vec{v}_j \cdot \nabla_j W_{ji} \\
&= -\sum_{ij}^{N_p} m_i m_j \Psi_i \vec{v}_j \cdot (\nabla_i W_{ij} + \nabla_j W_{ji}) \\
&= -\sum_{ij}^{N_p} m_i m_j \Psi_i \vec{v}_j \cdot (\nabla_i W_{ij} + \nabla_j W_{ij}) \\
&= 0.
\end{aligned} \tag{9.30}$$

Bibliography

[1] Raspa, V., Gaubert, C., Thiria, B.. Manipulating thrust wakes: A parallel with biomimetic propulsion. Europhysics Letters 2012;97(4):44008.

[2] Bhunia, S.K., Lienhard, J.H.. Splattering during Turbulent Liquid jet Impingement on Solid Targets. Journal of Fluids Engineering 1994;116:338–344.

[3] Lim, T.T., New, T.H., Luo, S.C.. Scaling of trajectories of elliptic jets in crossflow. AIAA Journal 2006;44:3157–3160.

[4] Couchman, H., Thomas, P., Pearce, F.. Hydra: an Adaptive-Mesh implementation of P 3M-SPH. Astrophysical Journal 1995;452:797–813.

[5] Chandrasekhar, S.. Hydrodynamic and hydromagnetic stability. Clarendon Press, Oxford; 1961.

[6] Rayleigh, J.W.S.. On the instability of jets. Proceedings of the London Mathematical Society 1879;10:4–10.

[7] Wang, L.F., Xue, C., Ye, W.H., Li, Y.J.. Destabilizing effect of density gradient on the Kelvin-Helmholtz Instability. Physics of Plasmas 2009;16(11):112104.

[8] Hartigan, P.. Shock waves in outflows from young stars. In: Jets in Young Stellar Objects. Springer; 2003, p. 111–122.

[9] Lada, C.J.. Cold outflows, energetic winds, and enigmatic jets around young stellar objects. Annual review of astronomy and astrophysics 1985;23(1):267–317.

[10] Mellema, G., Frank, A.. Outflow collimation in young stellar objects. Monthly Notices of the Royal Astronomical Society 1997;292(4):795–807.

[11] Huggins, P.. Jets and tori in proto-planetary nebulae. The Astrophysical Journal 2007;663(1):342.

[12] Sahai, R.. Sowing the seeds of asymmetry: Jet-like outflows in proto-planetary nebulae and agb stars. In: Asymmetrical Planetary Nebulae III: Winds, Structure and the Thunderbird; vol. 313. 2004, p. 141.

[13] Ferrari, A.. AGN jet Modeling: Setting the Stage. In: Virtual Astrophysical Jets. Springer; 2004, p. 15–26.

[14] Falcke, H., Biermann, P.L.. Galactic jet sources and the agn connection. arXiv preprint astro-ph/9506138 1995;.

[15] Chen, F.L., Siores, E.. The effect of cutting jet variation on striation formation in abrasive water jet cutting. International Journal of Machine Tools and Manufacture 2001;41(10):1479–1486.

[16] Tazibt, A., Parsy, F., Abriak, N.. Theoretical analysis of the particle acceleration process in abrasive water jet cutting. Computational Materials Science 1996;5(1):243–254.

[17] Leach, S.J., Walker, G.L., Smith, A.V., Farmer, I.W., Taylor, G.. Some aspects of rock cutting by high speed water jets. Philosophical Transactions of the Royal Society of London Series a, Mathematical and Physical Sciences 1966;260(1110):295–310.

[18] Martin, G.D., Hoath, S.D., Hutchings, I.M.. Inkjet printing - the physics of manipulating liquid jets and drops. Journal of Physics: Conference Series 2008;105(1):012001.

[19] Park, J., Hardy, M., Kang, S., Barton, K., Adair, K., Deep, K., et al. High-resolution electrohydrodynamic jet printing. Nature materials 2007;6(10):782–789.

[20] Singh, M., Haverinen, H.M., Dhagat, P., Jabbour, G.E.. Inkjet printingprocess and its applications. Advanced materials 2010;22(6):673–685.

[21] Flack, R.D.. Fundamentals of jet propulsion with applications. Cambridge University Press New York; 2005.

[22] Riggins, D.. The thermodynamic continuum of jet engine performance: the principle of lost work due to irreversibility in Aerospace systems. International Journal of Applied Thermodynamics 2003;6:107–120.

[23] Hughes, P.A.. Beams and Jets in Astrophysics. Cambridge University Press; 1991. Cambridge Books Online.

[24] Birkinshaw, M.. Instabilities in astrophysical jets. Astrophysics and Space Science 1996;242(1-2):17–91.

[25] Bazarov, V.G., Yang, V.. Liquid-propellant rocket engine injector dynamics. Journal of Propulsion and Power 1998;14(5):797–806.

[26] Li, Y., Kirkpatrick, A., Mitchell, C., Willson, B.. Characteristic and computational fluid dynamics modeling of high-pressure gas jet injection. Journal of engineering for gas turbines and power 2004;126(1):192–197.

[27] Lin, S.P.. Breakup of liquid sheets and jets; vol. 120. Cambridge University Press Cambridge, England; 2003.

[28] Basaran, O.A.. Small-scale free surface flows with breakup: Drop formation and emerging applications. AIChE Journal 2002;48(9):1842–1848.

[29] Jang, D.H., Kim, D.J., Moon, J.H.. Influence of fluid physical properties on ink-jet printability. Langmuir 2009;25(5):2629–2635.

[30] Pedretti, C., Kemp, M., Gingerich, O., et al. Codex Leicester: a masterpiece of science. American Museum of Natural History; 1996.

[31] Reitz, R.D., Bracco, F.V.. Mechanism of atomization of a liquid jet. Physics of Fluids 1982;25(10):1730–1742.

[32] Goedde, E.F., Yuen, M.C.. Experiments on liquid jet instability. Journal of Fluid Mechanics 1970;40(03):495–511.

[33] Fitzgerald, J.A., Garimella, S.V.. A study of the flow field of a confined and submerged impinging jet. International journal of heat and mass transfer 1998;41(8):1025–1034.

[34] Cooper, D., Jackson, D.C., Launder, B.E., Liao, G.X.. Impinging jet studies for turbulence model assessmenti. flow-field experiments. International Journal of Heat and Mass Transfer 1993;36(10):2675–2684.

[35] Webb, B.W., Ma, C.F.. Single-phase liquid jet impingement heat transfer. Advances in heat transfer 1995;26(2):105–217.

[36] Chen, C.J., Rodi, W.. Vertical turbulent buoyant jets: a review of experimental data. NASA STI/Recon Technical Report A 1980;80:23073.

[37] Kelso, R.M., Lim, T.T., Perry, A.E.. An experimental study of round jets in cross-flow. Journal of Fluid Mechanics 1996;306:111–144.

[38] Kamotani, Y., Greber, I.. Experiments on a turbulent jet in a cross flow. AIAA journal 1972;10(11):1425–1429.

[39] Margason, R.J.. Fifty years of jet in cross flow research. In: In AGARD, Computational and Experimental Assessment of Jets in Cross Flow 41; vol. 1. 1993,.

[40] Arai, M., Tabata, M., Hiroyasu, H., Shimizu, M.. Disintegrating process and spray characterization of fuel jet injected by a diesel nozzle. Tech. Rep.; SAE Technical Paper; 1984.

[41] Elkotb, M.. Fuel atomization for spray modelling. Progress in Energy and Combustion Science 1982;8(1):61–91.

[42] Beale, J.C., Reitz, R.D.. Modeling spray atomization with the Kelvin-Helmholtz / Rayleigh-Taylor hybrid model. Atomization and sprays 1999;9(6).

[43] Garimella, S.V., Rice, R.A.. Confined and submerged liquid jet impingement heat transfer. Journal of Heat Transfer 1995;117(4):871–877.

[44] Lee J. H. W. amd Cheung, V.. Generalized lagrangian model for buoyant jets in current. Journal of environmental engineering 1990;116(6):1085–1106.

[45] Wood, I.R., Bell, R.G.. Ocean disposal of wastewater; vol. 8. World Scientific; 1993.

[46] Koh, R.C.Y., Brooks, N.H.. Fluid mechanics of waste water disposal in the ocean. Annual Review of Fluid Mechanics 1975;7:187–211.

[47] List, E.J., Imberger, J.. Turbulent entrainment in buoyant jets and plumes. Journal of the Hydraulics Division 1973;99(9):1461–1474.

[48] Pietrzyk, J.R., Bogard, D.G., Crawford, M.E.. Hydrodynamic measurements of jets in crossflow for gas turbine film cooling applications. Journal of Turbomachinery 1989;111(2):139–145.

[49] Schlüter, J., Schönfeld, T.. LES of jets in cross flow and its application to a gas turbine burner. Flow, Turbulence and Combustion 2000;65(2):177–203.

[50] Wu, P.K., Kirkendall, K.A., Fuller, R.P., Nejad, A.S.. Breakup processes of liquid jets in subsonic crossflows. Journal of Propulsion and Power 1997;13(1):64–73.

[51] Swinney H. L. & Gollub, J.P.. Hydrodynamic instabilities and the transition to turbulence. Tech. Rep.; 1981.

[52] Feynman, R.P., Leighton, R.B., Sands, M.. The Feynman Lectures on Physics, Desktop Edition Volume I; vol. 1. Basic Books; 2013.

[53] Orszag, S.A.. Analytical Theories of Turbulence. Journal of Fluid Mechanics 1970;41:363–386.

[54] Wang, Z.H., He, P., Lv, Y., Zhou, J.H., Fan, J.R., Cen, K.F.. Direct Numerical Simulation of Subsonic Round Turbulent Jet. Flow, Turbulence and Combustion 2010;84(4):669–686.

[55] Jones, W.P., Launder, B.E.. The prediction of laminarization with a two-equation model of turbulence. International Journal of Heat and Mass Transfer 1972;15(2):301 – 314.

[56] Smagorinsky, J.. General Circulation Experiments with the Primitive Equations. Monthly Weather Review 1963;91:99.

[57] Lee, M., Malaya, N., Moser, R.D.. Petascale Direct Numerical Simulation of Turbulent Channel Flow on Up to 786K Cores. In: Proceedings of the International Conference on High Performance Computing, Networking, Storage and Analysis. SC '13; 2013, p. 61:1–61:11.

[58] Robertson, B.E., Kravtsov, A.V., Gnedin, N.Y., Abel, T., Rudd, D.H.. Computational Eulerian Hydrodynamics and Galilean Invariance. Monthly Notices of the Royal Astronomical Society 2010;401:2463–2476.

[59] Chen, F., Hagen, H.. A Survey of Interface Tracking Methods in Multiphase Fluid Visualization. In: Middel, A., Scheler, I., Hagen, H., editors. Visualization of Large and Unstructured Data Sets - Applications in Geospatial Planning, Modeling and Engineering (IRTG 1131 Workshop); vol. 19 of *OpenAccess Series in Informatics (OASIcs)*. Dagstuhl, Germany: Schloss Dagstuhl–Leibniz-Zentrum fuer Informatik; 2011, p. 11–19.

[60] Gingold, R.A., Monaghan, J.J.. Smoothed Particle Hydrodynamics - Theory and application to non-spherical stars. Monthly Notices of the Royal Astronomical Society 1977;181:375–389.

[61] Lucy, L.B.. A numerical approach to the testing of the fission hypothesis. The Astronomical Journal 1977;82:1013–1024.

[62] Monaghan, J.J.. Simulating Free Surface Flows with SPH. Journal of Computational Physics 1994;110(2):399–406.

[63] Brüggen, M., Hillebrandt, W.. Mixing through shear instabilities. Monthly Notices of the Royal Astronomical Society 2001;320(1):73–82.

[64] Junk, V., Walch, S., Heitsch, F., Burkert, A., Wetzstein, M., Schartmann, M., et al. Modelling shear flows with smoothed particle hydrodynamics and grid-based methods. Monthly Notices of the Royal Astronomical Society 2010;407(3):1933–1945.

[65] Wang, L.F., Ye, W.H., Li, Y.J.. Combined effect of the density and velocity gradients in the combination of Kelvin-Helmholtz and Rayleigh-Taylor Instabilities. Physics of Plasmas 2010;17(4):042103.

[66] Ye, W.H., Wang, L.F., Xue, C., Fan, Z.F., He, X.T.. Competitions between Rayleigh-Taylor instability and Kelvin-Helmholtz Instability with continuous density and velocity profiles. Physics of Plasmas 2011;18(2):022704.

[67] Alon, U., Hecht, J., Ofer, D., Shvarts, D.. Power Laws and Similarity of Rayleigh-Taylor and Richtmyer-Meshkov Mixing Fronts at All Density Ratios. Physical Review Letters 1995;74:534–537.

[68] Layzer, D.. On the Instability of Superimposed Fluids in a Gravitational Field. The Astrophysical Journal 1995;122:1–12.

[69] Zhang, Q.. The motion of a single bubble or spike in Rayleigh–Taylor unstable interfaces. IMPACT of Computing in Science and Engineering 1991;3(4):277 – 304.

[70] Oron, D., Arazi, L., Kartoon, D., Rikanati, A., Alon, U., Shvarts, D.. Dimensionality dependence of the Rayleigh–Taylor and Richtmyer–Meshkov instability late-time scaling laws. Physics of Plasmas 2001;8(6):2883–2889.

[71] Youngs, D.L.. Numerical simulation of turbulent mixing by Rayleigh-Taylor instability. Physica D Nonlinear Phenomena 1984;12:32–44.

[72] Youngs, D.L.. Modelling turbulent mixing by Rayleigh-Taylor instability. Physica D: Nonlinear Phenomena 1989;37(1-3):270–287.

[73] Andrews, M.J., Spalding, D.B.. A simple experiment to investigate two-dimensional mixing by Rayleigh-Taylor instability. Physics of Fluids 1990;2(6):922–927.

[74] Glimm, J., Grove, J.W., Li, X.L., Oh, W., Sharp, D.H.. A Criti-

cal Analysis of Rayleigh-Taylor Growth Rates. Journal of Computational Physics 2001;169(2):652 – 677.

[75] Adami, S., X.Y., H., Adams, N.. A new surface-tension formulation for multi-phase SPH using a reproducing divergence approximation. Journal of Computational Physics 2010;229(13):5011 – 5021.

[76] Kelvin, L.. Hydrokinetic solutions and observations. Philosophical Magazine 1871;42:362–377.

[77] Helmholtz, . XLIII. On discontinuous movements of fluids. The London, Edinburgh, and Dublin Philosophical Magazine and Journal of Science 1868;36(244):337–346.

[78] Rayleigh, J.W.S.. Investigation of the Character of the Equilibrium of an Incompressible Heavy Fluid of Variable Density. Proceedings of the London Mathematical Society 1882;s1-14(1):170–177.

[79] Taylor, G.. The instability of liquid surfaces when accelerated in a direction perpendicular to their planes. I. Proceedings of the Royal Society of London Series A Mathematical and Physical Sciences 1950;201(1065):192–196.

[80] De Silva, I.P.D., Fernando, H.J.S., Eaton, F., D. Hebert, D.. Evolution of Kelvin-Helmholtz billows in nature and laboratory. Earth and Planetary Science Letters 1996;143(14):217–231.

[81] Delamere, P.A., Wilson, R.J., Masters, A.. Kelvin-Helmholtz instability at Saturn's magnetopause: Hybrid simulations. Journal of Geophysical Research: Space Physics 2011;116(A10):2156–2202.

[82] Smyth, W.D., Moum, J.N.. Ocean Mixing by Kelvin-Helmholtz Instability. Oceanography 2012;23:140–149.

[83] Norman, M.L., Winkler, K.H.A., Smarr, L., Smith, M.D.. Structure and dynamics of supersonic jets. Astronomy and Astrophysics 1982;113:285–302.

[84] Cabot, W.H., Cook, A.W.. Reynolds number effects on Rayleigh-Taylor instability with possible implications for type ia supernovae. Nature Physics 2006;2(8):562–568.

[85] Freeman, J., Clauser, M., Thompson, S.. Rayleigh-Taylor instabilities in inertial-confinement fusion targets. Nuclear Fusion 1977;17(2):223.

[86] Kilkenny, J.D., Glendinning, S.G., Haan, S.W., Hammel, B.A., Lindl, J.D., Munro, D., et al. A review of the ablative stabilization of the Rayleigh-Taylor instability in regimes relevant to inertial confinement fusion. Physics of Plasmas 1994;1(5):1379–1389.

[87] Pozrikidis, C.. Introduction to Theoretical and Computational Fluid Dynamics. Oxford university press; 2011.

[88] Miles, J.. Richardsons criterion for the stability of stratified flows. Physics of Fluids 1994;29(10):3470–3471.

[89] Bayly, B.J., Orszag, S.A., Herbert, T.. Instability Mechanisms in Shear-Flow Transition. Annual Review of Fluid Mechanics 1988;20:359–391.

[90] Bellman, R., Pennington, R.. Effects of surface tension and viscosity on Taylor instability. Quarterly of Applied Mathematics 1954;12:151–162.

[91] Mikaelian, K.O.. Effect of viscosity on Rayleigh–Taylor and Richtmyer–Meshkov instabilities. Physical Review E 1993;47:375–383.

[92] Shu, F.H.. The Physics of Astrophysics: Gas dynamics II. University Science Books; 1991.

[93] Drazin, P.G.. Introduction to hydrodynamic stability. Cambridge University Press, Cambridge Texts in Applied Mathematics, Cambridge, England; 2002.

[94] Kundu, P.K., Cohen, I.M.. Fluid Mechanics. Elsevier Academic Press, Amsterdam; 3 ed.; 2004.

[95] Van Dyke, M.. Perturbation Methods in Fluid Mechanics. Parabolic Press; 1975.

[96] Mei, C.C.. Mathematical Analysis in Engineering. Cambridge University Press, Cambridge, England; 1997.

[97] Squire, H.B.. On the stability for three-dimensional disturbances of viscous fluid flow between parallel walls. Proceedings of the Royal Society of London Series A, Containing Papers of a Mathematical and Physical Character 1933;142(847):621 – 628.

[98] Yih, C.. Stratified Flows. Academic Press, New York; 1980.

[99] Hesla, T.I., Pranckh, F.R., Prezios, L.. Squires theorem for two stratified fluids. Physics of Fluids 1986;29(9):2808–2811.

[100] Chen, X., Fried, E.. Squire's theorem for the RayleighTaylor problem with a phase boundary. Tech. Rep. TAM Reports 1089,; Department of Theoretical and Applied Mechanics (UIUC); 2006.

[101] Orr, W.. The Stability or Instability of the Steady Motions of a Perfect Liquid and of a Viscous Liquid. Part II: A Viscous Liquid. Proceedings of the Royal Irish Academy Section A: Mathematical and Physical Sciences 1907;27:69–138.

[102] Orr, W.. The Stability or Instability of the Steady Motions of a Perfect Liquid and of a Viscous Liquid. Part I: A Perfect Liquid. Proceedings of

the Royal Irish Academy Section A: Mathematical and Physical Sciences 1907;27:9–68.

[103] Sommerfeld, A.. Ein beitrag zur hydrodynamische erklrung der turbulenten flssigkeitsbewegungen. Proceedings of the 4th International Congress of Mathematicians III 1909;27:116–124.

[104] Ezerskii, A.B.. Induced motions in shear flows with piecewise linear velocity profile. Fluid Dynamics 1983;18(1):153–158.

[105] Kolykhalov, P.I.. Dissipative instability of fluid flows with piecewise linear velocity profiles. Fluid Dynamics 1986;21(6):854–860.

[106] Kim, H., Padrino, J.C., Joseph, D.D.. Viscous effects on Kelvin-Helmholtz instability in a channel. Journal of Fluid Mechanics 2011;680:398–416.

[107] Batchelor, G.K.. An introduction to fluid dynamics. Cambridge University Press, Cambridge, England; 1967.

[108] McNally, C.P., Lyra, W., Passy, J.C.. A Well-Posed Kelvin-Helmholtz Instability Test and Comparison. The Astrophysical Journal Supplement Series 2012;201:18.

[109] Read, J.I., Hayfield, T., Agertz, O.. Resolving mixing in Smoothed Particle Hydrodynamics. Monthly Notices of the Royal Astronomical Society 2010;323:743.

[110] Price, D.J.. Modelling discontinuities and Kelvin-Helmholtz instabilities in SPH. Journal of Computational Physics 2008;227(24):10040 – 10057.

[111] Metropolis, N., Ulam, S.. The monte carlo method. Journal of the American Statistical Association 1949;44(247):335–341.

[112] Buhmann, M.D.. Radial basis functions. Acta Numerica 2000 2000;9:1–38.

[113] Thomas, Y.. A mesh-free numerical method for three-dimensional non-linear schrodinger equation. Master's thesis; Department of Computer Scienceand Information Systems, Birkbeck, University of London; 2010.

[114] Koshizuka, S., Ikeda, H., Oka, Y.. Numerical analysis of fragmentation mechanisms in vapor explosions. Nuclear Engineering and Design 1999;189(13):423 – 433.

[115] Harlow, F.H.. A machine calculation method for hydrodynamic problems. Tech. Rep.; Los Alamos Scientific Laboratory report; 1956.

[116] Silverman, B.W.. Density Estimation for Statistics and Data Analysis. London: Chapman & Hall; 1986.

[117] Wendland, H.. Computational aspects of radial basis function approximation. Studies in Computational Mathematics 2006;12:231–256.

[118] Li, S., Liu, W.K.. Meshfree Particle Methods. Springer Publishing Company, Incorporated; 2007.

[119] Monaghan, J.J.. Smoothed particle hydrodynamics. Annual review of astronomy and astrophysics 1992;30:543–574.

[120] Price, D.J., Monaghan, J.J.. Smoothed particle magnetohydrodynamics i. algorithm and tests in one dimension. Monthly Notices of the Royal Astronomical Society 2004;348(1):123–138.

[121] Schuessler, I., Schmitt, D.. Comments on smoothed particle hydrodynamics. Astronomy and Astrophysics 1981;97:373–379.

[122] Price, D.J.. Smoothed particle magnetohydrodynamics iv. using the vector potential. Monthly Notices of the Royal Astronomical Society 2010;401(3):1475–1499.

[123] Morris, J.P.. Analysis of sph with applications. Ph.D. thesis; Department of Mathematics, Monash University; 2005.

[124] Dehnen, W., Aly, H.. Improving convergence in smoothed particle hydrodynamics simulations without pairing instability. Monthly Notices of the Royal Astronomical Society 2012;425:1068–1082.

[125] Robinson, M., Monaghan, J.J.. Forced 2D wall-bounded turbulence using SPH. In: 3rd SPHERIC workshop. SPHERIC; 2009, p. 78–84.

[126] Robinson, M.. Turbulence and viscous mixing using smoothed particle hydrodynamics. Ph.D. thesis; Department of Mathematical Science, Monash University; 2009.

[127] Macia, F., Colagrossi, A., Antuono, M., Souto-Iglesias, A.. Benefits of using a wendland kernel for free-surface flows. "6th ERCOFTAC SPHERIC workshop on SPH applications, Hamburg University of Technology" 2011;:30–37.

[128] Liu, G., Liu, M.. Smoothed Particle Hydrodynamics A Meshfree Particle Method. World Scientific; 2003.

[129] Liu, M.B., Liu, G.R.. Restoring particle consistency in smoothed particle hydrodynamics. Applied Numerical Mathematics 2006;56(1):19 – 36.

[130] Liu, M.B., Liu, G.R., Lam, K.Y.. Constructing smoothing functions in smoothed particle hydrodynamics with applications. Journal of Computational and Applied Mathematics 2003;155(2):263 – 284.

[131] Morris, J.P.. Analysis of smoothed particle hydrodynamics with applications. Ph.D. thesis; Monash University; 1996.

[132] Price, D.J., Monaghan, J.J.. Smoothed Particle Magnetohydrodynamics - III. Multidimensional tests and the $divB = 0$ constraint. Monthly Notices of the Royal Astronomical Society 2005;364:384–406.

[133] Springel, V., . The cosmological simulation code GADGET-2. Monthly Notices of the Royal Astronomical Society 2005;364:1105–1134.

[134] Balsara, D.S.. Von neumann stability analysis of smoothed particle hydrodynamics-suggestions for optimal algorithms. Journal of Computational Physics 1995;121(2):357–372.

[135] Monaghan, J.J., Price, D.J.. Variational principles for relativistic smoothed particle hydrodynamics. Monthly Notices of the Royal Astronomical Society 2001;328:381–392.

[136] Eckart, C.. Variation Principles of Hydrodynamics. Physics of Fluids 1960;3(3):421–427.

[137] Rosswog, S.. Astrophysical smooth particle hydrodynamics. New Astronomy Reviews 2009;53(4):78–104.

[138] Springel, V.. Smoothed particle hydrodynamics in astrophysics. Annual Review of Astronomy and Astrophysics 2010;48:391–430.

[139] Bennett, A.. Lagrangian Fluid Dynamics. Cambridge University Press; 2006. ISBN 9780511734939. Cambridge Books Online.

[140] Monaghan, J.J.. SPH compressible turbulence. Monthly Notices of the Royal Astronomical Society 2002;335:843–852.

[141] Rankine, W.J.M.. On the thermodynamic theory of waves of finite longitudinal disturbance. Philosophical Transactions of the Royal Society of London 1870;160:277–288.

[142] Hugoniot, P.H.. Sur la propagation du mouvement dans les corps et spcialement dans les gaz parfaits (deuxime partie). Journal de l'cole Polytechnique (in French) 1889;58:1125.

[143] Landau L. D. & Lifshitz, E.M.. Fluid Mechanics; vol. 6 of *A Course of Theoretical Physics*. Pergamon Press; 1959.

[144] Shu, F.H.. The Physics of Astrophysics Volume II: Gas Dynamics. A Series of Books in Astronomy; 1 ed.; 2009.

[145] Bodenheimer, P., Laughlin, G.P., Rozyczka, M., Yorke, H.W.. Numerical Methods in Astrophysics: An Introduction. CRC Press; 2006.

[146] Von Neumann, J.. Proposal and analysis of a new numerical method for the treatment of hydrodynamical shock problems. Collected Works VI 1961;.

[147] Landshoff, R.. A numerical method for treating fluid flow in the presence of shocks. Tech. Rep. LA-1930; Los Alamos National Laboratory; 1955.

[148] Agertz, O., Moore, B., Stadel, J., Potter, D., Miniati, F., Read, J., et al. Fundamental differences between SPH and grid methods. Monthly Notices of the Royal Astronomical Society 2007;380:963–978.

[149] Shadloo, M.S., Yildiz, M.. Numerical modeling of Kelvin Helmholtz instability using smoothed particle hydrodynamics. International Journal for Numerical Methods in Engineering 2011;87(10):988–1006.

[150] Morris, J., Monaghan, J.. A switch to reduce sph viscosity. Journal of Computational Physics 1997;136(1):41 – 50.

[151] Rosswog, S., Davies, M.B., Thielemann, F.K., Piran, T.. Merging neutron stars: asymmetric systems. Astronomy and Astrophysics 2000;360:171–184.

[152] Cullen, L., Dehnen, W.. Inviscid smoothed particle hydrodynamics. Monthly Notices of the Royal Astronomical Society 2010;408:669–683.

[153] Read, J.I., Hayfield, T.. Sphs: smoothed particle hydrodynamics with a higher order dissipation switch. Monthly Notices of the Royal Astronomical Society 2012;422(4):3037–3055.

[154] Maron, J.L., Howes, G.G.. Gradient particle magnetohydrodynamics: a lagrangian particle code for astrophysical magnetohydrodynamics. The Astrophysical Journal 2003;595(1):564–572.

[155] Van Wylen, G.J., Sonntag, R.E.. Fundamentals of classical thermodynamics. Wiley Singapore; 1985.

[156] Ritchie, B.W., Thomas, P.A.. Multiphase smoothed-particle hydrodynamics. Monthly Notices of the Royal Astronomical Society 2001;323(3):743–756.

[157] Saitoh, T., Makino, J.. A Density-independent Formulation of Smoothed Particle Hydrodynamics. The Astrophysical Journal 2013;768(1):44.

[158] Hopkins, P.F.. A general class of Lagrangian smoothed particle hydrodynamics methods and implications for fluid mixing problems. Monthly Notices of the Royal Astronomical Society 2013;428:2840–2856.

[159] Oger, G., Doring, M., Alessandrini, B., Ferrant, P.. An improved sph method: Towards higher order convergence. J Comput Physics 2007;255(2):1472–1492.

[160] Abel, T.. rpsph: a novel smoothed particle hydrodynamics algorithm. Monthly Notices of the Royal Astronomical Society 2011;413(1):271–285.

[161] Colagrossi, A., Landrini, M.. Numerical Simulation of Interfacial Flows by Smoothed Particle Hydrodynamics. Journal of Computational Physics 2003;191(2):448–475.

[162] Flebbe, O., Muenzel, S., Herold, H., Riffert, H., Ruder, H.. Smoothed Particle Hydrodynamics: Physical viscosity and the simulation of accretion disks. Astrophysical Journal 1994;431:754–760.

[163] Hu, X.Y., Adams, N.A.. An incompressible multi-phase SPH method. Journal of Computational Physics 2007;227(1):264–278.

[164] Hu, X.Y., Adams, N.A.. A multi-phase SPH method for macroscopic and mesoscopic flows. Journal of Computational Physics 2006;213(2):844 – 861.

[165] Grenier, N., Antuono, M., Colagrossi, A., Touz, D., Alessandrini, B.. An Hamiltonian interface SPH formulation for multi-fluid and free surface flows. Journal of Computational Physics 2009;228(22):8380 – 8393.

[166] Monaghan, J.J., Rafiee, A.. A simple SPH algorithm for multi-fluid flow with high densityratios. International Journal for Numerical Methods in Fluids 2013;71(5):537–561.

[167] Kruisbrink, A.C.H., Pearce, F.R., Yue, T., Cliffe, K.A., Morvan, H.P.. SPH multi-fluid model with interface stabilization based on quasi-buoyancy correction. 7th international SPHERIC workshop, Prato, Italy 2012;:285–302.

[168] Korzilius, S.P., Kruisbrink, A.C.H., Yue, T., Schilders, W.H.A., Anthonissen, M.J.H.. Momentum conserving methods that reduce particle clustering in SPH. 9th international SPHERIC workshop, Paris, France 2014;:268–274.

[169] Souto-Iglesias, A., Macià, F., González, L.M., Cercos-Pita, J.L.. Addendum to "On the consistency of MPS". ArXiv e-prints 2013;.

[170] Korzilius, S., Kruisbrink, A.C.H., Yue, T., Schilders, W.H.A., Anthonissen, M.J.H.. Momentum conserving methods that reduce particle clustering in sph. "Proceedings 9th Int SPHERIC workshop, Paris, France" June 4-6,2014;:17–24.

[171] Kelager, M.. Lagrangian fluid dynamics using smoothed particle hydrodynamics. Master's thesis; University of Copenhagen, Copenhagen, Denmark; 2006.

[172] Meteer, O.. Interaction between sph fluids and dynamics particle-based objects using CUDA. Proceedings of the 15th Twente Student Conference on IT 2011;:23–30.

[173] Springel, V., Hernquist, L.. Cosmological smoothed particle hydrodynamics simulations: a hybrid multiphase model for star formation. Monthly Notices of the Royal Astronomical Society 2003;339:289–311.

[174] Ritchie, B.W., Thomas, P.A.. Hydrodynamic simulations of merging clusters of galaxies. Monthly Notices of the Royal Astronomical Society 2002;329(3):675–688.

[175] Canup, R.M.. Simulations of a late lunar-forming impact. Icarus 2004;168(2):433–456.

[176] Canup, R.M., Asphaug, E.. Origin of the moon in a giant impact near the end of the earth's formation. Nature 2001;412(6848):708–712.

[177] Benz, W., Slattery, W.L., Cameron, A.G.W.. The origin of the moon and the single-impact hypothesis i. Icarus 1986;66(3):515–535.

[178] Hopton, S.. Modelling open channel flow. Ph.D. thesis; University of Nottingham; 2010.

[179] Federico, I., Marrone, S., Colagrossi, A., Aristodemo, F., Antuono, M.. Simulating 2d open-channel flows through an SPH model. European Journal of Mechanics B Fluids 2012;34(0):35–46.

[180] Crespo, A.J., Gómez-Gesteira, M., Dalrymple, R.A.. Modeling dam break behavior over a wet bed by a sph technique. Journal of waterway, port, coastal, and ocean engineering 2008;134(6):313–320.

[181] Zou, S.. Coastal sediment transport simulation by smoothed particle hydrodynamics. Ph.D. thesis; Johns Hopkins University; 2007.

[182] Dalrymple, R.A., Rogers, B.D.. Numerical modeling of water waves with the SPH method. Coastal Engineering 2006;53:141–147.

[183] Price, D.J.. Smoothed particle hydrodynamics and magnetohydrodynamics. Journal of Computational Physics 2012;231(3):759 – 794.

[184] Vacondio, R., Rogers, B.D., Stansby, P.K., Mignosa, P.. A correction for balancing discontinuous bed slopes in two-dimensional smoothed particle hydrodynamics shallow water modeling. International Journal for Numerical Methods in Fluids 2013;71(7):850–872.

[185] Vacondio, R., Rogers, B.D., Stansby, P.K., Mignosa, P.. Shallow water SPH for flooding with dynamic particle coalescing and splitting. Advances in Water Resources 2013;58(0):10 – 23.

[186] Barnes, J., Hut, P.. A hierarchical O(N log N) force-calculation algorithm. Nature 1986;324:446–449.

[187] Altman, N.S.. An Introduction to Kernel and Nearest-Neighbor Nonparametric Regression. The American Statistician 1992;46(3):175–185.

[188] Coomans, D., Massart, D.L.. Alternative k-nearest neighbour rules in supervised pattern recognition : Part 1. k-nearest neighbour classification by using alternative voting rules. Analytica Chimica Acta 1982;136(0):15–27.

[189] Terrell, G.R., Scott, D.W.. Variable kernel density estimation. The Annals of Statistics 1992;20:1236–1265.

[190] Hockney, R.W., Eastwood, J.W.. Computer Simulation Using Particles. Bristol, PA, USA: Taylor & Francis, Inc.; 1988. ISBN 0-85274-392-0.

[191] Springel, V., White, S.D.M., Jenkins, A., Frenk, C.S., Yoshida, N., Gao, L., et al. Simulations of the formation, evolution and clustering of galaxies and quasars. Nature 2005;435:629–636.

[192] Springel V. & Hernquist, L.. The history of star formation in a Λ cold dark matter universe. Monthly Notices of the Royal Astronomical Society 2003;339:312–334.

[193] Machado, R.E.G., Lima Neto, G.B.. Simulations of the merging galaxy cluster Abell 3376. Monthly Notices of the Royal Astronomical Society 2013;430:3249–3260.

[194] Rogers, B.D., Dalrymple, R.A., Stansby, P.K.. Simulation of caisson breakwater movement using 2-D SPH. Journal of Hydraulic Research 2010;48:135–141.

[195] Gmez-Gesteira, M., Dalrymple, R.A.. Using a 3D SPH Method for Wave Impact on a Tall Structure. Ocean Engineering 2004;130:63–69.

[196] Khayyer, A., Gotoh, H.. Modified moving particle semi-implicit methods for the prediction of 2d wave impact pressure. Coastal Engineering 2009;56(4):419 – 440.

[197] Khayyer, A., Gotoh, H.. On particle-based simulation of a dam break over a wet bed. Journal of Hydraulic Research 2010;48:238–249.

[198] Gomez-Gesteira, M., Rogers, B., Crespo, A., Dalrymple, R., Narayanaswamy, M., Dominguez, J.. SPHysics-development of a free-surface fluid solver Part 1: Theory and formulations . Computers and Geosciences 2012;48(0):289 – 299.

[199] Gomez-Gesteira, M., Crespo, A.J.C., Rogers, B.D., Dalrymple, R.A., Dominguez, J.M., Barreiro, A.. SPHysics- development of a free-surface fluid solver-part 2: Efficiency and test cases. Computers and Geosciences 2012;48(0):300 – 307.

[200] Beck, K.. Test Driven Development: By Example. Addison Wesley; 2002.

[201] Beck, K.. Extreme programming: A discipline of software development (invited paper) (abstract only). SIGSOFT Softw Eng Notes 1999;24(6):1–.

[202] Allen Michael P & Tildesley, D.J.. Computer simulation of liquids. Oxford university press; 1989.

[203] Domnguez, J.M., Crespo, A.J.C., Gmez-Gesteira, M., Marongiu, J.C.. Neighbour lists in smoothed particle hydrodynamics. International Journal for Numerical Methods in Fluids 2011;67(12):2026–2042.

[204] Monaghan, J.J.. On the problem of penetration in particle methods. Journal of Computational Physics 1989;82(1):1 – 15.

[205] Jones, J.E.. On the Determination of Molecular Fields. II. From the Equation of State of a Gas. Royal Society of London Proceedings Series A 1924;106:463–477.

[206] Hairer, E., Lubich, C., Wanner, G.. Geometric Numerical Integration: Structure-Preserving Algorithms for Ordinary Differential Equations. Springer Series in Computational Mathematics; Springer; 2006.

[207] Howard, L.N.. Note on a paper of John W. Miles. Journal of Fluid Mechanics 1961;10:509–512.

[208] Thorpe, S.A.. Experiments on instability and turbulence in a stratified shear flow. Journal of Fluid Mechanics 1973;61(04):731–751.

[209] Linden, P.F.. Mixing in stratified fluids. Geophysical & Astrophysical Fluid Dynamics 1979;13(1):3–23.

[210] Patnaik, P.C., Sherman, F.S., Corcos, G.M.. A numerical simulation of Kelvin-Helmholtz waves of finite amplitude. Journal of Fluid Mechanics 1976;73:215–240.

[211] Klaassen, G.P., Peltier, W.R.. The evolution of finite-amplitude Kelvin-Helmholtz billows in two spatial dimensions. Journal of Atmospheric Sciences 1985;42:1321–1339.

[212] Caulfield, C.P., Peltier, W.R.. Three dimensionalization of the stratified mixing layer. Physics of Fluids 1994;6(12):3803–3805.

[213] Hazel, P.. Numerical studies of the stability of inviscid stratified shear flows. Journal of Fluid Mechanics 1972;51:39–61.

[214] Miczek, F.. Simulation of low mach number astrophysical flows. Dissertation; Technische Universitt Mnchen; Mnchen; 2013.

[215] Hubber, D.A., Falle, S., Goodwin, S.P.. Convergence of AMR and SPH simulations-I. Hydrodynamical resolution and convergence tests. Monthly Notices of the Royal Astronomical Society 2013;432(1):711–727.

[216] Shakibaeinia, A., Jin, Y.C.. MPS mesh-free particle method for multiphase flows. Computer Methods in Applied Mechanics and Engineering 2012;229(0):13 – 26.

[217] Jeong, S.M., Nam, J.W., Hwang, S.C., Park, J.C., Kim, M.H.. Numerical prediction of oil amount leaked from a damaged tank using two-dimensional moving particle simulation method. Ocean Engineering 2013;69(0):70 – 78.

[218] Roediger, E., Kraft, R.P., Nulsen, P., Churazov, E., Forman, W., Brggen, M., et al. Viscous Kelvin-Helmholtz instabilities in highly ionized plasmas. Monthly Notices of the Royal Astronomical Society 2013;436(2):1721–1740.

[219] Rosswog, S.. SPH Methods in the Modelling of Compact Objects. ArXiv e-prints 2014;.

[220] Sharp, D.H.. An overview of Rayleigh-Taylor instability. Physica D: Nonlinear Phenomena 1984;12(13):3–18.

[221] Sahu, K.C., Vanka, S.P.. A multiphase lattice Boltzmann study of buoyancy-induced mixing in a tilted channel. Computers & Fluids 2011;50(1):199 – 215.

[222] Akula, B., Andrews, M.J., Ranjan, D.. Effect of shear on Rayleigh-Taylor mixing at small Atwood number. Physical Review E 2013;87:033013–033027.

[223] Atzeni, S., Guerrieri, A.. Evolution of Multimode Rayleigh-Taylor Instability towards Self-Similar Turbulent Mixing. Europhysics Letters 1993;22(8):603–6011.

[224] Dimonte, G.. Dependence of turbulent Rayleigh-Taylor instability on initial perturbations. Physical Review E 2004;69:056305–056319.

[225] Ristorcelli, J.R., Clark, T.. Rayleigh Taylor turbulence: self-similar analysis and direct numerical simulations. Journal of Fluid Mechanics 2004;507:213–253.

[226] Shvarts, D., Alon, U., Ofer, D., McCrory, R.L., Verdon, C.P.. Nonlinear evolution of multimode Rayleigh–Taylor instability in two and three dimensions. Physics of Plasmas 1995;2(6):2465–2472.

[227] Cole, R.L., Tankin, R.S.. Experimental study of Taylor instability. Physics of Fluids 1973;16(11):1810–1815.

[228] Moscinski, J., Alda, W., Bubak, M., Dzwinel, W., Kitowski, J., Pogoda, M., et al. Molecular Dynamics Simulation of Rayleigh-Taylor Instability. Physics of Fluids 2001;13(3):1263–1267.

[229] Nie, X., Qian, Y.H., Doolen, G.D., Chen, S.. Lattice Boltzmann simulation of the two-dimensional Rayleigh-Taylor instability. Physical Review E 1998;58:6861–6864.

[230] Cheng, H.F., Jiang, S.Y., Bo, H.L., Duan, R.Q.. Numerical simulation of the Rayleigh–Taylor instability using the MPS method. Sci China Tech Sci 2012;55(10):2953–2959.

[231] Shadloo, M.S., Zainali, A., Yildiz, M.. Simulation of single mode Rayleigh–Taylor instability by SPH method. Comput Mech 2013;51(5):699–715.

[232] Brackbill, J.U., Kothe, D.B., Zemach, C.. A continuum method for modeling surface tension. Journal of Computational Physics 1992;100(2):335–354.

[233] Ramaprabhu, P., Dimonte, G., Young, Y.N., Calder, A., Fryxell, B.. Limits of the potential flow approach to the single-mode Rayleigh-Taylor problem. Physical Review E 2006;74(6):066308–066314.

[234] Waddell, J.T., Niederhaus, C.E., Jacobs, J.W.. Experimental study of Rayleigh–Taylor instability: Low Atwood number liquid systems with single-mode initial perturbations. Physics of Fluids 2001;13(5):1263–1273.

[235] He, X., Chen, S., Zhang, R.. A Lattice Boltzmann Scheme for Incompressible Multiphase Flow and Its Application in Simulation of RayleighTaylor Instability. Journal of Computational Physics 1999;152(2):642–663.

[236] Alon, U., Hecht, J., Mukamel, D., Shvarts, D.. Scale invariant mixing rates of hydrodynamically unstable interfaces. Physical Review Letters 1994;72:2867–2870.

[237] Plateau, . Statique experimentale et theorique des liquides soumis aux seules forces moleculaires. Gautier-Villars 1873;.

[238] Weber, C.. Zum zerfall eines flussigkeitsstrahles. ZAMM 1931;11:136–142.

[239] Lafrance, P.. Nonlinear breakup of a laminar liquid jet. Physics of Fluids 1975;18(4):428–432.

[240] Mead-Hunter, R., King, A.J.C., Mullins, B.J.. Plateau Rayleigh Instability Simulation. Langmuir 2012;28(17):6731–6735.

[241] Choi, Y.S., Kim, S.J., Kim, M.U.. Molecular dynamics of unstable motions and capillary instability in liquid nanojets. Physical Review E 2006;73:016309–016315.

[242] Shibata, K., Koshizuka, S., Oka, Y.. Numerical Analysis of Jet Breakup Behavior Using Particle Method. Journal of Nuclear Science and Technology 2004;41(7):715–722.

[243] Takashima, T., Ito, T., Shigeta, M., Izawa, S., Fukunishi, Y.. Simulation of Liquid Jet Breakup Process by Three-Dimensional Incompressible SPH Method. Seventh International Conference on Computational Fluid Dynamics (ICCFD7), Big Island, Hawaii, July 9-13 2012;.

[244] Sirotkin, F.V., Yoh, J.J.. A new particle method for simulating breakup of liquid jets. Journal of Computational Physics 2012;231(4):1650 – 1674.

[245] Morris, J.P.. Simulating surface tension with Smoothed Particle Hydrodynamics. Journal for Numerical Methods in Fluids 2000;33:333–353.

[246] Brackbill, J.U., Kothe, D.B., Zemach, C.. A continuum method for modeling surface tension. Journal of Computational Physics 1992;100(2):335–354.

[247] Rayleigh, J.W.S.. On the stability, or instability, of certain fluid motions. Proceedings of the London Mathematical Society 1879;29:57–71.

[248] Kruisbrink, A.C.H., Pearce, F., Yue, T., Morvan, H.P., Cliffe, K.A.. SPH surface tension model without need for calibration or evaluation of curvature. Proceedings 8th Int SPHERIC workshop, Trontheim, Norway June 4-6,2013;:31–37.

[249] Hou, Q., Kruisbrink, A.C.H., Pearce, F.R., Tijsseling, A.S., Yue, T.. Smoothed particle hydrodynamics simulations of flow separation at bends. Computers & Fluids 2014;90(0):138–146.

[250] Chernin, L., Masson, C., Gouveia dal Pino, E.M., Benz, W.. Momentum transfer by astrophysical jets. The Astrophysical Journal 1994;426:204–214.

[251] Elisabete, D.G.D.P.. Three-dimensional simulations of jet/cloud interactions: Structure and kinematics of the deflected jets. The Astrophysical Journal 1999;526(2):862–873.

[252] Elisabete, D.G.D.P.. The deceleration of giant herbig-haro flows. The Astrophysical Journal 2001;551(1):347.

[253] De Gouveia dal Pino, E., Benz, W.. Three-dimensional simulations of protostellar jets. The Astrophysical Journal 1993;410:686–695.

[254] Robinson, M., Monaghan, J.J.. Direct numerical simulation of decaying two-dimensional turbulence in a no-slip square box using smoothed particle hydrodynamics. International Journal for Numerical Methods in Fluids 2012;70:37–55.

[255] Violeau, D., Issa, R.. Numerical modelling of complex turbulent free-surface flows with the SPH method: an overview. International Journal for Numerical Methods in Fluids 2007;53(2):277–304.

[256] Chaniotis, A.K., Poulikakos, D., Koumoutsakos, P.. Remeshed Smoothed Particle Hydrodynamics for the Simulation of Viscous and Heat Conducting Flows. Journal of Computational Physics 2002;182(1):67–90.

[257] Xiong, Q.G., Li, B., Xu, J.. GPU-accelerated adaptive particle splitting and merging in SPH. Computer Physics Communications 2013;184(7):1701–1707.

[258] Kitsionas, S., Whitworth, A.P.. Smoothed Particle Hydrodynamics with particle splitting, applied to self-gravitating collapse. Monthly Notices of the Royal Astronomical Society 2002;330(1):129–136.

[259] Vance, S., Brown, J.. Layering and double-diffusion style convection in europa's ocean. Icarus 2005;177(2):506 – 514. Europa Icy Shell.

[260] German, C.R.. Hydrothermal exploration and astrobiology: oases for life in distant oceans? International Journal of Astrobiology 2004;3:81–95.